Faculty of Textile Engineering
Technical University of Liberec

STRUTEX

Structure and Structural Mechanics of Textile Fabrics

Struktura a strukturní mechanika textilií

24th international conference
24. mezinárodní konference

2024

CONFERENCE BOOK

SBORNÍK TEXTŮ

IN COOPERATION WITH

PARTNERS

SPONZORS

CLUTEX - cluster technical textiles

WE ASSOCIATE MANUFACTURERS OF TECHNICAL TEXTILES IN THE CZECH REPUBLIC. WE CONNECT TEXTILE, CHEMICAL, ENGINEERING AND OTHER SECTORS WITH COMMON RESEARCH TOPICS AND PROJECTS.

OUR MEMBERS TRANSFER SCIENCE AND RESEARCH INTO PRACTICE EVERY DAY.

CLUTEX, THAT IS:

1 the only textile cluster in the Czech Republic

17 years of experience, CLUTEX was founded in Hejnice in 2006

33 member companies

24 mil. EUR value of implemented projects

www.clutex.cz

clutex
cluster technical textiles
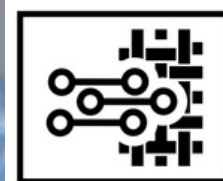
Co-funded by
the European Union

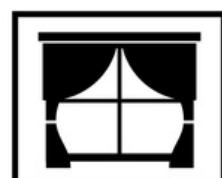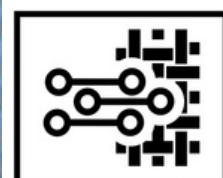**Healthtex** **Sporttex** **Indutex** **Protex** **Smarttex**

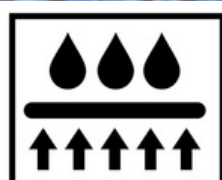**Clothtex** **Haberdashery** **Geotex** **Hometex** **Smarttex**

Autotex **Packtex** **Functional apparel** **Bonded** **Composites**
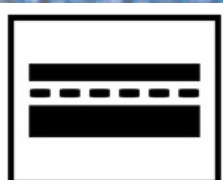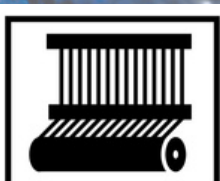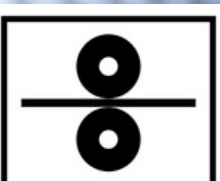
Machinery **Finishing** **Education** **Testing** **R&D**

MEMBERS

They are flexible and established companies that actively participate in creating new trends in the field of technical textiles. Among our members you will find SMEs as well as large enterprises, manufacturing companies or research institutes and universities.

Looking for a supplier or research partner?
A list of members with contacts will help you here:
More information about CLUTEX and membership options can be found on the website.

The most beloved sights of ^Liberec
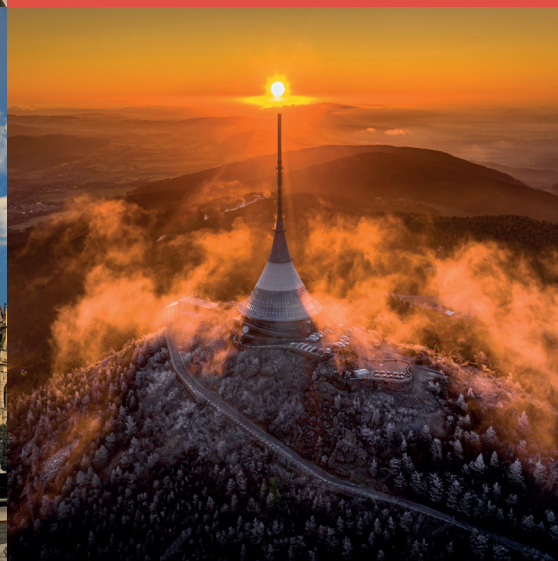
Visit^Liberec

City Information Centre
nám. Dr. E. Beneše 23, Liberec
phone: +420 485 101 709
e-mail: info@visitliberec.eu
www.visitliberec.eu, www.liberec.cz
www.facebook.com/visitliberec
#visitliberec

We greatly appreciate Technical University of Liberec for education of students in the field of textile. Without next generation textile experts we can not keep working and would be not able to develop new products.

with thanks

Caledon textile

People.Health.Care.

The Lohmann & Rauscher Company
is an international company
with a long history.
It has over 160 years
of experience in making
dressing materials
and medical devices
and it has always focused
on the needs of its
customers and patients.

The company is a world-leading supplier of medical devices and hygiene products of the highest quality. It develops individual solutions to the problems of patients and healthcare workers worldwide, from classic dressing materials, to modern therapy systems.

Plant in Nová Paka
Lohmann & Rauscher s.r.o.
Legií 265
509 01 Nová Paka
Czech Republic

Plant in Slavkov
Lohmann & Rauscher s.r.o.
Bučovická 256
684 01 Slavkov u Brna
Czech Republic

Headquarters • General inquiries
Telephone: +420 544 425 601
Fax: +420 544 227 331
E-mail: info.slavkov@cz.LRmed.com
https://www.lohmann-rauscher.com

Rieter CZ s.r.o.

Ústí nad Orlicí

Rieter CZ s.r.o. is part of the Swiss Rieter Group, which is one of the world's leading manufacturers of textile machinery and complete textile systems. Rieter CZ s.r.o. is characterised by a strong emphasis on innovations developed in the company's development centre. Other features include precision production of textile machines and components for modern technologies and processes.

www.rieter.cz • www.rieter.com

RIETER

ADFORS
People are our strength

2 production plants - in Litomyšl and Hodonice

more than **2000** employees

turnover **7.8 bn CZK**

120k tons of glass fibre per year

6 brands of unique glass fibre production

PEOPLE ARE OUR STRENGTH SO THEY ARE OUR FIRST PRIORITY.

Thanks to this approach, we already have been certified as a Top Employer for the last few years.

top EMPLOYER
CZECH REPUBLIC 2018
CERTIFIED EXCELLENCE IN EMPLOYEE CONDITIONS

We are still growing and investing in both our employees and our technology too.

Working for us is very fulfilling. Come and join us!

CONTACTS

HEADQUARTERS AND LITOMYŠL PLANT

SAINT-GOBAIN
ADFORS CZ s.r.o.
Sokolovská 106
570 01 Litomyšl

+420 461 651 111

HODONICE PLANT

SAINT-GOBAIN
ADFORS CZ s.r.o.
Zahradní 256
671 25 Hodonice

+420 515 207 111

HR department
kariera.adfors@saint-gobain.com

www.adfors.cz

PRAGUE

LITOMYŠL PLANT

HODONICE PLANT

SAINT-GOBAIN

STAP a.s. – Narrow Fabrics Manufacturer from Czech Republic

Our products are tailored to meet exacting specifications established by a number of NATO military forces. STAP a.s. is a major webbing manufacturer of military webbings, bindings and elastics to meet specifications in both IRR webbings and non-IRR webbings.

We are one of the few webbing suppliers who can offer our own in-house dying facilities to colour match to forces exacting shade requirements.

Our Multi Colour Camo printed webbing (up to 5 colours) is widely used on a variety of PLCE (Personal Load Carrying Equipment), MTP Webbing Systems & Pouches, Molle Webbing along our latest IRR Camo printed binding, designed to be used in conjunction with The Multi-Terrain Pattern (MTP) camouflage print.

We can offer bespoke custom printed webbing to match your military camouflage textile pattern.

Special treatments can be applied to the webbing straps including anti-bacterial, rotproof, water-repellent and flame-retardant finishes.

Webbings are cut to length and heat-sealed using our automatic machines and we are also able to offer a cutting and holing service using our ultrasonic facility.

Here we are able to create a wide range of made-up units, sewn webbing straps also with buckles.

We can also offer wide range of comercial products, like webbings, elastics, binding tapes, zippers, woven labels, braids, jacquard ribbons… **www.stap.cz**

Schoeller Křešice s.r.o.

is a major producer of combed wool, mixed and technical yarns.

The history of this factory dates back to 1907, and since then, worsted yarns have been continuously produced here. Since 1995, our company has been part of an Austrian group

Schoeller Spinning Group,

which is among the largest European suppliers of worsted yarn. This group is known on the market mainly due to its wide portfolio of yarns produced in the Czech Republic and close cooperation and customer orientation, for whom it strives to develop and adapt products according to their specific needs.

The largest part of the production portfolio consists of yarns that, thanks to their functional properties, are used for the production of firefighting suits (PBI), wool covers for electric cars (BMW, Volvo), airplanes or trains, as well as aramid yarns for the army, mixed for outdoor clothing, for the sock industry, but also conductive (Inox metal fibers) and core Dref 3.

Since 2018, the Schoeller Spinning Group has been part of a multinational company

Indorama Ventures Company.

Faculty of Textile Engineering
Technical University of Liberec

24th international conference
24. mezinárodní konference

STRUTEX

Structure and Structural Mechanics of Textile Fabrics

Struktura a strukturní mechanika textilií

CONFERENCE BOOK

SBORNÍK TEXTŮ

December / Prosinec 2024
Faculty of Textile Engineering
Technical University of Liberec

<u>President of the conference</u>

prof. Ing. Bohuslav Neckář, DrSc.
Technical University of Liberec

<u>Scientific committee</u>

prof. Luboš HES	Technical University of Liberec, Czech Republic
prof. S. M. ISHTIAQUE	Indian Institute of Technology Delhi, India
prof. Oldřich JIRSÁK	Technical University of Liberec, Czech Republic
prof. Yordan KYOSEV	Technische Universität Dresden, Germany
prof. Jiří MILITKÝ	Technical University of Liberec, Czech Republic
prof. Bohuslav NECKÁŘ	Technical University of Liberec, Czech Republic
dr. Vincent PLACET	University of Franche-Comté, France
prof. Jakub WIENER	Technical University of Liberec, Czech Republic
assoc. prof. Lukáš ČAPEK	Technical University of Liberec, Czech Republic
assoc. prof. Marcin BARBURSKI	Lodz University of Technology, Poland
assoc. prof. Brigita KOLČAVOVÁ SIRKOVÁ	Technical University of Liberec, Czech Republic
assoc. prof. Maroš TUNÁK	Technical University of Liberec, Czech Republic

CONTENTS

Evelyn SCHWEYNOCH

Institution:

M.A. Art History | Textile and Costume History
Director of the German Damask and Terry Cloth
Museum

Research Interest:

Head of the German Damask and Terry
Museum. Curator of the textile. Costume design
and make-up design.

Keynote Lecture:

TEXTILE HISTORY IN LUSATIA - AN OVERVIEW.

Short biography:

Studied art history, modern and contemporary history and Saxon regional history at the TU Dresden. Previously a women's tailor and costume assistant at the Saxon State Opera in Dresden. Several years of employment in museums with responsibility for textile collections. Since May 2022, head of the German Damask and Terry Museum. Current and recent projects: Head of the German Damask and Terry Museum in Großschönau, Lecturer at the Dresden University of Fine Arts for costume design and make-up design, Part of the team at the Kleinod shop gallery, Dresden. Past projects: Project manager for the scientific development of the sample archive of the former Tannenhauer weaving mill in Braunsdorf/Chemnitz, Research to create a replica of the Nochten traditional costume in the Sorbian Museum in Bautzen, replication of the traditional costume, Research into a stylistic history of Plauen lace for the Vogtlandmuseum Plauen, Advising the Waldenburg Natural History Cabinet and the Chemnitz Art Collections on the accessibility of exhibitions with a view to the added value for everyone, Special tours of the permanent exhibition "Electoral Wardrobe" in the Armory Chamber of the Dresden State Art Collections, Supervision of a Munich private collection of Gertrud Kleinhempel objects for digitization for the Deutsche Fotothek, Development of a pilot study to improve target group-oriented communication of museum offerings and building conditions for people with disabilities and development of projects to reduce barriers for the Saxon State Office for Museums, Employee in the digitization project "Die Gute Form" for the Deutsche Fotothek, Technical support for the exhibition "Silk, velvet and fine thread. Upper Lusatian clothing in the 19th century" in the Bautzen Museum, Curator of the textile collection in the GRASSI Museum for Applied Arts Leipzig, Employee in the provenance research project "Daphne" in the Museum of Saxon Folk Art with the puppet theater collection of the Dresden State Art Collections.

prof. Dr. Ing. Math. Yordan Kostadinov KYOSEV

Institution:

Chair of Development and Assembly of Textile Products, ITM, TU Dresden, Germany

Research Interest:

TBody Scanning, clothing development, material parameters of textile structures, geometrical and mechanical modeling of knitted and braided structures; application of FEM for the modelling of fiber and yarn based structures; braiding machines and technology; fuzzy logic.

Keynote Lecture:

MULTISCALE MODELLING OF SEWING SEAMS AND THE INTERACTION BETWEEN THE TEXTILE FABRICS AND SEWING THREADS.

Short biography:

His early carrier started in Sofia, Bulgaria at the Department of Textiles, where he was 1997 to 1999 as PhD student and external assistant processor and 1999-2003 as assistant professor for design of textile and sewing machines. 2003-2005 he acted as the Head Assistant Professor with the main teaching topics: knitting technology, design of textile and sewing machines, numerical methods in the Faculty of Applied Mathematics, technical mechanics (statistics, kinetics, dynamics, strength of materials) in the German Faculty for Engineering Education. After one year (2005-2006) at ITA- RWTH Aachen with Alexander von Humboldt Fellowship, he was appointed in 2006 as Professor at Hochschule Niederrhein-University of Applied Sciences, Mönchengladbach, Germany. In terms of teaching he was focused on: Textile Materials, Textile Technology – especially narrow woven and braided fabrics, Textile testing and quality management, Finite element modelling for textiles, Numerical simulation. In 2011 he founded the company TexMind UG, within which frame he provide industrial CAD software solutions for braiding, warp and weft knitting. In August 2019 he was appointed as professor and head of the Chair of development and assembly of textile products, ITM, TU Dresden. Germany. His team perform research in the area of 3D and 4D body scanning, functional clothing development and simulation, additive manufacturing, sewing and welding machines, automation and robotisation in the apparel production. Prof. Kyosev is editor-in-chief of Journal of Engineered Fibers and Fabrics (IF2.9); founder and co-editor in chief of the diamond open access journal "Communications in Development and Assembling of Textile Products" www.cdatp.org. He is author of the books "Braiding technology for textiles", "Warp knitting Fabrics construction", "Topology based modelling of textile fabrics and their assemblies", many book chapters and co-author of more over fifty papers in peer review journals and many conference works.

prof. Ing. Bohuslav NECKÁŘ, DrSc.

Institution

Professor on the Department of Technologies and Structures, Textile Faculty, Technical University of Liberec, Czech Republic.

Research Interest

Mathematical modeling of geometry and mechanics of fibrous assemblies of different textile structures, internal structures and mathematical modeling of yarns, modeling of woven and knitted fabrics, theoretical solving of directional orientation and mechanics of fibers in fiber layers and fibrous composites.
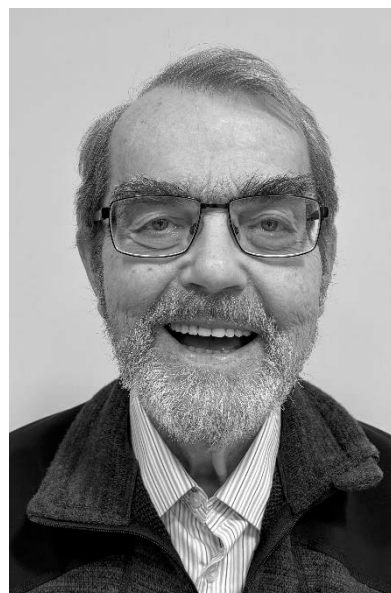
Keynote Lecture

DEVELOPING OF THEORY OF STRUCTURE AND MECHANICS OF TEXTILE FIBER PRODUCTS

Short biography

Born 1943 in Czechia. Graduated on University of Liberec – Ing. 1967, CSc. 1976, DrSc. 1991, assoc. prof. 1990, professor 1993. His professional carrier started in the research and development section of textile technologies in State Textile Research Institute (1967-1990). He solved different problems of spinning of yarn and applying them to the development of modified types of woven and knitted fabrics. He was co-operated also on the field of non-woven structures. In May 1990 he started academic carrier on the Textile Faculty (then VŠST, now the Technical University of Liberec – TUL) as professor, head of Department of spinning, later Department of textile structures, and vice – dean of faculty for science and development. Four years he was also the member of Academy Council of Czech academy of Science. As the professor of textile structures he created two new subjects oriented to the mathematical theory of textile fiber structures (fiber layers, yarns, woven and knitted fabrics, non-woven fabrics). They are teaching on TUL as well as on Indian Institute of Technology, Delhi (IITD) till now. For presentation of his concept to IITD students, prof. Neckář was 16 years invited to Delhi as the "honorary professor". Beside lot of journals articles Prof. Neckář published 3 original monographs. The first was "Yarn, building, structure, properties" (1990, in Czech). Others two monographs - "Theory of Structure and Mechanics of Fibrous Assemblies" (2012), and "Theory of Structure and Mechanics of Yarns" (2018) – he published together with his earlier PhD student D. Das.

prof. Marie-Ange BUENO

Institution:

ENSISA / University of Haute Alsace, Laboratory of Textile Physics and Mechanics

Research Interest:

Tribology of textile materials at fiber, yarn and fabric scales with a specific focus on skin-textile friction; knitting technology.

Keynote Lecture

SKIN-TEXTILE CONTACT AND FRICTION

Short biography

Marie-Ange BUENO is a textile engineer since 1991. She received her PhD in Engineering Sciences in 1995 from the University of Haute Alsace, in Mulhouse. She became assistant professor in 1997 and she is Full Professor since 2005 at the University of Haute Alsace and more particularly at the school of engineering, Ecole Nationale Supérieure d'Ingénieurs Sud Alsace (ex-ENSITM), and the Laboratory of Textile Physics and Mechanics. She teaches to students in both the Textile & Fibres and Mechanics diplomas. She was the head of the mechanical department of ENSISA and from 2015 to 2023 she was the head of the Laboratory of Textile Physics and Mechanics. She created with Prof. René Rossi from Empa, the French-Swiss Textile Research Group in 2017. She co-created and she is the deputy manager of a French research group dedicated to tactile (GDR CNRS TACT) since 2018. Her two research and teaching fields are knitting and tribology of fibrous materials from the fibre to the fabric. Since her doctoral thesis, she is particularly interested to textile-skin friction.

GEOMETRIC AND MECHANICAL MODELING OF WEFT-KNITTED FABRICS USING HELICOID SCAFFOLDS

David Breen[1*], Paras Wadekar[1], Chelsea Amanatides[2], Genevieve Dion[2], Randall Kamien[3]

[1]Department of Computer Science, Drexel University, Philadelphia, PA, USA
[2]Center for Functional Fabrics, Drexel University, Philadelphia PA, USA
[3]Department of Physics and Astronomy, University of Pennsylvania, Philadelphia, PA, USA
* 3675 Market Street, Philadelphia, PA 19119, USA, +1 215-895-2669, david@cs.drexel.edu

Abstract:

We present a bicontinuous, minimal surface (the helicoid) as a scaffold on which to define the topology and geometry of yarns in a weft-knitted fabric. Modeling with helicoids offers a geometric approach to simulating a physical manufacturing process, which should generate geometric models suitable for downstream analyses. The centerline of a yarn in a knitted fabric is specified as a geodesic path, with constrained boundary conditions, running along a helicoid at a fixed distance. The shape of the yarn's centerline is produced via an optimization process over a polyline. The distances between the vertices of the polyline are shortened and a repulsive potential keeps the vertices at a specified distance from the helicoid. These actions and constraints are formulated into a single "cost" function, which is then minimized. The yarn geometry is generated as a tube around the centerline. The optimized configuration, defined for a half loop, is duplicated, reflected, and shifted to produce the centerlines for the multiple stitches that make up a fabric. The approach provides a promising framework for estimating the mechanical behavior/properties of weft-knitted fabrics. Fabric-level deformation energy may be estimated by scaling the helicoid scaffold, computing new yarn paths, determining the amount of ensuing yarn stretch, and computing the total amount of yarn stretching energy. Computational results are calibrated and verified with measurements taken from actual yarns and fabrics.

Key words:

Minimal surface, computational modeling, weft-knitted fabrics, yarn geometry, optimization

1. Introduction

The calculus of variations is the cornerstone of classical mechanics, elasticity theory, and modern economics. When physical models are formulated as optimization problems, the equations governing motion, stretching or bending describe critical points of the objective function [8]. When the objective depends on geometric quantities, the minima, maxima, and other extrema are likewise geometric. Functionals of length lead to geodesic equations (shortest length), while functionals of area lead to minimal surfaces. Soap bubbles, for instance, minimize their area subject to a volume constraint leading to Plateau's classic rules for foams [14].

Since minimal surfaces are the solutions to many extremal problems in physics, we posit that they may be used to define the topology and shape of yarns in a weft-knitted fabric. In previous work, we demonstrated, with physical prototypes, how yarns of a weft-knitted fabric may lie on a scaffolding of alternating left- and right-hand helicoids, a type of minimal surface, with the form of the helicoids producing the characteristic spatial relationships between the yarns [7]. Here, we summarize the mathematics and algorithms that create geometric models of the yarns making up a weft-knitted fabric, which exploit the lattice-like structural features of bicontinuous helicoid surfaces. See Wadekar et al. [18,20] for more details. The centerline of the yarn is specified as a geodesic path, with constrained

boundary conditions, running along a helicoid at a fixed distance. The yarn geometry is then generated as a tube around the centerline. The helicoid therefore acts as a scaffold on which to define the shape of the yarns and their intertwinings.

The shape of a yarn's centerline is produced via an optimization process over a polyline [21]. The polyline is initially placed over a helicoid in the approximate configuration that will define a half loop of a stitch. The distances between the vertices of the polyline are shortened and a repulsive potential keeps the vertices at a set distance from the helicoid. In addition, the locations of the polyline's endpoints are constrained. This process effectively models the shrinking of the initial polyline, while performing collision detection/avoidance with the scaffold surface, producing a geodesic path along the helicoid. These actions and constraints are formulated into a single "cost" function, which is then minimized. The optimization process modifies the vertices to produce a minimum cost configuration that balances the inter-vertex stretching cost with the repulsive cost from the helicoid. This configuration, defined for a half loop, is then duplicated, reflected, and shifted to produce the centerlines for the multiple stitches that make up a fabric.

Surface scaffolds have been explored in the context of weft-knitting because they are able to produce physically plausible geometric models of yarns. Additionally, when keeping the yarn models on opposite sides of the scaffold surface, the form of the surface provides the critical function of maintaining the topology and spatial relationships between the yarns; thus removing the need to compute yarn-yarn intersections. An even more important feature of this approach is that it provides a framework for analyzing the mechanical properties of knitted fabrics. Deformations may be applied to the underlying scaffold, while the yarns stay in contact with the deformed surfaces. Energies of deformation are then computed at the yarn level to derive the mechanical properties of the fabric as a whole. Since these mechanical properties are computed via the geometric solutions furnished by the supporting surfaces, the scaffold-surface approach enables an efficient analysis technique that should support rapid exploration of the fabric's design space. This approach provides a potential alternative to compute-intensive FEM methods for estimating the mechanical behavior of knitted fabrics.

2. Related Work

The first published system to model and visualize complete knitted fabrics was developed by Eberhardt et al. [4,13]. Their system (KnitSim) accepts Stoll knitting machine commands and simulates the knitting process to produce an explicit topological representation of a knitted fabric, which can then be used to generate a 2D geometric layout of the fabric. Two decades later, a system with similar capabilities was developed by Counts [3]. Lin et al. [9] developed a modeling approach/system that works on various scales to model the yarns in and predict the mechanical properties of textiles, including knitted fabrics.

In ground-breaking work Kaldor et al. [5,6] simulated complete swatches and articles of clothing consisting of knitted fabrics by modeling the geometry and physics of individual yarns in these items. This work was extended by Yuksel et al. [23] and Wu et al. [22] to produce Stitch Meshes, an approach to generating Kaldor-style, yarn-level geometric models of knitted clothing from polygonal models that represent the clothing's surface. Cirio et al. [2] define a topological representation of knits consisting of a limited set of stitches. They developed a mechanical model based on the representation for the simulation of knitted clothing, which has been incorporated into a hybrid yarn/triangle model [1]. Liu et al. [10,12] perform Finite Element Modeling simulations of knitted fabrics based on solid yarn-level geometric models [19].   Others [11,15,17] utilize a homogenized model to simulate the mechanical behavior of knits.

Our work is novel compared to previous efforts in that it utilizes a helicoid-like bicontinuous surface to define the geometry and topology of yarns in a weft-knitted fabric. More importantly, it provides a unique approach for estimating the stretching energy of the fabric.

3. Yarn Model Definition

3.1. _Helicoid scaffold model_

The bicontinuous surface formulation employed as a yarn model scaffold is defined over u and v as a surface S such that

$$S(u, v) = [x, y, z], \tag{1}$$

where _x_ and _y_ are independent variables, and z is the set of values that satisfy Equation 2.

$$\tan z = \sin x \,/\, \cos y \tag{2}$$

Equation 2 defines a trigonometric approximation to the triply-periodic Schwarz D (Diamond) minimal surface, which has been shown to model physical structures (e.g., liquid crystalline phases) [4]. Equation 2 can be solved for z to produce

$$z = \tan^{-1}(\sin x \,/\, \cos y), \tag{3}$$

which defines a single z value for every (x, y) pair. Scale factors can be added to Equation 3 in order to control the size and spacing of the helicoids, which in turn scale the yarn models lying on them.

$$z = \gamma \tan^{-1}(\sin \eta x \,/\, \cos \varphi y), \tag{4}$$

where η and ψ control the spacing between the central axes of the helicoid structures in the x and y directions. The distance between the axes is π when η = ψ = 1. γ controls the height of each helicoid cycle, with the height of one cycle being 2π when γ = 1.

3.2 _Computing the yarn configuration_

The total configuration cost of the yarn is the sum of the costs computed at N −1 of the N vertices of the polyline that approximate it.

$$E_{total} = \sum_{i=1}^{N-1} E_{total}^i \tag{5}$$

The total cost associated with vertex i is given by

$$E_{total}^i = \alpha E_{len}^i + \beta E_{dist}^i. \tag{6}$$

The cost term used to shrink the yarn is

$$E_{len}^i = (Length^i - TargetLength)^2, \tag{7}$$

where $Length^i$ is the distance between vertex i and vertex i +1 and TargetLength is parameter that is adjusted in order to shorten the polyline. E_{dist}^i maintains the distance constraint between the polyline and the helicoid scaffold and is defined as

$$E_{dist}^i = (d^i - R_y)\log(d^i/R_y). \tag{8}$$

d^i is the distance between vertex i and the helicoid scaffold and R_y is the yarn radius. The distance cost is only computed for d^i values less than R_y. The equation is defined in this form in order to go to infinity at d = 0 and to have a value and derivative of 0 at d = R_y .

4. Generating Geometric Models

Polylines were placed over a helicoid scaffold defined by Eq. 4. The cost of the polyline, as defined by Eqs. 5 through 8, was minimized to produce a geodesic path on the scaffold. Tube-like geometry, with radius R_y, was defined around the polyline to produce solid geometric models of yarns in swatches of single Jersey, rib and garter knitted fabrics. The surface of the helicoid scaffold is shown in Fig. 1 (Left). A model of single loop of yarn is shown in Fig. 1 (Right). The color-coding of the surface demonstrates that the yarn remains on one side of the scaffold.
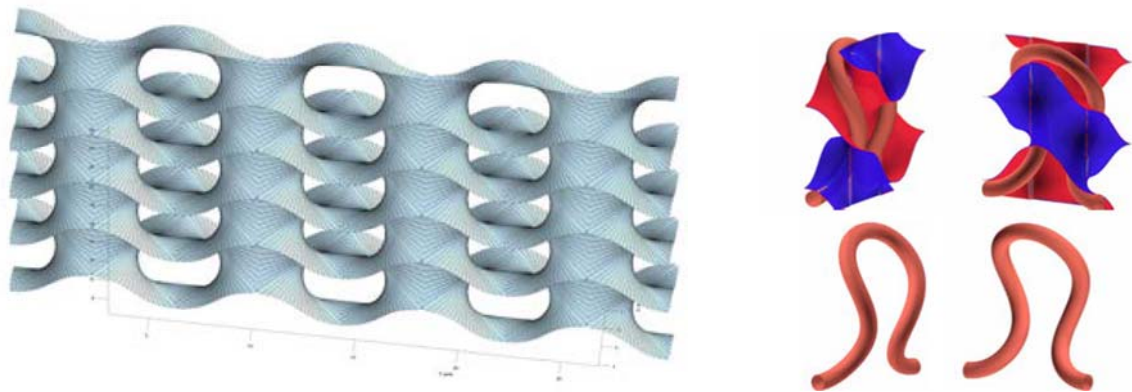
Figure 1. (Left) The helicoid scaffold surface. (Right) A model of a single loop of yarn is shown with and without the associated scaffold.
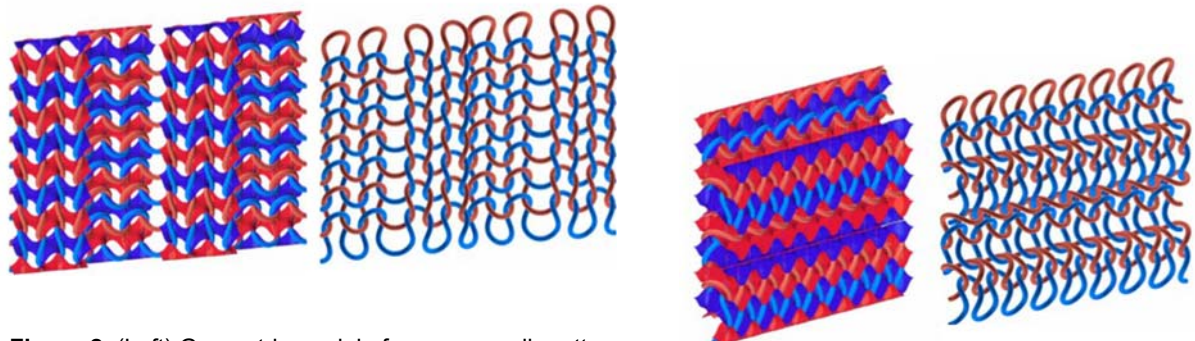
Figure 2. (Left) Geometric model of yarns on a rib pattern.
(Right) Geometric models of yarns in a garter pattern.

Figure 2 (Left) presents the yarn geometric model of an 8 x 8 swatch of stitches in a rib pattern (alternating columns of Knit and Purl stitches), with and without the helicoid scaffold. Figure 2 (Right) presents the yarn geometric model of an 8 x 8 swatch of stitches in a garter pattern (alternating rows of Knit and Purl stitches), with and without the helicoid scaffold. These results can be produced in several (5 to 10) seconds on a standard PC.

5. Estimating Fabric Stretching Energy

The helicoid scaffold model for knitted fabrics provides a framework for estimating the mechanical properties of a weft-knitted fabric. Specifically, the model supports the computation of the stretching deformation energy of the fabric. The process is detailed in Figure 3. The general approach involves stretching the scaffold that defines the yarns in the fabric and computing the tensile strain energy of the yarns arising from the fabric stretching deformation.
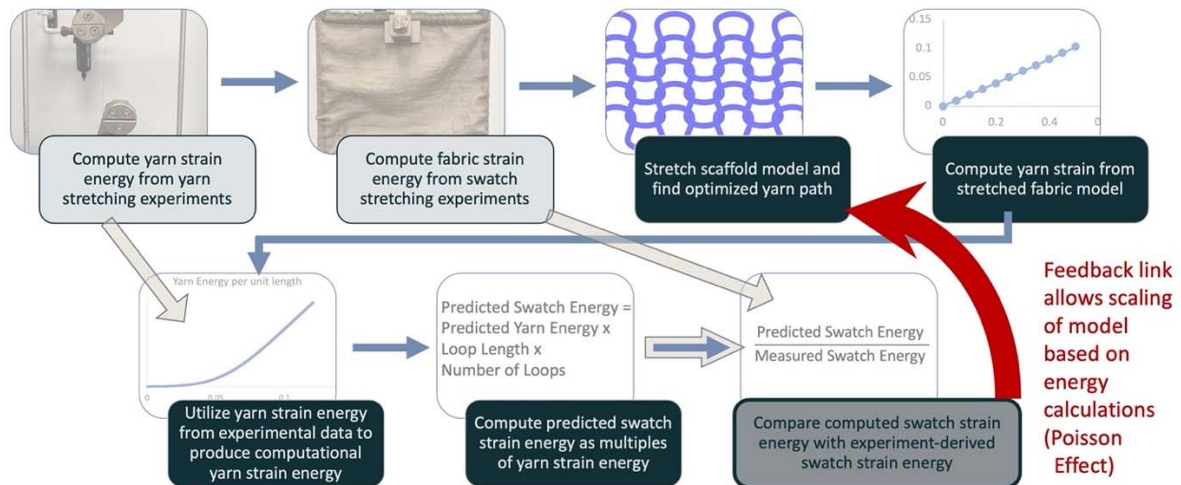
Figure 3. Process for computing fabric stretching energy using helicoid scaffolds.

The following outlines the steps in the process of computing knitted fabric stretching energy.

- Acquire force vs. displacement data for a yarn. Produce an all-Knit (single Jersey) fabric swatch from the yarn. Acquire force vs. displacement data for the knitted swatch.

- Convert the force vs. displacement data for the yarn into energy per unit length vs. strain by calculating the area under the curve.

- Convert the force vs. displacement data for the swatch into energy per unit swatch length vs. strain by calculating the area under the curve.

- Generate the yarn-level helicoid model using the size parameters of the fabric's stitches. The scale parameters for the loops are derived from the knitted swatch. (# stitches in a row/width of swatch; # rows/height of swatch).

- For a given amount of fabric stretching, generate the associated yarn-level helicoid models with stretched loops by increasing the scaffold width by the given swatch strain values.

- Decrease the scaffold thickness for these helicoid models and reoptimize the yarn path on the scaffold to adjust for the Poisson Effect.

- Compute the yarn strain for the stretched model compared to the original undeformed yarn model.

- Find the corresponding yarn energy per unit length for these yarn strain values using the yarn energy per unit length vs. strain data obtained earlier.

- Multiply the yarn energy per unit length by the loop length obtained from the undeformed yarn model to produce the energy per loop.

- Compute the final swatch energy prediction by multiplying the energy per loop by the total number of stitches in the swatch.

- Find the energy per unit length of the knitted swatch using the swatch energy per unit length vs. strain data obtained earlier.

- Multiply this swatch energy per unit length by the initial swatch length to obtain the measured swatch energy.

- Compare the model-based computed swatch energy with the measurement-based computed energy.

5.1 *Acquiring force vs. displacement data*

We measured the mechanical properties of a Merino wool yarn (Supra Merino, Silk City Fibers, New Jersey) with 3.5 twists per centimeter. Samples of the yarn were placed into a Shimadzu load frame, using capstan grips specifically suited for testing of yarns. The distance from grip to grip was 250 mm. The yarns were then pulled to breaking at a rate of 0.01 meters per second. This speed, which is close to the maximum speed for the Shimadzu load frame (max speed 0.016 m/s), was chosen to be as similar as possible to manufacturing speeds available on Shima Seiki weft knitting machines (minimum speed of 0.03 meters per second). Force and displacement data was recorded. See Figure 4 for the testing equipment and the results of measuring ten yarn samples.

The force vs. displacement data from four jersey fabric samples stretched in the wale direction is shown in Figure 5, with the displacement normalized to strain (mm/mm). It can be seen that each of the curves are well matched to the others, demonstrating consistent deformation behaviors.
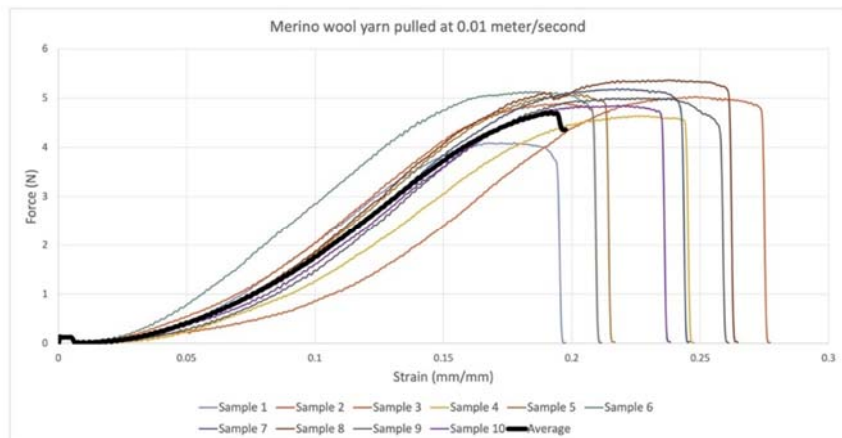
Figure 4. (Left) Merino wool yarn loaded in capstan grips on the Shimadzu load frame. (Right) Force vs. strain data for 10 samples of Merino wool yarn.

5.2 *Computing yarn and swatch deformation energy*

From the averaged force vs. displacement curves of the yarn, we can compute the force vs. strain values by dividing the displacement by the rest length of the yarn. Integrating force with respect to strain, which is effectively finding the area under the force vs. strain curve, gives us energy per unit length of the yarn.
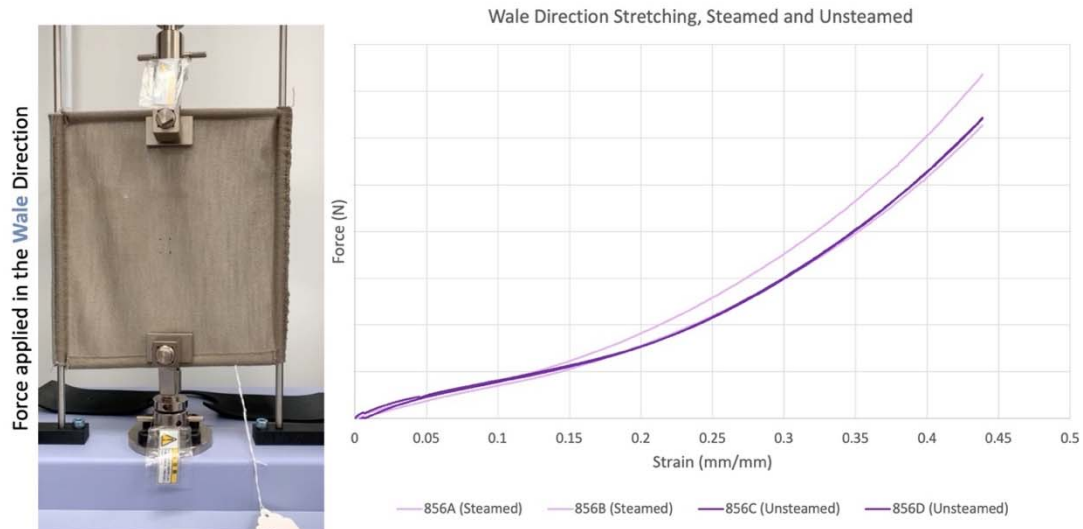
Figure 5. Stretching a single Jersey fabric with Merino wool yarn in the wale direction; (Left) experimental setup, (Right) force vs. strain data.

This is then multiplied by the yarn length to obtain the energy in a stretched yarn. This approach allows us to now measure the stretching behavior of actual yarns and incorporate their measured behavior in our computational models.

The process of computing the measured swatch energy is similar to that of the yarn energy. We stretch the swatch in the wale direction and plot the force vs displacement curve for this stretching. This is then converted to a force vs. strain curve by dividing the displacement by the total wale length of the swatch at rest. The area under this curve gives us energy per unit wale length of the swatch for a given strain.

5.3 _Generating and stretching the helicoid model_

Given the loop scale parameters that are derived from the physical swatch, a yarn-level helicoid-based geometric model is computed using the methods described in Sections 2 & 3 and [5,6]. The shape of the yarn arises from its interaction with the helicoid scaffold. For a fixed set of strain values, the scaffold is stretched by the associated scale values in the wale direction, and the yarn model is updated. See Figure 6. In order to adjust the model for the Poisson Effect, the model should be scaled in the direction orthogonal to the plane of the fabric. The method utilized to compute this scale factor is described in Section 5.5.
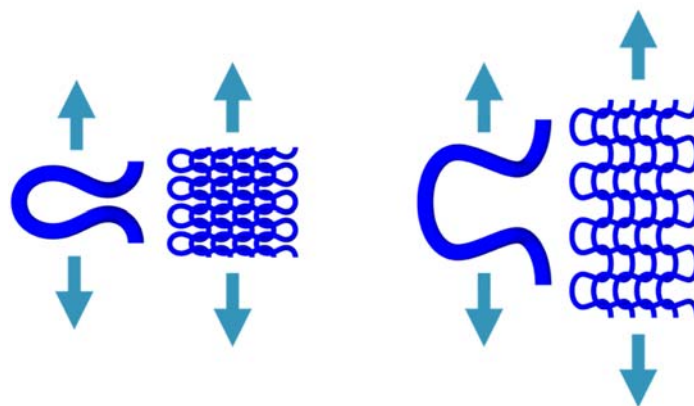
Figure 6. Stretching the helicoid yarn model in the wale direction.

5.4 _Computing swatch stretch energy from yarn stretch energy_

The length of the yarn through the fabric model is calculated both before and after the model is stretched, providing yarn strain vs. fabric strain data, as seen in the upper right block of Figure 3. The helicoid scaffold model plays a critical role in this step, allowing us to determine how much the yarn deforms as the fabric is stretched.

In the bottom left block of Figure 3, the experimental yarn strain data is combined with the computational yarn strain data to produce a data-derived yarn strain energy curve. The computed scaffold geometric model tells us how much the yarn strains during fabric stretching, the experimental yarn strain data then allows us to compute the amount of energy needed to stretch the yarn. In the next step, the predicted

swatch energy is computed by multiplying the length of a single loop, which is computed from the scaffold-based geometric model, by the predicted yarn strain energy, which gives us the energy needed to deform a single loop of yarn as the fabric is stretched. Multiplying this loop-level energy by the number of loops in the modeled swatch produces the predicted total energy needed to stretch the fabric sample.

In the final step the predicted swatch energy computed from the yarn-data-derived model is compared to the deformation energy that is based on the experimentally acquired swatch strain data. When this ratio is 1, the energy computed from our model exactly matches the energy that is acquired from measuring the associated fabric sample.
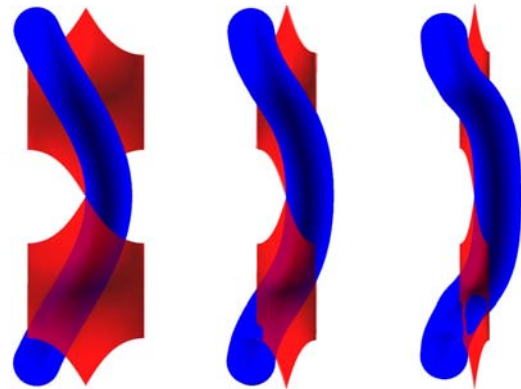
Figure 7. Effect of reducing scaffold thickness on loop shape and length.

5.5 _Adjusting fabric thickness_

In our initial experiments, we produced computational swatch stretch energies that matched the measured swatch energies to within a factor of 2, except when the fabric strain exceeded 15%, where the ratio of computed and measured energy was over 6. We hypothesized that the main source of this

high-strain anomaly was the absence of accounting for the Poisson Effect in the stretched computational model. To address this deficiency, we reran our computational pipeline and additionally adjusted the scaffold thickness to model the fabric thinning that occurs during stretching. See Figure 7. For each strain increment the scaffold thickness was decreased, with the yarn geometric model being accordingly modified. The scaffold thickness that produced an exact match between the computed and measured swatch energies was determined. This link, shown with the red arrow in Figure 3, forms a feedback loop that guides the adjustment of the thickness value.
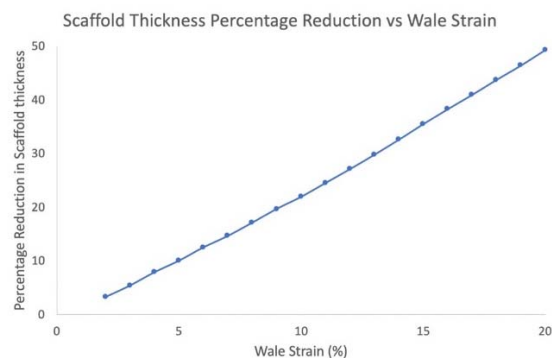
Figure 8. Scaffold thickness changes required to match the computed energy values to the measured values.

Table 1 contains some of the derived data from this task, showing the percentage reduction in scaffold thickness needed for various strain increments to produce the desired exact energy matches. Figure 8 presents a plot of all our percentage reduction of scaffold thickness vs. wale strain data. The data is observed to be linear with a very high R^2 value of above 99.8% in all the cases that were tested. The equation of the least-squares line fit to the data in Figure 8 is

$$\% \ thickness \ reduction = 2.6 \ \times \ wale \ strain - 3.2. \qquad (9)$$

The relation between the change in thickness of the fabric with respect to its stretching is similar to the Poisson Effect in solid materials. The linear relationship between swatch thickness reduction and wale strain provides encouraging evidence that our approach may be utilized to predict fabric deformation energies.

Table 1. Scaffold thickness reduction required to match the measured energy for different swatch strain values.

Swatch Strain (%)	Percentage reduction in scaffold thickness	Ratio of computed swatch energy values to measured swatch energy values
5	10.05	1.00
10	21.97	1.00
15	35.50	1.00
20	49.36	1.00

6. Discussion

The helicoid-based approach to estimating mechanical behavior demonstrates a number of advantages over more conventional methods. It shows promise for computing physical quantities of weft-knitted fabrics purely based on geometric calculations. Utilizing a helicoid, a type of minimal surface, as a scaffold for defining the topology and geometry of weft-knitted fabrics allows for the rapid calculation of yarn geometry, fabric deformation and deformation energy. These quickly produced results could support extensive exploration of the fabric's design space in a short amount of time. While the helicoid-based approach to estimating mechanical behavior of weft-knitted fabrics shows promise, it also clearly has several deficiencies. The swatch-level stretching energy calculations completely rely on the change in yarn length during fabric deformation, and do not include yarn bending energy and friction; two quantities that certainly affect knitted fabric mechanical behavior. It is notable though that experimental results can be computationally reproduced by just taking into account yarn stretching energies. It is also important to note that our results have been produced under low fabric strains, and it is anticipated that the relationship between yarn stretching energy and swatch stretching energy may change at higher strains, requiring additional model features and parameters for accurate prediction.

Finally, the helicoid-based approach provides a qualitative framework for analyzing and understanding the structural properties of knitted fabrics. For example, the approach readily explains, through an energy-based analysis, the curling behavior of knitted fabrics (Figure 9). Applying circular deformations to a single Jersey model and computing the total yarn stretching energy shows that bending backwards produces a lower energy configuration, compared to a flat and forward bent fabric; thus, explaining the natural curling behavior of the fabric, as seen in Figure 9 (Left). This conclusion can be reached purely through a geometric calculation and does not require a computationally intensive dynamic simulation.
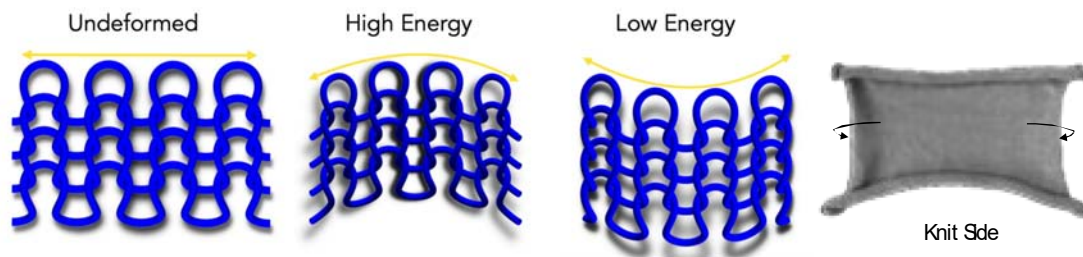
Figure 9. (Left) Generalized energy for two knit structure deformation modes. (Right) Natural curling of a single Jersey knitted fabric.

7. Conclusions

We have presented the mathematics and algorithms needed to utilize the helicoid, a bicontinuous, minimal surface, as a scaffold for defining the topology and geometry of yarns in a weft-knitted fabric. The geometry of a half-loop of yarn is specified as a geodesic path along the surface with fixed boundary conditions. This optimized path may be duplicated, reflected, and shifted to produce the centerlines for the multiple stitches that make up a fabric. The approach provides a promising framework for estimating the mechanical behavior/properties of weft-knitted fabrics. For example, fabric stretching energy may be estimated by scaling the helicoid scaffold, computing new yarn paths, determining the amount of ensuing yarn stretch, and computing the total amount of yarn stretching energy based on measurements of actual yarns. The total computed swatch stretching energy has been calibrated with the energy needed to stretch an associated actual knitted fabric. Additional research is required to advance the method towards a deployable design tool.

ACKNOWLEDGEMENTS

References

1. *Casafranca, J.J., Cirio, G., Rodrıguez, A., Miguel, E., Otaduy, M.A. (2020). Mixing yarns and triangles in cloth simulation. Computer Graphics Forum (Proc. Eurographics), 39, 101–110.*
2. *Cirio, G., Lopez-Moreno, J., Otaduy, M.A. (2017). Yarn-level cloth simulation with sliding persistent contacts. IEEE Transactions on Visualization and Computer Graphics, 23, 1152–1162.*
3. *Counts, J. (2018). Knitting with Directed Graphs. Master's thesis. Massachusetts Institute of Technology.*
4. *Eberhardt, B., Meissner, M., Strasser, W. (2000). Knit fabrics, in: House, D., Breen, D. (Eds.), Cloth Modeling and Animation. AK Peters. chapter 5, pp. 123–144.*
5. *Kaldor, J.M., James, D.L., Marschner, S (2008). Simulating knitted cloth at the yarn level. ACM Transactions on Graphics (Proc. SIGGRAPH), 27, 65:1–65:9.*
6. *Kaldor, J.M., James, D.L., Marschner, S. (2010). Efficient yarn-based cloth with adaptive contact linearization. ACM Transactions on Graphics (Proc. SIGGRAPH), 29, 105:1–105:10.*
7. *Knittel C.E., Tanis M., Stoltzfus A.L., Castle T., Kamien R.D., Dion G. (2019) Modelling textile structures using bicontinuous surfaces. Journal of Mathematics and the Arts, 14, 331–344.*

8. Lagrange J.L. (1772). *Essai sur une nouvelle methode pour determiner les maxima et minima des formules integrales indefinies. In: Miscellanea Taurinensia II., 173–195.*

9. Lin, H., Zeng, X., Sherburn, M., Long, A.C., Clifford, M.J. (2012). *Automated geometric modelling of textile structures. Textile Research Journal, 82, 1689–1702.*

10. Liu, D., Christie, D., Shakibajahromi, B., Knittel, C., Castaneda, N., Breen, D., Dion, G., Kontsos, A. (2017). *On the role of material architecture in the mechanical behavior of knitted textiles. International Journal of Solids and Structures, 109, 101–111.*

11. Liu, D., Koric, S., Kontsos, A. (2019). *A multiscale homogenization approach for architectured knitted textiles. Journal of Applied Mechanics, 86, JAM–19–1125.*

12. Liu, D., Koric, S., Kontsos, A. (2019). *Parallelized finite element analysis of knitted textile mechanical behavior. Journal of Engineering Materials and Technology, 141, MATS–18–1132.*

13. Meissner, M., Eberhardt, B. (1998). *The art of knitted fabrics, realistic & physically based modeling of knitted fabrics. Computer Graphics Forum (Proc. Eurographics), 17, 355–362.*

14. Plateau J. (1873). *Statique Expérimentale et Théorique des Liquides Soumis aux Seules Forces Moléculaires. Paris: Gauthier‐Villiard.*

15. Poincloux, S., Mokhtar, A.B., Lechenault, F. (2018). *Geometry and elasticity of a knitted fabric. Physical Review X, 8, 021075.*

16. Santangelo C., Kamien R. (2007) *Triply periodic smectic liquid crystals. Physical Review E, 75, 011702.*

17. Sperl, G., Narain, R., Wojtan, C. (2020). *Homogenized yarn-level cloth. ACM Transactions on Graphics (Proc. SIGGRAPH), 39, 48:1–48:16.*

18. Wadekar P., Goel P., Amanatides C., Dion G., Kamien R.D., Breen D.E. (2020). *Geometric modeling of knitted fabrics using helicoid scaffolds. Journal of Engineered Fibers and Fabrics, 15, pp. 1-15.*

19. Wadekar, P., Perumal, V., Dion, G., Kontsos, A., Breen, D. (2020). *An optimized yarn-level geometric model for finite element analysis of weft-knitted fabrics. Computer Aided Geometric Design, 80, 101883.*

20. Wadekar P., Amanatides C., Kapllani L., Dion G., Kamien R.D., Breen D.E. (2021) *Geometric modeling of complex knitting stitches using a bicontinuous surface and its offsets. Computer Aided Geometric Design, 89, 102024.*

21. Witkin A, Fleischer K, Barr A. *Energy constraints on parameterized models. In: Proc. ACM SIGGRAPH, July 1987, 225–232.*

22. Wu, K., Gao, X., Ferguson, Z., Panozzo, D., Yuksel, C. (2018). *Stitch meshing. ACM Transactions on Graphics (Proc. SIGGRAPH), 37, 130:1–130:14.*

23. Yuksel, C., Kaldor, J.M., James, D.L., Marschner, S. (2012). *Stitch meshes for modeling knitted clothing with yarn-level detail. ACM Transactions on Graphics (Proc. SIGGRAPH), 31, 37:1–37:12.*

THE RESISTANCE OF FIBER-REINFORCED 3D PRINTED STAB-PROOF ARMOR ELEMENTS: MATERIALS, GEOMETRIES, DIMENSION AND ORIENTATION

Dereje Berihun Sitotaw[1], Dominik Muenks[1], Yordan Kostadinov Kyosev[1]

[1]Chair of Development and Assembly of Textile Products, Institute of Textile Machinery and High Performance Material Technology, Faculty of Mechanical Science and Engineering, TU Dresden, 01069, Dresden, Germany
[2]Ethiopian Institute of Textile and Fashion Technology, Bahir Dar University, Bahir Dar, Ethiopia
Corresponding author email: dere96@yahoo.com

Abstract:

The majorities of stab protective armors limit several comfort parameters such as locomotion, movement, respiration, flexibility and weight which determine the efficient use by officers. Lightweight and effective protection with the necessary comfort parameters such as flexibility, respiration and free locomotion through the development of three dimensional printed (3DP) scales based on natural armors from fibers using continuous filament fabrication is the main objective of this research. In this study, stab protective armor scale-like elements with different materials, shapes, sizes and portions of a part investigated against stabbing force. Onyx, Aramid, carbon and different ratio Onyx/Kevlar by inserting fiber at different fiber filling angles $(0/45/90/135)_N$ were used in this investigation. The specimens were tested according to VPAM KDIW 2004. The result revealed that the scales with Onyx, Kevlar/Onyx and Kevlar fiber-reinforced protective scales failed while the carbon fiber resists the puncturing energy level K1 (25 J) with the penetration depth less than the maximum allowable penetration depth of the knife through the protectors. The large size protective elements and rectangular geometries withstand the impact energy relative to triangular geometries. The result revealed that the material type, its alignment, size and shapes of protection elements and portions of the scales where the weight dropped significantly influence the resistance against the impact energy to puncture with the intended energy level and sharp tipped knife.

Key words:

Protection armor, 3D printed scales, impact energy, penetration depth, fiber-reinforcement, geometries and their sizes, 3D printing, stab protection

1. Introduction

Protective clothing is one of the most important pieces of safety equipment to save lives. A stab resistant vest is a reinforced piece of body armor designed to resist knife or needle attacks specifically to the upper part of the body (chest, back and sides) and it can be worn either as covert or overt.
Early humans used comparatively primitive armors which were manufactured out of metal, horn, wood or leather lamellae [1, 2] but as civilizations evolved and knowledge advanced, body armor introduced. Then in the last century, with its two world wars, various attempts were made to advance the technology of body armor [1]. It was reported that the first soft body armor was developed by the Japanese and in that instance, was made of silk and was most effective against low-velocity bullets[3]. Thus the first so-called bullet-proof vests were designed in America in the two decades following World War I [4, 5] while the modern police body armor was introduced into practice in the 1970s [6].
Security officers are stabbed everywhere during their duty shift and most of the stabbed officers are killed immediately after stabbing by the suspected assailants. As the news and reports showed that the number of stabbed officers increased from year to year in developed countries, for example, in United

states of America, Germany, United Kingdom, but the stabbing frequency is more in developing, Saharan and sub Saharan countries [7-15]. The main reason for fatal injury is the officer's negligence to wear protective armor vest during their duty shift because most armor vests are heavy, non-permeable and reluctant mode of the officers. With all these limitations of most of the current armor vests police officers, military, transport and correction administrators should encourage their staffs to wear stab vests during the whole duty shift to save them from a fatal injury if stabbed in torso [16]. Armor vests might not be universal but has to be designed according to the level of protection, type of weapons and techniques of stabbing by assailants in the region with the desired comfort. The level of protection required in soft and sensitive bodily regions is determined by the type of attacks that are likely to be encountered [17]. The design of appropriate stab vests with the desired level of protection can be challenging for a wide range of weapons which are used for puncture and the stabbing techniques are different depending on assailants [18].

Though protection and comfort are conflicting, body armors for stab protection should also consider [19] flexibility and other ergonomic issues for acceptance along with coverage and duration [20-22].

The selection of advanced materials (both for performance and comfort) and appropriate armor design should ideally allow the flow of excessive metabolic heat away from the body (thermo-physiological property) which can be reflected by a combination of air permeability, thermal resistance, and moisture evaporation [23-25]. The garment should be able to transfer heat and moisture away from the skin to the atmosphere [25-27]. Tactile comfort, the feel or sensation on the skin when worn should be considered during design of protection gear [28, 29].

The use of body armor has always been an issue when ease of body movement and cognitive functions are considered [30, 31] and should not be drastically compromised by the design of the body armor[22]. Many biological systems possess hierarchical and fractal-like interfaces and joint structures that bear and transmit loads, absorb energy, resist puncture and accommodate growth, respiration and/or locomotion [32], which are determined by their geometry [33-35]. In the case of bio-inspired flexible protection, natural segmented armors from fish, alligator, snake, tonicella marmoreal, pangolin, scaly foot gastropods, arapaima or armadillos are attracting an increasing amount of attention because of their unique and highly efficient protective systems to resist mechanical threats from predation, while combining hardness, flexibility, breathability, thinness, puncture-resistance and lightweight [35-40]. These natural armors, which inspired researchers because of their diversity of geometrically structured interfaces and joints, are found in biology, for example in armored exoskeletons[41, 42], the cranium [33, 34], the turtle carapace [43] and algae [44].

Learning by imitation and further by linking all the data has probably been one of the most fruitful ways of development ever used. The extreme contrast of stiffness between hard scales and surrounding soft tissues gives rise to unusual and attractive mechanisms, which now serve as models for the design of bio-inspired armors. Despite this growing interest, there is little guideline for the choice of materials, optimum thickness, size, shape and arrangement for the protective scales [45].

The performance of 3D printed aramid FRP for stab resistance was studied for 2 mm, 4 mm and 6 mm thickness and the last two showed excellent performance for 25 J impact energy while 2 mm thick scales failed the puncturing test [46]. In this research, the scales are designed, developed and its performance is checked for energy level K1 (25 J) with a relatively low thickness, mass, production time and material usage as compared to the previous research result.

The aim of this research is to design and develop three dimensional (3D) printed stab resistant armor vest based on continuous filament fabrication (CFF) inspired by natural armors. The plan is to combine soft textile undergarment and hard stab protective elements in terms of fiber-reinforced plastic (FRP) of segmented scales. As a first step for the development of innovative stab protection clothing, the stab protection properties of 3D printed and fiber-reinforced functional elements are investigated based on material types, shape of the geometries of the scales and size of geometries, which are used for the development of a novel vest. The main novelty of this research is its comfort as studied and published in a reputable journal [47] by the same authors to this article. The comfort is found to be improved as compared to the current stab protective armor because the armor's protective elements in this research are segmented scales [47] without compromising the protection performance for the intended energy

level, as investigated in this research in terms of material types and its alignment during 3D printing, geometry and size.

2. Materials and Methods

2.1. *Materials*

3D printed stab protective elements in this research are produced as circular, quadrilateral and triangular scales with defined dimensions from thermoplastic composite filament (Onyx) and functional fibers such as Kevlar from aramid groups and carbon fibers with the mechanical properties shown in Table 1. Different blend layers ratio of fibers and plastics are used in Markforged Inc.'s Mark Two Desktop 3D printer [48] with its CFF process and two printing nozzles. One nozzle of the printer operates like a typical extrusion process to lay down a plastic filament that forms the outer shell and the internal matrix of the part. The second nozzle deposits a continuous strand of composite fibers such that carbon, Kevlar, glass and others on every defined layer [49, 50] inside a conventional fused filament fabrication (FFF) thermoplastic part [51].

Table 1. Mechanical properties of materials [48]

Properties	Onyx	Carbon	Kevlar
Tensile strength (MPa)	37	800	610
Tensile modulus (GPa)	2.4	60	27
Flexural strength (MPa)	71	540	240
Flexural Modulus (GPa)	3	51	26
Compressive strength (MPa)		420	130
Compressive modulus (GPa)		62	25
Density (g/cm^3)	1.2	1.4	1.2

(Association of Test Laboratories for Bullet Resistant Materials and Constructions, 2011),

The specimens were sliced at 0/45/90/-45 degrees of infill angles, with defined repetitions written as a subscript after the last bracket (see Table 2), using Eiger.io online software by Markforged Inc. Table 2 displays the material arrangement, design, and setup of the printing process to determine the optimum protective scales with the minimum possible thickness for Energy Level 1, which is 25 joules and a 20mm allowable deformation depth [52] of the knife through the 3D printed protective element. The materials and their arrangement in the 3D printed scales are shown in Table 2. The material ratio, expressed in percent (%), is based on the number of layers of reinforcing fibers relative to the layers of the whole part, but not the material volume, because the material volume depends on the density of the materials per unit volume of the geometry. The remaining layers, not shown in some of the rows in Table 2, are made from Onyx.

Table 2. Materials arrangement inside the 3D printed scales

No.	Material	Fiber angle (in degree-°) coding	Filling fiber layers over the total layer	Dimension	Shape
1	Onyx	No fiber			
2	50% Onyx/50%Aramid	(0/+45/90/-45)$_3$/0/45/90	15/30 = 50.00%	3 mm thickness and 50 mm diameter	Circular
3	27%Onyx/73Aramid	(0/+45/90/-45)$_5$/0/45	22/30 =73.33%		
4	Aramid	(0/+45/90/-45)$_7$	28/30 =93.33%		
5	Carbon	(0/+45/90/-45)$_5$/0/45	22/24 =91.67%		
6	Carbon	0/+45/90/-45	24/32 = 75%	100 mm x 100 mm x 4 mm	Quadrilateral plate
7			24/32 = 75%		Quadrilateral scales
8			24.59%		Triangular scales

2.2. *Methods*

The development of 3D printed scales begins with designing, followed by STL file generation in Autodesk Fusion 360 software. The generated STL file is then imported into Markforged Inc.'s online slicing software called "Eiger.io" to select the type of material, assign alignment composition for each layer of the final product, and arrange the materials accordingly before being transferred to the 3D printer. The samples used for this study are 3D printed from the materials listed in Table 1, with each sample having a specific ratio and filling alignment without symmetry.

The scales are designed to have a thickness of 3 mm and a diameter of 50 mm for material investigation. Additionally, various dimensions are explored, including quadrilateral scales with a thickness of 4 mm, triangular scales, and a square plate measuring 100 mm x 100 mm x 4 mm, for shape and size investigation. The designs of the target samples are illustrated in Figure 1A to Figure 1D, along with their corresponding standard triangle language (STL) files (Figure 1E) generated from Fusion 360.
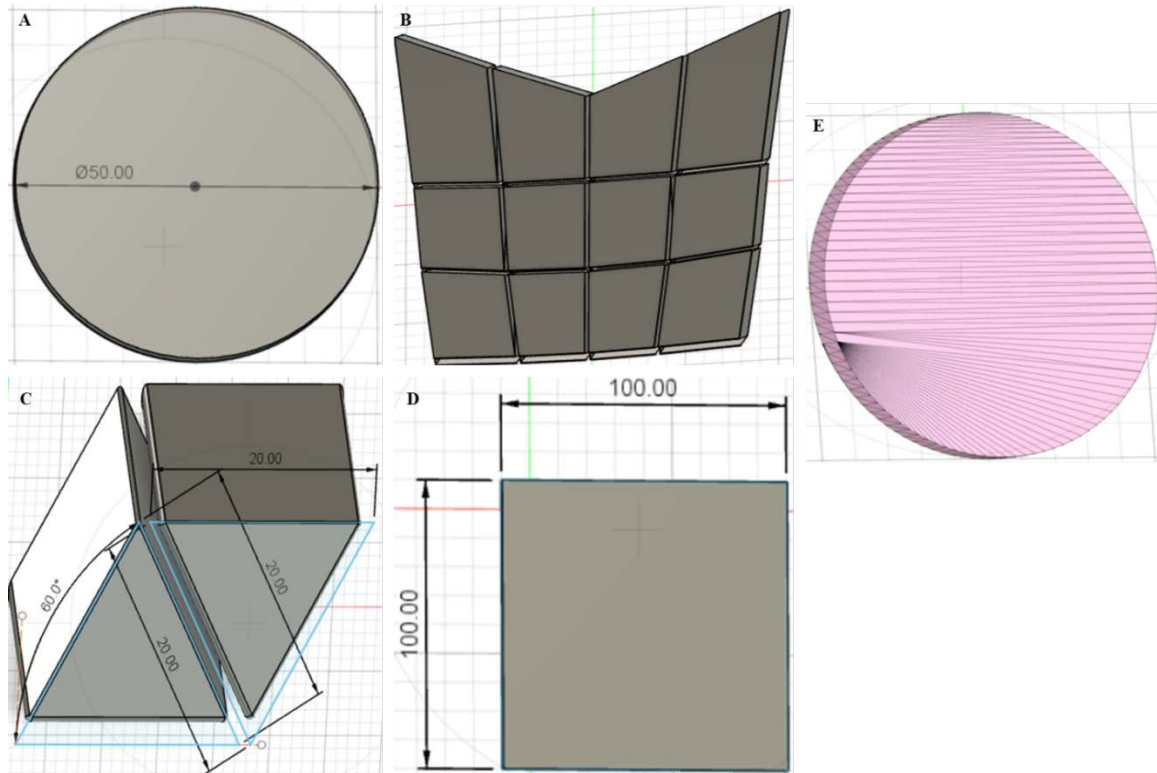
Figure1: Designs generated from Fusion 360 A) Circular scale 3mm thick B) Quadrilateral scales 4mm thick C) Triangular scales 4mm thick D) Square plate 4mm thick E) STL file

Figure 2 illustrates the material arrangement of every layer in the 3D printed scales. The layers are arranged with different material filling angles to potentially enhance protection while reducing the overall weight of the armor element (scales). The fiber angle coding follows the standard lamination theory for composite part production. To clarify the arrangement, for example, (0/+45/90/-45)N signifies that a reinforcement fiber is printed N times sequentially in the 0, +45, 90, and -45 filling angles to complete the construction. The repetition (N) of the print layers angle is determined by the fiber diameter. For instance, a carbon fiber with a diameter of 0.125 mm is printed approximately N = 5.5 times for the mentioned reinforcement fiber angles, while a Kevlar fiber from the aramid group with a diameter of 0.1 mm is printed approximately N = 7 times for the mentioned fiber angles arrangement. The first and last layers default to thermoplastic materials, which in this study is Onyx
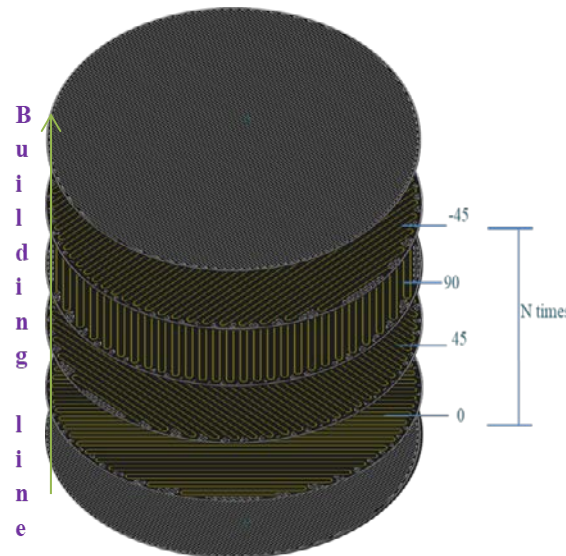
Figure 2: An example of material arrangement and printing order of polymers at filling angle (0/+45/90/-45)$_N$, generated from Eiger.io

Four specimens are produced, and three of them are tested for each sample following the test method of the Association of Test Centers for Anti-attack Materials and Constructions [52].

2.3. Experimental

The specimens are conditioned for a minimum duration of 24 hours at a temperature of 20±2 °C and a relative humidity of 65 ±5% [52]. The testing knife (blade), with specifications shown in Figure 3, is attached to the drop stand to test the resistance to puncture of the 3D printed scale-like armor elements. The dropping object, depicted in Figure 4a with the knife in Figure 4c, has a drop mass (m) of 2.51 kg, dropped from a height of 1.02 m at a speed (v) of 4.44 m/s, which is measured using an optical sensor to calculate the velocity right before impact. The kinetic energy (E_{kin}) applied to test the protection level of the specimens can therefore be calculated as follows:

$$E_{kin} = \frac{1}{2}m * v^2 = \frac{1}{2}2.51\ kg * (4.47\frac{m}{s})^2 = 25.07\ J$$

The kinetic energy used to test the specimens is 25.07 J, which is nearly identical to the specified energy in the corresponding inspection norm (K1=25 J) [52]. This energy level serves as an indicator of the specimen's protective performance, provided that the penetration depth does not exceed the standard allowable depth outlined in the norm.
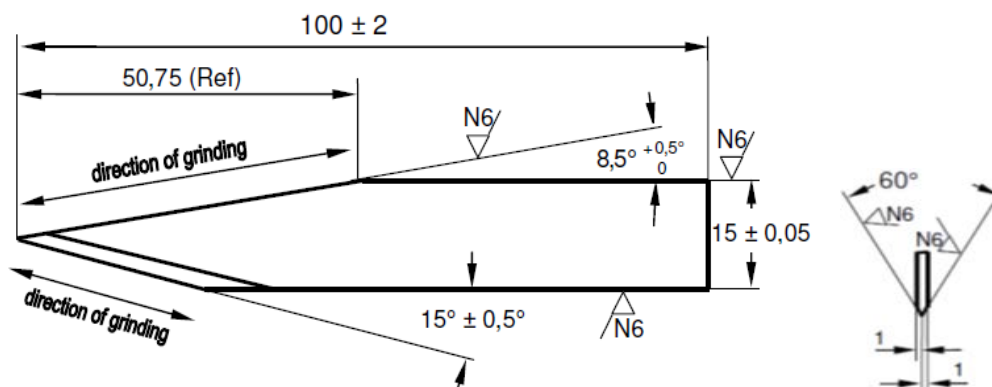
Figure 3: Geometry of the test blade P1/B (dimensions in mm) [52]

The testing procedures in this study involve applying impact energy to the specimens to puncture and evaluate the performance of the armor scales against this energy. This process primarily consists of three steps: preparation of the testing setup (depicted in Figure 4, Figure 5A, and Figure 5B), puncture testing (Figure 5C), and measurement of the penetration depth (Figure 5E).

The dropping object is released from the suspension bar by pulling the rope with the holding hooked rod, causing the knife with the dropping weight to fall onto the 3D printed sample in a closed chamber (as shown in Figure 5C). Afterward, the dropped object, along with the impacted specimen, is removed from the plastiline box to measure the penetration depth of the testing knife through the scales (as illustrated in Figure 5E).

The relative alignment of the knife to the specimen with respect to the fiber filling angles (0/+45/90/-45)N is random for all specimens, but the center of each scale of the specimens is aligned relative to the tip of the knife to avoid deflection of the specimen upon impact. Additionally, specimens with segmented scales and single plate protective elements are subjected to multiple drop tests at different parts of a sample made from carbon fiber reinforcement.

Figure 4: Drop test stand with: a) Dropping weight b) Dropping weight fixing hook c) Knife d) Safety path e) Hook pulling rope f) Safety bar g) Specimen of plastiline h) Plastiline
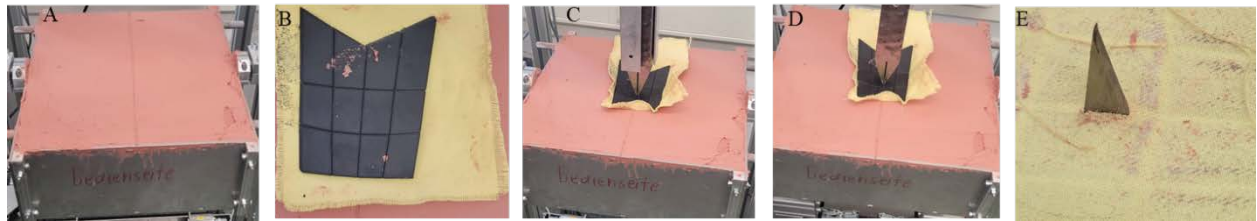
Figure 5: Test procedure of stab resistant scales using drop stand A) Leveling and center line of the plastiline B) Sample on the plastiline C) Dropped the knife with the weight D) Impacted object right after dropping E) dismantled the knife from the dropping object and measuring of the penetration depth of the knife

3. Results and Discussion

As indicated in research results, the minimum organ distance from skin is pleura 22 mm, pericardium 31 mm, spleen 23 mm, kidney 37 mm, thoracic aorta 64 mm, abdominal aorta 87 mm [53] and liver 22 mm [54, 55]. The maximum penetration depth of the knife should be lower than the minimum distance of the organ from the skin. On the other side, the maximum penetration depth of the knife for energy level K1 (25 J) set by VPAM standard is 20 mm [52]. If the specimens allow the knife to penetrate deeper than the penetration depth set in the norm, then the samples are considered as failed to resist the specified impact energy level K1. As seen from Figure 6A - Figure 6E, the scales have shown different depths of the knife penetrated through the 3DP protective armor elements because of the type of reinforcement fibers, the fiber contents in the plates, the size of the scales and the shape of the scales.

As shown in Table 3, the influence of materials on the stab resistance at the intended energy level is investigated using various compositions: Onyx/Aramid (50% each), Onyx-27%/Aramid-73%, Kevlar-100%, Carbon-100%, and Onyx-100%. According to the test results, 50 mm diameter 3D printed carbon scales showed potential resistance against stabbing with a knife dropped at 25 joules of energy level 1. However, other materials investigated in this research demonstrated the worst potential against the same intended impact energy, resulting in fatal injury if used to develop protective armor with a 3 mm thickness and without symmetry of material alignment during the 3D printing process. Carbon 3D printed scales do not allow the sharp tip of the knife to pass through, even for fractions of millimeters after the last layer of the 3DP protective scale, but the knife tip is deformed at every test.

The knife with the impact weight dropped on the 3D printed Kevlar scales fully passed through the plastiline with no resistance from the scale when it went through each of the aramid fiber layers. The main reason for this is the physical and mechanical properties of the materials, where the impact energy has a compression effect at first, then tensile and flexural effects. This means when an impact load is dropped on a specimen, it compresses the area, stretches it, and then deforms it. The material with the highest values for these parameters can relatively have high resistance against the intended impact energy. Carbon, with its 0.125 mm diameter, has the highest density, tensile, compression, and flexural strength and modulus (see Table 1), thus achieving the highest resistance against the intended impact energy.

The percentage of Onyx in the protective scales has no positive influence on resistance to the intended impact energy. Therefore, specimens with 3 mm thickness made from 100% Onyx and Kevlar from aramid fibers filled in the $(0/45/90/-45)_7$ degrees throughout the specimen have little to no resistance to puncturing because the penetration distance (>40 mm) is deeper than allowable within the testing standard [52]. Therefore, the analysis mainly focuses on the carbon and the Kevlar aramid fibers. Therefore, the analysis mainly focuses on carbon and Kevlar aramid fibers. The carbon fiber (Figure 6A) does not allow the tip of the knife to be seen behind the scale, even with fractions of a millimeter, while 100% Kevlar allows the knife to penetrate through the specimen without resistance to the impact energy (Figure 6B).
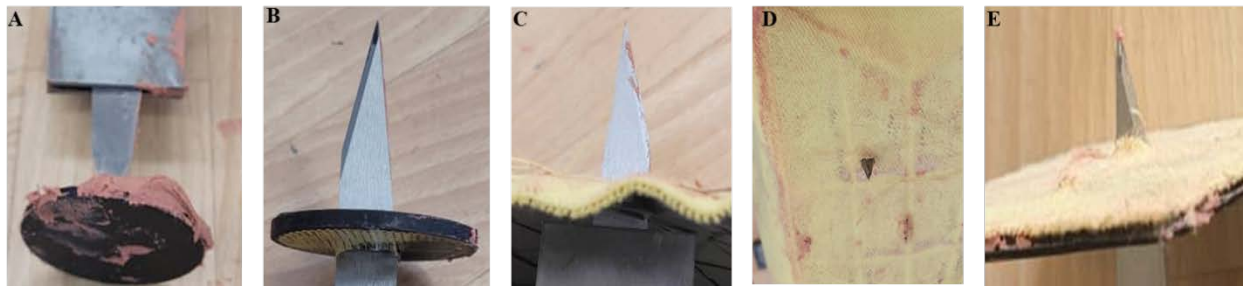
Figure 6: Appearance of scales right after impact; A) Carbon circular scale; B) Kevlar circular; C) Triangular plates; D) Quadrilateral scales on textiles E) Rectangular Plate

However, Kevlar with symmetry of material alignment (Figure 7) during printing showed potential resistance to the intended impact energy [56]. As the researchers reported in their paper, the symmetry of material alignment has a significant influence on the resistance to impact energy for stab protective armor. With this, Kevlar can withstand the intended impact energy when a 3mm thickness of the scale is 3D printed with mirroring the other half thickness of the scale because half of the directions of the fiber alignment are totally opposite to the alignment of the other half fiber layers so that the running speed of the knife is disturbed during stabbing, resulting in low penetration depth.
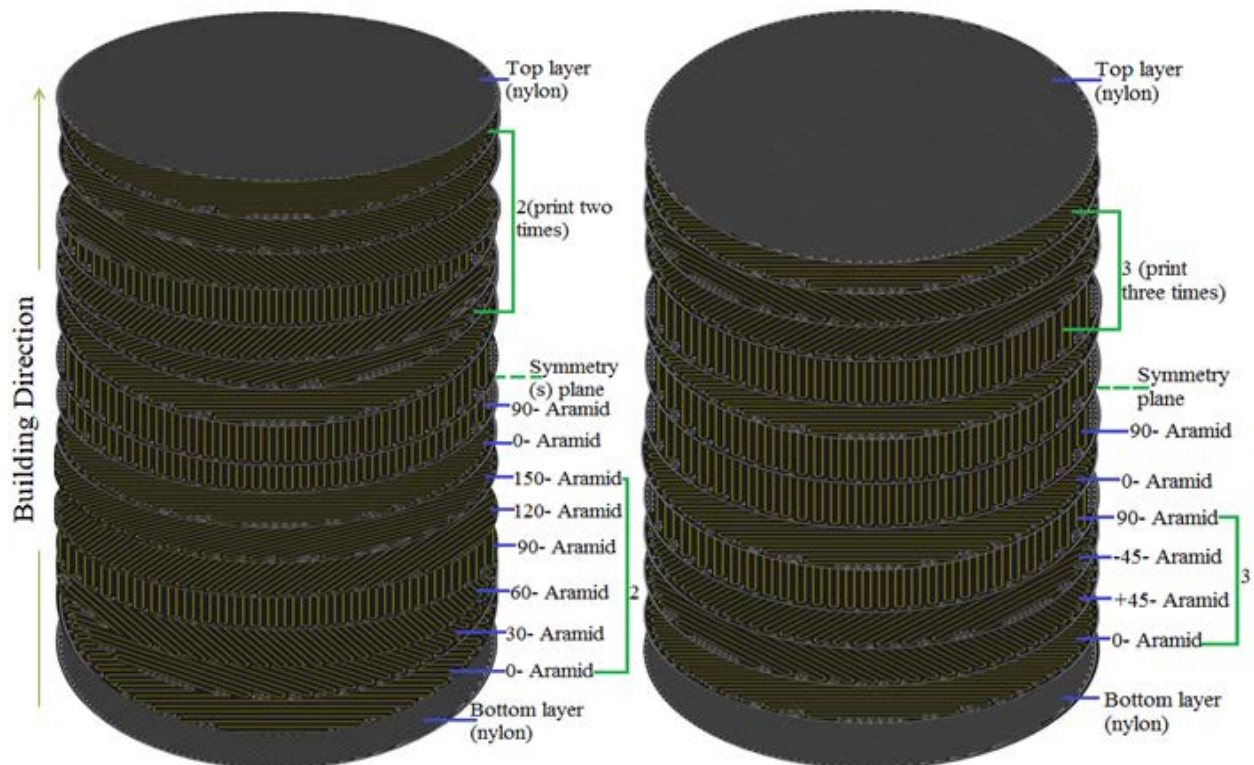
Figure 7: Example of material arrangement and printing order of aramid layers- at filling angles [(0/30/60/90/120/150)2/0/90]s and [(0/+45/90/-45)3/0/90]s, generated by Eiger.io o[56]

Table 3. Results of stab testing of FRP elements

Sample name	Test runs	Penetration of knife in mm	Depth of plastiline deformation	Thickness	Plastic volume	Fiber Volume
Onyx/Aramid (50%)	1	44.86	16.61	3	3.9	2.12
	2	45.7	17.5	3	3.9	2.12
	3	46.21	20.45	3	3.9	2.12
	Average	45.59				
Onyx-27%/Aramid-73%	1	45.68	14.3	3	2.05	3.89
	2	46.22	18.37			
	3	43.18	15.07			
	Average	45.03				
Kevlar-100%	1	45.6	37.54	3	1.39	4.8
	2	42.25	41.12			
	3	39.45	53.43			
	Average	42.43				
Carbon-100%	1	0	64	3	1.46	4.53
	2	0	63.09			
	3	0	64.48			
	Average	0				
Onyx-100%	1	>48,5		3	5.81	
	2	>48,5				
	3	>48,5				
	Average	>48.50				
100x100mm Square Onyx-Carbon	1	20.65		4	11.92	26.79
	2	9.24				
	3	18.62				
	Average	16.17				
Quadrilateral Segments attached on textiles	1	30.63	No significant	4	17.83	24.46
	2	13.47				
	3	23.88				
	4	41.53				
	Average	27.38				
Triangular segments attached on textiles	1	41.93	No significant	4	38.24	12.47
	2	42.17				
	3	40.14				
	Average	41.41				

Figure 8 presents the 3D printed protective scales immediately after being impacted by the knife with the drop weight. The carbon fiber 3D printed protective armor element demonstrates extreme resistance to the intended stabbing energy from the drop weight. As seen from left to right in Figure 8A, the protection is perfect due to the carbon fiber's resistive reaction to the impact energy. The tips of the knives are bent, broken, and damaged in every cycle of the drop test on carbon fiber 3D printed scales (See Figure 11A to Figure 11C).

In contrast to this, the Kevlar 3D printed protective armor elements totally failed to save the wearer from fatal injury. As one views from left to right in Figure 8B, the viewer is shocked by the penetration depth of the knife through the scales because the Kevlar filaments are not able to resist the intended impact energy to puncture with the current infill angle alignment unless produced with symmetrical alignment for half of the thickness of a scale at [(0/+45/90/-45)3/0/90]$_s$ so that the penetration depth is reduced because each layer crosses over the other layer either diagonally or at a right angle to disturb the downward running of the stabbing knife with the impact load [56].

Figure 8: Physical appearance of the 3D printed scales right after impacting drop weight on A) Carbon fiber B) Kevlar fiber from aramid group

In addition to the materials, the shapes of the protective elements also have a significant influence on the penetration depth of the knife from the impact energy. The content of the reinforcement carbon fiber in triangular scales is lower than the content in the quadrilateral scales. Figure 9 presents the running distance and turning edges because the shapes of the geometries have a significant influence on the content of the fibers (blue lines in Figure 9A and Figure 9B) to be accumulated during printing. As viewed from Figure 9A, the impact load with the knife is not able to fully penetrate after puncture and saved the wearer from fatal injury with reduced penetration depth (see Figure 9C). In contrast to quadrilateral geometries, triangular geometries allow the stabbing force with the knife to fully pass through the scales (Figure 9B) and result in fatal injury due to the shocking penetration depth of the knife (Figure 9D).
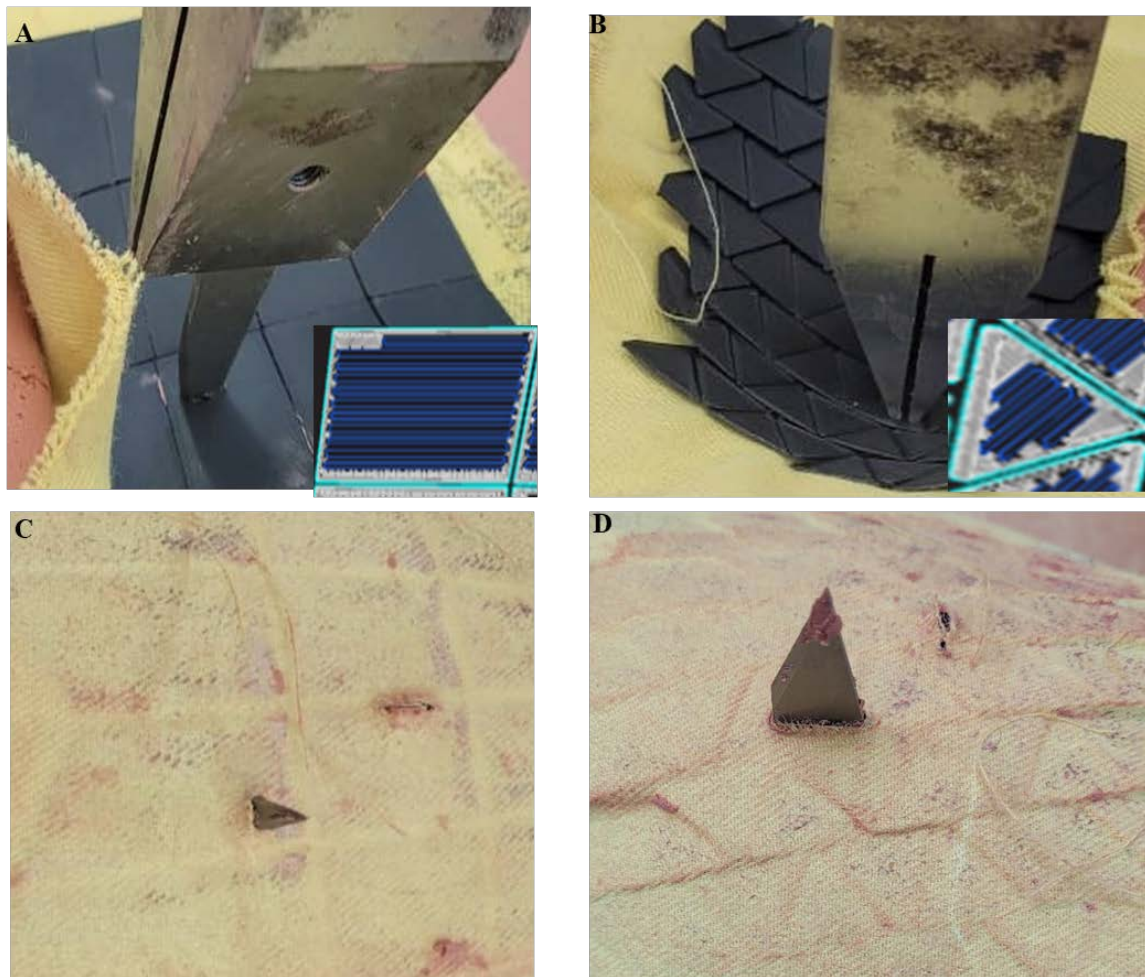
Figure 9: Appearance of the impact of drop knife on A) Quadrilateral scales B) Triangular scales and the penetration depth of knife through C) Quadrilateral D) Triangular scales

Another parameter investigated in this research is the size of the protective scales and its impact on resistance performance to stab impact energy. The size of the protective element refers to its surface area, classified as large (10,000 mm^2), medium (950-1,280 mm^2), and small size (640-750 mm^2) in this study. The large scale exhibited a penetration depth of 9.24 mm - 19.08 mm, the medium scale showed a penetration depth of 13.47 mm - 23.88 mm, and the small scales had a penetration depth greater than 30.63 mm observed during the experiment. The results showed that the sizes of the protective elements significantly influence the performance against puncture to penetrate through the scales (see Figure 6C and Figure 6E) due to the impact energy. The protection performance decreased as the dimensions of the scale became smaller. The difference in protection performance between the large scale and the small scale is akin to a saved life from fatal injury and life lost with fatal injury from the intended impact energy, according to standards and the minimum distance of sensitive organs from the skin [52-55]. The large size protective element bent the testing knife during the experiment, but the other sizes did not create physical damage to the testing knife. Previous research has revealed that the size of the protective element has an inverse relationship with comfort but is directly proportional to protection performance [56, 57] so optimization of comfort must be made without influencing protection performance.

The protection performance of the 3D printed scales also varies at different portions such as edges, joints, and the body of the protective element. As shown in Figure 10, a narrow puncture width is observed on the body (2), while a wider puncture hole is seen on the edges and joints (1, 3, and 4) of the protective elements due to less fiber accumulation of the scales in edges and joint lines. The puncture width on the edges of the scales could lead to fatal injury unless improvements are made to

the chamfered line in the joints of the protective elements for uniform distribution of the fibers in all parts of the scales, including the edges.
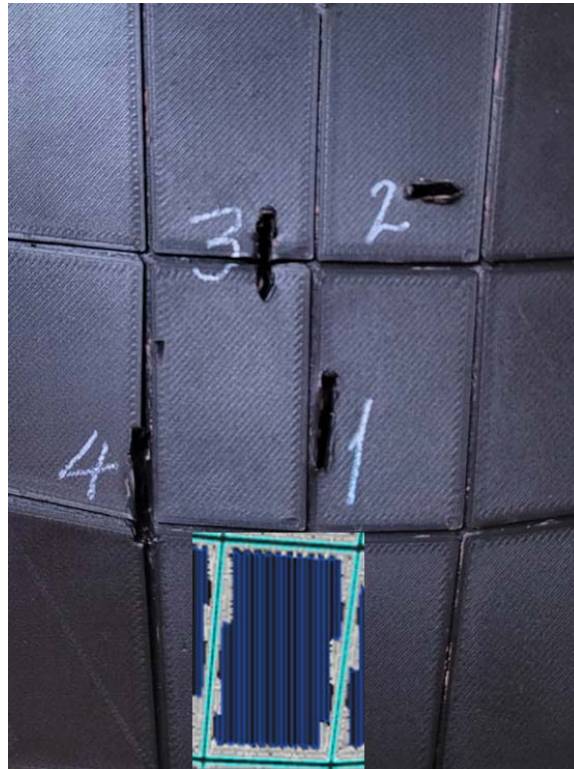
Figure 10: Appearance of the different parts of the scale right after puncture on the body (2), on the edges and joints (1, 3 and 4) of the protective elements

In summary, the knives are bent (Figure 10A – Figure 10E) after puncture testing and are not used to puncture repeatedly due to the high strength of the scales printed from carbon fiber in circular scales, quadrilateral scales on its body, and a 100 x 100 mm2 plate. The tips of the knives are broken, bent, or partially damaged during the drop test, according to the content of the carbon fiber in the scales. The knives in Figure 10A – Figure 10C are bent, damaged, and broken during the testing of circular scales made of carbon fiber. A knife in Figure 10D is bent during the testing of the 100 mm x 100 mm square plate, the tip of the knife in Figure 10E is bent during the testing of the body of the quadrilateral scales, while the physical appearance of the knife in Figure 10F remains unchanged during testing of the scales made from Kevlar fiber. The appearance of the tips of the knives in decreasing damage order from left to right is clearly shown in Figure 10G, with the first three knives impacted during testing carbon 3D printed scales, the fourth knife during testing of the 100 mm x 100 mm square plate, the fifth knife during the testing of the quadrilateral scales, and the last (on the right side) knife used during the testing of the circular scale made from Kevlar.
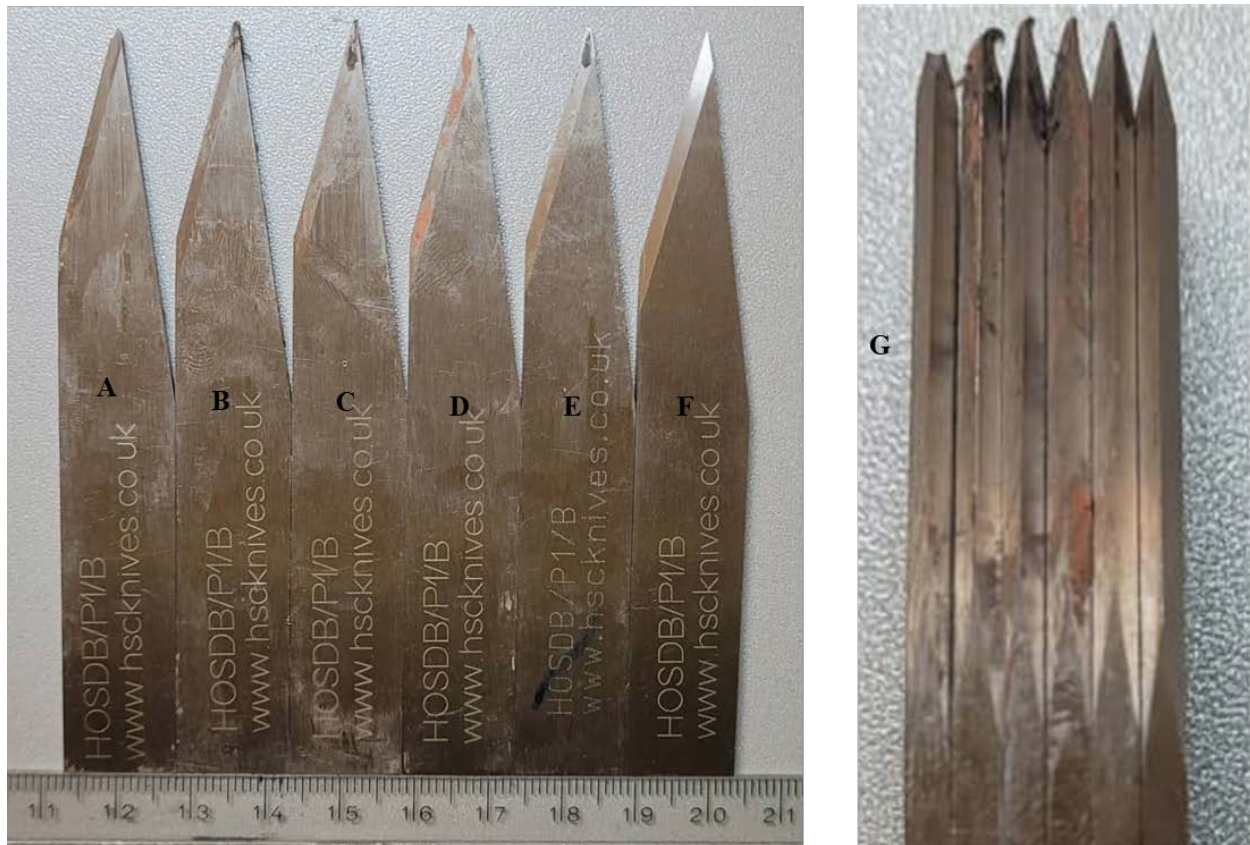
Figure 11: Damaged tip of the testing knife after impact

4. CONCLUSION

Stab protective armor is safety equipment designed to safeguard the lives of law enforcement workers for security assurance. This equipment should be capable of withstanding the intended stabbing impact energy level. This research primarily addresses the performance of continuous filament fabrication (CFF) 3D printed stab protective gear elements, considering various important factors such as the type of materials, shape of geometries, sizes of the protective elements, and related aspects. The results reveal that these considered factors significantly influence the ability to withstand stabbing impact energy from a knife with a drop weight.

The mechanical properties of materials, such as tensile strength (MPa), flexural strength (MPa), compressive strength (MPa), and their modulus (GPa), result in significantly different resistance to puncture force. Similarly, the density of the materials also plays a significant role in reducing the impact energy from the stabbing weight.

The types of geometries, described as shapes of protective scales in this study, were found to affect the penetration distance of the knife through the 3D printed protective elements because the turning point of the printer nozzle after running to print depends on the width of the printing line. The narrower the angle of the turning points of the nozzle, the lower the fiber accumulation. The sizes of the geometries influence the fiber content and affect the protection performance. The larger the geometry, the higher the fiber content, resulting in improved resistance to knife penetration through the protective element.

In general, the 3 mm thicker carbon fiber 3D printed protective scales fully resist the impact energy from the 25 joule drop weight. The tip of the knife was not measurable behind the last layer during all impact tests on carbon scales; instead, the tip of the knife is bent, broken, or damaged. Therefore, the investigators of this research suggest developing stab protective armor through 3D printing of

quadrilateral scales from carbon fiber with optimal dimensions for reduced weight, flexibility, permeability, and breathability. The novelty of this study can be explained in terms of materials mechanics as the fibers adhered to each other with crossing alignment when printing a layer over the layer. This creates an entangling path on the knife while running from layer to layer so as the impact energy is reduced by disturbing the falling speeding of the knife with its impact mass. These stab protective elements are designed for segmented arrangement for the possible flexibility with light weight from the thickness and material mechanics.

Future research activities will include the attachment method and adhesion between scales and fabrics, as well as the design and development of 3D printed scales for the full vest, and checking its performance both to protection and comfort.

ACKNOWLEDGEMENT

References

1. *Reiners, P., Investigation about the stab resistance of textile structures, methods for their testing and improvements. 2016, Université de Haute Alsace: HAL. p. 195.*
2. *Fenne, P., Protection against knives and other weapons. . Textiles for protection, ed. R.A. Scott. 2005, Cambridge: Woodhead Publishing, CRC.*
3. *Alil, L.-C., et al., Aspects regarding the use of polyethylene fibers for personal armor. Eastern Michigan University, 2004.*
4. *Cavallaro, P.V., Soft Body Armor: An Overview of Materials, Manufacturing, Testing, and Ballistic Impact Dynamics, N.U.W.C. Division, Editor. 2011, NUWCD-NPT-TR.*
5. *Laible, R., Ballistic Materials and Penetration Mechanics (Methods and phenomena, their applications in science and technology). 2012: Elsevier.*
6. *National Institute of Justice, O.o.J.P., U.S. Department of Justice, Stab Resistance of Personal Body Armor NIJ Standard–0115.00. 2000, US National Institute of Justice: Washington.*
7. *EMS1, Man accused of stabbing 2 police officers after killing 4 relatives. 2023.*
8. *VOA, Stabbing Attack in Tunisia, Suspect Detained 2022.*
9. *Staff, T., Police officer stabbed, 10 arrested at Tel Aviv protest over hit-and-run case, in The Times of Israel. 2023.*
10. *Jessup, S. and J.W. Kelly, Met Police officer speaks of ordeal as knife attacker is sentenced, in BBC News. 2023, BBC.*
11. *Amara, T., Tunisia national guard officer stabbed, police arrest attacker, R. Chang, Editor. 2023, Reuters.*
12. *Police1, N.M. officer killed in stabbing before suspect is shot and killed by witness. 2024, Associate Press.*
13. *Grieshaber, K., Stabbing attack at German gym leaves 4 severely injured, in Associate Press. 2023, AP.*
14. *zdfheute, Angriffe auf Bahn-Mitarbeiter 2022 gestiegen. 2023: Panorama.*
15. *Bundeskriminalamt(BKA), Bundeslagebild Gewalt gegen Polizeivollzugsbeamtinnen und Polizeivollzugsbeamte 2020. 2021: Bundeslagebild*
16. *LaTourrette, T., The life-saving effectiveness of body armor for police officers. J Occup Environ Hyg, 2010. **7**(10): p. 557-62.*
17. *Peleg, K., A. Rivkind, and L. Aharonson-Daniel, Does body armor protect from firearm injuries? J Am Coll Surg, 2006. **202**(4): p. 643-8.*
18. *Jaslow, C.R., Mechanical properties pf cranal sutures. Journal of Biomechanical, 1990. **23**(4): p. 313-321.*

19. Larsen, B., et al., *Body armor, performance, and physiology during repeated high-intensity work tasks.* Mil Med, 2012. **177**(11): p. 1308-15.

20. Greaves, I., *Military Medicine in Iraq and Afghanistan: A Comprehensive Review.* 2018: Taylor & Francis Group, CRC Press.

21. Ricciardi, R., P.A. Deuster, and L.A. Talbot, *Metabolic Demands of Body Armor on Physical Performance in Simulated Conditions.* MILITARY MEDICINE, 2008. **173**(9): p. 817.

22. Park, H., et al., *Impact of ballistic body armour and load carriage on walking patterns and perceived comfort.* Ergonomics, 2013. **56**(7): p. 1167-79.

23. Chinevere, T.D., et al., *Efficacy of body ventilation system for reducing strain in warm and hot climates.* Eur J Appl Physiol, 2008. **103**(3): p. 307-14.

24. Nayak, R., et al., *Body armor for stab and spike protection, Part 1: Scientific literature review.* Textile Research Journal, 2017. **88**(7): p. 812-832.

25. Nayak, R., et al., *Stab resistance and thermophysiological comfort properties of boron carbide coated aramid and ballistic nylon fabrics.* The Journal of The Textile Institute, 2018. **110**(8): p. 1159-1168.

26. Matusiak, M., *Thermal Comfort Index as a Method of Assessing the Thermal Comfort of Textile Materials* FIBRES & TEXTILES in Eastern Europe, 2010. **18**(2): p. 45-50.

27. Djongyang, N., R. Tchinda, and D. Njomo, *Thermal comfort: A review paper.* Renewable and Sustainable Energy Reviews, 2010. **14**(9): p. 2626-2640.

28. Nayak, R., et al., *Comfort properties of suiting fabrics.* Indian Journal of Fibre and Textile, 2009. **34**: p. 122-128.

29. philippe, F., et al., *Tactile Feeling: Sensory Analysis Applied to Textile Goods.* Textile Research Journal, 2004. **74**(12): p. 1066-1072.

30. Dempsey, P.C., P.J. Handcock, and N.J. Rehrer, *Impact of police body armour and equipment on mobility.* Appl Ergon, 2013. **44**(6): p. 957-61.

31. Legg, S.J., *Influence of body armour on pulmonary function.* Ergonomics, 1988. **31**(3): p. 349-53.

32. Li, Y., C. Ortiz, and M.C. Boyce, *Bioinspired, mechanical, deterministic fractal model for hierarchical suture joints.* Phys Rev E Stat Nonlin Soft Matter Phys, 2012. **85**(3 Pt 1): p. 031901.

33. Pritchard, J., J. Scott, and G. Girgis, *The structure and development of cranial and facial sutures.* Journal of Anatomy, 1956. **90**(1): p. 73-86.

34. Herring, S.W., *Mechanical influences on suture development and patency.* Front Oral Biol, 2008. **12**: p. 41-56.

35. Dunlop, J.W.C., R. Weinkamer, and P. Fratzl, *Artful interfaces within biological materials.* Materials Today, 2011. **14**(3): p. 70-78.

36. Vernerey, F.J. and F. Barthelat, *On the mechanics of fishscale structures.* International Journal of Solids and Structures, 2010. **47**(17): p. 2268-2275.

37. Dastjerdi, A.K. and F. Barthelat, *Teleost fish scales amongst the toughest collagenous materials.* J Mech Behav Biomed Mater, 2015. **52**: p. 95-107.

38. Zhu, D., et al., *Puncture resistance of the scaled skin from striped bass: collective mechanisms and inspiration for new flexible armor designs.* J Mech Behav Biomed Mater, 2013. **24**: p. 30-40.

39. Lin, Y.S., et al., *Mechanical properties and the laminate structure of Arapaima gigas scales.* J Mech Behav Biomed Mater, 2011. **4**(7): p. 1145-56.

40. Connors, M.J., et al., *Three-dimensional structure of the shell plate assembly of the chiton Tonicella marmorea and its biomechanical consequences.* J Struct Biol, 2012. **177**(2): p. 314-28.

41. Ji, B. and H. Gao, *Mechanical properties of nanostructure of biological materials.* Journal of the Mechanics and Physics of Solids, 2004. **52**(9).

42. Barthelat, F., et al., *On the mechanics of mother-of-pearl: A key feature in the material hierarchical structure.* Journal of the Mechanics and Physics of Solids, 2007. **55**(2): p. 306-337.

43. Krauss, S., et al., *Mechanical Function of a Complex Three-Dimensional Suture Joining the Bony Elements in the Shell of the Red-Eared Slider Turtle.* Advanced Materials, 2009. **21**(4): p. 407-412.

44. Garcia, A.P., N. Pugno, and M.J. Buehler, *Superductile, Wavy Silica Nanostructures Inspired by Diatom Algae.* Advanced Engineering Materials, 2011. **13**(10): p. B405-B414.

45. Martini, R., Y. Balit, and F. Barthelat, A comparative study of bio-inspired protective scales using 3D printing and mechanical testing. Acta Biomater, 2017. **55**: p. 360-372.

46. Ahrendt, D., et al., Hybrid material designs by the example of additive manufacturing for novel customized stab protective clothing, in Light Weight Armour Group for Defense and Security. 2019: Roubaix, France. p. 286-294.

47. Sitotaw, D.B., D. Muenks, and A.K. Kebash, 3D printing applications on textiles: Measurement of air permeability for potential use in stab-proof vests. Journal of Engineered Fibers and Fabrics, 2024. **19**: p. 15589250241232152.

48. Markforged. Markforged the Mark Two Desktop 3D Printer. 2019 [cited 2020 05 April]; Available from: https://markforged.com/mark-two/.

49. Langau, L., What is Continuous Fiber Fabrication (CFF)?, in Make Parts Fast, A Design World Resource. 2017.

50. Dean, A., A Review on Markforged Mark Two: the basics of how it works, in DEVELOP3D. 2016, DEVELOP3D: UK, London.

51. Crease, A., 3D Printer Types & Technologies 2019, Markforged.

52. Association of test laboratories for bullet resistant materials and constructions, Test Standard "Stab and Impact Resistance" - Requirements, classifications and test procedures (VPAM KDIW 2004). 2011.

53. Connor, S.E.J., A. Bleetman, and M.J. Duddy, Safety standards for stab-resistant body armour: a computer tomographic assessment of organ to skin distances. International Journal of the Care of the Injured, 1998. **29**(4): p. 297-299.

54. Su, S., et al., Skin-Liver Distance and Interquartile Range-Median Ratio as Determinants of Interoperator Concordance in Acoustic Radiation Force Impulse Imaging. Journal of Medical Ultrasound, 2019. **27**(4): p. 4.

55. Shen, F., et al., Impact of skin capsular distance on the performance of controlled attenuation parameter in patients with chronic liver disease. Liver International, 2015. **2015**: p. 9.

56. Sitotaw, D.B., et al., Investigation of Stab Protection Properties of Aramid Fibre-Reinforced 3D Printed Elements. Fibres and Textiles in Eastern Europe, 2021. **29**(3(147)): p. 67-73.

57. Sitotaw, D.B., et al., A Review on the Performance and Comfort of Stab Protection Armor. 2022. **22**(1): p. 96-107.

MODAL ANALYSIS OF A LAMINATE PLATE WITH 10 MM NOTCH FOCUSED ON THE EFFECT OF A FUNCTIONALLY ORIENTED FABRIC LAYUP WITH 20 MM WIDE CARBON STRIPS

Radek Zbončák

VÚTS, a. s., Virtual and applied mechanics, Liberec, Czechia, Svárovská 619,
radek.zboncak@vuts.cz

Abstract:

Functionally oriented fabric (FOF) is a woven textile featuring irregularly distributed secondary material strips in both warp and weft directions, designed to locally improve the mechanical properties of laminates, particularly around openings. This study investigates the impact of different FOF laminate layups on the natural frequencies of laminates with a 10 mm notch. The analyzed layup configurations include [0/90]s, [0/45]s, and [0/30/60]s, with 20 mm wide carbon strips incorporated into the glass fiber structure. The research demonstrates that the FOF structure significantly increases the natural frequencies about 20 % for bending modes of 0/90 layup. About 5 % and almost 30 % for twisting and bending modes respectively in the 0/30/60 layup, and over 20 % and about 40 % for twisting and bending modes respectively in the 0/45 layup. These enhancements help to prevent resonance in standard operating frequencies of mechanisms and machines, thus extending their operational lifespan. Additionally, the strategic placement of functional material strips around structural openings provides increased stiffness without the need for extra layers, effectively reducing the laminate's overall mass. This study highlights the potential of FOF to improve the dynamic performance and lifespan of laminated composite structures used in various engineering applications.

Key words:

Functionally oriented fabrics, Composite material, Modal analysis, Natural frequency, FEA, Circular notch

1. Introduction

Non-woven and woven fabrics are two basic types of fabrics used in composites. They differ in fiber processing. While non-woven fabric has fibers bonded together non-mechanically, woven fabrics are constructed by weaving yarns together. The vertical fibers are called 'warp' yarns, while so-called 'weft' yarns are weaved through the warp yarns along the horizontal width of the textile. Woven fabrics are called textiles. In the weaving process of composite textiles, a yarn is called a roving. The roving consists of straight fibers which are not spun or twisted [1].

Woven fabrics are generally sorted into two groups based on the roving material. In the first case, warp and weft roving is made of the same material. The second type of fabric is so-called 'hybrid fabric', where roving in warp direction consist of different fibers than roving in weft direction, typically carbon-aramid combination. Such a regular alternation of materials in the hybrid fabric leads to homogenization of the properties of the laminate layer. In contrast to these common types of fabrics, the functionally oriented fabric structure (FOF) has irregularly distributed fibers of different materials in the warp and weft (Fig. 1). The base material (BM) predominates in the fabric. Such material is usually cheaper and has worse mechanical properties than the functional one. The functional material (FM) has a minority in the fabric and has better mechanical properties and therefor it is in principle more expensive than the base material. The advantage of a FOF is the efficient use of expensive material with high mechanical performance quality.

The production of a functionally oriented fabric structure allows lamination without cutting the continuous fibers in the layer and so having better mechanical properties at the same time. FOF is intended for using in the layup to locally improve mechanical properties to increase strength or stiffness in required area. The suitable applications are laminates with holes for fasteners, or with openings such as windows or mounting openings providing access to machine parts under the laminate part [2]. Other application is a large format laminate in which the strip of functional material weaved in the fabric acts like a 'shell rib'.

Figure 1. Example of functionally oriented fabric (FOF)

The aim of this work is to determine first four modes of selected layups of FOF laminate. To evaluate natural frequencies of analyzed laminates and compare the obtained results. Finally, the conclusion of the effect of FOF layup on the natural frequency of a laminate with a notch will be made. The work is a continuation of the FOF parameter analysis. The presented results serve to the performance description of a FOF laminate.

2. Laminate

There are three regions of material type in sense of warp and weft roving combination in FOF laminate: glass-glass, glass-carbon (or carbon-glass) and carbon-carbon. The base material E-glass EC13 272 Z20 T63C roving is combined with the functional material carbon Tenax E HTA 40 E13 6K roving. Both are present in warp and weft directions in the way they form locally stiffened areas, as shown in Fig. 1. Both materials belong to the standard modulus materials. Glass fiber modulus is 71 GPa and carbon fiber modulus is 220 GPa. Mechanical properties of a laminate are estimated by theoretical elastic models [3] with use of an epoxy resin system with a modulus of cured system of 3 GPa.
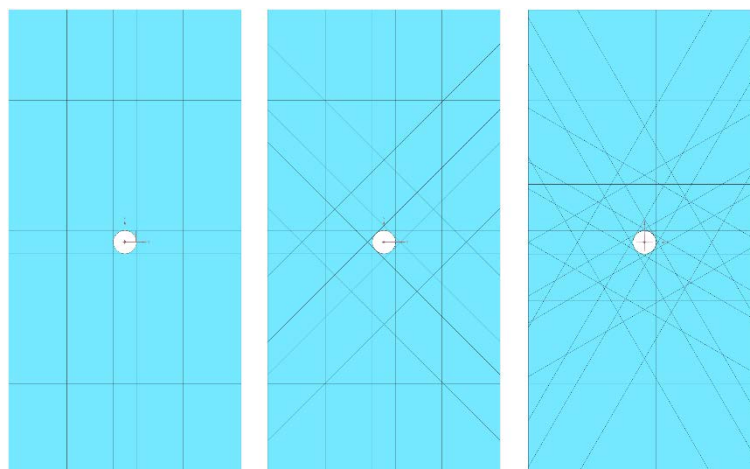
Figure 2. CAD model of FOF laminate layups: [0/90], [0/45] and [0/30/60]

A dimension of an analyzed plate is 100×200 mm (width×length). The size of a notch in the center of the plate is 10 mm. Thickness of the plate is given by its layup. The layups are [0°/90°]s, [0°/45°]s and [0°/30°/60°]s, see Fig. 2. A CAD model of the simulated specimen includes pads areas, as it would be in a real test setting. The purpose of the pads is to prevent a damage in the testing machine jaws. It clearly defines the area of load and constraints application in the simulation. The width of the carbon strips is 20 mm. FOF laminate simulation results are compared to results of base material only (glass) laminate with the same layup orientations and the notch size.

3. Modal analysis

The parametric finite-element model of a functionally oriented fabric laminate is created by the ply-based modelling method. The woven fabric lamina is defined by software as three layers of unidirectional fibers (UD). Two outer layers of UD (warp) and one intermediate layer of UD rotated by 90° (weft). Material orientation plays an essential role in proper composite material definition. Each material region must have a correctly defined system of coordinates to respect an orthotropic character of composite material.

In general, the first step in solving the dynamic properties of a structure is the determination of natural frequencies and mode shapes by performing a modal analysis of a free body without external load and any constraints. If damping is neglected, the results of such a simulation are real eigenvalues and normal modes. The first six modes have zero frequency, which corresponds to the six degrees of freedom of freely constrained (unconstrained) body. For typical material damping values of laminates, the damping does not significantly influence the natural frequencies and mode shapes. The damping reduces the vibration level near resonance.

4. Discussion

A plate laminated by standard process has layers of glass fabric and strips of carbon fibers in extra layers. That makes laminate thicker, which means heavier. The thickness in notch area is almost doubled. The mass of laminate plate with extra carbon strips is 0.08098 kg. The same size plate made of FOF with 10 mm notch has mass of 0.0488 kg. The difference is 40 % of total mass. The bigger size the plate is, the higher the absolute value of mass saving is. Another issue is the laminate symmetry and its A-surface quality. Laminate made of FOF has uniform thickness and can be made in a closed mold to get A-surface on both sides of the part.
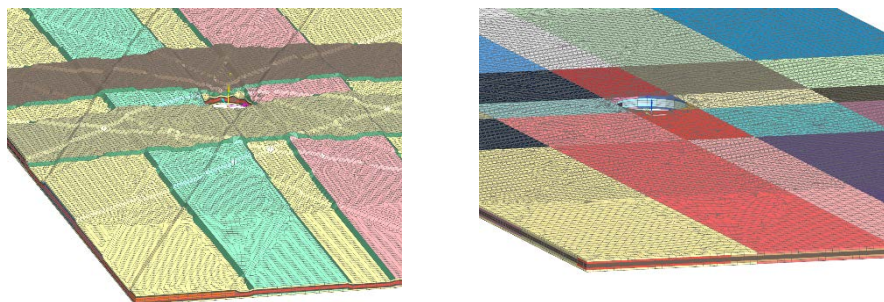
Figure 3. A FE model of laminate with carbon strips in extra layers (left) and a laminate made of FOF (right)

The shapes of first four non-zero modes are shown in Fig. 4. First two are twist and bending of the laminate plate. The shapes of modes for glass only laminates and for FOF laminates are the same. The results differ only in displacement and frequency values.

Natural frequencies of the mentioned four modes are summarized in Table 1. A glass-only and a FOF laminate plate are in the form of three layups. Significant benefit of carbon fiber strips in 0/90 layup is in second and fourth mode, which are the bending modes. Carbon strips make the plate frequency to increase about 27 % and 21 % in second and fourth mode respectively. The strips oriented in longitudinal and transverse direction increase the bending stiffness in 0/90 layup more than in twisting. That is

consistent with the theoretical assumption. According to increase of natural frequency in 0/45 layup with carbon fiber strips, that layup is most efficient in the increase in stiffness of all three analyzed layups. The growth is over 20 % for first and third mode (twisting), and about 40 % for second and fourth mode (bending). 0/30/60 layup has higher frequencies than 0/90 layup, but lower than 0/45 layup. That corresponds with the theory, as it respects the dependency of mechanical properties on fiber orientation.
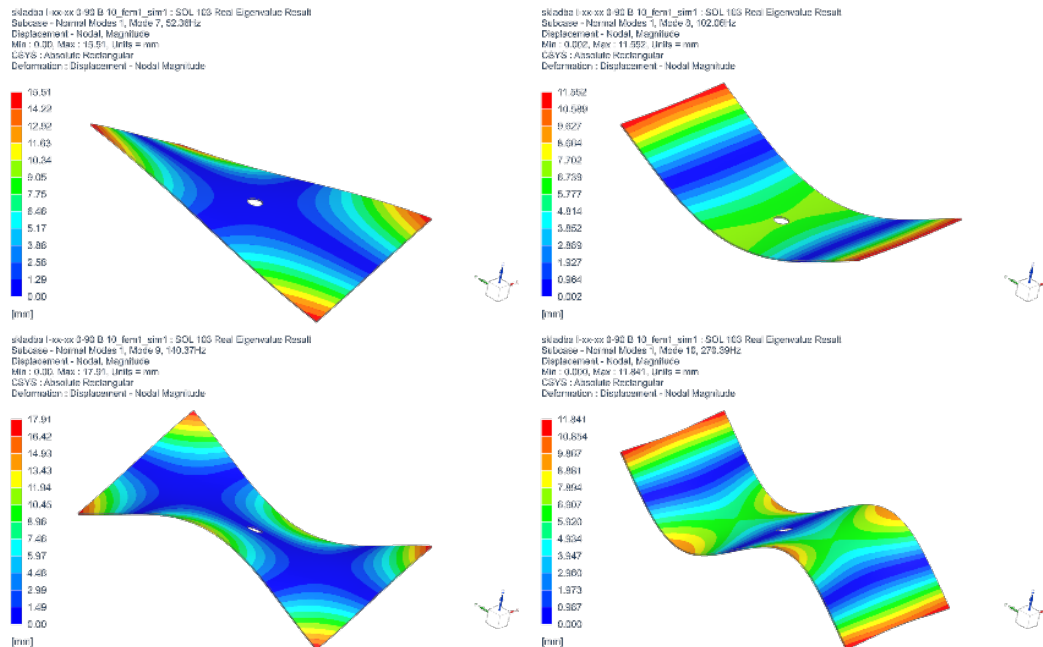
Figure 4. A FE model of laminate with carbon strips in extra layers (left) and a laminate made of FOF (right)

The frequency growth for 0/30/60 FOF layup is more than 25 % in bending modes and about 10 % in twisting modes compared to glass-only laminate. Frequency growth in bending modes is almost the same as for 0/90 laminate layup. Higher frequencies are in comparison of twisting modes.

Table 1. Natural frequencies (Hz) of a plate with a 10 mm notch

	[0/90]s			[0/45]s			[0/30/60]s		
	Glass	**FOF**	**Δ %**	**Glass**	**FOF**	**Δ %**	**Glass**	**FOF**	**Δ %**
1ˢᵗ mode	54.24	52.36	-3.5	63.60	79.32	24.7	103.6	116.8	12.7
2ⁿᵈ mode	80.33	102.1	27.1	78.16	111.6	42.8	114.1	148.0	29.7
3ʳᵈ mode	137.6	140.4	2.0	152.6	187.4	22.8	241.9	268.0	10.8
4ᵗʰ mode	223.0	270.4	21.3	217.0	299.8	38.2	316.6	393.8	24.4

5. Conclusion

The functionally oriented textile structure (FOT) or functionally oriented fabric (FOF) is a 2D woven fabric material for manufacturing of continuous fiber laminates. It is a type of fabric with non-randomly irregularly distributed threads of fibers of functional material. The benefit of such a woven structure are effectively distributed material properties in the specific areas where the best material performance is needed. Predominant material are low-cost fibers with average mechanical properties. Such a material is called a based material (BM). BM is combined with a functional material (FM), which has very good mechanical properties. FOF allows to reduce the number of layers in layup as there is no need to puzzle cuts of different materials. That can help to reduce waste in mass production. The carbon fiber

placement in warp and weft direction, strip width and span of strips can be modified during weaving process of FOF according the application requirements.

FOF structure helps to increase natural frequency of a laminate, which prevents standard operating frequency mechanisms and machines to reach the resonance. The functional material strips within the structure and especially around a structural opening (hole) helps to stiffen the laminate and the opening edge respectively. Speaking about resonance and stiffening the opening edge, the FOF has a potential to prevent the resonance of a mechanical joins, which can extend the joins' lifespan.

The results of simulations are consistent with the theory and show the potential of functionally oriented fabrics usage. The laminate layup customization allows tuning of laminate properties according to mode shape. Strips of functional material oriented in a longitudinal material direction have high effect on the bending modes. Strips angled from a longitudinal direction effect the twisting modes.

Analysis of FOF laminates with modified parameters are planned in the future to describe material performance and particular applications. After the evaluation of model with experimental data, simulations of FOF material in specific applications are going to be performed.

ACKNOWLEDGEMENTS

References

1. *Woven vs. non-woven. JPS Composite materials [online]. c2021 [cit. 2024-04-25]. Dostupné z: https://jpscm.com/blog/woven-vs-non-woven-fabrics/.*
2. *ZBONČÁK, Radek. Finite element model of a laminate made of functionally-oriented fabrics. In: DOUBRAVA, Karel, Kristýna KUBÁŠOVÁ, Zdeněk PADOVEC, Milan RŮŽIČKA a Radek SEDLÁČEK. Experimental stress analysis 2022. Book of extended abstracts. Prague: Czech Technical University in Prague, 2022, s. 144-145. ISBN 978-80-01-07010-9.*
3. *ZBONČÁK, Radek. Elastic properties prediction models of continuous fibers composites: composite materials. Liberec: VÚTS, 2018. ISBN 978-80-87184-81-3.*

PROPERTIES OF WOOL FIBERS REINFORCED COMPOSITES

Marcin Barburski, Tsegaye Lemmi, and Agata Poniecka

Lodz University of Technology, Faculty of Material Technologies and Textile Design, Institute of Architecture of Textiles, 116 Żeromskiego str. 90-924, Lodz, Poland
corresponding author e-mail: Marcin.barburski@p.lodz.pl

Abstract

Natural fiber-reinforced composites (NFRCs) have gained significant attention for their array of advantages, including biodegradability, low density, and cost-effectiveness compared to synthetic fiber-reinforced composites. The surge in interest is driven by a global shift towards sustainability and eco-conscious practices across various industries. Consequently, there has been a significant increase in exploration and innovation within the realm of natural fiber composites, reflecting a collective effort towards more environmentally friendly material solutions. Industries such as automotive, construction, aviation, and aerospace are increasingly exploring the use of natural fiber composites. However, the flammability of natural fiber-reinforced composites is a major challenge that needs to be addressed. Wool fiber, known for its natural flame-retardant and self-extinguishing properties, has been widely used in the textile industry to produce apparel, but its use in composite production has been limited. This study explores the feasibility of using wool fibers for composite reinforcement, primarily for applications where fire resistance is required. In this work, wool woven fabric and unidirectional (UD) wool roving were used as preforms, and a bio-based resin was applied through resin infusion techniques to produce the composites. The prepared composite samples were subjected to tensile, three-point bending, thermal insulation, and fire-resistance experimental investigations. The results obtained from the experimental investigations indicate that wool fiber has promising potential as a reinforcement material in composite applications mostly where fire resistance is critical.

Keywords:

Wool fiber; Composite; Fire resistance; Mechanical properties; Sustainability; Natural fibers

1. Introduction

Nowadays, most fiber-reinforced composites available on the market for various applications are made from glass or carbon fibers. However, due to the urgent environmental issues related to climate change and pollution, there is a growing need to focus on sustainable solutions and valuable alternatives. In light of these environmental challenges, there has been considerable interest in utilizing sustainable materials and processes [1,2]. Natural fibers have become particularly prominent among the various options explored, especially as reinforcement materials or fillers in composite manufacturing. In the last decade, Industries such as automotive, construction, aviation, and aerospace are increasingly exploring the use of natural fiber-reinforced composites. Various research has been carried out in recent years on flax and other natural fiber-based composites [3–5].

Despite multiple benefits, such as environmental sustainability, ease of disposal at end-of-life, recyclability, and low cost, the commercial use of natural fiber-reinforced composites (NFRCs) remains limited in engineering applications. Their adoption in commercial domains is hindered by challenges like high moisture absorption, low thermal stability, and poor fire resistance. Fortunately, the issue of moisture absorption has been successfully addressed through alkali treatment or acetylation. Recently,

the challenges of low thermal stability and poor fire resistance have also received attention. However, the main approaches used to address these challenges is the use of flame-retardant chemicals, but this have raised concerns about preserving the eco-friendly characteristics of NFRCs [6–8].

Therefore, in this work, the potential of using fibers with an inherent fire resistance property as a reinforcement material was explored. Wool fiber, primarily made of keratin, stands out as a noteworthy choice because of its renewable nature, biodegradability, flame resistance, and thermal insulation properties. Because of these qualities, wool fiber-reinforced composites are attractive options for use in a variety of industries where material performance and sustainability are crucial.

2. Experimental
2.1. Materials

The study utilized a wool fiber-based woven fabric with a plain structure and a unidirectional (UD) wool roving as the reinforcing phase, along with a bio-based resin as the matrix phase. The wool fiber was chosen primarily for its inherent thermal insulation, flame resistance, and biodegradability, making it advantageous for applications that require environmental sustainability and safety in temperature-sensitive environments. The wool fiber preforms utilized are shown in Figure 1. The matrix phase comprises a bio-based, low-viscosity green epoxy resin selected specifically for its compatibility with natural fibers and low environmental impact. Derived from renewable resources, this resin exhibits favorable mechanical strength, adhesion to natural fibers, and a reduced carbon footprint compared to petroleum-based alternatives. Additionally, it provides a stable polymer network upon curing, ensuring effective load transfer between the wool fiber reinforcement and the matrix.
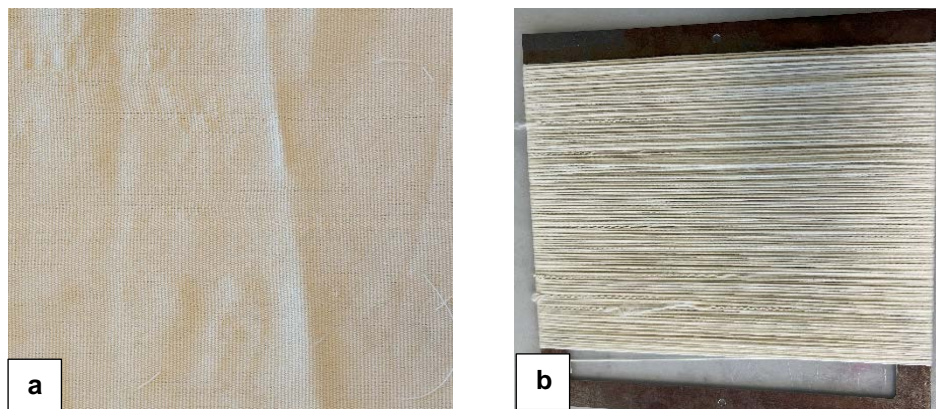
Figure 1. Wool fiber-based composite preforms. (a) Woven fabric, (b) Unidirectional wool roving.

2.2. Methods

The composite samples were prepared using a resin infusion technique, shown in Figure 2a. Two variants of composites, wool-woven fabric and UD wool roving reinforced composites, were prepared using the resin infusion technique. For the woven fabric-based composites, four layers of the fabric were used, while for the unidirectional (UD) composite, the equivalent density of yarn was overlaid based on the density of the yarns per centimeter of the four layers of woven fabric. The resin infusion process began by arranging the preform layers in the desired orientation on a glass plate treated to prevent adhesion. A peel ply and flow mesh were placed over the preform stack to aid resin flow, and the setup was sealed with a vacuum bag. After leak testing, a vacuum pump created a pressure differential to draw the resin, pre-mixed with hardener and degassed, through an inlet port and into the fiber layers. Once infused, the composite was cured under vacuum at room temperature and then post-cured at 50 °C for 24 hours in an autoclave to enhance mechanical properties. The final composite was inspected for uniformity and structural integrity before being subjected to experimental investigations.
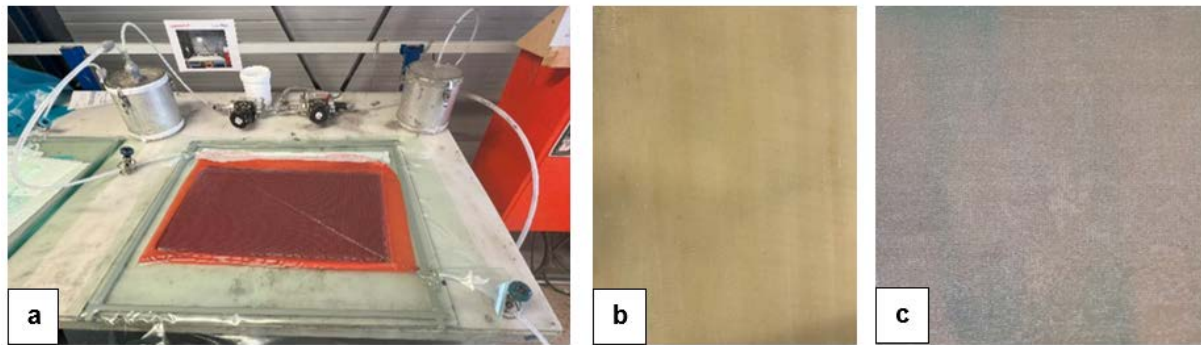
Figure 2. (a) Resin infusion technique, (b) UD wool roving reinforced composite, (c) Woven fabric reinforced composite.

2.2.1. *Experimental investigations of the composite samples*

The prepared composite samples were subjected to mechanical and thermal property investigations in order to evaluate the potential of using wool fiber-based preforms as a composite reinforcement. On the Instron testing machine, the tensile and three-point bending tests were conducted according to IS0 527-4: 1997(E) and ISO 14125:1998(E). The flammability experimental investigations were conducted according to ISO 4589-2. In addition to these experiments, the thermal property of the composite samples was also investigated. The number of specimens used for each test was based on the specimen size and amount described in each standard mentioned above for those specific experimental investigations.

3. Results and discussion

The results obtained from each experimental investigation carried out for both variants of composites produced are presented and discussed in this section.

The result of tensile and flexural bending investigation of both types of composite samples, as presented in Figures 3 & 4, indicates that the UD_wool fiber reinforced composite sample exhibited a 105.97% and 26.89% higher flexural bending and tensile strength, respectively, compared to the woven fabric-reinforced composite sample. However, in the perpendicular direction, the woven fabric-reinforced composite sample demonstrated relatively higher bending and tensile strength. This difference evolves around the orientation of fiber reinforcement; the UD alignment of fibers provides enhanced flexural resistance and tensile strength along the fiber direction, while woven composites contribute to higher resistance in orientations where unidirectional fibers are less effective.

The Limiting Oxygen Index (LOI) is defined as the minimum amount of oxygen required to sustain the flaming combustion of a material. The degree of flammability is ranked based on the LOI percentage of each material, where a material with an LOI of less than 20.95% is considered flammable, 20.95% < LOI < 28% is classified as slow-burning, 28% < LOI < 100% is considered self-extinguishing, and an LOI greater than 100% indicates a nonflammable material. To assess the flammability of the materials, an average LOI percentage of 24.55% and thermal resistance of 19.57K/W was obtained for both composite variants, with almost similar values for each variant. The LOI value obtained signifies that the use of wool fiber as a composite reinforcement can enhance the flammability of the composite.
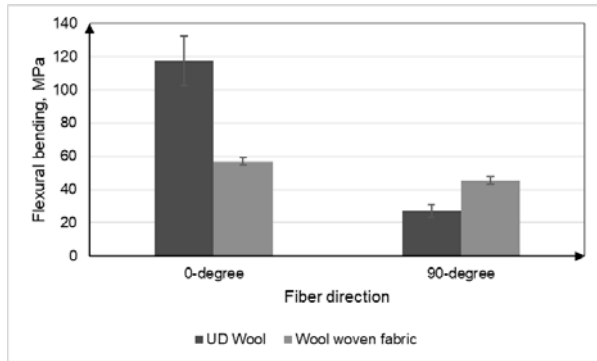
Figure 3. Flexural bending strength of the wool fiber reinforced composites.
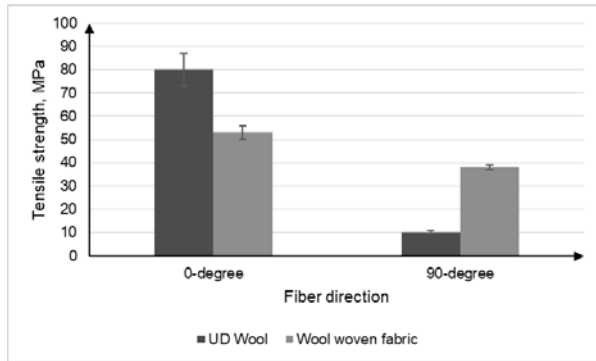
Figure 4. Tensile strength of the wool fiber reinforced composites.

CONCLUSIONS

This work investigated the possibility of using wool fiber-based preforms as a reinforcement material. The experimental investigation of UD and wool woven fabric reinforced composites has yielded several significant findings regarding their mechanical and flammability properties.

- It was observed that the mechanical properties of the wool woven fabric reinforced composites are notably lower compared to those of unidirectional (UD) wool roving reinforced composites in the fiber direction. This indicates that the reinforcement architecture significantly influences the composite's overall performance.
- The limited oxygen index (LOI) values obtained for the composite samples produced in this study demonstrate that wool fiber can effectively mitigate the flammability concerns associated with natural fiber-based composites. This finding highlights the potential of wool as a viable reinforcement material to enhance fire resistance.
- When examining the tensile and flexural bending strength properties obtained with the literature, the UD variant of the wool fiber-based composites exhibited commendable performance relative to other natural fiber-reinforced composites, such as flax and hemp. This suggests that wool fiber possesses reasonable mechanical characteristics within this sector.

In summary, the results of this research indicate that wool fiber has considerable potential as a reinforcement material when compared to more established natural fibers like flax and hemp. Although the mechanical properties of the wool-based composites developed in this study are promising, they remain lower than some alternative natural fibers available in the sector. Future research will focus on the incorporation of wool fibers with other reinforcement materials to further enhance the mechanical properties and to continue addressing the flammability issues inherent in natural fiber composites.

ACKNOWLEDGEMENTS

References

1. *Rajak, D. K., Pagar, D. D., Menezes, P. L., Linul, E. (2019). Fiber-reinforced polymer composites: Manufacturing, properties, and applications. Polymers, 11. https://doi.org/10.3390/polym11101667.*
2. *Kumar, S., Balachander, S. (2020). Studying the effect of reinforcement parameters on the mechanical properties of natural fibre-woven composites by Taguchi method. Journal of Industrial Textiles, 50, 133–148. https://doi.org/10.1177/1528083718823292.*
3. *Lemmi, T., Barburski, M., Samuel, B. (2021). Analysis of mechanical properties of unidirectional flax roving and sateen weave woven fabric-reinforced composites. Autex Research Journal, 21, 2–7. https://doi.org/10.2478/aut-2020-0001.*
4. *Poniecka, A., Barburski, M., Ranz, D., Cuartero, J., Miralbes, R. (2022). Comparison of mechanical properties of composites reinforced with technical embroidery, UD and woven fabric made of flax fibers. Materials, 15. https://doi.org/10.3390/ma15217469.*
5. *Baley, C., Gomina, M., Breard, J., Bourmaud, A., Davies, P. (2020). Variability of mechanical properties of flax fibres for composite reinforcement: A review. Industrial Crops and Products, 145, 111984. https://doi.org/10.1016/j.indcrop.2019.111984.*
6. *Islam, T., Chaion, M. H., Jalil, M. A., Rafi, A. S., Mushtari, F., Dhar, A. K., et al. (2024). Advancements and challenges in natural fiber-reinforced hybrid composites: A comprehensive review. SPE Polymers, 481–506. https://doi.org/10.1002/pls2.10145.*
7. *Rashid, M., Chetehouna, K., Cablé, A., Gascoin, N. (2021). Analysing flammability characteristics of green biocomposites. Fire Technology. https://doi.org/10.1007/s10694-020-01001-0.*
8. *Khatkar, V., Vijayalakshmi, A. G. S., Manjunath, R. N., Olhan, S., Behera, B. K. (2020). Experimental investigation into the mechanical behavior of textile composites with various fiber reinforcement architectures. Mechanics of Composite Materials, 56, 367–378. https://doi.org/10.1007/s11029-020-09888-0.*

HYDROPHOBIC TREATMENT OF JUTE REINFORCEMENT AND ITS EFFECT ON MOISTURE ABSORPTION AND MECHANICAL PROPERTIES OF COMPOSITES

[1]Asif Ali, [2]Mahrukh, [3]Abid Ali, [3]Waseem Ijaz, [3]Hadiqa Fatima, [4]Malaika Rasool, [3]Ayesha Iqbal

[1]University of Kuala Lumpur University, Malaysia
[2]Govt College University Faisalabad
[2]Department of Chemistry, Riphah International University, Faisalabad, Pakistan
[4]Department of Chemistry, University of Agriculture, Faisalabad, Pakistan

Abstract:

This research was proposed to go through fluorocarbon, hydrocarbon, and hybrid fluorocarbon effects on both mechanical properties and regain of moisture of composites reinforced with jute fiber. At the concentration of 40g/l a notable difference was spotted in moisture regain values of both treated and control (untreated) samples of reinforcement. Treated-based composites regain less content of moisture and present better mechanical properties (tensile strength and flexibility). The double nature (both hydrophilic and hydrophobic) of hybrid fluorocarbon causes treated jute fibre-based composites to display improved properties than the other 2 chemicals because of their good cooperation

Keywords:

Natural fibers, chemical treatment, moisture regain, composite material, Fluorocarbon

1. Introduction

The word "bio-composites" refers to composite materials that use biopolymers as the embedding matrix or natural reinforcing fibers [1]. Jute, flax, hemp, kenaf, and sisal are among the natural fibers that are most frequently utilized as reinforcement in bio-composites [2]. Because of its many unique qualities, affordability, ease of access, and environmental friendliness, jute is a highly valued degradable natural fiber in composites. The jute fiber has drawn consideration as support for composite materials due to its biodegradability, quality-to-weight proportion, and great insulation properties. In any case, higher dampness assimilation of these strands prevents the utilize of this fiber in composites. The dampness retention may cause the swelling and maceration of the strands, hence essentially diminishing its mechanical properties. So, the jute fiber got to be altered either physically or chemically to make strides the compatibility between the fiber and the polymer matrix. The surface of common filaments is ordinarily chemically altered to minimize the wetting of strands as well as to move forward the interface between the matrix and the reinforcement. A few chemical surface adjustment methods incorporate treatment with sodium chlorite[3], methaacrylate [4], isocyanate [5], silane treatment [6], acetylation [7], , mercerization [9], etherification [11], enzymatic treatment [12] , peroxide medications [10], benzoylation [9], dicumyl peroxide treatment [5], plasma treatment [13], ozone medications [17], and joining [19]. The oxidation of polyolefins [18], [19] has moreover been detailed to move forward the contradiction between the surfaces of characteristic fiber and polymer network. All these medications are pointed to decrease the dampness recapture of the characteristic strands and their resulting composites. It is well-documented that materials with lower surface free energy exhibit reduced moisture regain [20]. Fluorocarbons and hydrocarbons have lower surface free energy compared to most compounds used in previous studies. Despite their lower surface tension, fluorocarbons and hydrocarbons are not commonly utilized in treating jute fibers for composite applications. Therefore, the aims of this study were to decrease the moisture absorption of composite materials made from jute reinforcement treated with hydrocarbons, fluorocarbons, and hybrid fluorocarbons, to investigate the

properties of these composite materials, and to validate our assumptions regarding hybrid fluorocarbons. Composite samples made from treated and untreated jute fiber-reinforced composites were exposed to humid environment and their moisture regain, mechanical properties and fiber-matrix interface was tested at given time intervals until four weeks [21]. The composites produced with hydrophobic treated reinforcement showed lesser moisture regain and improvement in the tensile and flexural strengths compared to untreated fabric composite. A clear improvement in the fiber-resin interface was observed by scanning electronic microscopy. The dynamic mechanical analysis of treated and untreated composites was conducted in a temperature range of 20–140 °C. An increase in the storage modulus of treated composite materials was noted as compared to untreated ones [22]. Furthermore, it was concluded that developed composites lost their mechanical properties linearly with immersion time. However, this aging was slow in treated fabric composites especially hybrid fluorocarbon and fluorocarbon [23].

1.1. *Materials and method*

The plain woven textile with a density of 194±2 g/m2 served as reinforcement in the unsaturated polyester resin matrix. Methyl ethyl ketone and cobalt naphthenate 1% were used as a hardener and an accelerator. The three chemicals utilized in this investigation were purchased from HUNTSMAN (pvt) Limited: hydrocarbons (PHOBOL RSH), fluorocarbons (OLEOPHOBOL 7713), and hybrid fluorocarbons (OLEOPHOBOL CP-R). The composites were produced using the hand lay-up method. They used eight layers of woven jute fabric as reinforcement, with a composite plate size of 200×200 mm2 and a fiber volume fraction of 33% [24].The initial curing was done at room temperature for one hour, followed by post-curing at 120°C for 3 hours. Composites were created with untreated jute reinforcement and jute reinforcements treated with three types of hydrophobic chemicals. The specifics of the composite samples produced for the study are detailed in Table 4.

Table 2. Experimental design for composites samples

Sr. #	Samples ID	Reinforcement	Hydrophobic Chemicals	Concentration
1	S1	Jute	No	-
2	S2	Jute	F1	40 g/l
3	S3	Jute	F2	40 g/l
4	S4	Jute	F3	40 g/l
5	S5	Simple resin	No	-

Moisture regains test

The moisture regain test of jute fabric (untreated and treated with chemicals) was carried out by using the standard test method ASTM D2495, while that of composites and neat resin samples according to ASTM D5229. The composite sample was dried in an oven at 60˚C, till there was no further change in weight. This initial weight was recorded and the sample was immediately placed into the environmental system. Change in mass was measured after intervals of time till equilibrium was established. The graph was plotted between the weight gains versus the square root of time.

Mechanical characterization

The polymer matrix composite's in-plane tensile properties were evaluated according to ASTM D3039, with the ultimate tensile strength recorded as the peak load borne by the material before failure, utilizing a specimen measuring 200 mm in length, 25 mm in width, and tested at a speed of 100 mm/min, with a gauge length of 120 mm [25].The material's flexural properties were evaluated using a 3-point bending test, as per ASTM D7264. The test setup featured a specimen with dimensions of 5 mm thickness, 13 mm width, and a length exceeding the support span by 20%, with a span-to-thickness ratio of 20:1. The test was conducted at a slow and controlled speed of 1.0 mm/min [26].

2. Results and Discussion

2.1. *Moisture regain of reinforcement*

The moisture regain %age of untreated fabric sample and those samples treated with three different chemicals F1, F2 and F3 (hybrid fluorocarbons, hydrocarbons and fluorocarbons) as function of their concentrations is shown in Figure 1.
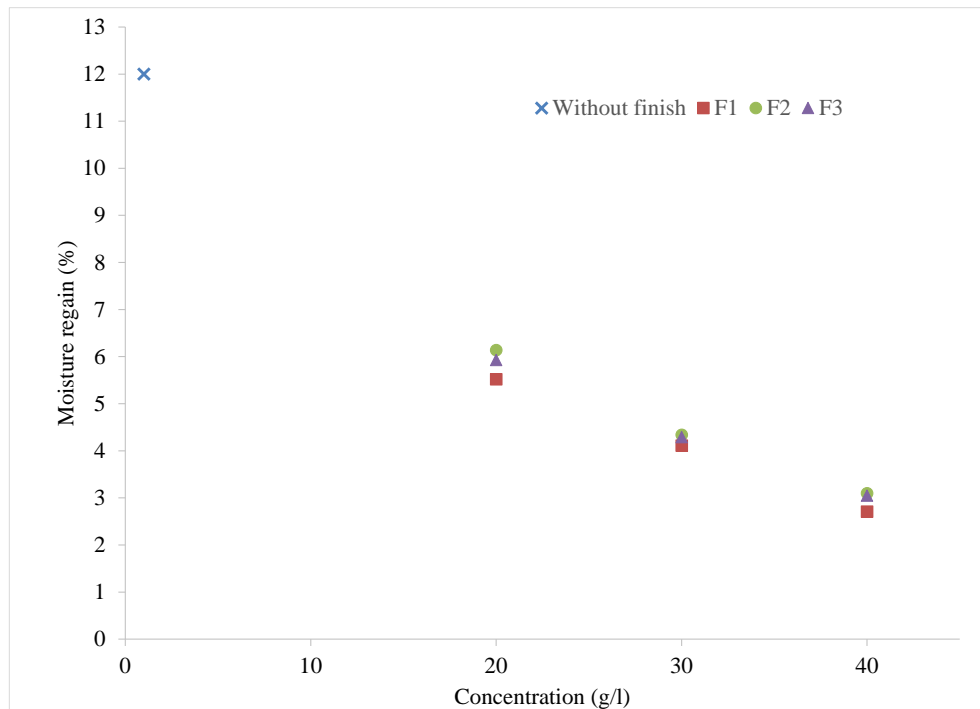
Figure 1. Moisture regain of untreated and treated fabric as function of chemical concentration

It can be easily noted from Figure 1 that untreated sample has moisture regain of about 12 % and treated sample has moisture regain of 2.71-6.14%. In addition, treated F1 reinforcement display lesser value of moisture regain such as 2.71% at 40g/l concentration. Whereas, the moisture regain values of F2 and F3 is about 3.10% and 3.05% at concentration of 40g/l. The difference between treated samples of F1,F2 and F3 moisture regains is not particularly necessary as the values of critical surface tension for all 3 chemicals are 14-28mNm^{-1}.

2.2. *Moisture regain of composite*

Moisture regain %age in equilibrium state of composite samples made from untreated and treated jute fabric is shown in Figure 2. The moisture regain % of neat resin sample was found to be 0.29%. Untreated jute composite sample absorbed 4% moisture whereas moisture regain of jute fabric was 12%.
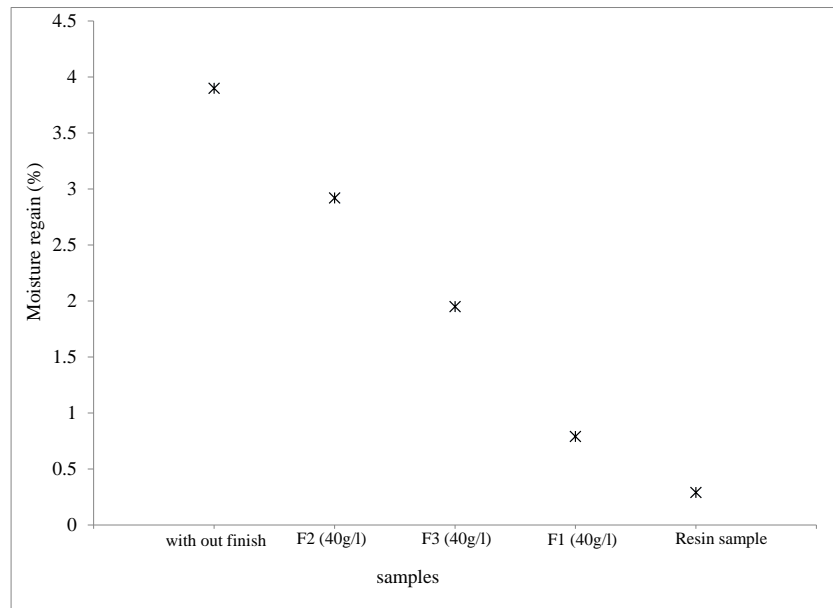
Figure 2. Moisture regain of resin and composite samples in equilibrium state

The regain of moisture in composites and samples of clear resins is normally plotted against the square root of time in Figure 4. It was observed that the intake of moisture is continuously increasing from beginning to 1000 mins in all the samples of composite.
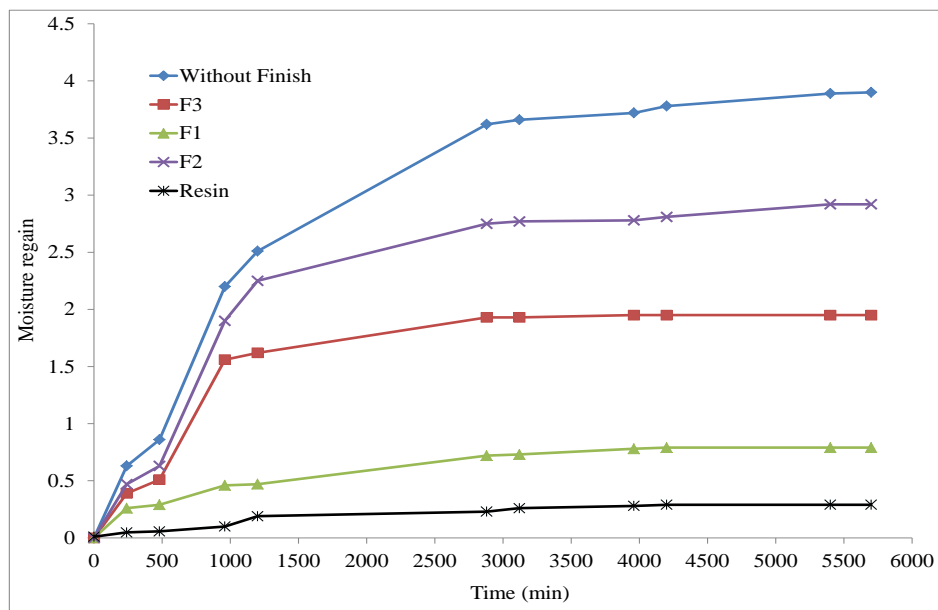
Figure 4. Moisture regains of composite samples

This is quite rational as specimen of tests were all fully dried. 1000 mins later, the specimen saturation start off while the rate at which moisture regain became decelerate. After 3000 mins, nearly all samples became saturated. The tests time were increased for the purpose of making sure that samples regained highest amount of moisture and attain the state of equilibrium.

2.3. Mechanical characterization

The flexural and tensile characteristics of composite materials were displayed in table 5. The values of the composite sample created with treated reinforcement and untreated reinforcement (F1, F2, and F3)

differ significantly. This is because the strength of the reinforcement primarily determines the strength of composite. The tensile strength of composites made from treated reinforcement varies, and the composite with F1 treated reinforcement has a higher tensile strength than the composites with F2 and F3 treated reinforcement. It's because F1 is a hybrid. The provided table makes it evident that the flexural strength of the treated reinforcement composites is greater than that of the sample of untreated reinforcement composites. It is due to the treated reinforcement is of greater strength than untreated reinforcement. The sample treated with F1 had the highest deflection, because of its excellent resin-matrix contact.

Table 5. Mechanical properties of composite materials

Sr. #	Composite samples	Reinforcement	Tensile Strength (MPa)	Flexural Strength (MPa)
1	S1	Simple jute reinforcement	32.34	38.71
2	S 2	F1 treated reinforcement (40g/l)	48.72	81.73
3	S 3	F2 treated reinforcement (40g/l)	42.56	67.11
4	S 4	F3 treated reinforcement (40g/l)	43.23	56.39

3. CONCLUSIONS

This study concludes that there is a notable difference in the moisture regain between untreated and treated reinforcements. The reinforcement treated with hybrid fluorocarbon exhibited the lowest moisture regain value of 2.71% at a concentration of 40 g/l, in contrast to the other treatments. Reinforcement in the composite absorbs more moisture, as the moisture regain % for the pure resin sample was only 0. undefined Untreated jute composite sample has a moisture regain of 4% whereas for the composites prepared by using the Hybrid Fluorocarbs treated reinforcement has the lowest moisture regain of 0. 79% thus conforming the moisture regain of the corresponding reinforcement. Mechanical result comparison between the composite sample with untreated reinforcement and treated reinforcement showed the difference exists. These findings underscore the efficacy of surface treatments in enhancing the moisture resistance of natural fiber reinforcements. These findings underscore the efficacy of surface treatments in enhancing the moisture resistance of natural fiber reinforcements. The reduction in moisture uptake is critical as it directly impacts the composite's long-term mechanical stability and durability. Additionally, a comparative analysis of mechanical properties between composite samples with untreated and treated reinforcements revealed significant differences, affirming the influence of moisture regain on mechanical performance. The treated reinforcement exhibited improved stability, suggesting potential for broader applications in industries requiring materials with enhanced moisture resistance and mechanical integrity. Future studies should focus on optimizing treatment concentrations and evaluating the environmental and economic implications of using such treatments at scale. Moreover, this study highlights the need to balance the ecological advantages of using natural fibers with the functional benefits offered by surface treatments. While hybrid fluorocarbons have demonstrated remarkable results, attention must be given to the environmental and health impacts associated with these chemical treatments. Future studies should optimize treatment concentrations, develop eco-friendly and biodegradable surface treatment alternatives, and evaluate their long-term performance. Evaluating the cost-effectiveness of large-scale implementation and understanding the life-cycle implications of treated composites are also crucial for broader industrial acceptance. Continued research into sustainable surface modification techniques and the development of more holistic approaches to enhance both mechanical performance and environmental sustainability will be key to advancing the practical use of natural fiber composites in various industries.

References

1. *F. C. Campbell, Structural Composite Materials. Ohio: ASM International, 2010.*

2. *D. Gay, S. V. Hoa, and S. W. Tsai, Composite Materials: Design and Applications, 1st ed. Florida: CRC Press, 2003.*

3. *G. M. A. Khan and S. Alam, "Surface chemical treatments of jute fiber for high value composite uses," J. Mater. Sci., vol. 1, no. 2, pp. 39–44, 2013.*

4. *Cantero, G.; Arbelaiz, A.; Llano-Ponte, R.; Mondragon, "Effects of fiber treatment on wettability and mechanical behaviour of flax/polypropylene composites," Compos. Sci. Technol., vol. 63, no. 9, pp. 1247–1254, 2003.*

5. *K. Joseph and S. Thomast, "Effect of chemical treatment on the tensile properties of short sisal fibre-reinforced polyethylene composites," vol. 37, no. 23, pp. 5139–5149, 1996.*

6. *S. Alix, S.; Lebrun, L.; Morvan, C.; Marais, "Study of water behaviour of chemically treated flax fibers-based composites: A way to approach the hydric interface," Compos. Sci. Technol., vol. 71, no. 6, pp. 893–899, 2011.*

7. *M. J. John and R. D. Anandjiwala, "Recent developments in chemical modification and characterization of natural fiber-reinforced composites," Polym. Compos., vol. 29, no. 2, pp. 187–207, 2008.*

8. *V. de Velde, Kathleen, and P. Kiekens, "Thermoplastic polymers: overview of several properties and their consequences in flax fibre reinforced composites," Polym. Test., vol. 20, no. 8, pp. 885–893, 2001.*

9. *K. Joseph et al., "Natural fiber reinforced thermoplastic composites," Nat. Polym. Agrofibers Compos., vol. 159, pp. 159–201, 2000.*

10. *M. Sreekala, M. Kumaran, S. Joseph, M. Jacob, and S. Thomas, "Oil palm fibre reinforced phenol formaldehyde composites: influence of fibre surface modifications on the mechanical performance," Appl. Compos. Mater., vol. 7, no. 6, pp. 295–329, 2000.*

11. *H. Matsuda, Chemical Modification of Solid Wood, 1st ed. New York: Marcel Dekker Inc., 1996.*

12. *S. Grönqvist, J. Buchert, K. Rantanen, L. Viikari, and A. Suurnäkki, "Activity of laccase on unbleached and bleached thermomechanical pulp," Enzyme Microb. Technol., vol. 32, no. 3, pp. 439–445, 2003.*

13. *T. Uehara and I. Sakata, "Effect of corona discharge treatment on cellulose prepared from beech wood," J. Appl. Polym. Sci., vol. 41, no. 7–8, pp. 1695–1706, 1990.*

14. *P. Hedenberg and P. Gatenholm, "Conversion of plastic/cellulose waste into composites. II. Improving adhesion between polyethylene and cellulose using ozone," J. Appl. Polym. Sci., vol. 60, no. 13, pp. 2377–2385, 1996.*

15. *H. Chtourou, B. Riedl, and B. V. Kokta, "Strength properties of wood-PE composites: Influence of pulp ratio and pretreatment of PE fibers," TAPPI J., vol. 80, no. 4, pp. 141–151, 1997.*

16. *D. N.-S. Hon, Graft copolymerization of lignocellulosic fibers. Washington D.C: American Chemical Society, 1982.*

17. *J. Meyer, Wood-polymer composites and their industrial applications, in Wood Technology: Chemical Aspects. Washington D.C: American Chemical Society, 1977.*

18. *F. Gugumus, "Thermooxidative degradation of polyolefins in the solid state-6. Kinetics of thermal oxidation of polypropylene," Polym. Degrad. Stab., vol. 62, no. 2, pp. 235–243, 1998.*

19. *T. Kotoyori, "Activation energy for the oxidative thermal degradation of plastics," Thermochim. Acta, vol. 5, no. 1, pp. 51–58, 1972.*

20. *B. Arkles, Y. Pan, and Y. M. Kim, "The Role of Polarity in the Structure of Silanes Employed in Surface Modification," Silanes and Other Coupling Agents, vol. 5, pp. 51–64, 2009.*

21. *"Akil, H. M., Santulli, C., Sarasini, F., Tirillo, J., & Valente, T. (2014, April). Environmental effects on the mechanical behaviour of pultruded jute/ glass fibre-reinforced polyester hybrid composites. Composites Science and Technology, 94, 62–70. doi:1".*

22. *"Ali, A., Shaker, K., Nawab, Y., Ashraf, M., Basit, A., Shahid, S., & Umair, M. (2015). Impact of hydrophobic treatment of jute on moisture regain and mechanical properties of composite material.*

Journal of Reinforced Plastics and Composites, 34, 2059–2068".

23. *M. H. Ameer et al., "Interdependence of moisture, mechanical properties, and hydrophobic treatment of jute fibre-reinforced composite materials," J. Text. Inst., vol. 108, no. 10, pp. 1768–1776, 2017, doi: 10.1080/00405000.2017.1285201.*

24. *A. Ali et al., "Impact of hydrophobic treatment of jute on moisture regain and mechanical properties of composite material," J. Reinf. Plast. Compos., vol. 34, no. 24, pp. 2059–2068, 2015, doi: 10.1177/0731684415610007.*

25. *A. Dong, Y. Yu, J. Yuan, Q. Wang, and X. Fan, "Hydrophobic modification of jute fiber used for composite reinforcement via laccase-mediated grafting," Appl. Surf. Sci., vol. 301, pp. 418–427, 2014, doi: 10.1016/j.apsusc.2014.02.092.*

26. *A. Ali et al., "Hydrophobic treatment of natural fibers and their composites—A review," J. Ind. Text., vol. 47, no. 8, pp. 2153–2183, 2018, doi: 10.1177/1528083716654468.*

INVESTIGATION OF THE EFFECT OF SOFTENERS ON COTTON KNITTED FABRIC STIFFNESS

Buket Güler[1], Ismet Ege Kalkan[2], Şamil Çelebi[3], Umut Kıvanç Şahin[4]

[1] TYH Textile Research and Development Center, Istanbul, Turkey, buketguler@tyh.com.tr
[2] Department of Textile Engineering, Istanbul Technical University, Istanbul, Turkey, kalkani15@itu.edu.tr
[3] TYH Textile Research and Development Center, Istanbul, Turkey, samilcelebi@tyh.com.tr
[4] Department of Textile Engineering, Istanbul Technical University, Istanbul, Turkey, sahinumut3@itu.edu.tr
Corresponding author: buketguler@tyh.com.tr

Abstract:

Textile comfort of the fabrics is becoming very popular and soft touch is one of the prominent features. The main desired properties of cellulosic knits are their pleasant appearance, softness, absorbency, breathability, texture and comfort, which make them ideal for use in casual wear, sportswear, underwear, etc. Improving the performance and properties of cellulosic knits such as dimensional stability, smoothness, drapability, etc. through functional finishes is becoming necessary to cope with the demands of consumers and garment manufacturers. In this novel study 2 types of knitted structures (single jersey and pique) made of 100% cotton were used. Three different softening chemicals (macro silicone, micro silicone and seam facilitator) were used and acetic acid were used as a binding agent. According to the results, it was determined that macro silicone softener in single jersey knitted fabric and seam facilitator softener in pique knitted fabric gave more effective results in terms of hand feeling properties.

Key words:

Comfort, finishing, hand feeling, softener, cotton

1. Introduction

Comfort is a fundamental characteristic in the evaluation of clothing products, making it a key focus for textile manufacturers [1]. The literature reveals that softeners are the most commonly used method to enhance fabric comfort, as they play an essential role in improving the hand feel, smoothness, appearance, and usability of textiles. Softening treatments are typically applied after dye finishing as part of the finishing processes to ensure a soft touch and appealing look [2,3,4].

Textile materials are composed of various polymers, including natural cotton, cellulosic fibers, synthetic polyesters, and blends of these fibers. The combination of fibers directly influences the final quality and tactile feel of the fabric, which drives manufacturers to continuously improve fabric quality, smooth its surface, and enhance performance. In this regard, softeners are indispensable in textile production, with silicone-based softeners being especially common in enhancing fabric softness and tactile appeal [5].

There are studies about softener effects in the literature. Süpüren Mengüç, Dalbaşı, Özgüney & Özdil (2019), investigated the effects of various softeners on the hand-feeling properties and washing durability of cotton and bamboo knitted fabrics. They determined that the softening process did not have

a successful performance in bamboo fabrics as in cotton fabrics. Hossain, Siddika & Islam (2019), examined the hand feel properties of single jersey fabric treated with three different types of cationic softener. They determined that aliphatic condensation softener gave the best results in terms of color fastness and hand feel properties of the fabric [6]. In another study; Illeez, Dalbaşı & Kayseri (2015), investigated the effects of parameters such as knitting structure, softener type and chemical concentration on sewability and seam shrinkage in ready-made clothing in cotton knitted fabrics. They found that softening treatments significantly improved sewability and seam shrinkage [7]. Silicone softeners are one of the most commonly used types of softeners in the textile industry. The use of silicone softeners is especially common in premium textile products and in areas that require high performance, such as sportswear and outerwear. These softeners are generally applied by the pad-dry-cure method and extend the life of textile products thanks to their long-term effects. These versatile advantages of silicone softeners make them a popular choice among textile manufacturers and consumers.

The aim of the study is to apply different types of softeners to fabrics with different knitted structures containing cotton and evaluate their findings. It is believed that the study will provide new data aimed at optimizing parameters such as overall user comfort. This study aims to provide scientific and practical information to textile manufacturers and researchers on the selection of softeners by examining in detail the effects of softeners on the hand feeling properties of fabrics.

2. Experimental

In the scope of the study, macro silicone, hydrophilic silicone and seam facilitating softeners were applied on cotton fabrics with different knitting type. Cotton was preferred in the study because it is one of the most widely used textile fibers in the world. For this purpose, single jersey and double pique fabrics were chosen for this study and treated with three types of softeners. Softener types were applied to the fabrics by pad-dry method. The concentration level applied was determined to be average, consistent with commercial practice. After the chemicals were applied, they were left to dry at 100 °C for half an hour. Then, stiffness test was performed and comparative analysis was carried out to evaluate the effect of different knitted structure. The bending strengths of the fabrics were determined with a digital pneumatic softness tester according to the ASTM (American Society for Testing and Materials) D 4032-08 circular bending test method. Details of the applied softeners are given in Table 1.

Table 1. Details of softener application process

Softener	pH	Concentration (g/L)	Pick up (%)
Macro silicone (polysiloxane)	5	40	80
Hydrophilic silicone	5	40	80
Seam facilitator (polyethylene emulsion)	5	40	80

3. Results and discussion

Bending strength tests were carried out on test specimens of knitted fabrics of different structures before and after softening treatment. The fabric stiffness tester measures the force applied to a fabric under a standard pressure and the results are expressed in kgf. The results of the test specimens are given in Table 2.

Table 2. Test results

Fabric	Stiffness (kgf)			
	Non-treated	**Softener 1 (macro silicone)**	**Softener 2 (hydrophilic silicone)**	**Softener 3 (seam facilitator)**
Single jersey	0.024	0.022	0.039	0.041
Pique	0.072	0.064	0.041	0.028

It was observed that macro silicone softener decreased the stiffness (hardness) value by 5% in single jersey fabric, while hydrophilic softener increased the hardness by 63% and seam facilitator softener increased the hardness by 72%. It was determined that macro silicone softened the pique fabric by 11.5%, hydrophilic silicone by 43% and sewing facilitator softener by 60%.

According to the tests, it was found that all softeners applied gave effective results on pique fabric. It was observed that hydrophilic silicone and seam facilitator finish had a negative effect on single jersey knitted fabric at the applied concentration. While it was observed that seam facilitator softener was more effective in pique fabric, it was determined that macro silicone was more effective in single jersey fabric.

In the literature, it is known that softeners cause a decrease in bending properties due to the decrease in friction forces between yarns caused by the lubrication effect. However, fabric structure plays a decisive role on the effectiveness of the finish [8]. It has been determined that the knitting structure and surface characteristics of the fabric can affect the way softeners penetrate the fabric and show their effects.

Single jersey fabrics have a fine and dense knitting structure. This structure makes the fabric more flexible and lighter. Therefore, it can be easier for softeners to penetrate the fabric. However, softeners that provide a thinner and homogenous spread to increase the feeling of softness will be more effective in jersey. Pique fabric, which has a thicker and bulkier structure, is usually heavier and stiffer than single jersey. In this fabric, the effect of softeners should be able to penetrate deeper. The softeners used in pique fabric may need to have a more intense effect due to the volume and textural differences in the knitting structure. In addition, softeners work on the fabric by different mechanisms. Macro silicone-based softeners provide lubricity by adhering to the fiber surface and it is thought that such softeners can create a more pronounced effect on thinner fabrics (such as single jersey). Hydrophilic silicone softeners increase the water absorbency of the fabric and give softness to the fabric. This type of softener is considered to be more effective on thicker fabrics with high moisture retention capacity, such as pique. The seam facilitating finish has a hydrophobic structure and is thought to facilitate sewing operations by reducing friction between the fibers and making the fabric smoother.

As a result, even though they are produced from the same raw material, the fact that single jersey and pique fabrics have different structure and surface properties causes the effects of softeners on the fabric to vary. The thickness and texture of the fabric and the chemical structure of the softeners are the main factors determining which softener is more effective. It is thought that the hardening effect of hydrophilic and seam facilitating softeners on single jersey fabrics is related to the applied concentration. For this reason, it has been observed that optimum concentration settings of softeners are important. Determining the ideal concentrations for different fabric structures is critical to achieve the desired results.

4. CONCLUSIONS

Within the scope of the study, the stiffness properties were analyzed by applying equal concentrations of macro silicone, hydrophilic silicone and seam facilitator (polyethylene emulsion) softening finishes to single jersey and pique fabrics containing 100% cotton. As a result, it was determined that macro silicone finish provided a low amount of softening in single jersey fabrics at the applied concentration, while other silicones made the fabric even stiffer. In pique fabrics, it was found that all softening chemicals provided softening, but the maximum softening was provided by the seam facilitator finish.

In conclusion, the investigation provides valuable insights into the role of softeners in modifying the stiffness of cotton knitted fabrics. The findings highlight that careful selection and application of softeners can significantly enhance the tactile properties of fabrics. Additionally, it contributes to the development of softer and more comfortable cotton garments. It is thought that by understanding the specific effects of different fabric softeners on fabric stiffness, manufacturers can make informed decisions about the types and concentrations of softeners to be used, and tailor their products to meet specific consumer preferences for softness and comfort. In the continuation of the study, it is aimed to apply softeners to fabrics at different concentrations and to perform tests and analyses.

References

1. *Cimilli Duru, S., & Şahin, U. K. (2019). Effects of yarn type, process history, softener type and concentration on wicking and drying properties of cotton plain knitted fabrics. The Journal of The Textile Institute, 1–10. doi:10.1080/00405000.2019.1689773*
2. *Hossain, Md. S., Siddika, A., & Islam, T. (2019). Investigation of different cationic softener effects on shade appearance, colour fastness and hand feel properties of 100% cotton circular weft knitted single jersey fabric. Journal of Engineering Science, 10(1), 85-92*
3. *Illeez, A.A., Dalbaşı, E.S., & Kayseri, G.Ö. (2015). Improving of sewability properties of various knitted fabrics with the softeners. Procedia - Social and Behavioral Sciences, 195, 2786 – 2795*
4. *Islam, Md. Shahidul., Sazal, Md. M.R., & Ripon, Md. M.I. (2017). Variation of knit dyed fabric quality on different percentage of silicon softener. International Journal of Scientific & Engineering Research, Volume 8, Issue 2, February-2017*
5. *Malwade S.R., Kulkarni R.R., Sayyed A.J., 2024. Effect of block copolymer silicone softener on textile fabric hydrophilicity, softness, and durability, Journal of the Indian Chemical Society,101(8).* https://doi.org/10.1016/j.jics.2024.101197.
6. *Orhan, M., Tiritoğlu, M., & Ozbarutcu, B. (2020). Silikon yumuşatıcıların pamuk ve viskon örme kumaşlar üzerinde etkileri. Uludağ Üniversitesi Mühendislik Fakültesi Dergisi, 25(2), 941-960. https://doi.org/10.17482/uumfd.660283*
7. *Süpüren Mengüç, G., Özgüney, A.T., Dalbaşı, E.S., & Özdil, N. (2019). A comparative study on handle properties of bamboo and cotton fabrics. Industria Textila.70(3), 278-284.*
8. *Gong, R. H., & Bhatia, A. (2009). Effects of Softeners on Mechanical Properties of Cotton Fabric. Research Journal of Textile and Apparel, 13(4), 45–50. doi:10.1108/rjta-13-04-2009-b006*

ANALYZING THE EFFECT OF BLENDING RATIO AND SPINNING SYSTEM ON THE PROPERTIES OF BAMBOO/COTTON FABRICS DYED WITH ACORN DYESTUFF

Memik Bünyamin Üzümcü[1], Esin Sarıoğlu[2], Tülin Nacarkahya[3], Şeyma Satıl[4], Burak Sarı[5]

[1] Gaziantep University, Fine Arts Faculty, Department of Textile and Fashion Design, Gaziantep, Türkiye, muzumcu@gantep.edu.tr
[2] Gaziantep University, Fine Arts Faculty, Department of Textile and Fashion Design, Gaziantep, Türkiye, sarioglu@gantep.edu.tr
[3] Karafiber Tekstil San. ve Tic. A.Ş.R&D Center, Gaziantep, Türkiye, tulin.kaya@karaholding.com
[4] Karafiber Tekstil San. ve Tic. A.Ş.R&D Center, Gaziantep, Türkiye, arge@karaholding.com
[5] Bitlis Eren University, Fine Arts Faculty, Department of Traditional Turkish Arts, Bitlis, Türkiye, bsari@beu.edu.tr
Corresponding author e-mail: buzumcu@gantep.edu.tr

Abstract

In the context of sustainable development goals, a diverse array of contributing studies has emerged within the textile sector. It is evident that the majority of these studies encompass both legal and customer obligations. The objective of contemporary businesses is to manufacture products that demonstrate a high level of environmental sensitivity. For instance, the objective is to reduce the quantity of waste products, to achieve energy-efficient production, to minimize the amount of chemicals employed, to reduce water consumption, to utilize energy derived from renewable sources, and thus to diminish the carbon footprint. From an environmental standpoint, the chemicals utilized in textile product manufacturing have emerged as a significant consideration. It is preferable that the chemicals employed in the dyeing process (dyestuffs, bleaching agents, softeners, etc.) are environmentally sensitive. Furthermore, the use of organic dyes in the dyeing process is also employed as a means of obtaining a more sustainable product. In the context of this study, the production of bamboo/cotton yarn was conducted at varying blend ratios (67/33%, 50/50%, and 33/67%) through the use of three distinct production methods (open end, vortex, and ring systems). Single jersey knitted fabrics were produced using these yarns with the same production parameters. Subsequently, the fabrics were dyed using acorn natural dyestuff. Pilling, fastness and CIELab analyses were performed on the fabric samples, and the results were subjected to statistical analysis.

Key words: *sustainability, organic dye, acorn dye, color fastness.*

1. Introduction

The production of textiles is a highly intricate process, encompassing various mechanical, chemical, and physicochemical steps. These processes often involve the use of hazardous substances, including heavy metals and pesticides. However, they are subject to extensive monitoring and regulation by standards such as ZDHC (Zero Discharge of Hazardous Chemicals), OEKO-TEX (International Association for Research and Testing in the Field of Textile and Leather Ecology), and GOTS (Global Organic Textile Standard), with the aim of ensuring safety and reducing environmental impact [1].

In the present era, environmental sustainability represents a pivotal concern for the textile industry. The rapid changing fashion industry and the intensive use of chemicals present a significant challenge to achieving a sustainable future, with adverse effects on both the environment and human health. The textile industry is seeking novel and creative solutions that will enable it to become environmentally sustainable, with a view to reducing its reliance on natural resources, minimizing its carbon footprint and eliminating the generation of harmful chemical waste. In this context, dyeing with natural sources are attracting attention as an alternative to dyeing with synthetic dyestuff, offering a promising potential for sustainability.

Dyeing with natural sources is generally defined as the process of imparting color to textile products through the use of pigments derived from plants, minerals and other organic materials. The extraction of natural dye process typically begins with the collection of plant materials like roots, leaves, flowers, or bark. The dyes are then extracted using methods such as boiling, soaking, or fermentation [2-4]. The production of natural colorants promotes plantation, contributing to the reduction of atmospheric CO_2 and increasing oxygen levels. It can be asserted that there are certain disadvantages associated with the use of natural colors. Despite the necessity for a certain amount of time to obtain natural colorants, the yields are typically very low. The commercial production of natural colorant sources is not feasible on a large scale. Consequently, the low yield of natural colorants results in correspondingly high production costs [5].

The literature includes studies that examine the properties of textile products obtained from a variety of natural dyes. These studies investigate the application of different natural dyes on diverse raw materials and the associated quality analyses [6-16].

This study examined the use of acorn natural dyestuff in the production of single jersey fabrics produced nine different yarns with varying blend ratio and spinning systems.

2. Experimental
2.1. Materials

In this study, bamboo and cotton fibers were used in order to produce yarn samples at three different blend ratios (67/33%, 50/50%, and 33/67%). Yarns and knitted fabrics were produced with these blends. Fabrics were dyed with natural acorn dyestuff. In these dyeing processes $KAl(SO_4)_2$ was used as mordant.

2.2. Methods

To examine and compare the spinning systems, open end rotor, ring and vortex systems were chosen for yarn spinning in this study. Ne 30/1 nine different yarn samples with α_e 3.6 twist coefficient were obtained, then these yarns were knitted at the same production parameters. Single jersey knitted fabrics were dyed with acorn natural dyestuff. Tenacity and elongation, hairiness, imperfections and unevenness properties were carried out in accordance with related standards. In addition, weight, thickness, pilling, color fastness to water and rubbing (dry and wet) properties were also determined with related standards. Results were analyzed statistically using SPSS package program.

3. Results and discussion
3.1. Fiber Properties

In this study, 2 types of fibres were used. The properties of these fibres are presented in Table 1. These fibres were blended at different blend ratios and used to produce yarns in 3 different systems (ring, open end rotor and vortex).

Table 1. Fiber Properties

Fiber	Fineness (dtex)	Staple Length (mm)	Density (g/cm^3)	Strength (cN/tex)
Cotton	1.2	32	1,52	31,2
Bamboo	1.33	38	1.32	34

3.2. <u>Yarn properties</u>

In this study, bamboo and cotton fibers with known fiber properties were blended in 3 different blend ratios and these blends were used in the production of ring, rotor and vortex yarns. Various yarn tests were carried out to determine the properties of the yarns produced. The measurements were taken in accordance with the following standards:

- TS EN ISO 2062 for strength and elongation tests,
- ISO 16549 for unevenness and yarn faults, and
- TS 12863 for unevenness determination.

In order to evaluate the results and ascertain the effects of the blend ratios of the fibers and the spinning system in which the yarn is produced, ANOVA tests were performed (Table 2). According to the results of this test, the spinning system has a statistically significant effect on all measured properties of the yarn. When the effect of blend ratio was analyzed, the effects of this parameter on yarn faults, strength and elongation were found to be significant.

Table 2. Analysis of Variance Results of Yarn Properties

Independent Variables	Dependent Variables				
	Unevenness (U%)	IPI	Hairiness (Uster H)	Elongation (%)	Tenacity (kgf*Nm)
Spinning system	**0.022***	**0.000***	**0.000***	**0.003***	**0.008***
Blend Ratio	0.086	**0.006***	0.262	**0.002***	**0.037***

*Statistically significant at 0.05 confidence level

When the yarn characteristics were analyzed (see Fig. 1), it was seen that ring-spun yarns have higher strength and elongation, lower yarn faults and unevenness values, and also the highest hairiness values. The lowest hairiness values were observed in vortex yarns for all blend ratios. Additionally, the tensile strength and elongation values of the yarns produced with the Vortex system are inferior to those of ring yarns. Rotor yarns were found to have the highest yarn faults, the highest unevenness values and the lowest strength and elongation. The data obtained in this study are similar to the literature [17,18].

When the yarn properties were evaluated within the framework of the blend ratio, it was found that an increase in the proportion of cotton in the blend caused higher unevenness values and more yarn faults. However, higher strength and elongation values were obtained in yarns with high bamboo content. It was an expected result that the increase in the ratio of bamboo fiber, which has higher strength, in the yarn positively affected the yarn strength. Hairiness was not much affected by the blend ratio. It was evident that hairiness was more influenced by the spinning system than by the raw material.
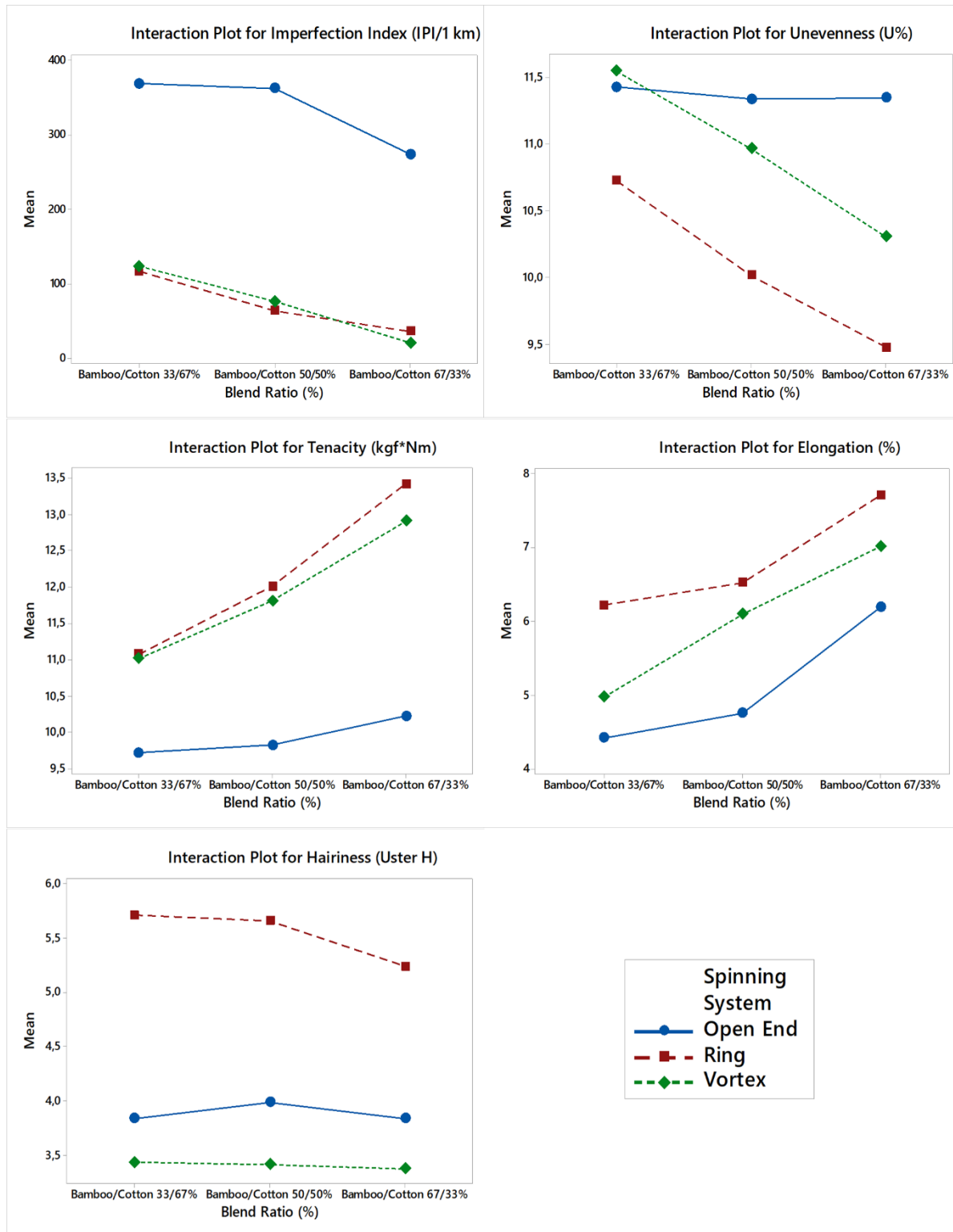
3.3. *Fabric properties*

As mentioned in the methods, single jersey fabrics were knitted using the same parameters. After fabric production all of these fabrics were dyed using acorn natural dyestuff. A number of tests were carried out to determine the properties of these dyed fabrics. The test results of these fabrics are given in Table 3.

Table 3. Fabric properies

Blend Ratio (B/C%)	Yarn Type	Thickness	Air Permeability	Pilling resistance
67/33	Ring	0,62	1358,68	2/3
50/50	Ring	0,59	1268,16	2/3
33/67	Ring	0,63	1415,42	2/3
67/33	Open End	0.53	1725,35	3/4
50/50	Open End	0.54	1866,49	3/4
33/67	Open End	0.57	1526,9	3/4
67/33	Vortex	0.62	1263,84	4/5
50/50	Vortex	0.62	1269,29	4/5
33/67	Vortex	0.65	1766,55	4/5

When the results given in Table 3 are analyzed, it is seen that the highest air permeability is found in open end fabrics. This is an expected result in view of the low hairiness of rotor yarns. The difference in terms of blend ratio and spinning system as independent variables, is statistically significant according to ANOVA tests ($p=0.001<0.05$ for spinning system and $p=0.031$ for blend ratio). When pill grade values were analyzed, it was determined that the highest pilling resistance was achieved in fabrics produced with vortex yarns.

Fabrics were dyed with acorn dyestuff as mentioned before. The color properties of these fabrics are given in Table 4. L value results indicate that the lightness of the fabrics increased with higher bamboo content. According to the other parameters in Table 4, it can be said that although there are some variations in the color of these fabrics, similar dyeing results were obtained.

Table 4. Color Properties of acorn dyed fabrics

Blend Ratio (B/C%)	Spinning System	Illuminant (D65 10 Deg)				
		L*	a*	b*	C*	h*
67/33	Ring	77,97	3,27	18,87	19,15	80,16
50/50	Ring	77,94	3,39	19,62	19,91	80,19
33/67	Ring	74,86	3,88	20,34	20,71	79,79
67/33	Open End	86,87	3,28	19,08	19,36	80,24
50/50	Open End	72,89	5,57	19,67	20,45	74,2
33/67	Open End	75,7	3,75	19,37	19,73	79,03
67/33	Vortex	77,06	3,61	19,37	19,7	79,43
50/50	Vortex	75,25	4,37	19,09	19,59	77,11
33/67	Vortex	75,15	4,29	19,66	20,12	77,69

Color fastness of these fabrics to water and rubbing (wet and dry) were also tested. Results of the staining on multifiber fabric after water treatment are given in Table 5. It can be seen from the results that the change in the spinning systems used for yarn production and the change in blend ratio for bamboo and cotton fibers did not affect these values.

Table 5. Color fastness to washing results

Blend Ratio (B/C%))	Spinning System	Staining					
		Acetate	Cotton	Nylon	Polyester	Acrylic	Wool
67/33	Ring	4/5	4	4	4/5	4/5	4/5
50/50	Ring	4/5	4	4	4/5	4/5	4/5
33/67	Ring	4/5	4	4	4/5	4/5	4/5
67/33	Open End	4/5	4	4	4/5	4/5	4/5
50/50	Open End	4/5	4	4	4/5	4/5	4/5
33/67	Open End	4/5	4	4	4/5	4/5	4/5
67/33	Vortex	4/5	4	4	4/5	4/5	4/5
50/50	Vortex	4/5	4	4	4/5	4/5	4/5
33/67	Vortex	4/5	4	4	4/5	4/5	4/5

Results of the staining on multifiber fabric after water treatment are given in Table 6. These results also indicate that there is no difference between the color fastness to rubbing results in terms of blend ratio and spinning system as independent variables.

Table 6. Color fastness to rubbing results

Blend Ratio (B/C%)	Spinning System	Rubbing	
		Dry	Wet
67/33	Ring	4	3/4
50/50	Ring	4	3/4
33/67	Ring	4	3/4
67/33	Open End	4	3/4
50/50	Open End	4	3/4
33/67	Open End	4	3/4
67/33	Vortex	4	3/4
50/50	Vortex	4	3/4
33/67	Vortex	4	3/4

4. CONCLUSIONS

In this study, acorn natural dyestuff was used in order to dye nine different types of single jersey bamboo-cotton blended knitted fabrics. Initially, yarns were produced with 3 different spinning systems (ring, rotor and vortex) with 3 different blend ratios (67%Bamboo-33%cotton, 50%bamboo-50%cotton and 33%bamboo-67%cotton). All these yarns were produced using the same αe 3.6 twist coefficient. After yarn productions single jersey fabrics were knitted using the same knitting parameters. In the end, fabrics were dyed, again, using the same dyeing parameters.

All the tests carried out during this study were done according to standards. These results were obtained at the end:

- Spinning system and blend ratio significantly affected yarn properties.

- Higher bamboo content in the blend resulted with lighter shades in fabrics.
- As both fibers are cellulosic and have similar structures, fastness results we investigated were similar (because of their interactions with the dye).

References

1. Karadag, R. (2023). Establishing a new international standard for natural dyed textile goods [Natural Organic Dye Standard (NODS)]. Journal of Natural Fibers, 20(1), 2162187.
2. Pranta, A. D., & Rahaman, M. T. (2024). Extraction of eco-friendly natural dyes and biomordants for textile coloration: A critical review. Nano-Structures & Nano-Objects, 39, 101243.
3. Bishal, A., Ali, K. A., Ghosh, S., Parua, P., Bandyopadhyay, B., Mondal, S.,Jana, M., Datta, A., Das, K.K., Debnath, B. (2023). Natural Dyes: Its Origin, Categories and Application on Textile Fabrics in Brief. European Chemical Bulletin, 12(8), 9780-9802.
4. Singh, K. A. R. U. N. A., Kumar, P. A. N. K. A. J., & Singh, N. V. (2020). Natural dyes: an emerging ecofriendly solution for textile industries. Poll Res, 39(2), 87-94.
5. Uddin, M. A., Rahman, M. M., Haque, A. N. M. A., Smriti, S. A., Datta, E., Farzana, N., Cowdhury, S., Haider, J., Sayem, A. S. M. (2022). Textile colouration with natural colourants: a review. Journal of Cleaner Production, 349, 131489.
6. Iqbal, M., Panhwar, A., Ahmed, K., Kandhro, A., Sultana, R., Mughal, J., & Solangi, Z. (2022). Textile dyeing of cotton and wool textile material with natural dyes extracted from bluish purple grapes. Bulgarian Chemical Communications, 54(1), 14-18.
7. Benli, H., Aydınlıoğlu, Ö., Yılmaz, F., & Bahtiyari, M. İ. (2023). Topping of naturally dyed wool fabrics with different natural dye sources. Coloration Technology, 139(2), 171-181.
8. Benli, H., & Bahtiyari, M. İ. (2022). Testing acorn and oak leaves for the UV protection of wool fabrics by dyeing. Journal of Natural Fibers, 19(14), 7925-7938.
9. Pars, A., & Karadag, R. Sustainable Bio-Dyeing of Cellulosic-Based Fabrics with Anthocyanins from Black Carrot (L.). Fibres & Textiles in Eastern Europe, 32(3), 50-56.
10. Chen, J., Suo, Q., Ni, Y., Yan, J., Wang, Y., Jiang, H., & Qi, H. (2024). Dyeing performance of wool fabric with natural pigment from Cordyceps militaris. The Journal of The Textile Institute, 115(9), 1672-1682.
11. Ghosh, J., Khan, F., Noor, T., Rupanty, N. S., & Das, S. C. (2024). Union dyeing of cotton-silk blended woven fabric using Tanin bio-mordant and thyme as a Colourant. Text Leather Rev, 7, 303-326.
12. Sankaralingam, B., Balan, L., Chandrasekaran, S., & Muthu Selvam, A. (2023). Anthocyanin: a natural dye extracted from Hibiscus sabdariffa (L.) for textile and dye industries. Applied Biochemistry and Biotechnology, 195(4), 2648-2663.
13. Nitayaphat, W., & Jintakosol, T. (2024). Dyeing of Pineapple Leaf Fibers Using Various Natural Dye Extracts and Mordants. Journal of Natural Fibers, 21(1), 2313867.
14. Melaku, A., Demeke, G., Aschale, M., Alemayehu, F., & Semegn, G. (2023). Extraction and Characterization of Natural Dye Stuff from Spent Coffee Ground and Bio-Mordant from Mango Bark. Journal of Natural Fibers, 20(2), 2276725.
15. Melaku, A., Demeke, G., Aschale, M., Alemayehu, F., & Semegn, G. (2023). Extraction and Characterization of Natural Dye Stuff from Spent Coffee Ground and Bio-Mordant from Mango Bark. Journal of Natural Fibers, 20(2), 2276725.
16. Rasool, W., Adeel, S., Batool, F., Ahmad, S. A., Mumtaz, S., & Hussaan, M. (2023). Environmental friendly silk and cotton dyeing using natural colorant of Bougainvillea (Bougainvillea glabra) flowers: the sustainable approach towards textile industry. Environmental Science and Pollution Research, 30(8), 21863-21871.
17. Anbumani, N., Rameshkumar, C., Anandkumar, P., Senthilnathan, P., & Jeevitha, R. (2008). Comparitive studies on ring rotor and vortex yarn knitted fabrics. Autex Research Journal, 8(4), 100-105.

18. *Erdumlu, N., Ozipek, B., Oztuna, A. S., & Cetinkaya, S. (2009). Investigation of vortex spun yarn properties in comparison with conventional ring and open-end rotor spun yarns. Textile Research Journal, 79(7), 585-595.*

ELECTROSPUN BIO-NANOCOMPOSITE WEBS BY CELLULOSE NANOCRYSTAL (CNC)-LOADED POLYLACTIDE AND ITS BLENDS

Handan Palak[1*], Burçak Karagüzel Kayaoğlu[1]

[1]Istanbul Technical University, Faculty of Textile Technologies and Design, Department of Textile Engineering, Istanbul, Turkey

(*) Email: palakh@itu.edu.tr

Abstract:

In this study, effects of polylactide (PLA) melt flow rate, and dichloromethane (DCM)/dimethyl sulfoxide (DMSO) solvent blend ratio on cellulose nanocrystal (CNC) dispersion quality in PLA/CNC bio-nanocomposites, prepared via solution casting, were studied. Besides, the electrospinning behaviour of CNC-loaded PLAs and its blends with poly(butylene adipate-co-terephthalate) (PBAT) was explored. The rheological analysis confirmed good CNC dispersion ability in PLAs with high melt flow rate specifically in solvents comprising DMSO. Besides, it was observed that CNC loading directly affected the morphological structure of the obtained nanofibrous webs. Thermal analysis indicated that CNCs acted as a nucleation agent and promoting the crystallization process by lowering cold crystallization temperatures and increasing the degree of crystallinity. The outcomes provide a groundwork for future studies on the fabrication of bio-nanocomposite webs from PLA/PBAT blends for a variety of applications.

Key words: *Polylactide, polybutylene adipate-co-terephthalate, cellulose nanocrystals, bio-nanocomposite, nanofiber*

1. Introduction

Cellulose nanocrystals (CNCs) are highly regarded as a leading nano-reinforcement for bio-nanocomposites (BNCs) due to their distinctive attributes, including nano-scale size, outstanding mechanical strength, ease of chemical modification, high aspect ratio, low density, renewability, biodegradability, and biocompatibility [1]. BNCs are composed of bioplastics combined with either organic or inorganic nanofillers. Although inorganic nanofillers may hinder biodegradability, organic nanofillers are more compatible with bioplastics and minimize phase separation due to improved interfacial adhesion and affinity. CNCs are produced through acid hydrolysis, which selectively targets and hydrolyzes the amorphous regions within cellulose microfibrils. Besides, sulfuric acid is commonly used in this method to generate more stable CNC suspensions [2]. On the other hand, the interacting hydroxyl groups on the surface of CNCs and the sulphate half-esters formed during the sulfuric acid hydrolysis process may cause CNCs to agglomerate in hydrophobic polymers, such as PLA. The characteristics of the matrix, including the polymer's molecular weight and crystallizability, can influence the dispersion of CNCs and the resulting properties of nanocomposites [3]. Besides, the characteristic of organic solvent, i.e., polar-nonpolar nature and dielectric constant, directly affect the dispersion of CNCs in a polymer matrix [4]. In addition, a significant breakthrough in processing CNC-reinforced BNCs is the use of electrospinning to create continuous one-dimensional fibers with diameters ranging from microscale to nanoscale. This technique enables the alignment of CNCs under strong electrostatic fields, orienting them along the fiber axis and greatly enhancing the axial strength of the electrospun nanocomposite fibers. Accordingly, in this study, polar/nonpolar binary solvent systems, and PLAs with different molecular weights were utilized to develop PLA-based nanocomposites via solution casting

method, and CNC dispersion quality was investigated. Afterwards, the electrospinnability of PLA-based systems with various solvents was controlled, and key properties of BNC nanofibers were investigated.

2. Experimental

2.1. *Materials*

Commercial semicrystalline PLAs with different melt flow rates (MFR) were kindly supplied by NatureWorks LLC, USA. PBAT, Ecoflex® F Blend C1200, having a polydispersity of 2.0 and an average molecular weight of $1.05{\times}10^5$ g/mol, was donated by BASF, Ludwigshafen, Germany. Spray-dried CNC in powder form was provided by CelluForce (Montreal, Canada). Organic solvents of dichloromethane (DCM) and dimethyl sulfoxide (DMSO) were purchased from Merck and Isolab Chemicals, respectively (Table 2).

Table 1. Properties of different PLA grades [5]

PLA Code	Melt flow rate (MFR: g/10 min, 210°C)
HPLA	6-10
MPLA	15-30
LPLA	70-85

Table 2. Properties of the solvents [6]

Solvent	Polarity	Solubility Parameter, δ (Cal/cm^3)$^{1/2}$	Dielectric constant, ε	Boiling Point (°C)
DCM	Non-polar	9.7	9.10	40
DMSO	Polar	12.9	48.9	189

2.2. *Methods*

CNCs were dispersed within the solvents in a water bath sonicator for 2.5 h at room temperature. Then, PLAs and PLA/PBAT granules were added to the CNC-solvent mixture and stirred on a magnetic stirrer for 3 h. Different solvent blends, i.e., 100%DCM (100DCM), 75%DCM/25% DMSO (75DCM/25DMSO), and 50%DCM/50%DMSO (50DCM/50DMSO) were employed. The CNC content in PLA based bio-nanocomposites was constant at 3 wt.%. When polymer granules were fully dissolved, polymer solutions were poured into glass petri dishes, and they were dried at 85°C in a vacuum oven.

The selected polymer solutions were individually loaded to a 1 mL syringe, with a metallic needle of 27 G, and delivered to the syringe pump in a horizontal electrospinning system. The electrospinning parameters of feed rate, voltage, and tip-to-collector distance were kept constant at 1.0 mL/h, 18-20 kV, and 15 cm, respectively. An MCR-301 rotational rheometer with a parallel plate geometry was utilized to conduct the small amplitude oscillatory shear rheological analysis. A scanning electron microscope, Tescan Vega3, was used to conduct morphological analysis at 20.00 kV. A Perkin Elmer DSC400 differential scanning calorimetry was utilized to investigate the crystallization and melting behaviors.

3. Results and discussion

3.1. *Rheological properties of BNCs*

Figure 1 shows the complex viscosity versus angular frequency of bio-nanocomposites of HPLA, MPLA, LPLA, and LPLA/PBAT samples with 3 wt.% CNC. The low frequency upturns in complex viscosity indicate CNC networking formation. Accordingly, the use of DCM solely allowed the lowest degree of CNC dispersion within all PLA matrices, while solvent blends with higher DMSO contents enabled the

most homogenous dispersion of CNCs. Among three types of PLAs, LPLA bio-nanocomposites had the highest relative increase in their complex viscosity with the DCM50/DMSO50 solvent blend, and with DCM75/DMSO25 also having a significant effect. On the other hand, CNC dispersion quality was suppressed in bio-nanocomposites with PLAs having higher molecular weights. Besides, when PBAT was blended with LPLA at different weight ratios, i.e., 25 wt.% and 50 wt.%, major upturns at the low frequencies were observed, indicating CNC networking formation, as well.
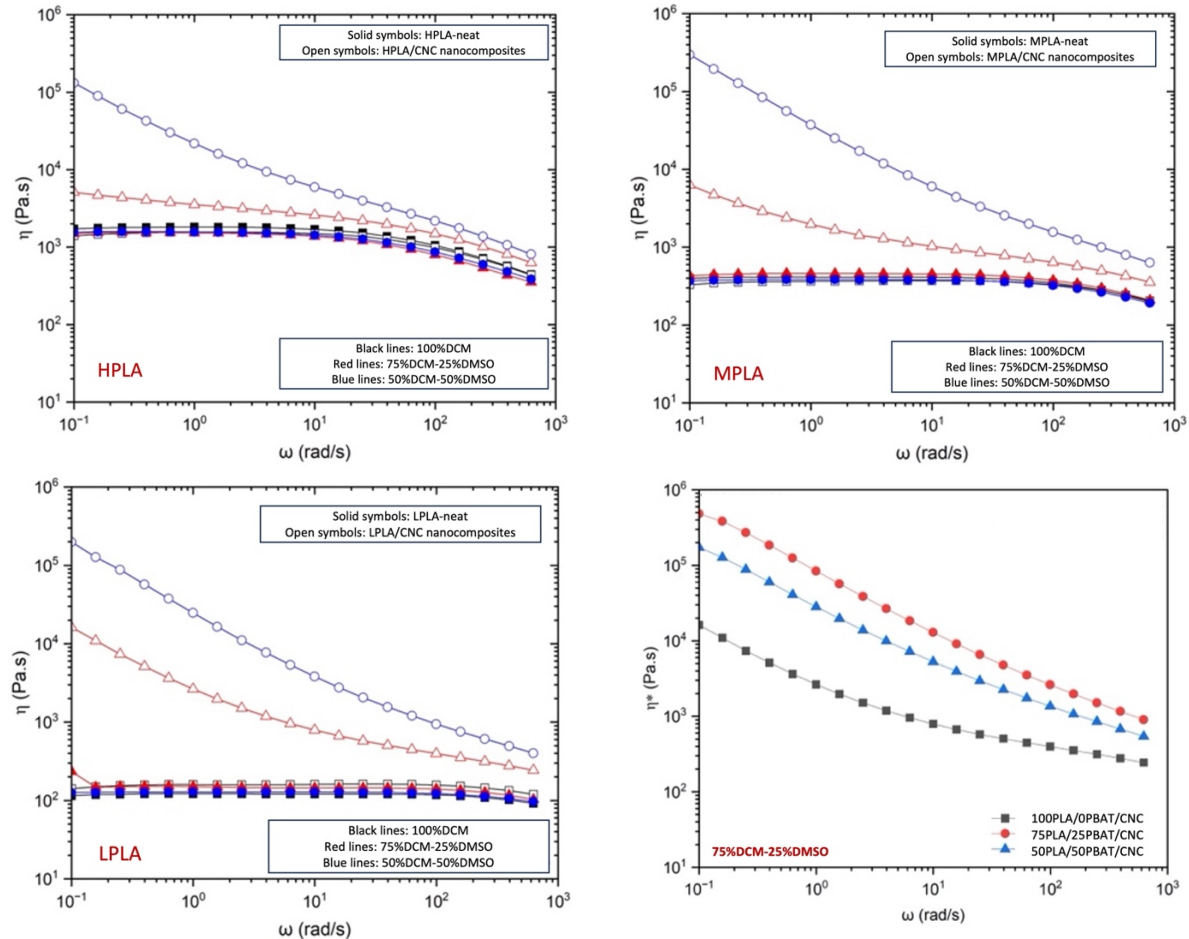
Figure 1. Complex viscosity versus angular frequency of bio-nanocomposites of (a) HPLA, (b)MPLA, and (c) LPLA (d) LPLA/PBAT blends with 3 wt.% CNC.

3.2. _Crystallization behavior of BNCs_

1st heating cycles showed that neither the solution-casted films of neat PLAs nor PLA/CNC bio-nanocomposites showed cold crystallization, indicating all PLAs were almost fully crystallized during the drying step of solution casted film production. At DMSO concentrations of 25% v/v, neat PLA samples exhibited a double melting peak, which could be due to imperfect crystallinity in the PLA, attributing to the plasticizing effect of residual DMSO within the polymer matrix. During 2nd heating scans, cold crystallization temperatures of neat PLAs were always higher than those of PLA/CNC bio-nanocomposites, indicating CNC acted as a nucleation agent and promoting the crystallization process by lowering T_{cc} and increasing the degree of crystallinity.

Table 3. Thermal properties of BNCs

Sample	1st heating			2nd heating		
	T_{cc} (°C)	T_m(°C)	X_c(%)	T_{cc}(°C)	T_m(°C)	X_c(%)
HPLA	-	162-166	56	-	167	5
HPLA/CNC	-	165	48	113	167	8
MPLA	-	158-162	53	-	162	5
MPLA/CNC	-	162	51	111	164	4
LPLA	-	158-169	35	105	169	23
LPLA/CNC	-	168	60	103	169	36

3.3. _Morphological structure of BNC-nanofibers_

Based on the rheological analysis, low molecular weight PLA was chosen as the optimum PLA grade and used in electrospinning method (Figure 3). Moreover, as the obtained results showed that the blend ratio of 75DCM/25DMSO provided a good CNC dispersion for LPLA grade, this blend ratio was selected to fabricate PLA/CNC bio-nanocomposite webs as well. The average fiber diameter of neat LPLA decreased from 1510±200 nm to 1218±205 nm with an addition of 1 wt.% CNC; then a dramatic drop to 342±97 nm was observed when the CNC ratio was 3 wt.%. The results showed that 3 wt.% CNC-loaded LPLA/PBAT bio-nanocomposite webs were successfully produced; however, bead formation was observed in 100PLA/0PBAT. The addition of PBAT, i.e., 25 w/v% and 50 w/v%, to the structure resulted in more homogenous fibers with a higher mean fiber diameter (Figure 4).
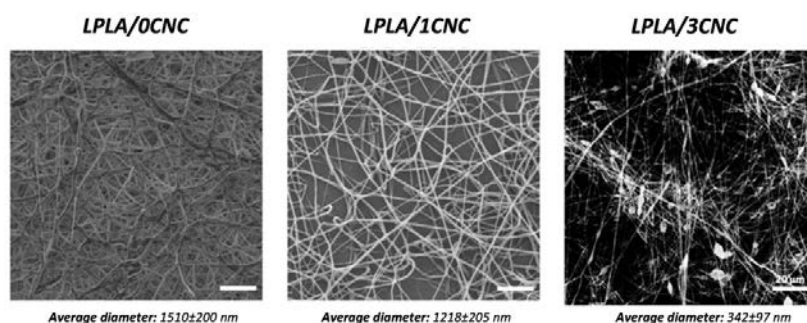
Figure 3. Electrospun bio-nanocomposite webs of LPLA having different CNC content levels
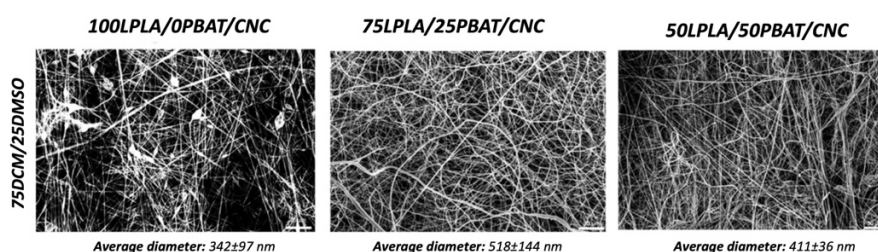
Figure 4. Electrospun bio-nanocomposite webs of LPLA/PBAT blends having 3 wt.% CNC

4. CONCLUSIONS

In this study, the effects of utilizing binary solvent system of DCM/DMSO at different weight ratios, PLAs with various melt flow rates, and PLA/PBAT blends, on CNC dispersion quality through rheological analysis were revealed. The effect of CNC addition on the thermal characteristic of solution cast films were also investigated; besides, the electrospinnability of the bio-nanocomposites were studied as well. The findings provide valuable insights for optimizing the preparation of PLA/CNC bio-nanocomposites, highlighting the importance of selecting appropriate solvent blends, molecular weight of PLA and PLA/PBAT blend ratios to achieve good dispersion quality via solution solution-casting and electrospinning.

ACKNOWLEDGEMENTS

References

1. *Mali, P., & Sherje, A.P. (2022). Cellulose nanocrystals: fundamentals and biomedical applications. Carbohydrate Polymers, 275, 118668.*
2. *R. J. Moon, A. Martini, J. Nairn, J. Simonsen, J. Youngblood, Cellulose nanomaterials review: structure, properties and nanocomposites, Chem. Soc. Rev., 40 (2011) 3941–3994,*
3. *Vatansever, E., Arslan, D., Sarul, D.S., Kahraman, Y., & Nofar, M. (2020). Effects of molecular weight and crystallizability of polylactide on the cellulose nanocrystal dispersion quality in their nanocomposites. International Journal of Biological Macromolecules, 154, 276–290.*
4. *Ozdemir, B & Nofar, M. (2021). Effect of solvent type on the dispersion quality of spray-and freeze-dried CNCs in PLA through rheological analysis, Carbohydrate Polymers, 268, 118243.*
5. *Natureworks. (n.d.). Retrieved January 15, 2024 from https://www.natureworksllc.com/technology-and-products/products*
6. *Casasola, R., Thomas, N. L., Trybala, A., & Georgiadou, S. (2014). Electrospun poly lactic acid (PLA) fibres: Effect of different solvent systems on fibre morphology and diameter. Polymer, 55(18), 4728–4737.*

DEVELOPING CNN-AUGMENTED MODELS TO PREDICT CIELAB OUTCOMES POST-BLEACHING OF DENIM GARMENTS

İbrahim Erdem Kalkan[1], Ebru Çalışkan[2], Cenk Şahin,[3] Onur Balcı[4], Yusuf Kuvvetli[5]

[1] *Çukurova University Department of Industrial Engineering Sarıçam / Adana, e-mail:*
iekalkan@cu.edu.tr
[2] *Baykan Denim R&D Center 2nd Organized Industrial Zone Yeşilyurt / Malatya, e-mail:*
ebru.caliskan@baykandenim.com
[3] *Çukurova University Department of Industrial Engineering Sarıçam / Adana, e-mail:*
cenksahin@cu.edu.tr
[4] *The University of Kahramanmaraş Sütçü İmam Textile Engineering Dep. 12 Şubat / K.Maraş, e-mail:*
obalci@ksu.edu.tr
[5] *Çukurova University Department of Industrial Engineering Sarıçam / Adana, e-mail:*
ykuvvetli@cu.edu.tr

Abstract:

Denim garment production demands efficient design processes to minimize waste, costs, and production delays. Bleaching, among other finishing processes, holds paramount importance due to its numerous variables and substantial impact on product value. Artificial neural networks have great potential to achieve superior performance in anticipating various process outcomes. Their parameterized structure effectively captures non-linear relationships between input features. This study aims to effectively predict fabric outcomes by developing an artificial neural network (ANN) model supported by convolutional neural networks (CNN) to provide additional features derived from raw and semi-processed fabric images. The study represents a comparison of CNN powered models with a common predictive ANN as base model. Competing models incorporate various process variables and fabric properties, such as dying number and elasticity to predict changes in denim CIELab properties after bleaching. The process features of the model are the number of bleaching cycles, total process time, and concentration of sodium hypochlorite (representing the total amount of chemical used). The mean absolute percentage error is used as the performance measure between predictions and desired outputs. This research plays a significant role in enhancing agility in denim production by providing businesses with more efficient approaches to digitized denim bleaching and Research and Development processes in the textile industry.

Key words:

denim, bleaching, effect, artificial neural networks

1. Introduction

Denim goes through various manufacturing processes that involve many variables, from fabric production to garment creation. The traditional denim processing begins with cotton fiber selection and dyeing the threads with indigo. Then, the denim fabric is woven using specific techniques [5]. After the garment is made, finishing processes are applied to achieve the desired aesthetic and comfort. These processes include techniques such as enzymatic washing, which can be optimized for fading color, comfort, and durability [6].

The bleaching effect is the process of removing or lightening the indigo from the surface of denim fabric. Typically, a strong oxidative bleach, such as sodium hypochlorite (NaOCl), potassium permanganate (KMnO4), or hydrogen peroxide (H2O2), is used, and the bleaching process can be done with or without the addition of stones [7]. This process is labor-intensive, reliant on skilled workers, and considered as

costly. Given the significance of bleaching, the importance of digitizing both bleaching-oriented production and related processes becomes apparent. By implementing decision support systems and associated predictive models, digitizing these processes will offer businesses a more agile and efficient approach. Efficiency improvements are crucially needed in the denim garment industry, particularly for businesses where labor, waste, and energy are significant costs.

The use of artificial neural networks (ANNs) in predicting the effects of processes applied to fabrics is encountered in studies. Farooq et al. employ an ANN system to predict the phenomenon of color change for different colors and shade percentages [8]. Mandal et al. model the relationships between measured fabric properties (such as thickness, weight, fabric count) and thermal protective performance and thermo-physiological comfort performance using an ANN to analyze garment performance [9]. Elkateb includes a study on predicting output properties of woven fabrics with ANNs across different characteristics [10].

Anomaly detection on textile textures using "Variational Autoencoders" can be cited as an example of the use of images in textiles. In this application, the reconstructed images are compared with the original images, and the calculated reconstruction error is directly used to compute the anomaly score [11]. Another study used deep learning methods to approximately determine input parameters in laser texturing. Different combinations of laser parameters were selected to perform laser fading experiments on denim fabrics using laser technology in data generation, and denim image datasets with various laser fading effects were obtained. The trained convolutional neural network-based (CNN) prediction model produced an approximate parameter group based on the fading image and showed good performance with low prediction error according to the validation dataset [12].

In this study, the proposed CNN prediction models will equip businesses with an agile and thus more efficient approach to digitized denim bleaching in the denim garment industry. Proposed models have been developed to forecast the color properties of denim garments. To the best knowledge, this is the first study to predict color values using fabric images on deep learning models.

2. Experimental Setup

This study aims to predict the possible changes in the physical properties of the denim garment after the sodium hypochlorite bleaching process, depending on the process variables and fabric properties to prevent production-related fabric defects. The basic steps of this effort are outlined in the following subsections: first, the material and its structure are described. Second, the data collection process and modeling details are presented, including explanations of the methods employed and the evaluation techniques use.

2.1. *Materials*

Prediction models have been developed based on collected data to forecast the "CIELab" color properties of denim garments. The CIELab color space, also known as L*a*b represents color using three parameters: L* for perceived lightness, and a* and b* for the four primary colors perceived by human vision: red, green, blue, and yellow. The models are built using 1,200 data points gathered from a full factorial design involving 1,200 experiments. The experiments focused on denim fabric type, process time, sodium hypochlorite concentration, and the replicate cycle of bleaching. The sodium hypochlorite bleaching process was conducted with two replicates. Three levels of process time were tested: 3, 5, and 7 minutes. Additionally, four concentration levels of bleach were selected: 2,000, 3,000, 4,000, and 5,000 ml. The bleaching cycle indicates how many times the same bleaching process is replicated to reach the desired visual effect.

50 different types of denim fabric are selected and four variables that can affect the color in the bleaching process have been included in the controlled experimental design. In addition, the constructional fabric properties as yarn count, weaving pattern and density, the CIELab values of raw and semi-processed

fabric are accepted as inputs of the models. The semi-processing stage refers to intermediate steps in the bleaching process that prepare the denim for a final, controlled whitening or fading effect. In that stage a controlled amount of hydrogen peroxide is applied to the denim fabric and acts as a mild bleaching agent.

Table 1. Input-Output configuration of models

|	Attributes		ANN	CNN1	CNN2
INPUTS	**Fabric Properties**	Type of Dyeing	✓	✓	✓
		Elasticity	✓	✓	✓
		Onz/yd^2	✓	✓	✓
		Yarn Count	✓	✓	✓
		Density	✓	✓	✓
		Type of Weaving	✓	✓	✓
		CIELab (Raw Fabric)	✓	✓	✓
		CIELab (Semi-processed Fabric)	✓	✓	✓
	Process Features	The Number of Bleaching	✓	✓	✓
		The Bleaching Process Time	✓	✓	✓
		Sodium Hypochlorite Concentration	✓	✓	✓
	Image Features	Raw Fabric Images		✓	
		Semi-processed Fabric Images			✓
OUTPUTS	**Color Properties of Processed Product**	CIELab L*	✓	✓	✓
		CIELab a*	✓	✓	✓
		CIELab b*	✓	✓	✓

2.2. _Methods_

ANNs, ranging from simple computational units to complex architectures, are a heavily researched area in deep learning. Known for their versatility, strength, and scalability, ANNs excel at handling large-scale, highly intricate machine learning challenges. Their applications span from classifying billions of images to enabling advanced speech recognition systems [1]. ANNs also serve as powerful tools for predicting the outcomes of the processes handled in this research.

With techniques like stochastic gradient descent, ANNs can converge, although the solution may not necessarily reach the global optimum due to the presence of multiple local minima [2]. Additionally, while other machine learning methods require manually engineered features to be fed into the model as input, ANNs can extract useful features from the data without requiring an additional effort, thanks to the mechanism of weight updates [3]. However, when dealing with non-structural data types like image data, fully connected layers struggle to represent important features effectively. For example, even a small 100x100-sized image contains 10,000 inputs, and even if the first hidden layer has a high number of neurons, like 1,000, it may not capture a significant portion of the information [1]. As a result, a specialized structure known as a convolutional layer, commonly referred to as convolutional neural networks (CNNs), is necessary and has consistently delivered successful outcomes.

The convolution is the process of sliding filters of certain sizes, such as 3x3 or 5x5, over the 3-dimensional input data, stopping at every possible position to extract the 3-dimensional patch of environmental features. This patch corresponds to the region covered by the filter at that position. The

process starts from the top-left corner of the data and continues towards the bottom-right corner. The weights of the filter are element-wise multiplied with the values in the patch, and the results are summed to produce a single value. This operation is applied to all positions where the filter is placed [4].

The architectural design of models used in this study is illustrated in Figure 1. Convolutional blocks represent convolution operation over image data. Other types of data are diffused multiple times in following layers. An algorithm called backpropagation will be used to update the weights backward based on the values calculated forward for each neuron [3]. The backpropagation algorithm will search for the parameter set that minimizes errors in this way.
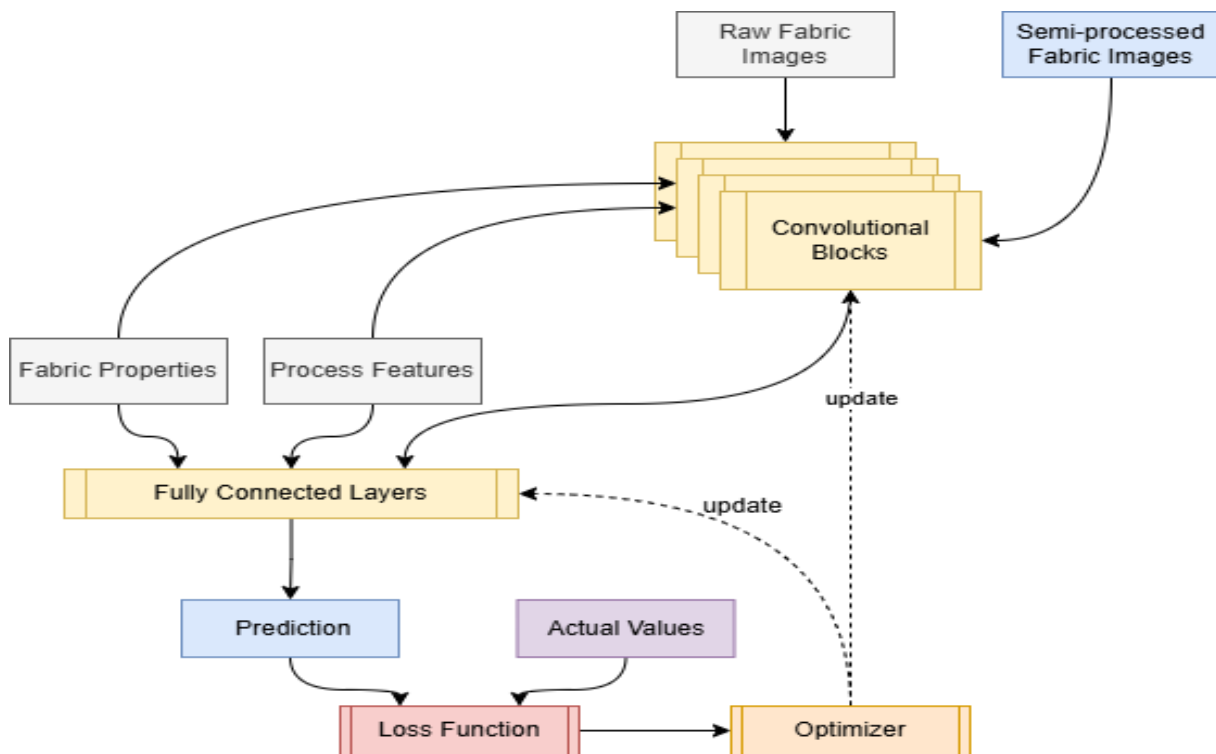

Figure 1. Proposed modeling schema

Data diffusion in Figure 1 involves propagating image data across convolutional layers to capture visual features, while feature data (fabric features and process features) are directly concatenated with features extracted from images before passing through fully connected layers. This integration allows the model to leverage both types of information (visual and non-visual) simultaneously for better predictions.

The loss function measures the difference between the predicted values and the actual values. This helps in quantifying how well the model is performing. The optimizer updates the parameters of the model to minimize the loss, iterating through the network to improve predictions over time. It receives feedback from the loss function and adjusts the weights in both the convolutional and fully connected layers accordingly.

3. Results and discussion

A straightforward cross-validation method was employed to evaluate the approach. For each model, the dataset was randomly split five times into a 90/10 ratio. In each split, the first portion (90%) was used for training, while the second portion (10%) was used for prediction. Models' performance was assessed using the mean absolute percentage error (MAPE) as the evaluation metric. MAPE measures the average of absolute percentage errors between actual values and predicted values. It's especially useful for understanding how far predictions deviate from actual results on average, in terms of percentage.
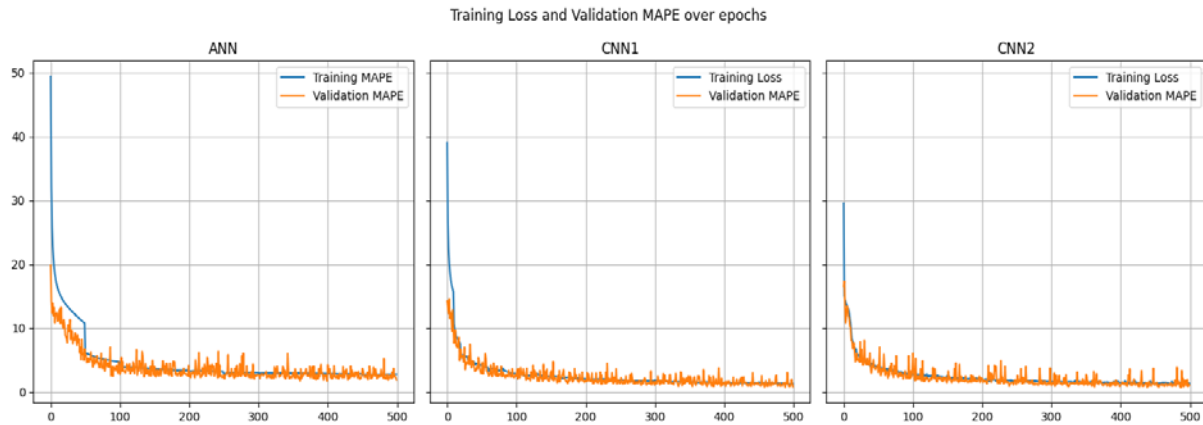
Figure 2. Tracking epochs for L* values
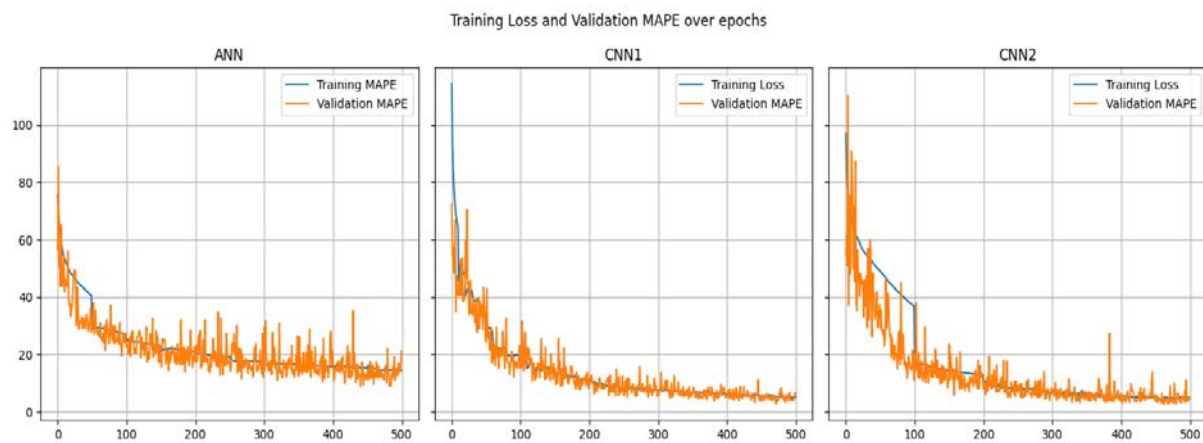
Figure 3. Tracking epochs for a* values
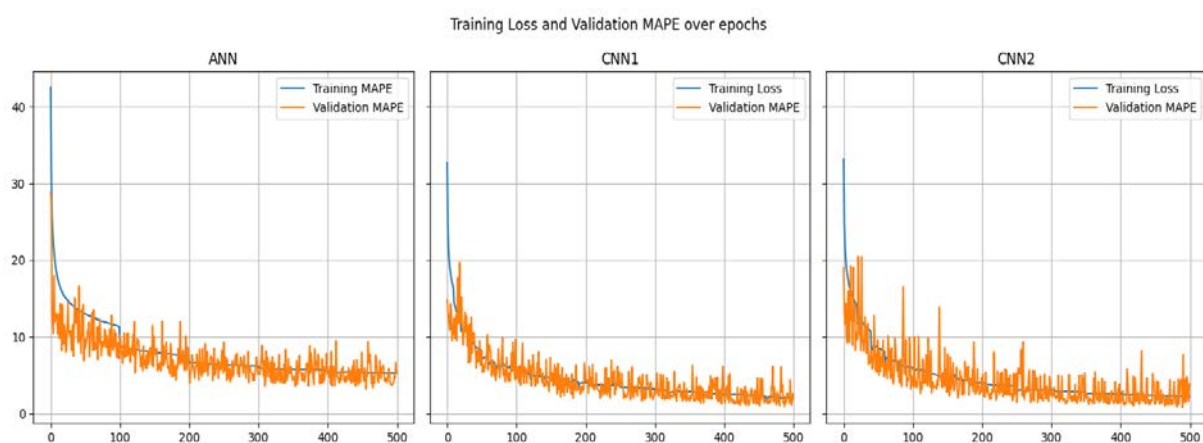
Figure 4. Tracking epochs for b* values

The models were initially trained for 500 epochs. Throughout the training, the loss values were monitored to determine when the models reached a relative plateau. Since the training loss of the ANN model was observed to still be decreasing, it was trained for an additional 500 epochs to allow for a fairer comparison. At the end of each epoch, a performance metric was calculated on the validation

dataset, which was kept separate from the training process. Figure 2-4 shows the progression of training and validation values over the first 500 epochs.show a rapid decrease in training loss early on, which then stabilizes, indicating effective initial learning.

Validation MAPE fluctuates more than training MAPE in all models, which is typical due to validation data variability. CNN2 seems to achieve the relatively stable and consistent performance for prediction of three properties.

Table 2 represents the average validation performance of three model types.

Table 2. Average prediction error for color parameters (Lower values indicate better performance)

Predicted Value	ANN	CNN1	CNN2
L*	2.04	1.04	1.05
a*	7.56	6.55	4.97
b*	2.78	2.60	2.26

CNN2 performs best overall, achieving the lowest prediction values for all three color parameters (L*, a*, and b*), suggesting it provides the most accurate predictions. CNN1 is the second-best model, with relatively low prediction values, though slightly higher than CNN2, indicating it still performs well across parameters.

4. CONCLUSIONS

In this research study, the prediction of outcomes of bleaching process used in ground effecting of denim garments was examined. It has been established that both the dataset utilized and the augmented models employed for predictions have a significant impact on the accuracy of the forecasts. It is concluded that a factory employing these models will be able to forecast process outcomes effectively, minimizing the risk of any losses.

The fact that images of semi-processed fabrics perform better due to being closer to the final product is an expected situation. The results have shown this trend as well. Furthermore, it is an important finding that including images in similar prediction models in denim manufacturing could enhance prediction performance.

ACKNOWLEDGEMENTS

References

1. *Géron, A. (2017). Hands-on Machine Learning with Scikit-Learn and TensorFlow: Concepts, Tools, and Techniques to Build Intelligent Systems. O'Reilly.*
2. *Goodfellow, I. Bengio, Y. Courville, A. (2016). Deep Learning. MIT Press.*
3. *Mitchell, T.M. (1997). Machine Learning. McGraw-Hill Education (Germany).*
4. *Chollet, F. (2018). Deep Learning with Python. Manning.*
5. *Paul, R. (2015). Denim: manufacture, finishing and applications.*
6. *Mondal, M.I.H., Khan, M.M.R. (2014). Characterization and process optimization of indigo dyed cotton denim garments by enzymatic wash. Fashion and Textiles 1(19).*
7. *Periyasamy, A. P., Periyasami, S. (2023). Critical Review on Sustainability in Denim: A Step toward Sustainable Production and Consumption of Denim. ACS Omega, 8(5), 4472-4490.*
8. *Farooq, A. Irshad, F. Azeemi, R. Iqbal, N. (2020). Prognosticating the shade change after softener application using artificial neural networks, Autex Research Journal, 21(1), 79-84.*

9. S. Mandal, N.U.S. Mazumder, R. Agnew, I. G. Grover, G. Song, R. Li, (2021), "Using Artificial Neural Network Modeling to Analyze the Thermal Protective and Thermo-Physiological Comfort Performance of Textile Fabrics Used in Oilfield Workers' Clothing," Int. J. Environ. Res. Public Health, 2021(18), p. 6991

10. Elkateb, N. (2022), Prediction of Mechanical Properties of Woven Fabrics by ANN, Fibres & Textiles in Eastern Europe, 30(4), 54-59

11. Chu, W.L. Chang, Q.W. Jian, B.L. (2024). Unsupervised anomaly detection in the textile texture database. Microsyst Technol.

12. Tong, Y. et al. (2023). Prediction of parameters in the laser fading process of denim using convolutional neural networks. Textile Research Journal, 93, 3790 - 3801.

THE DEVELOPMENT OF STONE WASHING PROCESS FOR DENIM WITH ALTERNATIVE MATERIALS USING FOAM APPLICATION TECHNIQUE

Onur Uslu[1], Serkan Yılmaz[2], Elif Aylin Pektaş[3]

[1] Cumhuriyet St. Old Hadimkoy Way, Inler Cihan Industrial Area, Apt C, Zip Code 34500, Büyükçekme ISTANBUL. Tayeks Textile Head Office, Design Centre, onur.uslu@tayeks.com.tr +902128661300 /ex.1330

[2] Ulas Organized Industrial Zone, 117 St, No:8, Ergene 2 OIZ, Zip Code 59930, Ergene TEKIRDAG , Tayeks Textile Laundry, R&D Centre, serkan.yilmaz@tayeks.com.tr +902826555707

[3] KSU Avsar Campus Technopark, Onikişubat KAHRAMANMARAŞ, Inovaktif R&D, eaylin@aktifarge.com +905072784688

Abstract:

Denim fabrics are fabrics dyed with indigo dye. As the garments produced from denim fabrics are washed, the indigo dye is easily removed from the product. The color of the product is bleached by the transfer of the dye in the product to the washing environment, the solution. Since indigo dye is a dye that can be easily eroded, especially by physical and chemical methods; it is also known as 'living dye'. In the conventional washing processes of denim products, the solution is first contaminated when the indigo dye passes into the solution. The return of this unbound dye found in the solution to the product is called 'back dyeing'. The most contaminated parts in back dyed products are the white pockets, labels and potassium permanganate ($KMnO_4$) applied parts of the product. Back dyeing occurs in the process called 'stone washing', where pumice stone is mostly used in wet processes. Pumice stone is a round and oval shaped stone with a rough surface collected from volcanoes. In order to obtain the desired appearance, the products are rotated in a wet environment in denim industrial washing machines with stones. Stones scrape off the dye particles from the surface of the dyed yarn and give the desired result. Stones can damage the garment and washing machine due to their high abrasion. They leave stone dust and residues on the garments and inside the pockets. This causes the addition of extra rinsing and manual pocket cleaning processes. The stone used as a physical abrasive melts after the abrasion effect and passes from the drain to the channel after a certain number of washes and becomes solid waste. By extending the abrasion feature of the stone, the physical waste rate left in the solution can be reduced. The dirt containing paint and stone waste coming out of the products after abrasion is carried to other products in the machine with the water in the solution. It causes the dirt to contaminate other products. For this purpose, physical abrasives that are not easy to melt and foam are combined in a water-free environment in the machine.

Key words:

Denim, Foam, Stone, Back staining, Abrasion, Effecting

1. Introduction

The most important element that adds value to denim garments is the mechanical and chemical washing processes performed after garment production. Some of these processes are stone, enzyme, ozone, softening, laser, sandpaper, laser, etc. washing. Stone washing is the most common of these and includes both mechanical and chemical interactions. Denim stone washing is a technique applied to give denim fabric a more worn and natural appearance. In this process, denim fabric is washed with stones

in large drum machines. Rough stones such as pumice stones are usually used. The fabric is worn by rubbing with the stones, thus obtaining a more faded and worn appearance. Stone washing creates a change in both the color and texture of the fabric, providing a more comfortable and soft denim experience. As a result, denim stone washing process adds a vintage air to jeans, which is preferred in the fashion world, while also providing comfort. However, this process has negative aspects for both the fabric and the environment due to both water consumption, its effects on the fabric, and the pumice waste that is formed. Denim stone washing literature includes many academic studies and research related to textile industry and fashion technology [1-8].

The basic titles and topics covered in the literature regarding denim stone washing can be listed as stone washing process, combinations with chemical methods, environmental effects, effects on physical and chemical properties of the fabric, fashion and consumer trends, alternative washing techniques.

Another topic to be examined in the study is foam application technique. Foam application is a technique generally used in the application of finishing processes in the textile industry. Foam finishing application has been developed as an alternative to the traditional impregnation method and offers advantages such as lower chemical consumption, water saving and energy efficiency. Foam finishing application is increasingly preferred in the textile industry as a sustainable technology that provides water and energy saving while also improving the performance of fabrics.

In this study, it is aimed to reduce back-dyeing, reduce the amount of water used in the cleaning processes of the products, save energy, shorten the production process, improve the physical strength tests of the product and the service life of the washing machine by eliminating the solid waste in the process with the alternative washing agent and method developed. The study includes innovations in terms of the effecting agent and washing method.

2. Experimental

The project implementation consists of two stages. The first of these is the development of an alternative synthetic stone material to pumice, and the second is related to the application of this stone to clothing. In the study, a synthetic stone was developed and examined in order to extend the wear life compared to conventional pumice stone. In this context, material development was carried out with 3 different recipes. The stone washing process was carried out without using water by injecting foam into the machine simultaneously. As it is known, in the conventional method, the washing process is carried out with water using auxiliary chemicals in industrial drum washing machines. Therefore, both water and chemicals are used in the application. In the scope of the project, the foam application technique was preferred instead of this process. In the scope of the study, Yılmak brand foam generator and Yılmak RF-60 brand drum washing machine were used. The foam generator and drum washing machine are seen in Figure 1.

Figure 1. Foam generator and washing machine used in the study

2.1. *Materials*

The pumice stone is a natural, porous rock formed by the rapid cooling and solidification of lava as a result of volcanic eruptions. This stone creates many air spaces (pores) because of the rapid escape of gases in the lava, which creates the light and spongy structure of pumice. Its density is very low, and it can float on water. The use of pumice stone in the textile industry has an important place, especially in the processing of denim products. The main use of pumice stone in textiles is to create an abrasive effect on the surface of denim fabrics, giving them an old appearance. It is known that this process is carried out with a technique called "stone wash". During the grinding of denim fabrics, the fabrics are washed with pumice stone in large industrial washing machines. In this process, the pumice stone rubs on the surface of the denim fabric, abrading the fibers of the fabric and giving the fabric a soft, aged appearance.

Within the scope of the study, firstly a synthesis of polypropylene (PP), calcite ($CaCO_3$) mixture was made, and it was named Recipe 1. Recipe 2 was obtained by mixing glass fiber, broken stone, polypropylene and calcite. Thus, it was tried to create the advantage of increasing the impact resistance, reusing the waste stone and increasing the abrasion effect. Recipe 3 was obtained by mixing polyethylene, polypropylene, glass fiber, broken stone, silicate and calcite. Thus, it was tried to create the advantage of increasing the impact resistance, reusing the waste stone and increasing the abrasion effect. The photographs of these materials pumice stone are seen in Figure 2.

Pumice Stone (Conventional)

Recipe 1   Recipe 2   Recipe 3

Figure 2. The photograph of stone obtained by Recipe 1-2-3 and pumice stone

Within the scope of the study, clothes made from 3 different denim fabrics (Fabric A-B-C) were used. The same amount of stone was used in the trials carried out in conventional washings and newly developed washings. A total of 4 washes were made, 1 reference (pumice stone) and 3 new.

2.2. *Methods*

The foam generator used is given in Figure 1. RUCO FO 4010 was used as a foaming agent in the foam recipe and liquid cellulase enzyme was used to increase the effect. The stone materials obtained with Recipe 1-2-3 were used as abrasives. The washing process was carried out in a Yılmak RF-60 machine with 10 kg capacity, with 10 kg trousers. Foaming process was carried out using 9,6 liters of water each time. The process lasted at cold temperature and 30 minutes. After foam application, drying was carried

out in the Yılmak HMS 600 dryer machine, at 70°C temperature and for 40 minutes. Liquor ratio 1:1 at the rate 1 kg/trousers were used in the processes from the stones obtained with the newly developed recipes. After the trials, photographs of the samples were taken and their performances were compared with the tensile and tear strength tests. The tests were carried out according to Tensile Test; EN ISO 13934-2-EQV method, Tear Test; EN ISO 13937-1-EQV, Stretch and Growth ASTM D3107, Color Fastness to Water EN ISO 105 E01, Color Fastness to Perspiration EN ISO 105 E04, Color Fastness to Crocking AATCC 8 and Color Fastness to Rubbing EN ISO 105X12 standards.

3. Results and discussion

Figure 3-4-5 shows the visual results of foam washing done with Recipe 1-2-3 with Fabric A-B-C.

Figure 3. Recipe 1-2-3 and conventional washing effect of Fabric A

Figure 4. Recipe 1-2-3 and conventional washing effect of Fabric B

Figure 5. Recipe 1-2-3 and conventional washing effect of Fabric C

What is expected from this washing trial is that the new recipes will give a similar bleaching effect with the application of pumice stone. When Figure 3-4-5 is examined, it can be seen that the effects are similar. This similarity showed that the newly developed synthetic stones (Recipe 1-2-3) worked successfully.

Table 1 shows the performance values of the Fabric 1 obtained from 3 recipes and conventional applications.

Table 1. The physical performance of specimens from Fabric 1

Test Methods	Fabric Direct	Conventional	Recipe 1	Recipe 2	Recipe 3
Tensile Strength (kg)	Warp	35	69.3	67.9	65.0
	Weft	29,7	43.9	42.5	39.7
Tearing Strength (g)	Warp	3937	5486	5207	4952
	Weft	2472	3909	3725	3480
Elasticity (%)	-	31,4	35,7	33,1	38,4
Growth	-	6,9	6,5	6,7	6,6
Color Fastness to Crocking	Dry	3/4	4/5	4	3/4
	Wet	1/2	1	1/2	1/2
Color Fastness to Rubbing	Dry	4	4	3/4	3/4

The pumice stone is a material that affects the physical properties of fabric. Because the pumice stone and similar materials are based on friction, abrasion and snatching of the fiber from the fabric surface. Thus, the part in the center of the yarn that does not absorb indigo dye is revealed and the effect occurs.

When Table 1 is examined, it has been determined that the stones and prescriptions that provide friction cause positive difference in the physical properties. When the strength results were examined, it was determined that the samples made with Recipe 1-2-3 gave similar results among themselves, but the results were higher compared to conventional applications. While a similar effect is achieved with Recipe 1-2-3 (Figure 3-4-5), this results in a lower strength reduction. When the fabric elasticity and growth results were examined, no significant differences were detected.

Table 2. The color fastness to perspiration of specimens from Fabric 1

Fabric Type	Type	Color Change	Staining					
			Wool	Acrylic	Polyester	Nylon	Cotton	Acetate
Conventional	Acid	4/5	4/5	4	4/5	4/5	4/5	4
	Alkaline	4/5	4/5	4	4/5	4/5	4/5	4
Recipe 1	Acid	4/5	4/5	4	4/5	4/5	4/5	4
	Alkaline	4/5	4/5	4	4/5	4/5	4/5	4
Recipe 2	Acid	4/5	4	4/5	4/5	4/5	4/5	4/5
	Alkaline	4/5	4	4/5	4/5	4/5	4/5	4/5
Recipe 3	Acid	4/5	4/5	4	4/5	4/5	4/5	4
	Alkaline	4/5	4/5	4	4/5	4/5	4/5	4

Table 3. The color fastness to water of specimens from Fabric 1

Fabric Type	Color Change	Staining					
		Wool	Acrylic	Polyester	Nylon	Cotton	Acetate
Conventional	4/5	4/5	4/5	4/5	4/5	4/5	4/5
Recipe 1	4/5	4/5	4	4/5	4/5	4	4/5
Recipe 2	4/5	4/5	4/5	4	4/5	4	4
Recipe 3	4/5	4/5	4/5	4/5	4/5	4/5	4/5

When the fastness results in Table 1-Table 2 and Table 3 are examined, it was determined that the applications made with pumice stone and new polymer mixtures showed similar performance, and the type of the stone did not significantly affect the fastness results.

4. CONCLUSIONS

At the end of the study, an alternative material and washing method were developed. When compared to the conventional method, a total of 3 baths and 600 liters of water were saved. The processes were carried out at room temperature and energy savings were achieved in this respect. Accordingly, 20% energy savings were achieved. Not using pumice stone and repeated use of new materials reduced waste generation. Since stone reduces the strength of the fabric, clothes washed with the traditional method carry the risk of wear. On the other hand, with the proposed method, only half as much stone was used compared to the traditional method and a positive development was determined in terms of fabric strength. Since the new method requires 15 minutes less machine operation time compared to the traditional method and the foam process is applied at room temperature, less energy will be consumed. When the process is examined in terms of chemical consumption, a 20% cost gain can be predicted. In the proposed washing method, less back staining risk was observed. No back staining was observed in the proposed washing method.

References

1. *Cheriaa, R., & Baffoun, A. (2015). Effects of cross linkers combination, for three dimensional effects, on denim garment properties. Fibers and polymers, 16, 1150-1155.*
2. *Choudhury, A. K. R. (2017). Environmental impacts of denim washing. In Sustainability in Denim (pp. 49-81). Woodhead Publishing.*
3. *Hoque, S., Rashid, M. A., Chowdhury, S., Chakraborty, A., and Haque, A. N. M. A. (2018). Alternative washing of cotton denim fabrics by natural agents. American Journal of Environmental Protection, 7(6), 79-83.*
4. *Hoque, M. S., Hossain, M. J., Imtiaz, M. A., Das, S., & Rashid, M. A. (2018). Scope of dry wood & wood composite alternate to stone in case of acid wash on denim fabric. International Journal of Current Engineering and Technology, 8(2), 382-388.*
5. *https://www.cottonworks.com/en/topics/sourcing-manufacturing/denim/sustainable-denim-finishing/*
6. *https://www.cottonworks.com/wp-content/uploads/2018/09/Denim-Webinar_Final.pdf*
7. *https://denimdudes.co/future-of-wash-sustainable-solutions-for-stone-and-acid-wash-in-the-denim-industry/*
8. *https://www.abiteks.com.tr/blog/sustainable-solutions-for-denim-processing*

DESIGN OF ELECTRICALLY CONDUCTIVE, HIGHLY STRETCHABLE, HYGIENIC ELECTRODES FOR ELECTROTHERAPY

[1]**Azam Ali,** [1]**Jiri Militky,** [1]**Blanka Tomkova,** [1]**Muhammad Zaman Khan,** [2]**Samiuddin,** [2]**Saba Nosheen,** [2]**Iqra Suleman,**

[1]Department of Material Engineering, Faculty of Textile Engineering, Technical University of Liberec
[2]Department of chemistry, Riphah International University Faisalabad
Corresponding author Email: azam.ali@tul.cz

Abstract:

The main objective of this study was to create versatile and wearable electrically conductive electrodes for Transcutaneous Electrical Nerve Stimulation (TENS) application, ensuring they are comfortable by depositing silver particles directly onto the carbon particles imparted rubber electrodes. Scanning Electron Microscopy (SEM) was used to analyze the shape of the deposited silver particles. To enhance the electrode's performance during body movements, the conductive fabrics were stretched repeatedly, and changes in resistivity were observed. The electrical resistance showed minimal variation with small extensions, remaining relatively constant between 0–70% stretch. Resistance increased significantly after 80% stretch, but the fabric's resistivity remained stable even after over 100 stretching cycles. Additionally, there was no significant change in resistivity over time at a constant current. The study also investigated the antibacterial properties of the deposited particles against bacteria like Staphylococcus aureus and Escherichia coli. The antifungal activity assessment using C. albicans further underscores the benefits of the silver-plated elastomers in combating fungal growth. Finally, the durability of the coated fabrics concerning comfort and electrical properties was evaluated through multiple pressure applied, showing good particle retention and only a slight decrease in conductivity.

Key words:

Silver electroplating, carbon particles, Multifunctional electrodes, Electrostimulation and Antibacterial.

1. Introduction

To improve treatment efficacy and patient comfort, electrodes for electrotherapy must be designed to be electrically conductive, extremely flexible, and hygienic. The quality and functioning of electrodes play a critical role in the effectiveness of electrotherapy, which uses the accurate transmission of electrical currents to stimulate muscles, control pain, and encourage recovery. Due to their lack of flexibility or potential for introducing hygienic issues with prolonged usage, traditional electrodes frequently struggle to maintain conductivity and comfort during dynamic movements. The use of electrotherapy, specifically Transcutaneous Electrical Nerve Stimulation (TENS), in physiotherapy and rehabilitation to manage pain and improve mobility. TENS therapy involves applying electric current to stimulate body nerves, typically using conductive hydrogel electrodes. While self-adhesive hydrogel electrodes are commonly used for TENS, they have drawbacks like discomfort, skin irritations, and hygiene issues [1]. Other types of electrodes, such as carbon rubber electrodes or metal plates covered with nonconductive fabric, have also been utilized but can pose challenges. Despite these challenges, the use of electrodes remains prevalent in TENS applications [2]. Modern electrode designs aim to overcome these limitations by developing electrically conductive materials that can withstand high stretch levels without affecting performance. Moreover, incorporating antimicrobial and biocompatible characteristics promotes skin safety and hygiene, particularly during extended or repeated therapy sessions [3].

In this research, a unique substrate made of cotton, nylon, and lycra was chosen, and a special method for depositing silver nanoparticles onto fibers and within fabric structures was developed. This

approach resulted in the creation of conductive fabric-based electrodes with excellent conductivity, flexibility, and stretchability to ensure comfort during use. The study also explored changes in electrical conductivity with repeated stretching to enhance the adaptability of carbon embedded silver plated electrodes for human body movements during electrotherapy sessions [4]. Additionally, these electrodes demonstrated good washing durability, resistance to cracking when stretched, and exhibited qualities like drape, softness, and a comfortable feel. The electrodes were engineered by directly plating of very fine silver nanoparticles on them. These electrodes significantly reduced the risk of contact dermatitis and can be safely applied to wounded or injured skin due to the antibacterial and hygienic properties conferred by the silver nanoparticles in the developed carbon embedded rubber electrodes [5].

2. Experimental and characterizations

A reagent grade chemical was obtained from sigma Aldrich. Firstly, 8g of carbon particles were added into methanol solution and then ultrasonicated for 30 min. After ultrasonics 100 mL of silicon elastomer solution was added slowly to the reaction mixture. Then the mixture further ultrasonicated for I hour to produce a conductive elastomer. The methanol was evaporated by placing the beaker in the oven at 50°C. Subsequently, silver electroplating was done at various time intervals over carbon embedded polymeric rubber. The utilization of SEM and XRD for surface morphology analysis, along with ASTM D257-07 for electrical volume resistivity measurement, indicates a comprehensive approach to characterizing the material properties. Additionally, the Zone of Inhibition test for qualitative measurements and quantitively assessments using AATCC 100-2004 standards, provide valuable insights into the material's antimicrobial properties. This multi-faceted evaluation is crucial for understanding the performance and potential applications of the silver-coated elastomers in various settings. Behrens and Karber's technique were used to calculate the virus titer reduction from the basic viral titer of infectivity (107) titer.

3. Results and discussion

3.1 *Electrical resistivity*

Figure 1 is showing the effect of electroplating and weight gain percentage against the electrical resistivity. Increase in electroplating time tends to increase in silver plating and eventually decrease in electrical resistivity values. Although it improves conductivity by forming a more continuous conductive layer, this tendency indicates the ideal electroplating duration is required to get low resistance. The percentage of weight gain indicates the quantity of silver coating that has been contributed to the electrode; greater percentages indicate more silver deposition and better conductivity [6]. The evaluation of the electrical resistivity of the silver-plated samples and the analysis of resistivity at different stretch percentages provide valuable insights into the behavior of the electrodes. The data from Figure 2 showing the resistivity value graphs for each sample is essential for understanding the variations among the samples. The observations regarding resistivity changes at different stretch levels, especially the significant increase in resistivity beyond 60% stretch up to approximately 45 K Ω.mm at 100% stretch, highlight the material's response to mechanical stress [7].This data shows silver-plated samples exhibit low resistance when stretched moderately, but their conductive performance drastically decreases when stretched excessively. This highlights the significance of striking a balance between conductivity and stretch ability when designing electrodes. The durability testing of sample S10, with resistivity measurements at different stretch levels and the calculation of the mean resistivity during one complete cycle, offers a comprehensive assessment of the sample's performance under repeated stretching and release cycles. This detailed analysis is crucial for evaluating the reliability and stability of the electrodes in practical applications. As it helps choose materials and design parameters that assure long-term performance and consistency in electrotherapy applications, the study is essential for applications where electrodes are subject to constant movement [8].
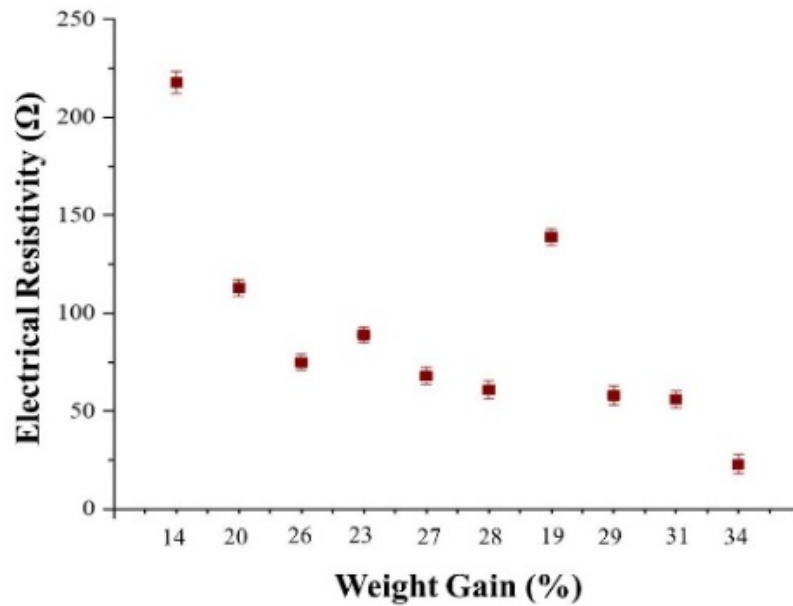
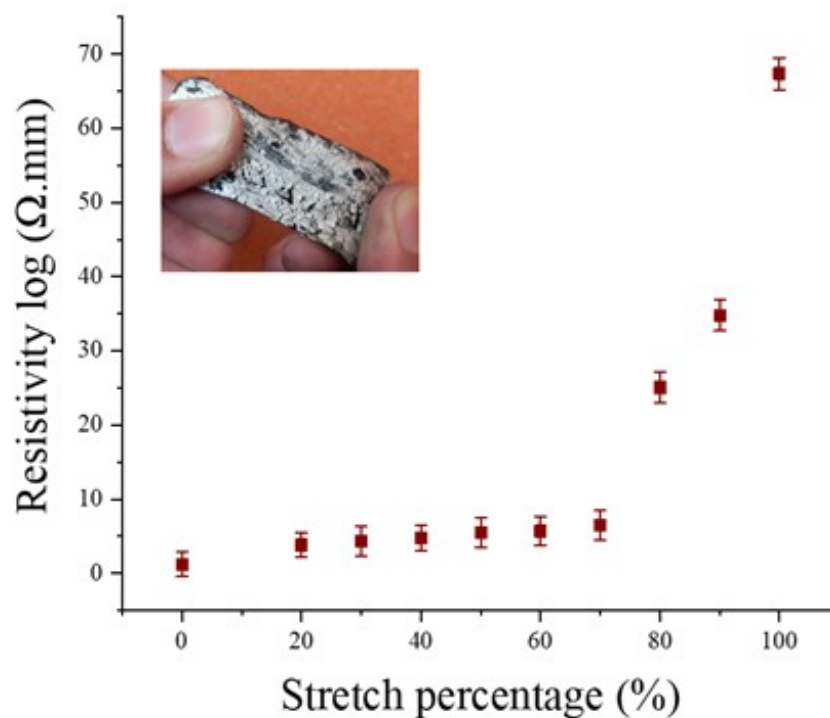**Figure 1.** Electrical resistivity at normal stretch

Figure 2. Electrical resistivity at different stretch percentage

3.2 Antipathogenic properties of developed electrodes

In addition to their excellent conductivity, silver-plated electrodes for TENS applications are becoming increasingly common due to their fundamental antipathogenic qualities. Strong antibacterial properties of silver are well recognized, and they are especially advantageous in therapeutic and medical devices which come into direct contact with the skin. By lowering the possibility of bacterial and fungal contamination, these characteristics improve the safety and hygienic conditions of TENS electrodes used for extended wear or repeated sessions [9].By incorporating silver plating, TENS electrodes benefit

from both improved conductivity and enhanced antipathogenic properties, offering a dual-functionality that aligns with the high standards needed for medical and therapeutic applications. This feature is particularly advantageous in clinical environments and for individuals who use TENS devices frequently, as it contributes to better skin health, reduces maintenance, and extends the electrode's usable life [10].

The Gram-negative *E. coli* and Gram-positive *S. aureus* were used for testing the antibacterial activity of silver-plated elastomers. Figure 3 display the zones of inhibition around the samples after one day of incubation in dark at temperature 37 °C. The results clearly show that the silver coating on the elastomers was effective in creating zones of inhibition against both Staphylococcus aureus and Escherichia coli. The antimicrobial properties of the metal coating, with its unique features like microparticles and biomolecules such as polynuclear acids and proteins, contribute to its effectiveness. This character makes silver-plated electrodes a valuable option for TENS devices because they lessen the chances of infections and skin irritations often linked with long-term electrode usage. The antibacterial behavior of the silver coating may be due to chemical interactions, physical interactions, or a combination of both, making the prepared electrodes highly hygienic and ideal for hospital environments [11].
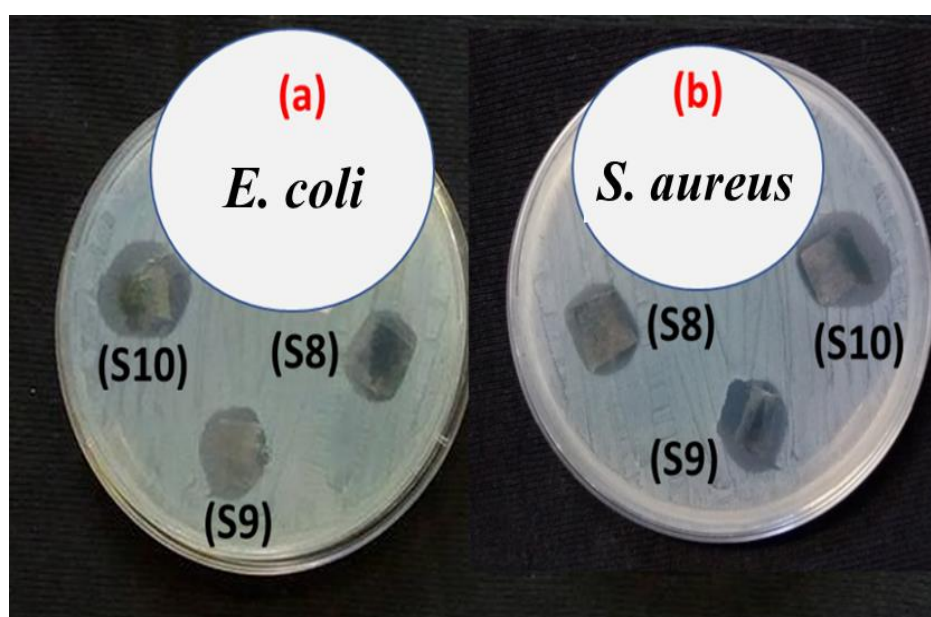

Figure 3. Antibacterial properties with Zone of inhibition

A crucial component of ensuring the sanitary and safe operation of silver-plated electrodes for electrotherapy is the evaluation of their antifungal activity, specifically concerning Candida albicans. Especially in wet skin areas where electrotherapy electrodes are frequently used, Candida albicans is a prevalent fungal pathogen linked to infections. The broad-spectrum antibacterial and antifungal qualities of silver cause it to release silver ions, which disrupt fungal cell processes, impair membrane integrity, and stop growth. The antifungal activity assessment using C. albicans further underscores the benefits of the silver-plated elastomers in combating fungal growth. Figure 4 display the percentage reduction of fungi (*C. albicans*) with raw sample and samples loaded with silver. In order to test silver-plated electrodes against Candida albicans, one must either measure the number of fungal colonies present or evaluate the fungal inhibition zone. Significant inhibition of Candida albicans growth surrounding the silver-plated electrode would be an indicator of effective antifungal performance, suggesting that the released silver ions are actively inhibiting fungal proliferation. The silver-plated sample exhibit maximum antifungal activity because the metal particles coated elastomer having suitable antibacterial properties. Hence, the percentage reduction of silver nanoparticles greater as compared to phytochemicals. Clinical safety is enhanced by employing silver-plated electrodes with antifungal qualities in electrotherapy devices, especially for patients with sensitive skin or lengthy therapy sessions.
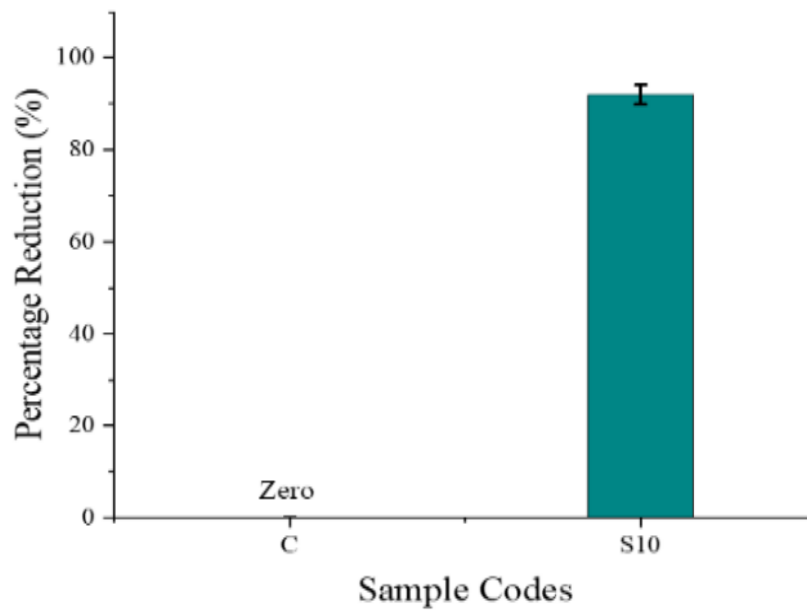
**Figure 4.** Antifungal activity of silver coated textile

Figure 5(a) display a graph which shows the virus infectivity titer log against contact time (0 h and 60 mins). Behrens and Karber's method was used for the calculation of virus titers reduction from the starting viral titter of infectivity (107) titer. The Figure 5(a) describes the infectivity titer change of corona virus (0 h and 60 mins) at 25°C for uncoated elastomer and silver coated elastomer S10. It was examined that there is a major decrease in infectivity titer for fabrics coated sample after 60 mins instead of 0 hrs whereas no reduction in virus activity titer was calculated in vase of uncoated elastomer sample. While, Figure 5 (b) exhibit virus percent reduction for uncoated and coated S10 sample. The elastomer treated with silver reduces 84% in virus titer separately uncoated elastomer remained ineffective against virus. The antiviral action exhibited through elastomer treated with silver could be due to the binding of metallic surface with glycoproteins at the viral surface working as an inhibitory action for viruses.
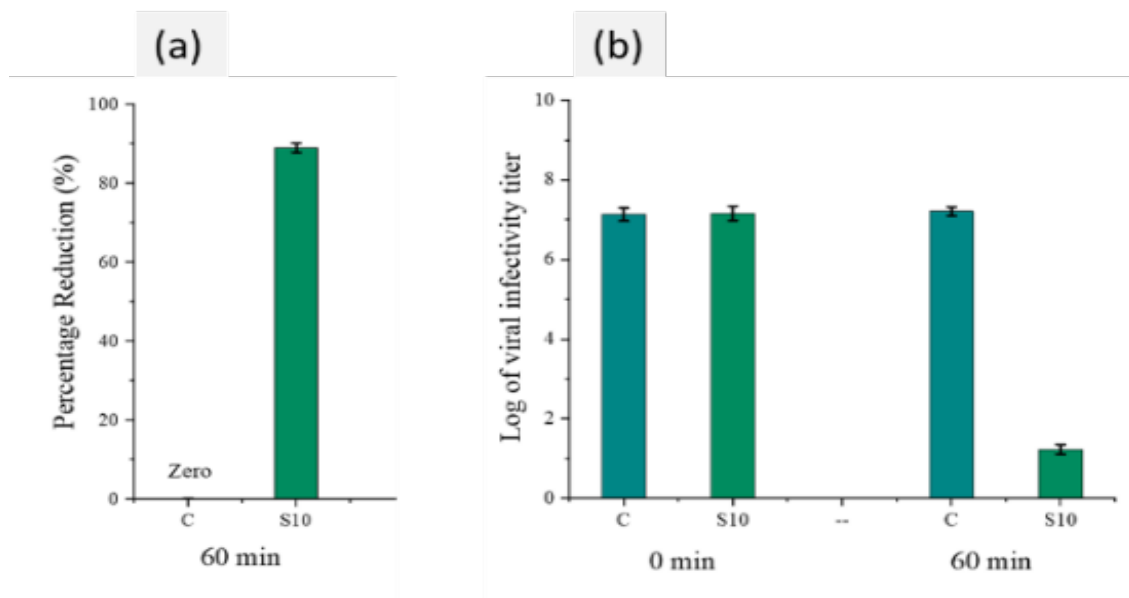
Figure 5. Reduction in viral infectivity titer (a) and percentage reduction (b) calculated from viral infectivity for untreated and treated fabrics at a contact time of 0 and 60 min

3.3 The effect of applied pressure on electrode resistivity during electrotherapy

Electrode resistivity, which in effect influences how effectively current is delivered to the targeted tissue, is greatly affected by the pressure that is applied to the electrodes during electrotherapy. Applying enough pressure enhances the electrode-skin contact, which lowers resistance and promotes better current flow [12]The therapeutic advantages of electrotherapy are increased by this optimized current distribution. But excessive or insufficient pressure may adversely affect resistivity, which can either make patients uncomfortable or decrease the effectiveness of treatment. For electrotherapy applications to produce reliable and efficient effects, applied pressure must be controlled. The high potential signals from the skin are captured using wet and dry electrodes, even when the body is in motion. In our current research, we explored the effects of applying loads of 200g, 400g, and 600g on a 10cm × 10cm sample, which translates to pressures of 2 N/cm^2, 4 N/cm2, and 6 N/cm2 [13].The trend line values of electrical resistivities with respective applied pressure are shown in Figure 6. The pressure applied had a significant impact on the electrical resistivity of the electrodes. An evident decrease in resistivity was noted with increasing pressure. Initially, the resistivities of samples S3, S6, S9, and S10 were 75 Ω.mm, 61 Ω.mm, 56 Ω.mm, and 23 Ω.mm, respectively. When the pressure reached 6 N/cm^2, the values decreased to approximately 23 Ω.mm, 17 Ω.mm, 14 Ω.mm, and 1 Ω.mm. A similar approach was taken in a previous study that explored the effect of pressure on dry textile electrodes for obtaining ECG signals. They observed that increased pressure led to lower impedance. Specifically, the impedance decreased as the contact area between the conductive network and skin increased. Since polymers and textiles are soft materials, squeezing them improves the contact interface, resulting in better signal acquisition [14].
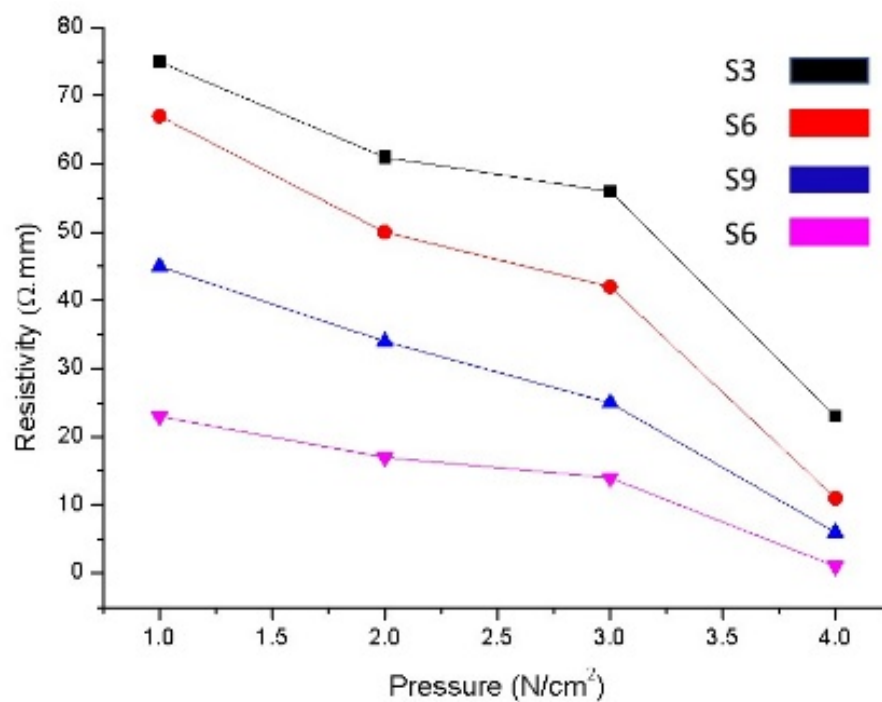
Figure 6. Trend line values of electrical resistivity with respective applied pressure

4. CONCLUSION

The development of those electrically conductive and highly stretchable electrodes for TENS machines sounds really impressive! Achieving a minimum resistivity of 1183 Ω.mm at 8% carbon particles and a volume resistivity of 23 Ω.mm in the conductive elastomer samples is quite remarkable. The fact that these electrodes also demonstrated significant effectiveness against various pathogens in antipathogenic testing is a great advantage. The silver electroplating over the carbon-embedded electrodes seems to have enhanced their properties further. The potential applications of these electrodes in electrostimulation and electrotherapy fields hold a lot of promise for future use. The development of these electrically conductive and highly stretchable electrodes for TENS machines is indeed impressive and marks a significant advancement in the field of electrotherapy. Achieving a minimum resistivity of 1183 Ω.mm at 8% carbon particles and a volume resistivity of 23 Ω.mm in the conductive elastomer samples is noteworthy. Additionally, their demonstrated effectiveness against various pathogens in antipathogenic testing is a substantial benefit, highlighting their potential to improve hygiene and safety standards in clinical settings. The silver electroplating over the carbon-embedded electrodes appears to have further enhanced their electrical and antimicrobial properties, ensuring not only reliable conductivity but also effective pathogen control. This dual functionality could pave the way for broader applications, including personalized medical treatments, rehabilitation therapy, and even wearable health-monitoring devices. The integration of these innovative electrodes into current and future electrostimulation and electrotherapy technologies holds significant promise, potentially leading to better therapeutic outcomes and enhanced patient experiences.

References

1. R. Melzack and P. D. Wall, "Pain mechanisms: A new theory," Pain Clin., vol. 7, no. 1, pp. 57–72, 1994, doi: 10.1017/cbo9780511759048.009.
2. Brown L, Holmes M, Jones A (2009) The application of transcutaneous electrical nerve stimulation to acupuncture points (Acu-TENS) for pain relief: a discussion of efficacy and potential mechanisms. Phys Ther Rev 14:93–103. https://doi.org/10.1179/174328809X405964
3. Sueaseenak D, Uburi T, Tirasuwannarat P (2017) Optimal placement of multi-channels sEMG electrod for finger movement classification. ACM Int Conf Proceeding Ser 78–83. https://doi.org/10.1145/3168776.3168802
4. Watson T (2000) The role of electrotherapy in contemporary physiotherapy practice. Man Ther 5:132–141. https://doi.org/10.1054/math.2000.0363
5. Ryu CY, Nam SH, Kim S (2005) Conductive rubber electrode for wearable health monitoring. Annu Int Conf IEEE Eng Med Biol - Proc 7 VOLS:3479–3481. https://doi.org/10.1109/iembs.2005.1617228
6. SINGH Y (2013) Electrical Resistivity Measurements: a Review. Int J Mod Phys Conf Ser 22:745–756. https://doi.org/10.1142/s2010194513010970
7. Radoeva M, Radoev B (1995) Ohm resistivity of electroless copper layers as a function of their thicknesses. J Mater Sci 30:2215–2219. https://doi.org/10.1007/BF01184563
8. Tallman DE, Petersen SL (1990) Composite electrodes for electroanalysis: Principles and applications. Electroanalysis 2:499–510. https://doi.org/10.1002/elan.1140020702
9. Jo G, Choe M, Lee S, et al (2012) The application of graphene as electrodes in electrical and optical devices. Nanotechnology 23:. https://doi.org/10.1088/0957-4484/23/11/112001
10. Li Q, Zhang J, Li Q, et al (2019) Review of printed electrodes for flexible devices. Front Mater 5:. https://doi.org/10.3389/fmats.2018.00077
11. Carlone GM, Valadez MJ, Pickett MJ (1982) Methods for distinguishing gram-positive from gram-negative bacteria. J Clin Microbiol 16:1157–1159. https://doi.org/10.1128/jcm.16.6.1157-1159.1982
12. (1994) Electrode arrays for measuring groundwater flow direction and velocity. Int J Rock Mech Min Sci Geomech Abstr 31:196. https://doi.org/10.1016/0148-9062(94)91096-0
13. Ali A, Baheti V, Militky J, Khan Z (2018) Utility of silver-coated fabrics as electrodes in

electrotherapy applications. J Appl Polym Sci 135:. https://doi.org/10.1002/app.46357

14. *Chen PY, Cheen JR, Jheng YC, et al (2022) Clinical applications and consideration of interventions of electrotherapy for orthopedic and neurological rehabilitation. J Chinese Med Assoc 85:24–29. https://doi.org/10.1097/JCMA.0000000000000634*

ADSORPTION OF METHYLENE BLUE DYE FROM AQUEOUS SOLUTION USING BIO-WASTE POPLAR FIBER

Canan Usta[1*], Aybeniz Seyhan[1], Alper Gürarslan[1]

[1]Istanbul Technical University, Textile Engineering Department, Istanbul, Türkiye
*cananusta@itu.edu.tr

Abstract

Poplar fiber corresponds to the seed hairs of the Populus genus trees and is a naturally abundant lignocellulosic fiber with the features of thin-walled large lumen, lightweight and hydrophobic properties. Based on the structure and properties exhibited by poplar fiber nominate it as a highly favored adsorbent material for cationic dyes. This study aims to determine the adsorption efficiency for methylene blue (MB) dye with chemically enhanced poplar fibers and compare its capacity with milkweed fibers. Prior to adsorption experiments, the fibers were treated with NaOH solution to remove the wax coating attached on the fiber surface. Adsorption studies were performed in a batch system using dye solution with initial dye concentration of 50 mg L^{-1}. The adsorbent dosage was evaluated at 10 g L^{-1} amount, with contact time of 3 h and without pH adjustment. After the experiments, the remaining dye concentration in liquid was quantified in UV-Vis spectrophotometry. The results revealed that poplar fiber exhibited higher adsorption capacity compared with milkweed fiber. Poplar fibers were efficient to decolorize MB dye solution, reaching a higher color removal percentage than milkweed fibers. It can be concluded that poplar fibers were alternative adsorbents for removing cationic dyes due to their hollow structure.

Key words:

Poplar fiber, dyeing, adsorption, cationic dye, methylene blue

1. Introduction

Waste generation during industrial processes significantly contributes to various environmental pollution problems. Particularly, textile processes consume large amounts of water and synthetic dyes, leading to the generation of colored effluents. The presence of dye contaminants in wastewater is a major concern for both human health and the environment, as even trace amounts of dye are noticeable in water [1]. Among the common dyes, methylene blue (MB), the structure shown in Figure 1, is widely used in textile processing due to its water solubility. While not highly toxic to humans, MB can cause eye and skin irritation and has systemic effects. Hence, the removal of the dye from wastewater is critical in addressing water pollution.
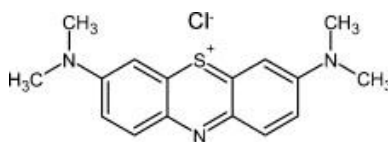
Figure 1. Chemical structure of Methylene Blue.

Several methods are widely used for the removal of dye from wastewater, including membrane filtration, ion exchange, reverse osmosis, coagulation and adsorption [2, 3]. Among these, adsorption stands out as one of the simplest and most cost-effective physico-chemical treatment process for removing dye molecules from aqueous solutions. This study focuses on adsorption due to its practicality and efficiency.

There is an increasing demand for cost-effective alternative technologies or adsorbents for dye removal. Natural agricultural materials, which are readily available in large quantities, may serve as low-cost and effective adsorbents.

Poplar fibers are a type of trichome fiber and grow as seed hair fibers on the branches of poplar trees. The variation in poplar species over time can be attributed to factors such as human activities, biological processes and genetic pollution from hybrid poplars [4]. Each poplar tree is capable of generating approximately 25 kg of poplar seed fibers [5]. The length of these fibers depends on the specific tree and the region where they are harvested, and lengths ranging from 3 to 16 mm have been reported in the literature [6-7]. Poplar fibers typically have a diameter between 5 and 10 µm. These fibers have large hollow lumen, allowing them to float in the air and facilitating their dispersal. The internal diameter of the fibers accounts for approximately 90% of the total fiber diameter, resulting in an extremely low density of around 0.3 g/cm³ [7]. Poplar fibers have similar properties to milkweed and kapok fibers due to their hollow structure. While extensive studies were conducted on these fibers, the potential of poplar fibers have not been thoroughly investigated about water treatment capacity. Therefore, this study aims to investigate the potential of poplar fiber as a viable solution for the adsorption of cationic dye from wastewater and provide an environmentally friendly and efficient approach to water purification.

2. Experimental

2.1. *Materials*

Poplar fibers were directly collected during the blooming period in mid-May in the Kırklareli region of Türkiye. Milkweed fibers were obtained in partnership with Pangai Materials Science, Italy. Both of the fibers were mechanically cleaned to remove contaminants such as seeds, leaves, dust etc. Sodium hydroxide, 99% (Merck) and methylene blue were used as received without further purification.

2.2. *Methods*

Pretreatment of poplar and milkweed fibers

Aqueous NaOH solution was prepared and cooled to room temperature in a glass bottle. Then, 1.0 g of fiber was added immediately into this solution. Subsequently, the generated fiber/solution mixture was placed into the Gyrowash vessels to be processed at 70 °C for 1 hour. Then, fiber sample was washed with distilled water at ambient room temperature until no residual chemicals could be detected on the fiber surface. The wet pretreated fibers were dried at 40 °C for 24 h.

Measurement of the adsorption capacity

The adsorption capacity was measured by calculation of methylene blue dye concentration in the aqueous solution after adsorption. The adsorption process was conducted in 50 mg L^{-1} of methylene blue solution. A glass flask containing 1 g of the modified fibers and 50 ml of the MB solution was shaken for 3 h at room temperature. Then, fibers were filtered and the residual solution was analyzed at λ_{max} of 660 nm using UV-Vis Spectrophotometer.

Scanning electron microscopy (SEM)

The morphology of milkweed and poplar fibers was examined by scanning electron microscopy using TESCAN VEGA3 instrument with 10 kV accelerated voltage and 2.08-6.92 mm working distance. Surface images were taken at 5 kX magnification. Before analysis, fiber samples were coated with Au/Pd under vacuum conditions for 3 min.

3. Results and discussion

Hollow fibers have become widely adopted across numerous industries, with wastewater treatment being one of the primary applications. Their unique structure, featuring a high surface area-to-volume ratio, enables efficient separation and filtration processes, making them ideal for removing contaminants from wastewater [8]. Characterizing the structural morphologies of hollow milkweed and poplar fibers is essential for advancing adsorption technologies.

Scanning electron microscope (SEM) analysis of the fibers revealed a smooth surface, free from rough structures. This smoothness is likely due to a natural wax coating adhered to the fiber surface, as previously reported [9]. Structurally, each fiber resembles a cylindrical microtube with nano-scale surface wrinkles, as seen in Figure 2. Poplar and milkweed fibers exhibit a hollow tubular shape, with diameters around 10 μm and 25 μm, respectively. The presence of a large air-filled lumen in both fibers makes them highly suitable for applications requiring lightweight materials with high absorbency [10].
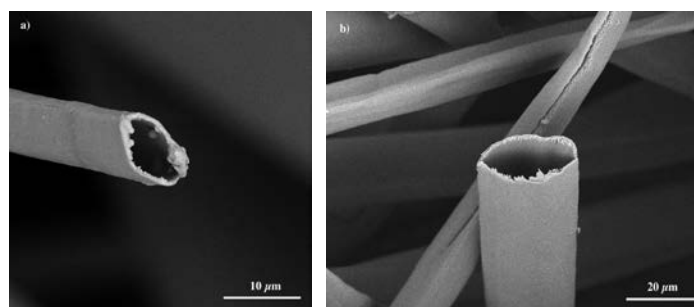

Figure 2. SEM images of raw (a) poplar and (b) milkweed fiber.

Chemical treatment, particularly using NaOH, effectively removed the waxy surface of poplar and milkweed fibers. This treatment also facilitated deesterification, breaking down the ester bonds attached to the aromatic rings of lignin [11]. Delignification resulted in an increased proportion of amorphous cellulose, which reduced the hydrophobicity of the fiber (as evidenced by the decrease in the static water contact angle) as reported in the literature [12,13]. NaOH treatment altered the naturally smooth surface of both fibers, causing the surface to become rougher and increasing the overall surface area [14]. Hence, the adsorption capacity of treated fibers is affected by their chemical reactivity and the porosity of the functional groups present on their surfaces. The structural changes after treatment improved the adhesion of the dye to the outer surface of the fiber and improved its penetration into the inner lumen, thus increasing the dye removal in the chemically treated fiber compared to the untreated fiber.

In this study, an oxidation pretreatment using sodium hydroxide (NaOH) was performed to remove wax, oil, pectin, lignin, and hemicellulose from poplar and milkweed fibers. Then, the increased hydrophilic properties of the treated fibers were used for organic pollutant removal application. Usage of natural milkweed and poplar fibers in removal of methylene blue from wastewater was studied and the decolorization effect was observed. Figure 3 shows the absorbance spectra of methylene blue (MB) at initial and post-adsorption concentrations. The maximum absorbance peak for all concentrations appears consistently at 660 nm in the visible light waveband, which is in agreement with other studies reporting that the absorbance peak of MB occurs at 660 nm in UV-Vis spectrophotometric analysis [15]. In our study, this peak was used to analyze the removal efficiency of methylene blue. As seen from Figure 3, it is clearly observed that the MB concentration decreases with adsorption by NaOH-treated milkweed and poplar fibers, leading to a corresponding decrease in the peak absorbance values. This behavior follows the Lambert-Beer law, which describes the quantitative analysis by UV-VIS spectrophotometry based on measuring the absorbance of MB solution at 660 nm due to equation (1) as follows [16]:

$$A = \varepsilon c l. \qquad \text{Eq. (1)}$$

where A represents absorbance, ε is the molar absorption coefficient, c is the concentration, and l is the optical path length. Thus, the absorbance peak trend in the MB solutions can be effectively used to determine MB concentrations based on this relationship.
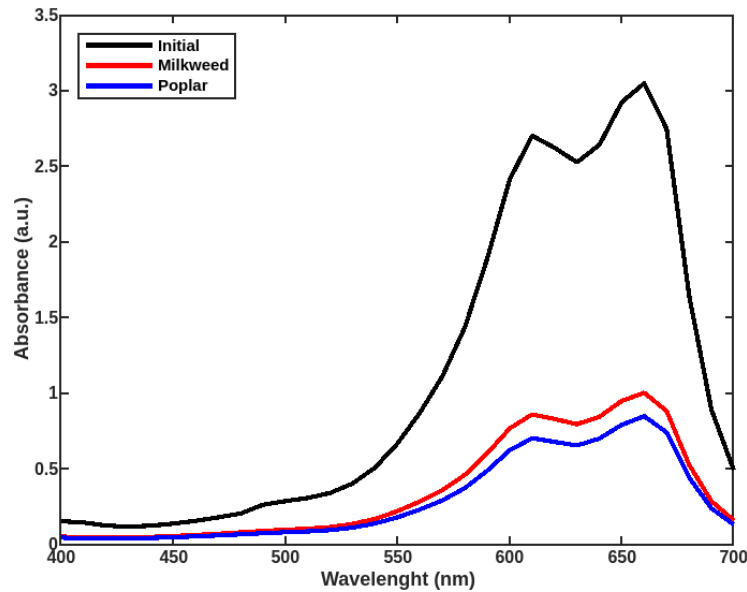
Figure 3. Absorbance curve of MB solution before and after the treatment with milkweed and poplar fibers.

In Figure 3, the changes in the absorbance curve of MB around 660 nm wavelength before and after treatment with milkweed and poplar fibers were presented. It is seen that the absorbance peak decreases when treated with both fibers and reaches a minimum value with poplar fiber. According to the Lambert-Beer law in Equation (1), this indicates that the MB concentration in the solution will decrease when treated with poplar fiber.

Using the relationship between the absorbance value at 660 nm and the concentration of MB as given in equation (1), the degree of decolorization (% decolorization) can be calculated using the formula:

$$\% \text{decolorization} = \frac{c_{initial(MB)} - c_{treated(MB)}}{c_{initial(MB)}} \times 100 \qquad \text{Eq. (2)}$$

where $c_{initial(MB)}$ is the initial absorbance value (before decolorization), and $c_{treated(MB)}$ is the absorbance value after treatment with poplar and milkweed fibers [17]. This calculation provides a quantitative measure of the effectiveness of the decolorization process with different fiber types.

Table 1. The percent value of MB concentration after the adsorption process.

	Milkweed Fiber	**Poplar Fiber**
MB Concentration (%)	~67%	~72%

The results for MB concentration percentages in this study are presented in Table 1, demonstrating that both treated fibers enhanced adsorption capacity effectively, showcasing the efficiency of these fibers for color removal. Particularly, poplar fiber presented slightly better performance compared to milkweed fiber. This improvement can be attributed to the structural differences between the fibers; specifically, poplar fiber's shorter length and smaller diameter increase its surface area, a critical factor since adsorption occurs on the fiber surface [18]. This increased surface area of poplar fiber facilitates greater adsorption capacity, emphasizing its suitability for efficient color removal.

4. CONCLUSIONS

This study investigated the potential of poplar fiber as an adsorbent for the decolorization of methylene blue (MB) dye in wastewater. The base modified milkweed and poplar fibers can be used as an effective alternative low-cost adsorbent for the removal of MB from its aqueous solutions. The amount of MB dye uptake on modified poplar fiber was found to be higher than milkweed fiber. Experimental results indicated that NaOH-treated poplar fiber facilitates a higher percentage of MB removal, showing its effectiveness as a decolorizing agent. It was found that the absorbance value of 0.8435 occurred for the initial dye concentration of 50 g L^{-1} by modified poplar fiber, whereas for modified milkweed fiber it was 0.9985 for the same experiment conditions. When compared to milkweed fiber, poplar fiber demonstrates slightly better performance due to its structural characteristics, such as fine short length and fiber diameter which enhance its adsorption capabilities. The successful application of poplar fiber in this process suggests it as a promising, eco-friendly alternative for treating dye-contaminated wastewater, providing a sustainable solution for water purification.

ACKNOWLEDGEMENTS

References

1. *Yu, Z., Qi, T., Qu, J., Wang, L., Chu, J. (2009). Removal of Ca(II) and Mg(II) from potassium chromate solution on Amberlite IRC 748 synthetic resin by ion exchange. J Hazard Mater, 167, 406–412.*
2. *Dawood S, Sen TK (2012). Removal of anionic dye congo red from aqueous solution by raw pine and acid-treated pine cone powder as adsorbent: equilibrium, thermodynamic, kinetics, mechanism and process design. Water Res 46:1933–1946*
3. *Mohammod M, Sen TK, Maitra S, Dutta BK (2011). Removal of Zn2+ from aqueous solution using castor seed hull. Water Air Soil Pollut 179:363–372.*
4. *Ciftci, A. and Kaya, Z. (2019). Genetic diversity and structure of Populus nigra populations in two highly fragmented river ecosystems from Turkey. Tree Genetics & Genomes, 15(4): 66.*
5. *Liu, Y., Lyu, L., Xiong, X., Qian, Y., Li, H. and Guo, J. (2020.) Structural characteristics and sound absorption properties of poplar seed fibers. Textile Research Journal, 90(21–22), 2467–2477.*
6. *Gurarslan, A. & Narinç, M. E. (2019). Investigating the rose oil and toluene absorption of populus fiber. Textile Research Journal, 89(10), 1952–1963.*
7. *Chen, H.-L. & Cluver, B. (2010). Assessment of Poplar Seed Hair Fibers as a Potential Bulk Textile Thermal Insulation Material. Clothing and Textiles Research Journal, 28(4), 255–262.*
8. *Huang, J-H., Zhou, C-F., Zeng, G-M., Li, X., Niu, J., Huang, H-J., Shi, L-J., He, S-B. (2010) Micellar-enhanced ultrafiltration of methylene blue from dye wastewater via a polysulfone hollow fiber membrane, Journal of Membrane Science, 365 (1-2), 138-144.*
9. *Sangalang, R.H. (2021) Kapok Fiber-Structure, Characteristics and Applications: (A Review), Oriental Journal Of Chemistry, 37(3), 513-523.*
10. *Usta, C., Seyhan, A., Gurarslan, A. (2024) Utilization of poplar fibers in needle punched nonwovens, Cellulose 31, 8351–8367. https://doi.org/10.1007/s10570-024-06062-w.*
11. *Futalan, C. M., Choi, A. E. S., Soriano, H. G. O., Cabacungan, M. K. B., Millare, J. C. (2022) Modification Strategies of Kapok Fiber Composites and Its Application in the Adsorption of Heavy Metal Ions and Dyes from Aqueous Solutions: A Systematic Review. International Journal of Environmental Research and Public Health, 19(5), 2703. https://doi.org/10.3390/ijerph19052703.*
12. *Wolok, E., Lahay, I. H., Machmoed, B. R., Pakaya, F. (2019) Modification And Characterization Of Ceiba Pentandra (L.) Gaertn. (Kapok) Fiber: Physical Properties, International Journal of Research -GRANTHAALAYAH, 7(7):381-390.*

13. *Liu, Y., Wang, J., Zheng, Y., Wang, A. (2012) Adsorption of methylene blue by kapok fiber treated by sodium chlorite optimized with response surface methodology, Chemical Engineering Journal, 184, 248–255.*

14. *Mohamed, M. A., W Salleh, W. N., Jaafar, J., Ismail, A. F., Abd Mutalib, M., Mohamad, A. B., M Zain, M. F., Awang, N. A., Mohd Hir, Z. A. (2017) Physicochemical characterization of cellulose nanocrystal and nanoporous self-assembled CNC membrane derived from Ceiba pentandra. Carbohydr Polym., 57, 1892-1902. doi: 10.1016/j.carbpol.2016.11.078.*

15. *Tseng, K-H., Chung, M-Y., Chang, C-Y., Cheng, T-S. (2017). A Study of Photocatalysis of Methylene Blue of TiO2 Fabricated by Electric Spark Discharge Method, Hindawi Journal of Nanomaterials, Volume 2017- 9346201, https://doi.org/10.1155/2017/9346201.*

16. *Hołysz, L., Rek, P., Huber, M. et al. (2024) Evaluation and comparison of various methods used for aggregates investigations, Adsorption, 30, 265–277. https://doi.org/10.1007/s10450-023-00393-z.*

17. *Tiandho, Y., Afriani, F., Evi, J. et al. (2021) Kinetic evaluation of methylene blue decolorization by CuO as a Fenton-like catalyst, IOP Conf. Ser.: Earth Environ. Sci., 926, 012103, doi:10.1088/1755-1315/926/1/012103.*

18. *Chatterjee, S., Kumar, A., Basu, B., Dutta, S. (2012) Application of Response Surface Methodology for Methylene Blue dye removal from aqueous solution using low cost adsorbent, Chemical Engineering Journal, vol. 181–182, pp. 289-299, https://doi.org/10.1016/j.cej.2011.11.081.*

EVALUATING BIODEGRADATION RATES IN NEAT PCL- AND PCL/PLA-BASED BIOCOMPATIBLE TUBULAR SCAFFOLDS

Janset Oztemur[1*], Suzan Ozdemir[1], Havva Tezcan-Unlu[2], Gulsah Cecener[2], Hande Sezgin[1], Ipek Yalcin-Enis[1]

[1]Textile Engineering Department, Istanbul Technical University, Istanbul, Turkey
[2] Department of Medical Biology, Faculty of Medicine, Bursa Uludag University, Bursa, Turkey
*oztemurj@itu.edu.tr

Abstract:

Vascular grafts are synthetic tubular structures that play an important role in replacing damaged vessels in the treatment of cardiovascular diseases. Existing grafts, especially in small-diameter vessels, face persistent issues such as thrombosis, immune rejection, and mechanical limitations. Vascular grafts designed with an innovative perspective to overcome these deficiencies are tubular scaffolds with a biodegradable structure and a layered design that mimics the native artery structure. This study focuses on the development of biodegradable and biocompatible tubular scaffolds with randomly distributed and radially oriented fibers in different layers to replicate the native structure of artery, utilizing neat polycaprolactone (PCL) and PCL/polylactic acid (PLA) blend with 4/1 polymer blend ratio. Electrospinning technique is employed to fabricate tubular fibrous structures. The biodegradation profiles of these scaffolds are assessed at 3, 6, and 9 months, with comparative analyses conducted to explore how polymer type and orientation level influence degradation rates and the structural integrity of the materials over time. The findings reveal that scaffolds with randomly distributed fibers exhibit higher biodegradation rates compared to those with oriented fibers, particularly in the PCL/PLA blends. Specifically, the study identifies PCL_R as having the highest degradation rate at 61% weight loss by the 9th month. Importantly, while PCL is known for its slow degradation, the high molecular weight of PLA leads to a slower degradation profile in the PCL/PLA samples. These insights underscore the critical role of scaffold morphology and composition in optimizing the performance and functionality of vascular grafts, highlighting the need for scaffolds that support cellular activities while effectively degrading to facilitate tissue regeneration without toxic effects.

Key words:

Polycaprolactone, polylactic acid, tissue engineering, electrospinning, biodegradability

1. Introduction

Tissue engineering aims to develop scaffolds that serve as effective substitutes for damaged tissues by facilitating biological activities and controlled biodegradation during tissue regeneration, while maintaining mechanical integrity [1]. The design of advanced biomaterials and the integration of implants with tissues are intricately linked to cell-scaffold interactions. Three-dimensional (3D) fibrous scaffolds that mimic the extracellular matrix (ECM) are essential, as they support critical cellular activities such as attachment, migration, proliferation, and differentiation necessary for tissue regeneration [2-3]. On the other hand, cardiovascular diseases have become a major health problem, causing high rates of death and disability worldwide. The inadequacy of autologous vessels and the problems such as mismatch, thrombosis and occlusion in small-diameter replacements of existing commercial grafts have triggered the need for tissue-engineered vascular grafts [4-6].

Biodegradable polymers offer considerable advantages over non-biodegradable materials by minimizing the need for surgical removal and reducing the necessity for long-term immunosuppressive treatments [7]. The design of biodegradable vascular grafts focuses on fostering the development of an autologous vessel concurrently with scaffold degradation. In particular, the formation of a regenerated structure that will replace the damaged vessel and the realization of endothelialization require a long-term process, and at this point the importance of biodegradability in vascular graft structures emerges. The biodegradability period of the vascular graft should be slow enough to allow time for new tissue formation, but it should not cause a toxic effect during this process [8]. This approach aims to address issues related to immunogenicity and thrombus formation by ensuring that the scaffold's degradation rate is synchronized with the rate of neovascularization [9]. The degradation kinetics of the scaffold are influenced by several factors, including the choice of polymer, production techniques, and scaffold architecture. Thus, achieving a balance between degradation and tissue regeneration is critical for maintaining the scaffold's mechanical properties and functional performance throughout the regenerative process. In this context, the choice of material becomes pivotal. Although synthetic polymers such as polyurethane (PU), poly(ethylene glycol) (PEG), poly(glycolic acid) (PGA), poly(lactic acid-co-glycolic acid) (PLGA), poly(vinyl alcohol) (PVA), PLA, poly(L-lactic acid-co-ε-caprolactone) (PLCL), and PCL exhibit varying biodegradation times, they are frequently preferred in tissue engineering applications due to their high strength and comparatively slow degradation rates relative to natural polymers [10]. Among these materials, PCL and PLA are particularly noteworthy for their biocompatibility, adjustable degradation rates, and mechanical properties, making them highly cited in the literature as preferred polymers in various vascular graft applications [11-14].

On the other hand, using layered structures in vascular grafts and designing each layer to mimic the native artery structure is important in terms of obtaining the desired physical, mechanical and biological properties [15]. In this context, at least a two-layer graft design is envisaged and the inner layer is produced with random fiber distribution to mimic the *tunica intima*, the inner most layer of an artery that is in contact with blood, while the outer layer contains fibers with radial orientation to mimic the *tunica media*, the middle layer of an artery responsible for mechanical features [16]. This structural property, in addition to the material type, has an impact on the biodegradable values of the grafts [17].

This study investigates the biodegradation behavior of biocompatible scaffolds designed for vascular graft application. Utilizing electrospinning techniques, tubular scaffolds with randomly distributed and radially oriented fibers made from both neat PCL and PCL/PLA blend are developed. The biodegradation of these scaffolds is assessed over 3, 6, and 9 months. The biodegradability rates of the developed scaffolds are discussed comparatively, taking into account PLA addition and fiber orientation.

2. Experimental

2.1. Materials

PCL (Mn 80,000), PLA (Mn 230,000; Ingeo 2003 D with 4.3 mol% D-lactide content), and the components of solvent systems (chloroform (CHL), ethanol (ETH), and acetic acid (AA)) are supplied from Sigma Aldrich.

2.2. Methods

Scaffold fabrication

Neat PCL and PCL/PLA blend are dissolved in CHL/ETH/AA (8/1/1 wt.) solvent system, and polymer concentrations are kept constant at 8%. Blend ratio is selected as 4/1 by weight for PCL/PLA. Each polymer solution system is stirred for 2 hours at room temperature. Tubular structures with 6 mm diameter are fabricated using electrospinning set-up with a custom designed rotating feeding unit (Nanospinner, Basic System, Inovenso, Turkey). Scaffolds are produced at 200 rpm for randomly distributed fibers and 10,000 rpm for randomly oriented fibers. Randomly distributed fibers are indicated with the suffix _R, whereas surfaces with oriented fibers are denoted with the suffix _O.

Scaffold Sterilization

Samples are sterilized by washing once in 70% ethanol, followed by three rinses in sterile phosphate buffered saline (PBS). The fibrous webs are then exposed to UV light for 30 minutes on both sides. All UV sterilization processes are conducted in a laminar flow cabinet.

Biodegradation Analysis

Sterilized surfaces are cut into 1x1 cm pieces, with measurements taken at 3rd, 6th, and 9th months. Initial weights are recorded using a precision balance. The samples are placed in 24-well plates with 300 μl of PBS and incubated at 37°C in a 5% CO_2 humidified incubator (Panasonic, Osaka, Japan). Degradation rates are determined by measuring the mass loss of the samples over the 9-month period.

3. Results

The biodegradation results of fibrous samples featuring randomly distributed and oriented fibers are presented in Figures 1 and 2. It is observed that scaffolds with randomly distributed fibers degrade more rapidly than samples with aligned fibers, owing to their loosely packed structure. The densely packed arrangement of the scaffolds, together with aligned fibers, establishes a barrier that impedes PBS penetration, thereby effectively decelerating the degradation process [18]. In the present study, it is noted that in both sample groups—PCL and PCL/PLA—the surfaces with randomly distributed fibers exhibited higher degradation rates, especially at the 6th and 9th months, compared to samples with radially orientated fibers. In a 12-month biodegradation assessment, Oztemur et al. (2024) observed that electrospun PCL surfaces with randomly distributed fibers displayed a relatively higher degree of degradation than their aligned fiber counterparts [16]. Similarly, Mirzaei et al. (2020), in a study utilizing blends of polyethylene oxide (PEO) and PCL, found that by the 7th day, surfaces with randomly distributed fibers demonstrated a slightly higher degradation rate, independent of the blending ratio [19].
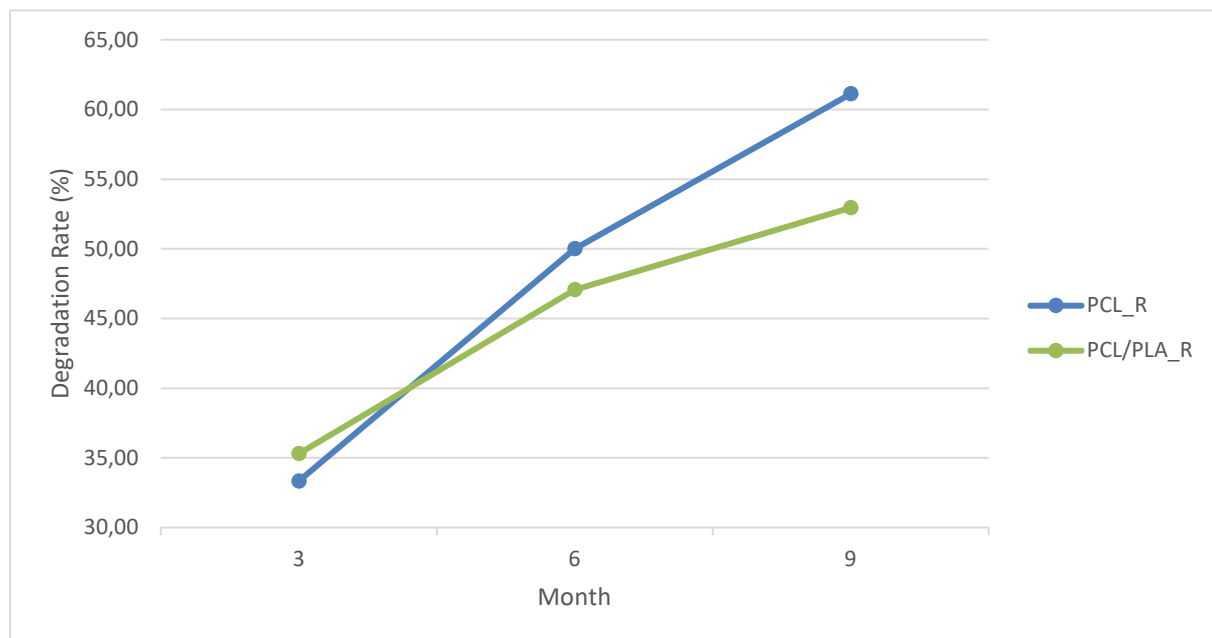
Figure 1. Biodegradation rates of PCL_R and PCL/PLA_R scaffolds

From a material-centered perspective, when the sample groups are compared, it is observed that both the scaffolds with randomly distributed fibers and those with radial orientation exhibit similar degradation rates within the initial 3 months. PCL degradation primarily occurs through the hydrolytic cleavage of ester bonds, which is generally a slow process taking approximately two to three years [20]; however,

in the present study, PCL_R displays a more rapid degradation trend by the 6th and 9th months. This accelerated degradation rate in the PCL sample may be attributed to its substantially lower molecular weight in comparison to PLA. Molecular weight is a crucial factor in the hydrolytic degradation rate of polymers; higher molecular weights are known to correspond to a more stable degradation rate. Conversely, when molecular weight decreases below a specific threshold, degradation accelerates due to increased molecular mobility, a greater presence of hydrophilic groups, and enhanced water diffusion [19]. Additionally, among the radially oriented samples, while PCL_O exhibits a significant increase in degradation rate from the 3rd to the 6th month in comparison to PCL/PLA_O, by the end of the 9th month, both PCL_O and PCL/PLA_O have reached comparable values, with degradation rates of 47% and 46%, respectively.
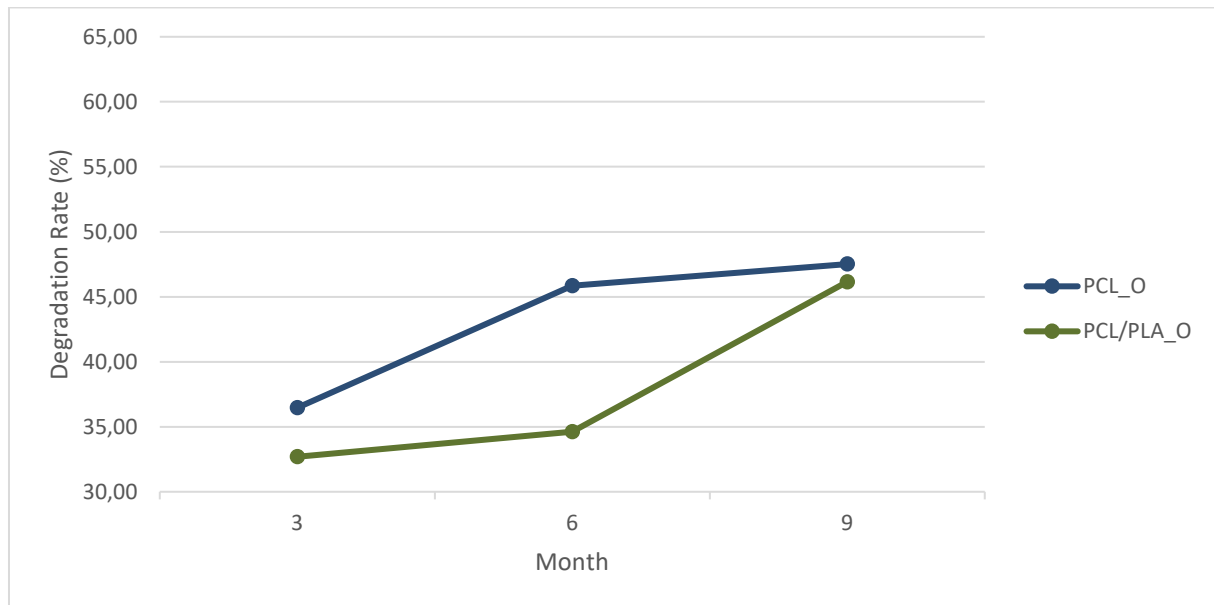
Figure 2. Biodegradation rates of PCL_O and PCL/PLA_O scaffolds

4. Conclusion

In this study, the influence of fiber orientation and material type on the biodegradation profiles of electrospun scaffolds is evaluated to refine scaffold design for enhanced control over degradation kinetics in tissue engineering applications specifically, in vascular grafts. Through an analysis of fiber alignment and molecular weight variations, the study offers critical insights for optimizing scaffold composition to achieve precise biocompatibility and functional longevity in targeted biomedical applications. In this context, it is necessary to emphasize the following points as the key outcomes of the study:

- Fiber orientation significantly influences biodegradation behavior, with PCL_R and PCL/PLA_R, which possess randomly distributed fibers, exhibiting greater degradation compared to the oriented fiber counterparts, PCL_O and PCL/PLA_O, by the end of the 9-month period.
- Among all samples, PCL_R demonstrated the highest degradation rate at 61% weight loss by the end of the 9th month.
- Although PCL is generally recognized as a relatively slow-degrading biopolymer, the high molecular weight of PLA utilized in the PCL/PLA sample groups resulted in slower degradation rates in this study.

ACKNOWLEDGEMENTS

References

1. *Liu, S., Qin, S., He, M., Zhou, D., Qin, Q., & Wang, H. (2020). Current applications of poly (lactic acid) composites in tissue engineering and drug delivery. Composites Part B, 199(December 2019), 108238. https://doi.org/10.1016/j.compositesb.2020.108238*

2. *Ermis, M., Antmen, E., & Hasirci, V. (2018). Bioactive Materials Micro and Nanofabrication methods to control cell-substrate interactions and cell behavior : A review from the tissue engineering perspective. Bioactive Materials, 3(3), 355–369. https://doi.org/10.1016/j.bioactmat.2018.05.005*

3. *Hao, D., Lopez, J., Chen, J., Iavorovschi, A. M., Lelivelt, N. M., & Wang, A. (2022). Engineering Extracellular Microenvironment for Tissue Regeneration. Bioengineering, 9, 1–17.*

4. *Daum, R., Visser, D., Wild, C., Kutuzova, L., Schneider, M., Lorenz, G., Weiss, M., Hinderer, S., Stock, U. A., Seifert, M., & Schenke-Layland, K. (2020). Fibronectin Adsorption on Electrospun Synthetic Vascular Grafts Attracts Endothelial Progenitor Cells and Promotes Endothelialization in Dynamic In Vitro Culture. Cells, 9(3). https://doi.org/10.3390/cells9030778*

5. *Loh, Q. L., & Choong, C. (2013). Three-dimensional scaffolds for tissue engineering applications: Role of porosity and pore size. Tissue Engineering - Part B: Reviews, 19(6), 485–502. https://doi.org/10.1089/ten.teb.2012.0437*

6. *Vaduganathan, M., Mensah, G. A., Turco, J. V., Fuster, V., & Roth, G. A. (2022). The Global Burden of Cardiovascular Diseases and Risk: A Compass for Future Health. Journal of the American College of Cardiology, 80(25). https://doi.org/10.1016/j.jacc.2022.11.005*

7. *Hartley, E. (2022). Biodegradable Synthetic Polymers for Tissue Engineering : A Mini-Review. Reinvention, 15, 48–70.*

8. *Fukunishi, T., Best, C. A., Sugiura, T., Shoji, T., & Yi, T. (2016). Tissue-Engineered Small Diameter Arterial Vascular Grafts from Cell-Free Nanofiber PCL / Chitosan Scaffolds in a Sheep Model. PLoS ONE, 11(7), 1–15. https://doi.org/10.1371/journal.pone.0158555*

9. *Wu, J., Hu, C., Tang, Z., Yu, Q., Liu, X., & Chen, H. (2018). Tissue-engineered Vascular Grafts: Balance of the Four Major Requirements. Colloids and Interface Science Communications, 23(February), 34–44. https://doi.org/10.1016/j.colcom.2018.01.005*

10. *Sankaran, K. K., Krishnan, U. M., & Sethuraman, S. (2014). Axially aligned 3D nanofibrous grafts of PLA-PCL for small diameter cardiovascular applications. Journal of Biomaterials Science, Polymer Edition, 25(16), 1791–1812. https://doi.org/10.1080/09205063.2014.950505*

11. *Li, C., Wang, F., Ge, P., Mao, Y., & Wang, L. (2017). Anti-acute thrombogenic surface using coaxial electrospraying coating for vascular graft application. Materials Letters, 205, 15–19. https://doi.org/10.1016/j.matlet.2017.06.050*

12. *Liu, K., Wang, N., Wang, W., Shi, L., Li, H., Guo, F., Zhang, L., Kong, L., Wang, S., & Zhao, Y. (2017). A bio-inspired high strength three-layer nanofiber vascular graft with structure guided cell growth. Journal of Materials Chemistry B, 5(20), 3758–3764. https://doi.org/10.1039/c7tb00465f*

13. *Ozdemir, S., Oztemur, J., Sezgin, H., & Yalcin-enis, I. (2023). Optimization of Electrospun Bilayer Vascular Grafts through Assessment of the Mechanical Properties of Monolayers. ACS Biomaterials Science and Engineering. https://doi.org/10.1021/acsbiomaterials.3c01161*

14. *Sankaran, K. K., Krishnan, U. M., & Sethuraman, S. (2014). Axially aligned 3D nanofibrous grafts of PLA-PCL for small diameter cardiovascular applications. Journal of Biomaterials Science, Polymer Edition, 25(16), 1791–1812. https://doi.org/10.1080/09205063.2014.950505*

15. *Enis, I. Y., Sadikoglu, T. G., Horakova, J., & Lukas, D. (2018). The post-morphological analysis of electrospun vascular grafts following mechanical testing. Journal of Polymer Engineering, 38(6), 525–535. https://doi.org/10.1515/polyeng-2017-0157*

16. *Ozdemir, S., Yalcin-Enis, I., Yalcinkaya, B., & Yalcinkaya, F. (2022). An Investigation of the Constructional Design Components Affecting the Mechanical Response and Cellular Activity of*

Electrospun Vascular Grafts. Membranes, 12(10), 929.
https://doi.org/10.3390/membranes12100929

17. *Oztemur, J., Ozdemir, S., Tezcan-unlu, H., Cecener, G., Sezgin, H., & Yalcin-Enis, I. (2023). Investigation of biodegradability and cellular activity of PCL / PLA and PCL / PLLA electrospun webs for tissue engineering applications. Biopolymers, 1–10. https://doi.org/10.1002/bip.23564*

18. *Subramanian, A., Krishnan, U. M., & Sethuraman, S. (2012). Axially aligned electrically conducting biodegradable nanofibers for neural regeneration. Journal of Materials Science: Materials in Medicine, 23(7), 1797–1809. https://doi.org/10.1007/s10856-012-4654-y*

19. *Oztemur, J., Ozdemir, S., Tezcan-Unlu, H., Cecener, G., Dogruok, Y.S., Hockenberger, A., Yalcin-Enis, I. (2024). Static and Dynamic Cell Culture of Small Caliber Bilayer Vascular Grafts Electrospun from Polycaprolactone. International Journal of Polymeric Materials and Polymeric Biomaterials. https://doi.org/10.1080/00914037.2024.2421837*

20. *Mirzaei, Z., S. Kordestani, S., Kuth, S., Schubert, D. W., Detsch, R., Roether, J. A., … Boccaccini, A. R. (2020). Preparation and Characterization of Electrospun Blend Fibrous Polyethylene Oxide:Polycaprolactone Scaffolds to Promote Cartilage Regeneration. Advanced Engineering Materials, 22(9), 1–12. https://doi.org/10.1002/adem.202000131*

21. *Cipitria, A., Skelton, A., Dargaville, T. R., Dalton, P. D., & Hutmacher, D. W. (2011). Design, fabrication and characterization of PCL electrospun scaffolds - A review. Journal of Materials Chemistry, 21(26), 9419–9453. https://doi.org/10.1039/c0jm04502k*

22. *Gorrasi, G., Pantani, R. (2017). Hydrolysis and Biodegradation of Poly(lactic acid). In: Di Lorenzo, M., Androsch, R. (eds) Synthesis, Structure and Properties of Poly(lactic acid). Advances in Polymer Science, vol 279. Springer, Cham. https://doi.org/10.1007/12_2016_12*

SUTURE RETENTION STRENGTH OF BILAYER VASCULAR GRAFTS MADE OF PCL, PLA AND THEIR COPOLYMER

Suzan Ozdemir[1],*, Janset Oztemur[1], Atıf Yolgosteren[2], Hande Sezgin[1] and Ipek Yalcin Enis[1]

[1]Istanbul Technical University, Textile Engineering Department, Istanbul, Turkey
[2]Bursa Uludag University, Cardiovascular Surgery, Bursa, Turkey
*ozdemirsu@itu.edu.tr

Abstract:

The mechanical characteristics of small-diameter vascular grafts, including factors like modulus, elasticity, compliance, burst strength, and suture retention strength, need to be in line with those of native blood vessels. Even a slight mismatch in mechanical properties between the graft and the native vessel can lead to graft failure. Suture retention strength, a critical mechanical aspect, represents the force needed to remove a stitch from the graft or cause the graft wall to rupture. This property is vital for preventing leaks, maintaining proper blood flow, aiding tissue healing, ensuring long-term durability, and reducing complications in vascular grafts. In this study, bilayered vascular grafts are fabricated by electrospinning using polycaprolactone (PCL), poly (lactic acid) (PLA), and poly(l-lactide-co-caprolactone) (PLCL) polymers. The actual suturing conditions of vascular scaffolds are simulated and how the choice of polymer for the inner layer affects suture retention strength is assessed. At the post-mechanical stage, the morphologies of the scaffolds are investigated to gain a clearer understanding of how the material reacts to applied forces. The findings reveal that all the fabricated bilayer vascular scaffolds exhibit excellent suture performance, with strength values exceeding 10 N, and that polymer selection for the inner layer for the grafts significantly influences the results. Blending PCL and PLA in the inner layer is found to reduce suture retention strength, while using neat polymers results in better retention strength. This experiment offers a more precise assessment of suture retention strength for bilayer vascular grafts, facilitating further optimization of tissue-engineered grafts to meet specific mechanical requirements.

Key words:

suture retention strength, vascular grafts, blood vessels, tissue engineering

1. Introduction

Currently, due to global aging, cardiovascular disease (CVD) causes 17.3 million deaths each year, and this number is projected to rise to over 23.6 million by 2030 [1]. One of the most preferred treatments for cardiovascular diseases is graft bypass surgery using autologous blood vessels, allogenic blood vessels, or artificial blood vessels [2]. At present, various commercial artificial blood vessels made from synthetic materials like Dacron and e-PTFE are widely used for vascular replacement. However, these artificial grafts are nondegradable and often elicit long-term foreign-body responses [3]. In recent years, due to the collaborative efforts of researchers worldwide, tissue engineering vascular grafts (TEVGs) have made significant advancements. Large-diameter artificial blood vessels (greater than 6 mm) have shown considerable therapeutic success in clinical settings. However, it is unfortunate that small-diameter artificial vascular grafts (less than 6 mm), such as those used for inguinal and coronary artery transplants, have not yet achieved satisfactory outcomes [4]. Electrospinning is a well-established technique for creating customized vascular grafts. This process enables the fine-tuning of the

mechanical properties of the final product. By using various materials, making micro- and macrostructural modifications, incorporating additives, and altering the electrospinning process, the mechanical properties can be adjusted and optimized [5]. Designing multi-layered electrospun vascular scaffolds is regarded as an effective method to replicate the structure and function of natural blood vessels [6].

Researchers have emphasized that the graft must be resilient and possess mechanical strength comparable to that of native vessels [7]. An ideal TEVG should have properties similar to those of the native artery and integrate seamlessly with it, as any disparity in mechanical properties between the TEVG and adjacent blood vessels can lead to graft rupture or blood leakage. TEVGs must withstand distortion and compression, possess adequate tensile and shear strength to endure the forces exerted during suturing and implantation, and maintain circumferential strength to resist hemodynamic pressure. This ensures the prosthesis avoids rupture, scattering, edge wear, seam tearing, and retains structural integrity [8]. The mechanical properties of electrospun fibers are heavily influenced by the raw materials used [1]. Recently, researchers have shown significant interest in synthetic biomaterials like PCL, PLA, and their copolymers to address the mechanical limitations observed in natural biopolymers [9]. Because of its exceptional biocompatibility, moderate degradation rate, and demonstrated tensile strength and elongation capabilities, PCL is highly recommended as a biodegradable polymer for developing vascular grafts. Additionally, PLA is favored in biomedical applications for its excellent mechanical strength and modulus, biocompatibility, rapid biodegradation, lack of toxicity, and composition derived from aliphatic bio-based sources [10].

In clinical applications, the suture retention strength typically determines the reliability of the anastomosis [11]. The suture retention strength assessment measures the force needed to tear a suture from a scaffold or cause rupture of the scaffold wall. It is noted that the human saphenous vein has an suture retention strength of 1.81 ± 0.02 N [12]. Thus, there have been many research attempts to examine the suture retention strength of vascular grafts along with other mechanical features. The study by Kim et al. (2013) focused on fabricating a tubular double-layered scaffold using the PLCL gel spinning method and salt leaching. Suture retention strength tests were conducted on PLCL scaffolds with different thicknesses (ranging from 1 mm to 1.5 mm) and compared to ePTFE grafts. The results showed no significant difference in suture retention strength between the PLCL scaffolds and ePTFE grafts. Suture retention strength values for PLCL scaffolds with varying thicknesses ranged from 5.89 N to 10.28 N [13]. In another study, Meng et al. (2019) investigated the suture retention strength of P(LLA-CL) tissue-engineered vascular grafts. The results demonstrated that P(LLA-CL) tissue-engineered vascular scaffolds exhibited excellent suture performance. The study also emphasized the influence of fiber direction and number of stitches on suture retention strength. Specifically, the highest suture retention strength, ranging between 2 and 2.5 N, was observed when the suture was perpendicular to the fibers (in the circumferential direction) [8].

This study aims to create bilayered vascular grafts through electrospinning with different polymers (PCL, PLA, PLCL), simulate suturing conditions, and evaluate how the choice of inner layer polymer affects suture retention strength. Post-mechanical testing examines scaffold morphologies under stress. Results indicate that all grafts exhibit strong suture performance (>10 N), with significant variation depending on inner layer polymer. Blending PCL and PLA lowers retention strength compared to using neat PCL.

2. Experimental
2.1. Materials

PCL (Mw 80,000), PLA (Mw 230,000), and PLCL are utilized as the polymers. The solvent system includes chloroform (CH), acetic acid (AA), and ethanol (ETH). All polymers and solvents are procured from Sigma Aldrich.

2.2. *Methods*

Bilayer scaffold fabrication

To create bilayer tubular scaffolds with fibers that are either randomly distributed or radially oriented, PCL, PLA, and PLCL polymers are dissolved in a CHL/ETH/AA mixture (with a weight ratio of 8/1/1). The samples codes and blending ratios are provided in Table 1. PCL and PLA solutions are prepared in both pure and blended forms, while PLCL is used in its pure form. The blending ratio is adjusted in 10% increments, ranging from 80% to 100%. The polymer concentration for pure PCL, as well as PCL-PLA blends, is maintained at 8%, whereas PLCL solutions are at 10%. PLCL is utilized for the outer layers of all scaffolds, while the inner layer employs both neat and blended fibrous surfaces to examine their impact on suture retention strength.

A custom-built electrospinning unit, equipped with a vertical feeding direction and a closed chamber from Inovenso, Turkey (Nanospinner, Ne100+), is used to fabricate the tubular scaffolds from PCL, PLA, and PLCL polymers. The neat and blended polymer solutions are delivered using a 10 ml plastic syringe pump at a controlled flow rate of 3±1 ml/h. They are subjected to an electric potential of 11 ± 1 kV over a distance from the needle tip, with an inner diameter of 0.6 mm, to a collector positioned 20 cm away. Tubular vascular grafts are produced using rotating rod collectors with a 5 mm diameter. The rotation speeds applied are 200 rpm for randomly distributed fibers (inner layer) and 10,000 rpm for radially oriented fibers (outer layer). The production time is set at 20 minutes for the inner layer and 55 minutes for the outer layer.

Table 1. Sample codes and blending ratios

Samples	PCL/PLA blending ratio
PCL_R+PLCL_O	100/0
PCLPLA90_R+PLCL_O	90/10
PCLPLA80_R+PLCL_O	80/20

Scanning Electron Microscope (SEM) Analysis

The morphology of the scaffolds is examined using FEI Quanta FEG 250 SEM after conducting suture retention tests. The samples are coated with a gold-palladium (Au-Pd) alloy in a sputter coating machine (Quorum SC7620) for observation.

Suture retention strength

To test the suture strength of the developed bilayer grafts, the grafts are cut into tubular pieces 1 cm in length, and two graft pieces are joined using continuous stitching, with 7/0 monofilament polypropylene thread applied to a standard vessel during surgery (Figure 1). The strength of the sutures in the scaffolds is evaluated by employing a Zwick-Roell Z005 universal testing machine fitted with a 200N load cell. The tubular segments, after being sewn, undergo testing in longitudinal direction. This examination is conducted at a cross-head speed of 10 mm/min and a gauge distance of 5 mm.

Figure 1. Images of the polypropylene thread used for stitching and the surfaces sewn with continuous stitching

3. Results and discussion

SEM Analysis

SEM images of bilayer samples after suture retention strength can be seen in Fig. 2. When the suture areas are examined, it is seen that although the samples are damaged, they are not completely torn and are only opened from the seam areas.
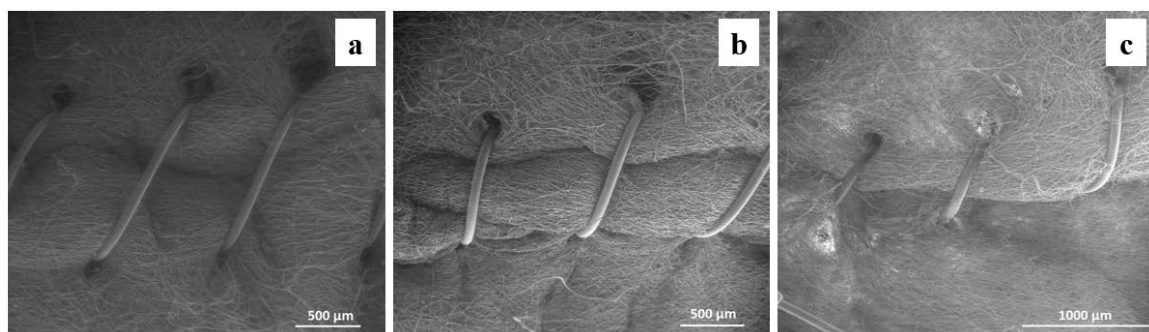
Figure 2. SEM images at 100x magnification of samples (a) PCL_R+PLCL_O, (b) PCLPLA90_R+PLCL_O, and (c) PCLPLA80_R+PLCL_O.

Suture retention strength

Suture retention strength results are presented in Table 2. Upon examination, it is observed that the suture strength values of all samples fell within the range of approximately 11-16 N. This indicates superior results compared to the human saphenous vein, which typically exhibits suture retention strength between 2-3 N, known as the gold standard [14]. Furthermore, the highest suture retention strength is observed in the sample using neat PCL in the inner layer. In samples where PCL and PLA are blended, a decrease in results is noted with increasing PLA ratio. This decrease can be attributed to reduced mechanical integrity of the grafts, stemming from the immiscibility of PCL and PLA polymers, as well as increased incompatibility between the inner and outer layers due to blending polymers in the inner layer [10]. Phase separation results from the weak adhesion forces between the polymer chains in these scaffolds during the electrospinning process, which prevents the blending from being adequately achieved [15].

Table 2. Suture retention strength results of bilayer samples

Samples	Suture retention strength (N)
PCL_R+PLCL_O	15.81 ± 4.06
PCLPLA90_R+PLCL_O	14.00 ± 3.47
PCLPLA80_R+PLCL_O	11.50 ± 0.63

4. CONCLUSIONS

Based on the findings of this study, it is evident that the suture retention strength of bilayered vascular grafts is critically influenced by the choice of polymers used in the inner layer. The experiments demonstrated that grafts utilizing neat PCL in the inner layer exhibited superior suture retention strength compared to those incorporating PCL-PLA blends. The observed decrease in strength with increasing PLA content highlights the challenges posed by polymer immiscibility and phase separation during fabrication. SEM analysis further supported these findings, revealing structural integrity despite damage at suture sites. These insights underscore the importance of careful polymer selection and processing methods in optimizing the mechanical properties of vascular grafts for enhanced durability and clinical efficacy. Future research should focus on refining polymer blending and graft construction to better align with the demanding mechanical requirements of vascular applications.

References

1. *Maleki, S.; Shamloo, A.; Kalantarnia, F. Tubular TPU/SF Nanofibers Covered with Chitosan-Based Hydrogels as Small-Diameter Vascular Grafts with Enhanced Mechanical Properties. Sci Rep, 2022, 12 (1). https://doi.org/10.1038/s41598-022-10264-2.*
2. *Li, M. X.; Wei, Q. Q.; Mo, H. L.; Ren, Y.; Zhang, W.; Lu, H. J.; Joung, Y. K. Challenges and Advances in Materials and Fabrication Technologies of Small-Diameter Vascular Grafts. Biomaterials Research. BioMed Central Ltd December 1, 2023. https://doi.org/10.1186/s40824-023-00399-2.*
3. *Jia, W.; Li, M.; Weng, H.; Gu, G.; Chen, Z. Design and Comprehensive Assessment of a Biomimetic Tri-Layer Tubular Scaffold via Biodegradable Polymers for Vascular Tissue Engineering Applications. Materials Science and Engineering C, 2020, 110. https://doi.org/10.1016/j.msec.2020.110717.*
4. *Yang, L.; Li, X.; Wu, Y.; Du, P.; Sun, L.; Yu, Z.; Song, S.; Yin, J.; Ma, X.; Jing, C.; et al. Preparation of Pu/Fibrin Vascular Scaffold with Good Biomechanical Properties and Evaluation of Its Performance in Vitro and in Vivo. Int J Nanomedicine, 2020, 15, 8697–8715. https://doi.org/10.2147/IJN.S274459.*
5. *Stoiber, M.; Grasl, C.; Frieberger, K.; Moscato, F.; Bergmeister, H.; Schima, H. Impact of the Testing Protocol on the Mechanical Characterization of Small Diameter Electrospun Vascular Grafts: Dynamic Testing of Electrospun Small Diameter Vascular Grafts. J Mech Behav Biomed Mater, 2020, 104. https://doi.org/10.1016/j.jmbbm.2020.103652.*
6. *Do, T. M.; Yang, Y.; Deng, A. Porous Bilayer Vascular Grafts Fabricated from Electrospinning of the Recombinant Human Collagen (Rhc) Peptide-Based Blend. Polymers (Basel), 2021, 13 (22). https://doi.org/10.3390/polym13224042.*

7. *Liu, D.; Han, J.; Zhuang, X.; Gao, Y.; Wang, W.; Qin, D.; Dong, X. Evaluation of Mechanical Properties and Biocompatibility of Three-Layer PCL/PLLA Small-Diameter Vascular Graft with Pore Diameter Gradient. Eur Polym J, 2023, 186. https://doi.org/10.1016/j.eurpolymj.2023.111864.*

8. *Meng, X.; Wang, X.; Jiang, Y.; Zhang, B.; Li, K.; Li, Q. Suture Retention Strength of P(LLA-CL) Tissue-Engineered Vascular Grafts. RSC Adv, 2019, 9 (37), 21258–21264. https://doi.org/10.1039/c9ra04529e.*

9. *Ozdemir, S.; Oztemur, J.; Sezgin, H.; Yalcin-Enis, I. Optimization of Electrospun Bilayer Vascular Grafts through Assessment of the Mechanical Properties of Monolayers. ACS Biomater Sci Eng, 2023. https://doi.org/10.1021/acsbiomaterials.3c01161.*

10. *Ozdemir, S.; Oztemur, J.; Sezgin, H.; Yalcin-Enis, I. Structural Design and Mechanical Analysis of Small-Caliber Bilayer Vascular Prostheses. International Journal of Polymeric Materials and Polymeric Biomaterials, 2024. https://doi.org/10.1080/00914037.2024.2325968.*

11. *Zhang, F.; Bambharoliya, T.; Xie, Y.; Liu, L.; Celik, H.; Wang, L.; Akkus, O.; King, M. W. A Hybrid Vascular Graft Harnessing the Superior Mechanical Properties of Synthetic Fibers and the Biological Performance of Collagen Filaments. Materials Science and Engineering C, 2021, 118. https://doi.org/10.1016/j.msec.2020.111418.*

12. *Montini-Ballarin, F.; Abraham, G. A.; Caracciolo, P. C. Mechanical Behavior of Polyurethane-Based Small-Diameter Vascular Grafts. In Advances in Polyurethane Biomaterials; Elsevier Inc., 2016; pp 451–477. https://doi.org/10.1016/B978-0-08-100614-6.00015-9.*

13. *Kim, S. H.; Mun, C. H.; Jung, Y.; Kim, S. H.; Kim, D. I.; Kim, S. H. Mechanical Properties of Compliant Double Layered Poly(L-Lactide-Co-ε- Caprolactone) Vascular Graft. Macromol Res, 2013, 21 (8), 886–891. https://doi.org/10.1007/s13233-013-1095-5.*

14. *Rodriguez, M.; Kluge, J. A.; Smoot, D.; Kluge, M. A.; Schmidt, D. F.; Paetsch, C. R.; Kim, P. S.; Kaplan, D. L. Fabricating Mechanically Improved Silk-Based Vascular Grafts by Solution Control of the Gel-Spinning Process. Biomaterials, 2020, 230. https://doi.org/10.1016/j.biomaterials.2019.119567.*

15. *Carvalho, J. R. G.; Conde, G.; Antonioli, M. L.; Dias, P. P.; Vasconcelos, R. O.; Taboga, S. R.; Canola, P. A.; Chinelatto, M. A.; Pereira, G. T.; Ferraz, G. C. Biocompatibility and Biodegradation of Poly(Lactic Acid) (PLA) and an Immiscible PLA/Poly(ε-Caprolactone) (PCL) Blend Compatibilized by Poly(ε-Caprolactone-b-Tetrahydrofuran) Implanted in Horses. Polym J, 2020, 52 (6), 629–643. https://doi.org/10.1038/s41428-020-0308-y.*

INVESTIGATION OF THE PRODUCTION OF TRICLOSAN/CHITOSAN NANOCAPSULES FOR FUNCTIONAL SURFACE APPLICATIONS

Mehmet Dasdemir[1,2], Serap Gamze Serdar[2*], Hatice Ibili[2]

[1]The Nonwovens Institute, North Carolina State University, Raleigh, NC 27606, USA

[2]Gaziantep University, Textile Engineering Department, Gaziantep, 27310, Türkiye

[*]corresponding author e-mail: sgserdar@gantep.edu.tr

Abstract:

This study focuses on producing monodisperse nanocapsules with a triclosan/chitosan core-shell structure using the coaxial electrospray method. The coaxial electrospraying method enables the production of core/shell structured nanocapsules in a single step. The effects of flow rate, core-to-shell flow rate ratio, and needle size on the coaxial electrospray process were systematically analyzed. The resulting nanocapsule structures were characterized using scanning electron microscope (SEM), transmission electron microscope (TEM) and size measurements. The experiments demonstrated that fibrillation more likely occurred when the chitosan content was highest.

Key words:

Coaxial electrospray, encapsulation, chitosan, triclosan

1. Introduction

Chitosan (CS), a natural polysaccharide-based biopolymer derived from chitin deacetylation. It has diverse applications in drug delivery, tissue engineering, encapsulation, nano- and microparticle formation, plant protection thanks to its biocompatibility, biodegradability, low toxicity, and antibacterial properties [1–4]. Triclosan (Irgasan), another widely used antibacterial agent, is often applied on synthetic fibers like polyester, polypropylene, nylon, cellulose acetate, and acrylic, and is valued for its durability during washing [5,6]. It can be applied on textile material by several application methods, exhaustion during or after dyeing, pad-dry-cure and melt mixing [7]. Electrospraying is increasingly recognized as an advanced method for encapsulating sensitive bioactives with minimal damage or structural loss [1,8]. Coaxial electrospraying is also a one-stage process given in multiple studies to capsulate varied materials [9–11]. Nano- and microparticles provide larger surface area and consequently allows greater bioavailability of the encapsulated substances. Several studies reported that both solution parameters as well as process parameters directly affect particle size and formation [1].

Because of chitosan's cost-effectiveness, non-toxicity, antibacterial properties, and compatibility with biological systems, it is viewed as an ideal encapsulating agent for textile applications [12]. Several methods can be used for the formation of chitosan micro- and nanospheres, including solvent evaporation, coacervation/precipitation, ionic gelation and spray drying [13]. For microencapsulation process, techniques such as emulsification, spray drying, coaxial electrospray systems, freeze-drying, coacervation, in situ polymerization, extrusion, fluidized-bed coating, and supercritical fluid technology can be utilized [12]. Cotton fabric was treated with antimicrobial peptides encapsulated in alginate-chitosan microcapsules, for potential textile applications [14]. O. sanctum leaf extract was encapsulated in chitosan and applied to cotton garments, showed exceptional antibacterial activity and wash durability [15]. Hui et al. [16] microencapsulated Traditional Chinese Herbs in chitosan–sodium alginate blend matrix and grafted onto the cotton fabric's surface for the clinical treatment of atopic dermatitis. Another study reported excellent antimicrobial efficacy of electrosprayed chitosan onto wool surface [17].

Triclosan loaded chitosan and alginate-based microcapsules have been used for coating applications in surfaces such as textiles or plastics [18]. Santos Alves de Lima [5] investigated these microcapsules using 2.5 wt% to 3 wt% of triclosan in both shell and core structures produced through emulsification method. These microcapsules were aimed for future applications in antibacterial textiles and other materials such as medical device materials and plastics [18–21]. For antibacterial purposes, triclosan, silver and chitosan were used via pad-dry-cure method and showed significant performance against Gram-positive and Gram-negative bacteria [22]. Ouerghemmi et al. [23] focused on the manufacture of core-sheath nanofibers (NFs) based on chitosan (CHT) as sheath and cyclodextrin polymer (PCD)/triclosan as core triclosan using coaxial electrospinning method. They investigated the nanofibrous structure. This study, differing from previous researches, aims to produce monodisperse distributed nanocapsules with a triclosan/chitosan core/shell structure using the coaxial electrospray method. The influences of flow rate, core/shell flow rate ratio, and needle size on the coaxial electrospray process, which facilitates single-step production, were systematically investigated. The resulting nanocapsule structures were characterized through SEM images, TEM images and size measurements.

2. Experimental
2.1. _Materials_

Chitosan polymer was purchased from Sigma Aldrich (448869, low molecular weight; DDA ≤75.0%). Acetic acid (Merck & Co., Inc.) was used as solvent for chitosan. Chitosan solutions were prepared according to weight/volume percent (wt/v%) which was the ratio of solute quantity as volume in 100 unit of solution. Chitosan solutions were prepared by dissolving chitosan polymer (2 wt/v%) in acetic acid, 90/10 v/v% acetic acid/distilled water. Triclosan was purchased from Sigma Aldrich (72779, ≥97.0%). Ethanol (Merck & Co., Inc.) was used as solvent for triclosan. Triclosan solutions were prepared by (1 wt/v%) in 50/50 v/v% ethanol/distilled water.

2.2. _Methods_

The coaxial electrospraying process was carried out using a vertically arranged electrospraying setup which consists of a high voltage power supply (Gamma High Voltage Series ES100P), a syringe pump (New Era NE-1000X), a nozzle, and a grounded collector. Chitosan solution is fed from the outer needle tip while the triclosan solution is fed from inner needle tip through dual syringe pumps via micro pumps. The resulting samples were collected on aluminum foil (200x200 mm) placed over the grounded plate. The coaxial electrospraying application is carried out at 2.5 kV.cm^{-1} electrical field, 8 cm distance between the needle and collector for 5 min. Different co-fluids flow rates are studied throughout the study. First, total flow rates are arranged as 5 µl.min^{-1}, 10 µl.min^{-1}, 20 µl.min^{-1}, and 40 µl.min^{-1}. Different coaxial needle sizes were also investigated. Moreover, varied core/shell flow rates are studied as 25/75%, 50/50% and 75/25% for 10 µl.min^{-1} total flow rate.

Co-axial electrosprayed nanocapsules were examined with SEM (JEOL JSM 6390) for determining morphology. Before SEM investigation, samples were coated with Au/Pd in SC 7620 Sputter Coater. SEM pictures were taken at 5-20 kV accelerating voltage and 12-15 mm working distance with magnifications between 100 and 5000. MALVERN Zetasizer Nano ZS was also used to determine the dimension of nanocapsules. Transmission electron microscopy (TEM, FEI Tecnai G2 F30) was used to reach a high-level resolution for identification of nanocapsules' formation. Electrosprayed nanocapsules were collected onto Cu grids during co-electrospraying.

3. Results and discussion
3.1. _Effects of Total Flow Rates on Chitosan Nanocapsule Formation_

To investigate the effect of total flow rate on the formation of chitosan/triclosan nanocapsules, four different total flow rates were determined; 5 µl.min^{-1}(2.75/2.25), 10 µl.min^{-1} (5.5/4.5), 20 µl.min^{-1} (11/9) and 40 µl.min^{-1} (22/18). Core/shell flow rate ratios were calculated as 55/45%. In Figure 1, it is seen clearly flow rate of the solution has a major impact on the particle formation. At higher flow rates (20

µl.min^{-1} and 40 µl.min^{-1}), the nanocapsules began to lose their spherical morphology and exhibited a tendency to aggregate. Higher flow rates lead to the formation of larger particles as the increased supply of polymer solution causes the droplets from the needle to exceed the rate of solvent evaporation, resulting in the production of these larger particles [1,24]. Particles generated at higher flow rates exhibited a tendency to agglomerate or adhere to one another, leading to the absence of distinct independent particles [9,25]. Irregular morphology may observe due to insufficient drying time. Conversely, reducing the flow rate leads to smaller droplet formation at the needle and enhances solvent evaporation, resulting in the production of smaller particles [1]. At 5 µl.min^{-1} total flow rate, even though the smaller particles were seen, fibrillation was also observed which may occur at low total flow rates due to the rapid drying of nanocapsules, without sufficient time to separate from each other. At 10 µl.min^{-1} total flow rate, no fibrillation was observed, and the particle size was smaller compared to those at higher flow rates.
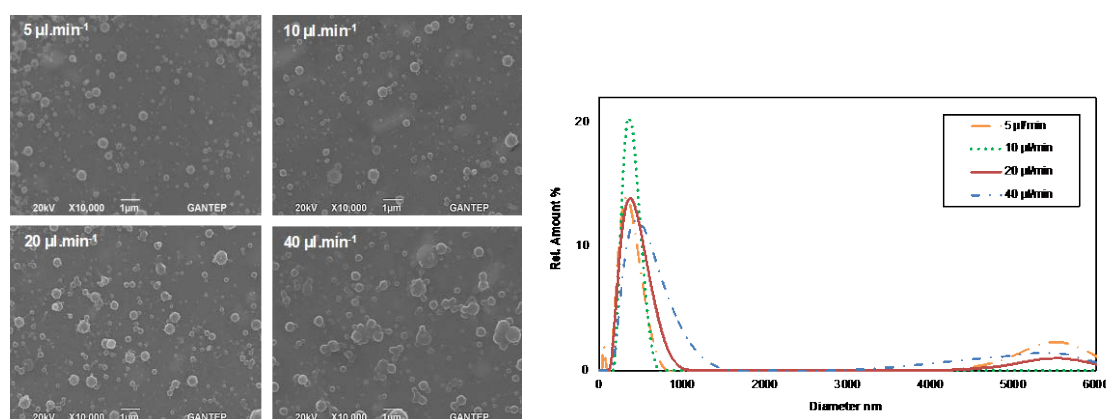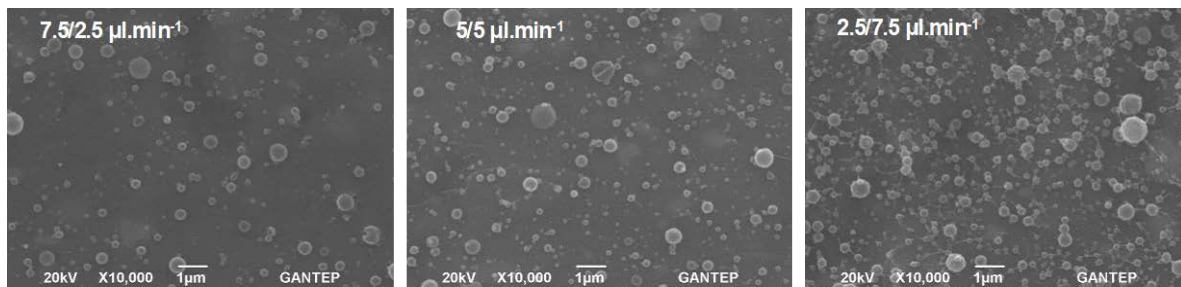

**Figure 1.** SEM images and size distributions (intensity) of nanocapsules at various total flow rates

In the size distribution graph, all flow rate conditions, with the exception of 10 µl.min^{-1}, exhibit a measurable percentage of larger particles within the distribution. At a flow rate of 10 µl.min^{-1}, monodisperse distribution is observed (Figure 1). Both the SEM analysis and the particle size distributions indicated that the 10 µl.min^{-1} flow rate was optimal.

3.2. Effects of Core/Shell Flow Rate Ratios on Chitosan Nanosphere Formation

A specific flow ratio between the core and shell solutions must be maintained to achieve a stable cone-jet mode during electrospraying [26]. To investigate the effects of core/shell flow rate ratios on nanocapsule formation, three different ratios were selected; 75/25%, 50/50%, 25/75%, respectively. Total flow rate was kept constant at 10 µl.min^{-1}. SEM images and size distributions of electrosprayed nanocapsules at various core/shell flow rate ratios are presented in Figure 2 and Figure 3, respectively. Since the core solution, triclosan, is water-based and has a low concentration, a higher core flow rate promoted film formation. Conversely, reducing the core flow rate while increasing the shell flow rate—and thus the chitosan concentration—enhanced nanocapsule formation. As concentration rises, interactions between chains lead to intermolecular entanglement, which limits the mobility of individual chains [27]. The lowest shell flow rate resulted in fewer particles being formed, as a low shell flow rate may lead to inadequate encapsulation of the core [28]. As the shell flow rate increased, particle formation correspondingly increased. However, at higher shell flow rate ratios, particles tended to agglomerate and fibrillate. Higher flow rates hindered complete solvent evaporation, leading to adhesion and clumping, which reduced the formation of individual particles [25].

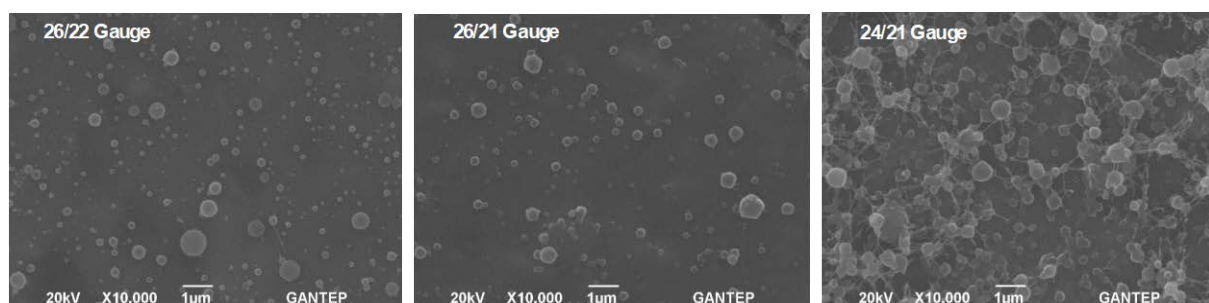**Figure 2.** SEM images of nanocapsules at various core/shell flow rate ratios
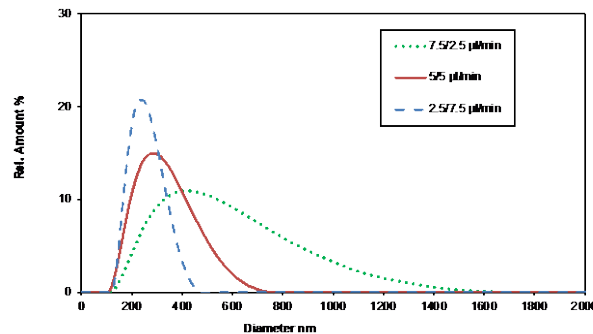
Figure 3. Size distributions (intensity) of nanocapsules at various core/shell flow rate ratios

Even though the sizes of the nanocapsules were similar at different ratios, higher chitosan content led to fibril formation between the nanocapsules. Although the 2.5/7.5 µl.min^{-1} core/shell flow rate ratio yielded the most uniform size distribution (Figure 3), because of the fibrillation, the 5/5 µl.min^{-1} core/shell flow rate ratio represented the most optimal configuration. Wang et al. [29] was reported smaller particle sizes at higher shell flow rate too.

3.3. Effects of Needle Size on Chitosan Nanosphere Formation

Modifying the needle characteristics in electrospray processing directly affects the operating conditions and the outcomes of the process [30]. Different needles with varied gauge were employed to assess the impact of needle size on nanocapsule formation and size. Nanocapsule formation was examined using 26/22 gauge, 26/21 gauge, and 24/21 gauge needles for core/shell solutions, respectively. SEM images of nanocapsules produced with different needles are presented in Figure 4. Nanocapsules were successfully formed with all needle configurations. However, significant fibrillation was observed with 24/21 gauge needles. Larger needle diameter leads unseparated particles. A smaller needle diameter results in reduced droplet size at the nozzle tip due to a smaller meniscus and increased surface tension. This requires a greater Coulombic force to initiate the jet, which slows down jet acceleration and extends flight time, providing more opportunity for Rayleigh disintegration and further breakdown into smaller droplets [9]. The use of 26-gauge needle for the core solution yielded more uniform spherical structures.


Figure 4. SEM images of nanocapsules at various needle size

The size distribution of the nanocapsules is illustrated in Figure 5. Among the configurations with comparable SEM image appearances, the 26/22 gauge needle combination demonstrated a more monodisperse distribution than 26/21 gauge. Consequently, the 26/22 gauge needle configuration was selected to achieve better distribution.
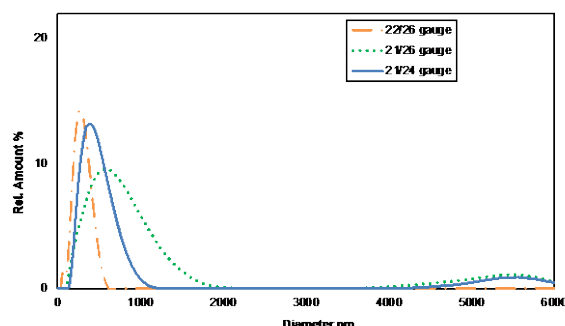
Figure 5. Size distributions of nanocapsules at various needle size (intensity)

The TEM image of the nanocapsule at a 5/5 µl.min^{-1} flow rate ratio and a 26/22 G needle, shown in Figure 6, clearly displays both the core and the shell in spherical structure, indicating successful encapsulation.
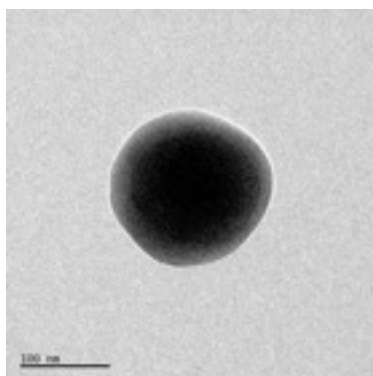
Figure 6. TEM image of nanocapsules at 5/5 µl.min^{-1} flow rate ratio and 26/22 G needle

4. CONCLUSIONS

The objective of this study is to produce chitosan-based nanocapsules with a spherical structure and monodisperse distribution. To achieve this, experiments were conducted with various process parameters, including total flow rates, flow rate ratios for core/shell solutions, and core/shell needle sizes. When the total flow rate was reduced, fibrillation was observed between the capsules, while at higher rates, the capsules tended to aggregate, leading to deformation of their shapes. In the experiments focused on core/shell flow rate ratios, fibrillation was noted when the chitosan content as shell material was at its highest. In comparison with other flow rate ratios, the study with an equal core/shell ratio demonstrated the most promising size distribution. Smaller needle diameters produced smaller particles, while larger needles resulted in poorly separated capsules. The optimal results were achieved using the smallest needle gauge.

ACKNOWLEDGEMENTS

References

1. *Kurakula, M., Raghavendra Naveen, N. (2021). Electrospraying: A facile technology unfolding the chitosan based drug delivery and biomedical applications. Eur Polym J. 147:110326.*

2. *Massella, D., Giraud, S., Guan, J., Ferri, A., Salaün, F. (2019) Textiles for health: a review of textile fabrics treated with chitosan microcapsules. Environ Chem Lett. 17(4):1787–800.*

3. *Muñoz-Bonilla, A., Echeverria, C., Sonseca, Á., Arrieta, M.P., Fernández-García, M. (2019). Bio-Based Polymers with Antimicrobial Properties towards Sustainable Development. Materials. 12(4):641.*

4. *Ibili, H., Dasdemir, M. (2022). Formation, Characterization and Multifunctional Activity of Chitosan Nanoparticle Coating. Fibers Polym 23, 1856–1869.*

5. *Lima, C.S.A.D., Varca, G.H.C., Costa, S.M.D., Ferraz, H.G., Santos, A.C.D.S., Lopes, P.S., et al. (2020) Development of natural polymeric microcapsules for antimicrobial drug delivery: triclosan loaded chitosan and alginate-based microcapsules. Drug Dev Ind Pharm. 46(9):1477–86.*

6. *Tania, I.S., Ali, M., Arafat, M.T. (2021). Processing techniques of antimicrobial textiles. In: Antimicrobial Textiles from Natural Resources [Internet]. Elsevier; [cited 2024 Aug 16]. p. 189–215. Available from: https://linkinghub.elsevier.com/retrieve/pii/B9780128214855000020*

7. *Liyanage, S., Parajuli, P., Hossain, M.T., Chaudhari, H., Abidi, N. (2021). Antimicrobials for protective clothing. In: Antimicrobial Textiles from Natural Resources [Internet]. Elsevier; [cited 2024 Aug 16]. p. 349 – 376. Available from: https://linkinghub.elsevier.com/retrieve/pii/B9780128214855000068*

8. *Wang, J., Jansen, J.A., Yang, F. (2019). Electrospraying: Possibilities and Challenges of Engineering Carriers for Biomedical Applications—A Mini Review. Front Chem. 25(7):258.*

9. *Alfatama, M., Shahzad, Y., Choukaife, H. (2024). Recent advances of electrospray technique for multiparticulate preparation: Drug delivery applications. Adv Colloid Interface Sci.325:103098.*

10. *Park, J.E., Kim, Y.K., Kim, S.Y., Choi, J.B., Bae, T.S., Jang, Y.S., et al. (2023). Biocompatibility and Antibacterial Effect of Ginger Fraction Loaded PLGA Microspheres Fabricated by Coaxial Electrospray. Materials. 16(5):1885.*

11. *Zhang, Y., Tremblay, P.L., Zhang, T. (2023). Electrosprayed trilayer poly (d,l-lactide-co-glycolide) nanoparticles for the controlled co-delivery of a SGLT2 inhibitor and a thiazide-like diuretic. J Drug Deliv Sci Technol. 81:104311.*

12. *Valle, J.A.B., Valle, R.D.C.S.C., Bierhalz, A.C.K., Bezerra, F.M., Hernandez, A.L., Lis Arias, M.J. (2021). Chitosan microcapsules: Methods of the production and use in the textile finishing. J Appl Polym Sci. 138(21):50482.*

13. *Arya, N., Chakraborty, S., Dube, N., Katti, D.S. (2009). Electrospraying: A facile technique for synthesis of chitosan-based micro/nanospheres for drug delivery applications. J Biomed Mater Res B Appl Biomater. 88B(1):17–31.*

14. *Antunes, L., Faustino, G., Mouro, C., Vaz, J., Gouveia, I.C. (2014). Bioactive microsphere-based coating for biomedical-textiles with encapsulated antimicrobial peptides (AMPs). Ciênc Tecnol Mater. 26(2):118–125.*

15. *Rajendran, R., Radhai, R., Kotresh, T.M., Csiszar, E. (2013). Development of antimicrobial cotton fabrics using herb loaded nanoparticles. Carbohydr Polym. 91(2):613–617.*

16. *Hui, P.C.L., Wang, W.Y., Kan, C.W., Ng, F.S.F., Wat, E., Zhang, V.X. Chan, C.L., Lau, C.B.S., Leung, P.C. (2013). Microencapsulation of Traditional Chinese Herbs—PentaHerbs extracts and potential application in healthcare textiles. Colloids Surf B Biointerfaces. 111:156–161.*

17. *Islam, S., Jadhav, A., Fang, J., Arnold, L., Wang, L.J., Padhye, R.J., Wang, X.G., Lin, T. (2011). Surface Deposition of Chitosan on Wool Substrate by Electrospraying. Adv Mater Res. 331:165–170.*

18. *Silva, A.C.Q., Silvestre, A.J.D., Freire, C.S.R., Vilela, C. (2021). Modification of textiles for functional applications. In: Fundamentals of Natural Fibres and Textiles [Internet]. Elsevier; [cited 2024 Aug 16]. p. 303–65. Available from: https://linkinghub.elsevier.com/retrieve/pii/B9780128214831000103*

19. *Abbaszad Rafi, A., Mahkam, M. (2015). Preparation of magnetic pH-sensitive microcapsules with an alginate base as colon specific drug delivery systems through an entirely green route. RSC Adv. 5(6):4628–4638.*

20. *Elisseeff, J. (2008). Structure starts to gel. Nat Mater. 7(4):271–273.*

21. *Karzar Jeddi, M., Mahkam, M. (2019). Magnetic nano carboxymethyl cellulose-alginate/chitosan hydrogel beads as biodegradable devices for controlled drug delivery. Int J Biol Macromol. 135:829–838.*

22. *Dhiman, G., Chakraborty, J.N. (2015). Antimicrobial performance of cotton finished with triclosan, silver and chitosan. Fash Text. 2(1):13.*

23. *Ouerghemmi, S., Degoutin, S., Maton, M., Tabary, N., Cazaux, F., Neut, C., et al. (2022). Core-Sheath Electrospun Nanofibers Based on Chitosan and Cyclodextrin Polymer for the Prolonged Release of Triclosan. Polymers. 14(10):1955.*

24. *Chang, M.W., Stride, E., Edirisinghe, M. (2010). Controlling the thickness of hollow polymeric microspheres prepared by electrohydrodynamic atomization. J R Soc Interface [Internet]. [cited 2024 Nov 1]. Available from: https://royalsocietypublishing.org/doi/10.1098/rsif.2010.0092.focus*

25. *Liu, Y., Li, S., Li, H., Alomgir Hossen, M., Sameen, D.E., Dai, J., Qin, W., Lee, K. (2021). Synthesis and properties of core-shell thymol-loaded zein/shellac nanoparticles by coaxial electrospray as edible coatings. Mater Des. 212:110214.*

26. *Tsai, S., Ting, Y. (2019). Synthesize of alginate/chitosan bilayer nanocarrier by CCD-RSM guided co-axial electrospray: A novel and versatile approach. Food Res Int. 116:1163–1172.*

27. *Dasdemir, M., Ibili, H. (2017) Formation and characterization of superhydrophobic and alcohol-repellent nonwovens via electrohydrodynamic atomization (electrospraying). J Ind Text. 47(1):125–46.*

28. *Rathore, P., Schiffman J.D. (2021). Beyond the Single-Nozzle: Coaxial Electrospinning Enables Innovative Nanofiber Chemistries, Geometries, and Applications. ACS Appl Mater Interfaces. 13(1):48–66.*

29. *Wang, Y., Yu, D.G., Liu, Y., Liu, Y.N. (2022). Progress of Electrospun Nanofibrous Carriers for Modifications to Drug Release Profiles. J Funct Biomater. 13(4):289.*

30. *Ahmad, Z., Zhang, H.B., Farook, U., Edirisinghe, M., Stride, E., Colombo, P. (2008) Generation of multilayered structures for biomedical applications using a novel tri-needle coaxial device and electrohydrodynamic flow. J R Soc Interface. 5(27):1255–61.*

ENHANCE THE ANTIBACTERIAL PROPERTIES OF SILVER PARTICLES COATED COTTON BANDAGES FOLLOWED BY NATURAL EXTRACTED DYE

[1]Saba Rashid, Toba Latif [1], Majid Ali[1], Aneela Jamil [3], Laiba Shahzad, Ruba Tariq, Aqsa Sarwar[1], Azam Ali[2]

[1]Department of chemistry, Riphah International University Faisalabad
[2]Department of Material Engineering, Faculty of Textile Engineering, Technical University of Liberec
[3]Department of education, Govt College University Faisalabad
Corresponding author Email: sabarasheed345@gmail.com

Abstract:

We have fabricated antibacterial stretchable medicated textiles. At first, the versatile one-pot green synthesis approach was used to make a concentrated and stable colloidal solution of silver nanoparticles (Ag-NPs) through the self-assembly of tannic acid, without using any other hazardous chemicals. The silver particles were then applied to the cotton fabrics. SEM, dynamic light scattering, and XRD were used to examine the surface morphologies and metal presences. In second step, natural antibacterial dye was extracted from pomegranate peel and applied on the silver coated cotton fabrics in accordance with the exhaust dyeing method. The CILAB (L*, a*, b*, C, h, and K/S) and color fastness properties of dyed fabric samples were determined. Furthermore, antipathogenic (antibacterial, antiviral, and antifungal) properties were determined for all coated fabrics.

Keywords:

Silver nanoparticles, antibacterial bandages, natural dyes, green synthesis, aesthetic properties

1. Introduction

Silver nanoparticles are ascertained to be nanomaterials with dimensions in the range of 1-100 nm. They have shown enhancement in volume capacity and greater surface area (area-to-volume ratio) than silver in bulk. At the nanoscale, this material displays distinct electrical, optical, and catalytic properties, which has resulted in research and production of materials designed for targeted drug delivery, diagnosis, detection, and imaging [1]. However, the remarkable antibacterial properties that AgNPs possess have captured the interest of researchers and industries in this nanomaterial. AgNPs have exhibited multidrug-resistant bacterial populations, other infectious and pathogenic microorganisms, and the ability to possess antimicrobial activity [2]. The nanoscale enhancement of the antibacterial action of Ag has been most helpful in medicine and health care sectors, for the incorporation of AgNPs into hundreds of products such as surgical and food contact appliances, clothing, cosmetics, dental products, catheters, and dressings have been investigated. It has been established that AgNPs can act as antibiotics based on many mechanisms of action that affect microorganisms with numerous structures at once, enabling them to combat different strains of bacteria [3]. The Ag NP is a commonly known strong antibacterial, which is widely applied in multiple commercial products, including the textile sector, to prevent microbial contamination. Numerous authors have proposed Ag NPs as ideal antibacterials to ensure the fabrics are free from microorganisms like fungi, viruses, and bacteria. The Ag NP greatly enhances the inhibition of the wound dressing sprayed fabric. Most Ag NP antimicrobial composites were made of Ag NPs, highly effective against nearly 650 bacterium strains. Various methods of preparation of nanoparticles result in different physical-chemical properties of the particles [4]. Synthesis of chemicals requires the use of toxic substances, which may have side effects on humanity and the

ecosystem. Currently, fabrics have been coated with nanoparticles using screen printing, padding squeezing, spray, sonochemical, and dip coating. The coating process aims to ensure that the coating chemicals are used to enhance the adsorption and stability of the nanoparticles on the fabric. In this regard, the resultant NPs must behave in a stable structure, whether colloidal or metallic. These parameters are taken into account for coating purposes [5]. The researchers primarily focused on obtaining stable Ag NPs and achieving size control while avoiding harmful chemicals. In this work, green-synthesized nanoparticles were used instead. This precluded the application of cryogenically synthesized nanoparticles and, therefore, their adverse effects. In this green synthesis method, nanoparticles do not contain toxic substances and the Ag NPs were obtained in colloidal form [6]. Within the confines of the present investigation, the flower extract of *Peltophorum pterocarpum* was effective in serving as a non-toxic reducing and binding agent in the Ag NPs synthesis protocol. Furthermore, the dip and sonication methods required no adhesive because the green synthesized Ag NPs were coated on cotton textiles. Medical products containing silver compounds can treat burns, wounds, and numerous infectious diseases. The inability to treat certain infections due to antibiotic resistance is an increasing concern in the combat against contagious diseases. Without appropriate regulation, the current excess consumption of antibiotics will dilute numerous bacterial pathogen's effectiveness. Because of that, antimicrobial dressings have been produced most widely using biological polymers integrated with antimicrobial components [7]. Each of these types aids wound healing. However, scientists need to gain profound knowledge that will help them devise wound dressings that are otherwise free of toxins, last longer, provide stronger resistance, and have clinical acceptability. Out of available materials, cotton could be a reasonable candidate for such modified dressings. It has been the norm in most countries that cotton is used in dressing wound sites to prevent contamination of the affected area [8]. Wounds like cuts or grazes are likely to heal faster with applying cotton and do not irritate sensitive skin. However, the treatment of wounds using cotton pads creates a lot of obstacles, most of which are while immersed in the fluids of the wound, cotton fibers adhere like glue to it. From this bonding, as soon as cotton gets dragged out, the cells within the healing area of the wound also get ripped off, causing side effects like prolonged healing time and painting during dressing since the sites are extra sensitive. This, in turn, is entirely negated by using chitosan, a structural biopolymer, due to its hydrogel formation ability and anti-pathogenic capabilities, making wound management easier. Glycogen, a safe and nontoxic animal polysaccharide, helps with the same problem. Further, it prevents tissue scarring when the areas of injury form albumin and get dressed, further promoting healing [9]. Clinical textiles employed in hospitals are also referred to as 'hospital textiles,' they must fulfill specific standards like being non-toxic, anti-allergic, antimicrobial, and anti-inflammatory. Several agents, including metal particles and particular treatments, cure textile materials with antibacterial properties. More recently, however, metallic compounds in the form of nanoparticles have been used to incorporate beneficial properties into fabrics to curtail the spread of diseases and microbial growth. Cu, ZnO, TiO$_2$, Ag, Cu$_2$O, CuO, and Mgo polycrystalline are widely used compounds because of their effectiveness. Silver and its compounds are outstanding for their surface disinfectant effect, including their antiviral, antibacterial, and antifungal effects on various pathogens. Cotton fabric coated with silver nanoparticles was found to be effective against harmful microbes by Ali et al., i.e., this cotton fabric was termed multifunctional textile material thanks to the silver coating. In response to these needs, this article proposes a novel method to produce antimicrobial cotton fabrics covered with silver that have good aesthetic and functional properties. The aim is to see how these fabrics might benefit commercial and medical applications because they will acquire more excellent antibacterial activity after dyeing. These fabrics may also be used in pillow covers, bedsheets, and even wear for patients apart from uses like compression bandages [10]. The cotton fabric is a marvel of textile engineering, with better comfort, absorbance, and breathability performance. Admittedly, cotton fabric sometimes lacks the strength or the tenacity of other materials, but it maintains its high global demand because of its standout characteristics. Today, consumers' expectations are more in terms of aesthetics, and so there is a requirement for cotton fabrics that are stylish, convenient, and comfortable. Nanotechnology brings excitement to the possibility of modifying the cotton textile to meet all those desirable modern requirements that have never been met [11]. In textile manufacturing, greater emphasis has now been placed on specific finishes due to the necessity of achieving multifunctional properties. Such finishes,

which are now commonplace, include but are not limited to antistatic, durability, antimicrobial, dirt repellent, flame resistance, water repellent, easy crease recovery, self-cleaning, and UV protection. Enhancing the surface of textiles is thus one way of augmenting these functional characteristics. Using noble metal nanoparticles has recently been an effective strategy in fabricating fabrics with multiple useful functions [12]. Different types of nanoparticles possess distinct characteristics that are important in textile surfaces. For example, zinc oxide nanoparticles provide UV protection in garments; silver nanoparticles have antibacterial properties; titanium dioxide is used in self-cleaning fabrics, and silver and zinc oxide are added to produce bright, conductive fabrics [13]. These types of nanoparticles are instead used on cotton fabric surfaces. Hence, they can be suitable for clothing manufactured for various sports, everyday casual dressing, and in medical facilities for bandages, absorbent pads, gauzes, padding materials, gowns, sets, etc [14]. However, the moisture-rich cellulose-containing cotton fibers make them susceptible to invasion by microbes, which are a favorable environment for bacterial and fungal growth. Silver nanoparticles, as we know, have excellent anti-microbial attributes for application in textile materials. Their antibacterial characteristics become more effective with the decreasing size of particles. Thus, anisotropic silver-based silver-based nanoparticles can be used to dye cotton fabrics in a wide range of colors and also give antibacterial characteristics [15]. Most research has been directed towards evaluating antimicrobial properties, while wash durability has rarely been studied. Particle size, shape, concentration, and surface treatment, both pre-and post-application, can influence different levels of antimicrobial activity. This research pointed out that wash durability was enhanced. To date, no investigation has evaluated color uniformity in AgNP-coated cotton materials [16].

2. Experimental

2.1. _Materials and Methods_

Cotton-Nylon–spandex (80:15:05) stretch fabrics and the chemicals used for the synthesis and deposition of nanoparticles had 99.99% purity and were obtained from Sigma-Aldrich. The pretreated fiber's surface were treated with 12 wt% aqueous NaOH solution at room temperature for 10 min and rinsed with distilled water. We applied three different concentrations (1M, 0.5M and 0.25M) of silver nitrate (AgNO3) for making the solution. The aqua ammonia (28wt%) was added drop wise into previous solutions and stirred continuously until a transparent solution of [Ag(NH3)2]+ was obtained. Alkali treated fabrics were dipped in each solution for 10 minutes and dried at 90°C for 10 minutes. The dipping and drying process was repeated for 10 times to deposit the maximum concentration of [Ag(NH3)2]+and Ag+ ions on the fabrics. Ultimately, the resulting fabrics were immersed into 0.3M glucose stock solution, and the remaining [Ag(NH3)2]+ solution was also poured into glucose solution [17].

2.2. _Application of dye on fabric_

The tint procured was used to dye fabrics covered with silver particles using an exhaust dyeing process. The material-to-liquid (M: L) ratio was 1:40. The alkali sodium hydroxide (1 g/L) was added first, followed by the electrolyte sodium sulfate (40 g/L). The stained cloth was removed from the dye bath and washed with tap water.

2.2.1. Impregnation of silver and copper nanoparticles onto cotton bandages

The gauze was cut into pieces, and 2.5 g measure was put in 250 mL of 1 mM silver nitrate-containing solution. Then 50 mL A. paniculata extracts were added to this solution and incubated on the orbital shaker at 100 rpm for 24 hrs at dark room temperature. The phytochemicals present in the flower extract and the root extract were responsible for reducing silver ions into metallic silver, which subsequently deposited as nanoparticles over the cotton bandages. After 24 hours, the pieces of cotton bandage were collected from the solution. The silver nanoparticles containing cotton gauze were washed with deionized water and placed in an oven at 55 °C for drying [18]. The same procedure was repeated for impregnating CuNPs on the cotton bandages.

2.2.2. Confirmation of nanoparticle impregnation using SEM

Scanning electron microscopy images were taken at an accelerating voltage of 15kV using a Carl Zeiss SEM to study the surface features of cotton bandages incorporated with silver nanoparticles (AgNPs) and copper nanoparticles (CuNPs). A plain cotton bandage provided the control [19].

2.2.3. Synthesis of silver nanoparticles

The silver nanoparticles were prepared according to the previous report [20]. As per the routine in obtaining the plant extract, the flowers of 'P. Pterocarpum was used to measure the weight of approximately 1 gram. The flowers were soaked in deionized water to wash off any remaining soil and dust from the flowers. After being washed, the flowers were boiled at a hot temperature of 80 degrees Celsius for 20 minutes in 100 mL of deionized water and then filtrated to separate the floral solid substances from the extracted liquid. The extract was then stored in a fridge at four degrees Celsius to avoid contamination. Twenty milliliters of P. pterocarpum flower extract was added slowly to 100 mL of 0.01 M silver nitrate solution as it stirred at room temperature to reduce the silver ions to silver metal.

2.2.4. Coating of silver nanoparticles on fabric

The cotton fabric was then cropped to a size of 2 × 2 cm square pieces and dipped into the synthesized colloidal solution of Ag nanoparticles, where it was left undisturbed in darkness for 24 hours. In another experiment, the fabric was ultra-sonicated using a Cyberlab CB2020 ultrasonic cleaner at a frequency of 46 kHz and power of 80 W for 30 minutes duration. Post-treatment, the fabric was washed with ethanol and several washes with distilled water to remove any unattached or surplus Ag nanoparticles. The fabrication process of the sheet was completed by drying the fabric at 60°C before further analysis [20].

3. Results and discussion

3.1. *Colorimetric data measurement*

The CIELAB values of silver coated dyed and undyed fabrics differs considerably. The K/S values for dyed sample was relatively high (11.31) than for undyed fabric (7.47), indicating that dyeing has altered the light-colored silver coated fabric to a relatively dark-colored fabric. The variation in L* values among both fabrics confirmed the dark shade of the colored fabric. The L* value of the dyed fabric was relatively low (37.15) than the L* value of the undyed fabric (55.35), indicating that the dyed sample has a darker shade than the undyed sample. The chroma (C*) for the dyed fabric was also relatively low (34.98) than for the undyed sample (37.79), indicating that the undyed samples had a sharper shade and the dyed sample had a darkened and duller shade. The a* and b* values were positive for both dyed and undyed fabric, indicating a reddish and yellowish shade.

### 3.2. *Levelness of silver treated undyed and dyed fabric*

The results of dye levelness were checked to evaluate how evenly the dyed fabric looked. A spectrophotometer was used to measure the reflectance of both dyed and undyed fabrics coated with silver. K/S values were measured at 12 different points. The table displays the K/S values and the standard error calculated from them. The standard error for dyed silver-coated fabric was 0.12, indicating excellent levelness with even dye distribution. In contrast, the standard error for silver-coated undyed fabric was 2.21, showing a highly uneven appearance. These results suggest that dyed silver-coated fabrics have a smoother and more even look compared to undyed silver-coated fabrics. Visual assessment rated dyed fabrics as grade 5 (excellent levelness) and undyed fabrics as grade 2 (poor levelness), supporting the conclusion that dyeing silver-treated fabrics results in a more even and smooth appearance [21].

Table 1. Reflectance measurement data for the undyed and dyed silver coated fabrics

Number of Scans	K/S Values dyed sample	Standard deviation (S.D)	K/S Values undyed sample	Standard deviation (S.D)
Reading 1	11.32		13.75	
Reading 2	11.56		16.56	
Reading 3	11.21		7.34	
Reading 4	11.98		12.56	
Reading 5	11.65	0.12	6.45	2.21
Reading 6	11.45		11.35	
Reading 7	11.99		14.67	
Reading 8	11.56		7.65	
Reading 9	11.25		12.34	
Reading 10	11.42		8.45	

3.3. _Morphology of silver coated knitted dyed cotton fabrics_

Figures 1 (a) The average particle size distribution for silver nanoparticles was found to be approximately 11.2 ±1.7 nm. Visuals in Figure 1 (a) displayed nanometer-scale images of silver particles pre-application on fabric, showing spherical features without aggregations. The claim was supported by Zeta potential and polydispersity index (PDI) values of -51.63 ± 5.19 mV and approximately 0.292, respectively. These values indicated even particle distribution and high polydispersity. Tannic acid acted as a capping agent, forming a poly tannic acid (PTA) layer during nanoparticle synthesis through self-polymerization. Scanning electron microscopy (SEM) revealed structural morphologies of silver particles on fabrics pre and post dyeing in Figures 1 (b,c), showing a more consistent and denser silver coating with increasing particle concentration from 1mg to 3mg. XRD analysis was used to determine the phase composition of silver nanoparticles. Figure 1 (f) presented XRD spectra in the range of 20 to 80 ° with a 0.02-degree step, showing ideal indexing to the silver structure, confirming the phase purity of the synthesized silver nanoparticles.
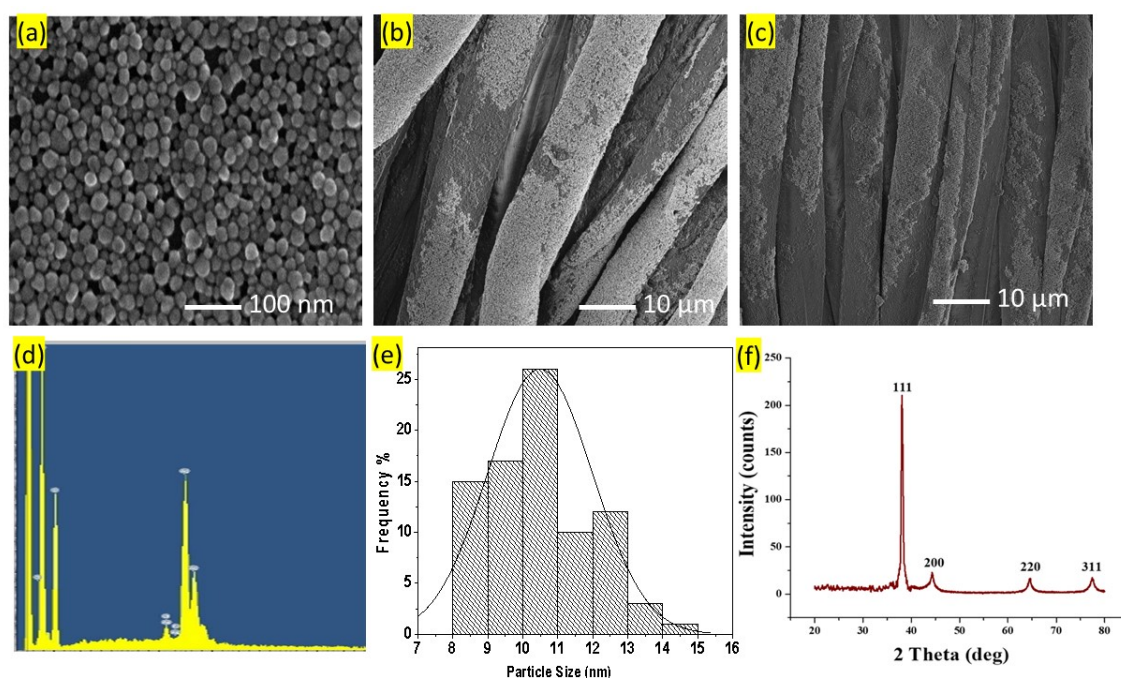
Figure 1. SEM images of (a) silver particles, (b) silver particles coated cotton fibers, (c) silver particles coated and dyed cotton fibers, (d) EDX analysis, (e) Size analysis and (f) XRD of silver particles.

3.4. *Antibacterial activity, antifungal and antiviral activity*

The antibacterial efficacy of both undyed and dyed silver treated textile substrates was assessed through qualitative and quantitative standard testing protocols.

3.5. *Zone of inhibition test (qualitative measurements)*

The AATCC-147 (disc-diffusion method) protocol was used for the qualitative evaluation of all treated samples. All samples were tested for antibacterial effectiveness towards Gram-negative (E. coli) and Gram-positive (S. aureus) pathogens. Fig. 2 shows ZOI for antibacterial efficacy of both undyed and dyed silver-treated textile substrates was evaluated using the AATCC-147 (disc-diffusion method) protocol. The samples were tested against Gram-negative (E. coli) and Gram-positive (S. aureus) pathogens. In Figure 2, the Zone of Inhibition (ZOI) for silver-coated dyed fabrics was observed to be greater than that for silver-coated undyed fabrics. The increased ZOI values for silver-coated dyed fabrics suggest that the antibacterial properties of silver nanoparticles were not compromised by the presence of antibacterial dye on the fabrics. The higher ZOI values for silver-coated dyed fabrics indicate that the use of antibacterial dye on silver-coated fabrics did not mask the antibacterial action of silver nanoparticles. The higher ZOI values for silver-coated dyed fabrics indicated that the use of antibacterial dye on silver-coated fabrics has not masked the antibacterial action of silver nanoparticles.

The antifungal activity of all treated fabric samples (both dyed and undyed) was evaluated using the AATCC-100 method against A. niger fungal species. In Figure 2(a), the results show the percentage reduction in fungal spore germination for all samples. It was observed that all treated fabric samples exhibited good antifungal activity against the A. niger fungus. The antifungal activity of the dyed samples was enhanced, indicating that the dye used has excellent antifungal properties. Among the undyed samples, sample S3 and sample S3D showed the most significant reduction in fungal growth, with antifungal actions of 89% and 91%, respectively. The untreated fabric did not exhibit any inhibitory effect on the test microbe, confirming that the antifungal properties in all treated samples (dyed and undyed) were attributed to the presence of silver nanoparticles and antimicrobial dye. Overall, the study demonstrated superior antifungal properties of silver-coated dyed fabric. This observation aligns with a related study where green-synthesized silver particles showed a similar reduction in the percentage of fungus. The present study showed better antifungal properties of silver-coated dyed fabric is justified by the results and comparison with related studies.

The sample S3 (among all undyed fabrics) and S3D (among all dyed fabrics) showed the highest reduction in antiviral activity, with 80% and 84% effectiveness, respectively. The antiviral effect of silver-treated undyed and dyed fabrics can be explained by the binding of metallic nanoparticles and the phenolic part of the polyphenols to glycoproteins on the viral surface, which inhibits the viruses. In a recent study, fabric coated with silver particles using the photo deposition method exhibited a 97% reduction in the specific viral load of SARS-CoV-2. The antiviral activity of silver-treated undyed and dyed fabrics is due to the presence of silver nanoparticles and natural antimicrobial dye, which inhibit viruses by binding to glycoproteins on the viral surface.[22].
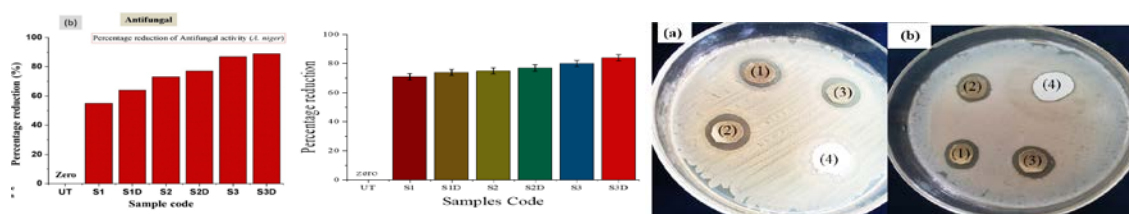

Figure 2. (a) Antifungal activity (b) Antiviral reduction in percentage (c) ZOI antibacterial

4. Conclusion

A total of 6 hygienic samples (3 dyed and 3 undyed) were developed using nanoparticle of silver along with varying the concentrations. The surface morphology and presence of metals were analysed through SEM and XRD. It was observed that ZOI for dyed silver coated samples is higher than undyed silver coated fabrics. The strongest antibacterial effect was found for the dyed fabric sample S3D. In case of quantitative analysis, the samples S3 and S3D showed highest reduction in surviving bacterial colonies, with CFU values dropping to 0 from 7.34 and 6.44 for E. coli and S. aureus, respectively.

References:

1. *Yaqoob A.A., Ahmad H., Parveen T., Ahmad A., Oves M., Ismail I.M.I., Qari H.A., Umar K., Mohamad Ibrahim M.N. Recent Advances in Metal Decorated Nanomaterials and Their Various Biological Applications: A Review. Front. Chem. 2020;8:341. doi: 10.3389/fchem*

2. *Marambio-Jones C, Hoek EMV (2010) Marambio-Jones, C.; Hoek, E. M. V. A Review of the Antibacterial Effects of Silver Nanomaterials and Potential Implications for Human Health and the Environment. J. Nanopart. Res. 2010, 12, 1531– 1551, DOI: 10.1007/s11051-010-9900-y. J Nanoparticle Res 12:1531–1551*

3. *Cheng G., Dai M., Ahmed S., Hao H., Wang X., Yuan Z. Antimicrobial drugs in fighting against antimicrobial resistance. Front. Microbiol. 2016;7:470. doi: 10.3389/fmicb.2016.00470. [DOI] [PMC free article] [PubMed] [Google Scholar]*

4. *Babapour, A, Akhavan, O, Moshfegh, AZ, Hosseini, AA, "Size Variation and Optical Absorption of Sol–Gel Ag Nanoparticles Doped SiO2 Thin Film." Thin Solid Films, 515 (2) 771–774 (2006)*

5. *Ulacha, AB, Rybicki, E, Zgondek, EM, Pawlaczyk, A, Szynkowska, MI, "A New Method of Finishing of Cotton Fabric by in Situ Synthesis of Silver Nanoparticles." Ind. Eng. Chem. Res., 53 (11) 4147–4155 (2014)*

6. *Goodsell, DS, Bionanotechnology: Lessons from Nature. Wiley, Hoboken (2004)*

7. *Kaushik M, Niranjan R, Thangam R, et al (2019) Investigations on the antimicrobial activity and wound healing potential of ZnO nanoparticles. Appl Surf Sci 479:1169–1177. https://doi.org/10.1016/j.apsusc.2019.02.189*

8. *Božanić DK, Dimitrijević-Branković S, Bibić N, et al (2011) Silver nanoparticles encapsulated in glycogen biopolymer: Morphology, optical and antimicrobial properties. Carbohydr Polym 83:883–890. https://doi.org/10.1016/j.carbpol.2010.08.070*

9. *Dahl M V. (1993) Suppression of immunity and inflammation by products produced by dermatophytes. J Am Acad Dermatol 28:S19–S23. https://doi.org/10.1016/S0190-9622(09)80303-4*

10. *Hasanin M, Swielam EM, Atwa NA, Agwa MM (2022) Novel design of bandages using cotton pads, doped with chitosan, glycogen and ZnO nanoparticles, having enhanced antimicrobial and wounds healing effects. Int J Biol Macromol 197:121–130. https://doi.org/10.1016/j.ijbiomac.2021.12.106*

11. *Gorenšek, M.; Recelj, P. Nanosilver Functionalized Cotton Fabric. Text. Res. J. 2007, 77, 138–141. [Google Scholar] [CrossRef]*

12. *Islam, S.U.; Mohammad, F. High-Energy Radiation Induced Sustainable Coloration and Functional Finishing of Textile Materials. Ind. Eng. Chem. Res. 2015, 54, 3727–3745. [Google Scholar] [CrossRef]*

13. *Becheri, A.; Dürr, M.; Nostro, P.L.; Baglioni, P. Synthesis and characterization of zinc oxide nanoparticles: Application to textiles as UV-absorbers. J. Nanopart. Res. 2008, 10, 679–689. [Google Scholar] [CrossRef]*

14. *Czajka, R. Development of medical textile market. Fibres Text. East. Eur. 2005, 13, 13–15. [Google Scholar]*

15. *Tang, B.; Zhang, M.; Hou, X.; Li, J.; Sun, L.; Wang, X. Coloration of Cotton Fibers with Anisotropic Silver Nanoparticles. Ind. Eng. Chem. Res. 2012, 51, 12807–12813. [Google Scholar] [CrossRef]*

16. Ilic, V.; Šaponjić, Z.; Vodnik, V.; Potkonjak, B.; Jovančić, P.; Nedeljkovic, J.; Radetić, M. The influence of silver content on antimicrobial activity and color of cotton fabrics functionalized with Ag nanoparticles. Carbohydr. Polym. 2009, 78, 564–569.

17. Neely, A.N.; Orloff, M.M. Survival of Some Medically Important Fungi on Hospital Fabrics and Plastics. J. Clin. Microbiol. 2001, 39, 3360–3361. [Google Scholar] [CrossRef] [PubMed] [Green Version]

18. Vivekanandhan S, Laura C, Manjusri M, Mohanty AK (2012) Green process for impregnation of silver nanoparticles into microcrystalline cellulose and their anti-microbial bionanocomposite films. J Biomater Nanobiotech 3:371–376.

19. Senthamarai Kannan M, Hari Haran PS, Sundar K, et al (2022) Fabrication of anti-bacterial cotton bandage using biologically synthesized nanoparticles for medical applications. Prog Biomater 11:229–241. https://doi.org/10.1007/s40204-022-00190-x

20. Balamurugan, M, Kandasamy, N, Saravanan, S, Ohtani, N, "Synthesis of Uniform and High-Density Silver Nanoparticles by Using Peltophorum pterocarpum Plant Extract", Jpn. J. Appl. Phys. 53 (5S1) 05FB19 1–7 (2014)

21. Li B, Li D, Wang J. Copper deposition on textiles via an automated dispensing process for flexible microstrip antennas. Text Res J 2014; 84: 2026–2035.

22. Kumar A, Nath K, Parekh Y, et al (2021) Antimicrobial silver nanoparticle-photodeposited fabrics for SARS-CoV-2 destruction. Colloids Interface Sci Commun 45:. https://doi.org/10.1016/j.colcom.2021.100542

CUTTING ROOM SOFTWARE: ENHANCING EFFICIENCY IN GARMENT PRODUCTION

Raşit Arsoy

Kafkas University, Fine Art Faculty, Department of Textile and Fashion Design, 36000, Kars, Turkey, +905077776250, rasit.arsoy@kafkas.edu.tr

Abstract

The rapid growth of the ready-to-wear industry has created a need for continuous improvement, along with the necessity to shorten production times and increase quality. The processes in this industry comprise a series of sequential activities carried out by machines and workers in a specific order. Particularly before cutting, checking model information is critically important. However, the various document formats used in the industry and the software employed to manage this data can complicate the work for personnel. In this context, there is a need for user-friendly software to enhance operational efficiency and minimize errors. This research aims to develop software focused on cutting processes. The developed software allows users to quickly and effectively access model and fabric information, measurement charts, and warehouse data, while simplifying complex processes. Additionally, its simple interface enables use without the need for special training and allows for the remote management of processes. As a result, the software aims to increase operational efficiency while reducing errors and workload.

Key words:

Software, Cut Order Plan, Wastage, Depot

1. Introduction

The rapid growth in the apparel industry has created a need for manufacturers to increase production speed, ensure product quality [10,4], and reduce material waste [7,17], particularly in the cutting process, leading to a demand for advanced approaches aimed at operational efficiency [20]. In this context, cutting, as a fundamental phase of the clothing production process, has a decisive impact on direct material usage, labor costs, and the quality of finished products [25,6,24].

Efficient cutting operations require the accurate and integrated management of technical drawings, model specifications, fabric details, measurement charts, and cut order plans (COP). However, this data is often stored in disconnected formats such as Excel sheets, PDFs, and JPEGs, and is delivered to the cutting room as physical files, which complicates efficient data sharing among departments.

These traditional methods can lead to inefficiencies, fabric waste, increased labor demands, and cost-increasing delays that jeopardize product standards, often relying on manual measurements, basic planning tools, and isolated data storage [18]. To overcome these issues, automation has emerged as a key solution for enhancing accuracy and efficiency [12,5].

In particular, the use of computer-aided software in garment production allows for the optimization of sewing room operations, machinists, cycle times, and the order of processes. These software solutions have the capacity to identify potential problems and test various scenarios to enhance production

efficiency [2]. Moreover, cutting optimization systems supported by advanced algorithms create automatic cutting plans that reduce costs, minimize errors, and increase overall management efficiency [22].

However, while some manufacturers prefer to use comprehensive production management software [16,3], these systems often contain dense data and require extensive training for operators [1]. This complexity limits the ability to access and modify task-specific data quickly, particularly considering the needs of the cutting room. The lack of software specifically tailored for cutting rooms has further highlighted the need for automation solutions that cater to the unique requirements of this department.

Software designed exclusively for cutting room operations resolves these issues by enabling operators to quickly access technical data, fabric information, measurement and layout details, inventory updates, and order changes. Such a system not only reduces the likelihood of human error but also allows the cutting department to rapidly adapt to changing production demands. The software contributes to an integrated structure of business processes by facilitating information connections among different departments. This enables rapid and effective communication of data across departments, allowing them to work in coordination rather than in isolation. This structural integrity enhances communication efficiency while simplifying access for all employees in every department.

This user-friendly, centrally managed data interface, accessible from any internet-connected device, reduces workforce requirements, increases productivity, and helps operators make timely, informed, and effective decisions. The use of software systems in cutting rooms not only provides better control over the production process but also contributes to significant improvements in quality and efficiency in the apparel industry by ensuring consistency and coherence in production.

2. Material and Method

In this study, a system has been developed to model the use of software before and after the cutting process in the ready-to-wear industry. Through this system, technical information about models and fabrics, measurement charts, and COP can be viewed, warehouse data can be entered, and calculations for fabric waste can be made. The information conveyed to the cutting room is organized by the production planning department, and access to this data is provided through a touch monitor located in the cutting room via the developed software. This integrated data/information system supports cutting room management processes by strengthening interdepartmental coordination and contributes to the effective management of resource utilization in production processes. The necessary operations in the study were performed using the Microsoft Visual Studio C# programming language. The reason for selecting this language is its widespread use and compatibility with Windows.

2.1. Main Interface

The program named Ready- to-Wear Cutting Room Plan (RWCOPlan), shown in Figure 1, consists of three main sections: New, Open Folder, and Quit. The program provides access to product model and fabric information, measurement charts, and COP, allowing for the entry and tracking of warehouse data. Additionally, the program has the capability to perform calculations for fabric waste.

When the "New" section in the interface is clicked, a window opens for adding and calculating new product data, consisting of six stages: general model, fabric sample, COP, measurement chart, waste, and warehouse. In this section, product data entered by the user is calculated by the software. The "Open Folder" section is for loading previous data, while "Quit" is used to close the software.

Figure 1. RWCOPlan programme's splash screen

2.2. Model Interface Section

In the Model section of the program, model information is entered into the system in the first step. At this stage, technical drawing information is also included in the system. The technical drawing of the garment is typically defined as a projection reflecting the correct proportions, lines, and silhouette details, often presented in a frontal or isometric view. These critical drawings convey the silhouette, structure, and design elements of the garment with clear and precise lines [15]. The cutting room staff can access the technical report of the model to be sewn, accurately understanding the product's proportions, stitching layout, finishing lines, and model details. A schematic of a new product model is shown in Figure 2.
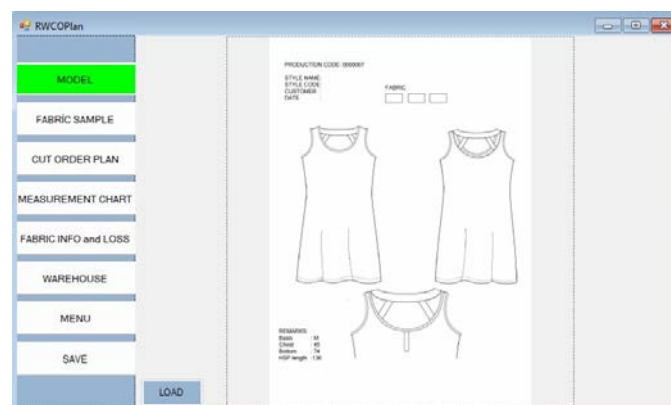
Figure 2. Technical drawing information interface page

2.3. Fabric Sample Interface Section

At this stage, information regarding fabric visuals related to the product is entered into the system. The pattern information page is shown in Figure 3.

Figure 3. Fabric sample section of the interface

2.4. Cut Order Plan Interface Section

The spreading length, ply and layer counts, and size distribution for each layer can be tracked from the COP created in the software. This report includes information such as the amount of fabric in the warehouse, total usage needs, and consumption values. This allows the operator to make the correct fabric selection, check the cutting quantities for ply, and conduct pre-cut pattern checks. COP is one of the challenging aspects of garment production and can be significantly improved through automation. The primary goal of COP is to optimize fabric usage, which generally constitutes 50% of production costs [23]. COP involves the layout design of garment parts and is carried out considering variables such as fabric properties and production volume. The intuitive algorithms used in this process provide optimized cutting plans that reduce material waste, cutting time, and cost [19,14]. Traditional COP methods are labor-intensive and prone to errors, potentially leading to unnecessary fabric waste. It is vital for the cutting room operator to verify COP data and compare it with the patterns on the fabric to minimize waste.

Figure 4. Cut Order Plan section of the interface

2.5. Measurement Chart Interface Section

In the next stage, measurement data is entered into the system. The measurement information from the technical file is shown in Figure 5. The creation of ready-to-wear products requires the formation of patterns according to standard sizing, measurement charts, and grading guidelines based on body measurements of the model [21]. The cutting room operator needs this data to verify pattern measurements on the fabric when necessary.

Figure 5. Measurement Chart section

2.6. Fabric Info and Loss Interface Section

At this stage, fabric information is entered, and the weight information obtained from the rested fabric rolls is recorded in the system. The difference in meterage indicated on the technical documents of fabric rolls and the meterage after resting is identified by the cutting room staff [8]. After the data is entered, the system automatically calculates the actual meterage. The values of waste such as fabric errors during spreading and cutting, excess fabric pieces, roll ends, and scraps are entered by the operator, allowing the total fabric loss to be calculated [13,9,11].

Figure 6. Fabric Info and Loss section

2.7. Warehouse Interface Section

In the final stage, warehouse codes and numbers are entered to easily locate the fabric's position in the warehouse. Efficient use of the workspace is essential for successful production. Organizing the shelves allows for easy access to fabric rolls and other materials, providing quick access during production. Software systems regulate inventory management by tracking the usage of fabric rolls in cutting rooms and ensure a workflow compatible with all production stages.

Figure 7. Warehouse section

3. CONCLUSION

In this study, it is aimed to create a software that enables the management of the information of the ready-to-wear enterprise with the support of an integrated data / information system within the scope of cutting room management and at the same time provides inter-departmental control.

The cutting room management software developed in the study stands out as a powerful tool that enables the effective fulfilment of critical functions such as planning, raw material selection, waste management and monitoring of production activities in garment production. Unlike complex general-

purpose production software, this software responds to the specific needs of cutting departments by offering a user-friendly and comprehensive interface. In particular, it allows operators to make quick adjustments by providing easy access to basic data such as cutting orders, fabric specifications and warehouse management. The simplicity and clarity of the interface is expected to not only increase productivity but also contribute to the operators to be more agile and responsive in the production process by minimising errors.

References

1. *Chaudhary, S., Pardeep, K., Johri, P. (2020). Maximizing Performance of Apparel Manufacturing Industry through CAD Adoption. International Journal of Engineering Business Management, 12, 1-4. doi:10.1177/1847979020975528.*

2. *Cocks, T., Harlock, S. (1989). Computer-aided Simulation of Production in the Sewing Room of a Clothing Factory. Journal of The Textile Institute, 80, 455-463. https://doi.org/10.1080/00405008908658298.*

3. *Cosma Technology. (2024). Digital Cutting Room Software. Retrieved June 15, 2024. https://cosmatechnology.com/software/digital-cutting-room-software-5.*

4. *Eroglu, D., Orbak, Â. (2019). Simulated Annealing Algorithm and Implementation Software for Fabric Cutting Problem. Textile and Apparel, 30(1), 10-19. https://doi.org/10.32710/tekstilvekonfeksiyon.521944.*

5. *Fernandes, S., Vidhya, D. S. (2021). Designing a Prototype of Automated Fabric Cutter. 2021 IEEE Bombay Section Signature Conference (IBSSC), 1-4. https://doi.org/10.1109/IBSSC53889.2021.9673395.*

6. *Guo-ning, Q. (2012). Two Stage Optimization Method of Cut Order Planning for Apparel Mass Customization. Computer Integrated Manufacturing Systems, 18(3), 479-485.*

7. *Indrie, L., Ilieva, J., Zlatev, Z., Tripa, S., Sturza, A. (2023). Development of an Algorithm for Textile Waste Arrangement. Sustainability, 15, 11399, https://doi.org/10.3390/su151411399.*

8. *Kalkancı, M., Kurumer, G. (2017). An Investigation About the Effects of Knitted Fabrics Dimensional Change on the Pattern Size in Garment Production. Pamukkale University Journal of Engineering Sciences, 23(7), 833-840.*

9. *Magowan, J. (1982). Optimising Material Utilisation. Readywear, 11, 28-31.*

10. *Michelini, R., Razzoli, R. (2013). Robotics in Clothes Manufacture. International Journal of Mechanical Engineering and Applications, 1, 17. https://doi.org/10.11648/J.IJMEA.20130101.13.*

11. *Milokhina, V.A., Burlakin, A.I., and Skututa, M.A. (1986). Use of a Regression Model to Calculate Fabric Loss along the Length of the Overlays. Tekhnologiya Legkoi Promyshlennosti, 29, 1(169), 90-91.*

12. *Nayak, R., Padhye, R. (2018). Introduction to Automation in Garment Manufacturing. (Nayak, R., Padhye, R. eds). In The Textile Institute Book Series, Woodhead Publishing, 1-27. https://doi.org/10.1016/B978-0-08-101211-6.00001-X.*

13. *Ng S.F., Hui, C.L., Leaf, G.A.V. (1998). Fabric Loss During Spreading: A Theoretical Analysis and its Implications. The Journal of The Textile Institute, 89(4), 686-695, doi: 10.1080/00405000.1998.11090907*

14. *Ranaweera, R., Rathnayaka, R., Chathuranga, L. (2023). Optimal Cut Order Planning Solutions Using Heuristic and Meta-Heuristic Algorithms: A Systematic Literature Review. KDU Journal of Multidisciplinary Studies. https://doi.org/10.4038/kjms.v5i1.66.*

15. *Rukavishnikova, A.S. (2016). Technical Drawıng in the System of Training of Bachelors Designers of Clothes. Modern Problems of Science and Education, 3.*

16. *Sentez Business Solutions. (2024). Cutting Card. Retrieved June 15, 2024. https://www.sentez.com/upload/Books/SenVogue/content/kesim.htm*

17. *Silva, E., Viães, C., Oliveira, J., Carravilla, M. (2015). Integrated Cutting and Production Planning: A Case Study in a Home Textile Manufacturing Company. (Póvoa, A., Miranda, J. eds). In:*

Operations Research and Big Data. Studies in Big Data, 15. Springer, Cham, 213-220. https://doi.org/10.1007/978-3-319-24154-8_25.

18. Silva, P., Lanel, G., Perera, M. (2017). Integer Quadratic Programming (IQP) Model for Cut Order Plan. IOSR Journal of Mathematics, 13, 76-80. https://doi.org/10.9790/5728-1302027680.

19. Tsao, Y., Linh, V., Liao, L. (2020). Hybrid Heuristics for the Cut Ordering Planning Problem in Apparel Industry. Computers and Industrial Engineering, 144, 106478. https://doi.org/10.1016/j.cie.2020.106478.

20. Ünal, C., Yüksel, A. (2020). Cut Order Planning Optimisation in the Apparel Industry. Fibres & Textiles in Eastern Europe, 28, 8-13. https://doi.org/10.5604/01.3001.0013.5851.

21. Vinué G., León, T., Alemany, S., Ayala, G. (2014). Looking for Representative Fit Models for Apparel Sizing. Decision Support Systems, 57, 22-33. https://doi.org/10.1016/j.dss.2013.07.007.

22. Wang, X., Huang, Z., Qiu, M., Zhang, F. (2012). Research in Garment Cutting Plan Optimization System. In: Soft Computing in Information Communication Technology. Springer Berlin Heidelberg, 403-409. https://doi.org/10.1007/978-3-642-29148-7_56.

23. Wong, W., Leung, S. (2008). Genetic optimization of fabric utilization in apparel manufacturing. International Journal of Production Economics, 114, 376-387. https://doi.org/10.1016/J.IJPE.2008.02.012.

24. Wong, W., Leung, S. (2013). Optimizing Cut Order Planning in Apparel Production Using Evolutionary Strategies. Optimizing Decision Making in the Apparel Supply Chain Using Artificial Intelligence (AI): From Production to Retail, Woodhead Publishing, 81-105. https://doi.org/10.1533/9780857097842.81.

25. Yan-mei, L., Shao-cong, Y., Shu-ting, Z. (2011). Research on Cut Order Planning for Apparel Mass Customization. In: Deng, H., Miao, D., Wang, F.L., Lei, J. (eds) Emerging Research in Artificial Intelligence and Computational Intelligence. AICI 2011. Communications in Computer and Information Science, 237. Springer, Berlin, Heidelberg, 267-271. https://doi.org/10.1007/978-3-642-24282-3_36.

THE TYPES OF TEXTİLES USED İN THE FAÇADE AND ROOFİNG SYSTEMS OF STADİUM FACİLİTİES İN TÜRKİYE

Yelda Durgun Şahin*, Mehmet Okur

Adana Alparslan Türkeş Science and Technology University, Faculty of Design and Architecture, Architecture Department, Adana, Türkiye, ydurgunsahin@atu.edu.tr*
Adana Alparslan Türkeş Science and Technology University, Institute of Graduate School, Adana, Türkiye, 23800901015@ogr.atu.edu.tr

Abstract:

Technical textiles are functional fabrics that have applications across including both construction (BuildTech) and architecture (ArchiTech). These technical textile is developed for high-tech and high-performance applications. In modern architecture, high-performance textile materials are highly valued and widely used in various applications, including self-cleaning, low-maintenance structures, fabric canopies, and energy-efficient buildings. They are also utilized for high-performance façades, energy-harvesting curtains, flexible mega-structures, responsive phase-change materials, air-supported fabric constructions, thermal regulation, green roofs, smart living spaces, acoustic solutions, advanced building materials, and creating habitable spaces in extreme weather conditions.

In this study, the types of textiles used in the façade and roofing systems of stadium facilities in Türkiye have been examined. The advantageous properties of textiles employed in stadium structures characterized by substantial roof and façade openings at the structural scale have been critically analyzed in relation to other conventional building materials. The technical textile material summary demonstrates the tremendous diversity of today's membrane materials using stadium facilities in Türkiye.

Key words:

Technical textiles /stadium facilities / façade and roofing system

1. Introduction

Technology-driven materials, designs, and construction techniques play a major role in façades and roofing systems, becoming essential elements of modern architecture (Göppert and Paech,2015).

Technical textile provide limitless opportunities for architectural expression, allowing for free-form and complex geometries that are both structurally viable and economically appealing in stadium building.

In Architextile composite structures, the use of glass, ceramic, carbon fibers, aramids, liquid crystal polymers, and high-modulus polyethylenes provides textile materials with high performance and quality (Gezer, 2008).

In a building, façade cladding materials serve different functions based on their various applications. When assessing the potential demands for each cladding material, the following can be highlighted as the most important.

That are protection from external environmental conditions (wind, rain, temperature, sun, etc.), creation of private interiors, cladding to withstand outer loads (wind, temperature,maintenance loads, etc.), thermal performance, solar/light performance, fire behaviour, durability, acoustic performance, aesthetic surface appearance (translucency, colour, etc.), possible complex architectural geometries, material weight for substructure design, material cost, installation cost/time and modularity, maintenance requirements, and/or replacement methods, recyclability, sustainability (Göppert and Paech,2015., Hernández, 2006).

According to the literature, it can be observed that studies on the performance of textile materials used in the façades and roof coverings of stadium structures have focused on topics a, b, and c.

The relationship between early textile architecture in history and in modern period textile façade and roofing systems differs from a period where materials were applied in layer by layer to a more technologically advanced approach that integrates these layers together.

A wide variety of fabric materials are used in architecture. These are evaluated as PVC Fabric (PVC-Coated Polyester), PVDF, PVF, PTFE Fabric (PTFE Coated Fiberglass), Fabric options – PVC and PTFE, PVC / Polyester fabric, and PTFE / Fiberglass fabric (Gandi, 2020., Kamal, 2020).

In stadium structures, a wide variety of textile membrane composite materials are used in façade systems. Based on the expected demand requirements from these materials, combinations of various materials are utilized for textile membrane composites. Architectural fabrics are commonly woven from polyester (PES) yarns coated with polyvinyl chloride (PVC) or from glass fiber yarns coated with either polytetrafluoroethylene (PTFE) or silicone. The purpose of the coating is to shield the yarn fibers from environmental factors while also enabling individual membrane segments to be welded together. Uncoated fabrics are typically composed of PTFE or polyvinylidene fluoride (PVDF).

Uncoated fabrics are typically made from PTFE or polyvinylidene fluoride (PVDF). Textile membranes can either be fully coated to create a water- and wind-proof fabric with translucencies of approximately 0–40%, or woven with gaps between the yarns to form an open mesh membrane with localized yarn coatings. These mesh membranes are commonly used for sunscreens and architectural envelopes that provide views in two directions. Various mesh patterns are available, differing in size and arrangement of open areas. Both glass/PTFE and PES/PVC membranes come in multiple colors, with some being printable for a customized appearance. Depending on structural requirements, different strength classes are offered. Recently, laminated open mesh membranes have been developed, featuring a continuous lamination of transparent fluoropolymers, offering high transparency (>50%) and material strengths up to 60 kN/m (Göppert and Paech,2015).

Different fibrous materials shaped by knitting and weaving techniques in textile technology are also used in architectural façades (Gezer, 2007/a; Garcia, 2006). Woven and knitted fabrics made from metal fibers, as well as steel wire meshes, are examples of materials used in stadium façades.

The performance of fabric structures is significantly influenced by the environment in which they are located. Key factors affecting fabric performance include geographic latitude and temperature, UV radiation, humidity, pollution levels, dust accumulation, cleaning frequency, deposition of plant matter, staining from rainwater runoff, and exposure to rainfall that helps remove dirt and dust (Tolani, 2016., Kamal, 2020). The characteristics of textile materials used in stadium structures built in Türkiye have been grouped according to these factors. The grouping has been evaluated based on regions, taking into account the differing seasonal characteristics.

2. The Roofing Materials Used in Stadium Structures

Factors determining the selection of roofing materials include climate, architectural and structural design, and cost estimation. The roof surface is a layer exposed to external elements. The roofing material must be resistant to atmospheric conditions. Therefore, the covering material should have water and thermal insulation properties, a long service life, and be lightweight while also conforming to the shape of the roof (Durgut, 2019).

3. Material Properties

Materials should be selected and designed according to the function of the structure. The materials used for the façade and covering systems of stadium structures directly affect user comfort. Therefore, the compatibility between structure and covering materials in stadium buildings is a crucial issue that must be addressed (Durgut, 2019). Materials have a direct impact on visual, acoustic, and climatic comfort. Technological advancements and innovations in façade and covering materials have brought criteria such as long-term durability, fire resistance, ease of replacement and repair, material permeability, sustainability, and user comfort to the forefront. With a material selected for its permeability feature, daylight can easily enter the field, ensuring the healthy growth of the field grass (Seçgin, 2023).

With advancing technology, newly developed materials are frequently preferred due to characteristics such as their lightness, strength, flexibility, and load-bearing capacity. Today, a wide variety of materials are predominantly used in stadium structures, including steel, concrete, new-generation plastics (ETFE, PTFE, PVC, etc.), aluminum, galvanized sheet metal, and smart materials.

PVC (Polyvinyl Chloride) and PVDF (Polyvinylidene Fluoride) Membrane Covering

While the lifespan of PVC is between 10 and 15 years, it can extend up to 25 years with a PVDF (Polyvinylidene Fluoride) coating. It offers a variety of colors and is more cost-effective than other building materials. PVC is waterproof and, with its light-transmitting property, allows natural light to enter the space, reducing the need for artificial lighting. It has strong UV resistance, high fire resistance, and is a lightweight, recyclable material (Alioğlu, 2018; Uğurlu, 2021).

PTFE (Polytetrafluoroethylene) Textile Membrane

PTFE is a textile material used in façade and covering systems, consisting of fiberglass fabric coated with Teflon resin. Commercially known as Teflon, it has a lifespan of approximately 30-50 years and starts to degrade above 250 degrees Celsius. It offers strong UV resistance, high fire resistance, and reflects about 60% of light. It does not mold or yellow under atmospheric conditions and is waterproof. PTFE withstands temperatures ranging from -73°C to +232°C. Single-layer membrane structures made with PTFE reflect 75% of sunlight and absorb 10% of it (Krüger, 2009; Durgut, 2019).

ETFE (Ethylene Tetrafluoroethylene) Membrane Covering

ETFE is a fluorine-based plastic material used in air-supported covering systems, with a thickness between 0.05 and 0.20 mm. It has high light and UV transmittance, an approximate lifespan of 100 years, and is recyclable (Compagno et al., 2004; Durgut, 2019). ETFE allows 90-97% of light to pass through. Thanks to the air between the foil layers in ETFE cushions, it provides better insulation than glass panels. ETFE foils are flame-resistant and can withstand temperatures up to 270°C (Durgut, 2019). ETFE material can also be integrated with textile materials in façade and covering systems.

Carbon Fiber (CF)

Carbon fiber is a technologically advanced material with a fibrous structure composed of tar, nylon, and orlon, known for being rigid, lightweight, and durable. It offers high strength, is resistant to corrosion and fire, and is non-flammable. Although it is costly, its application requires specialized experience and equipment (Bajpai, 2013).
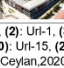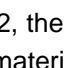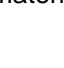
4. Review of Stadiums in Türkiye According to Roof and Facade Material Selections

In the literature, due to the direct impact of materials on comfort, Türkiye's 7 climate zones have been examined, and façade and roof covering material selections for stadium structures have been analyzed according to these regions. Table 1 provides an overview of technical textiles used in stadium architecture applications in Türkiye.

The use of textiles as façade and roofing materials is achieved through one of the textile types: plain PVC, perforated (mesh), PTFE (Teflon), and ETFE materials. When grouping these textile types according to regions, eight stadium structures built in the Marmara Region were examined. Of these, one stadium uses only PVC membrane covering, while three use a combination of PVC membrane covering and other cladding materials. One stadium uses both PVC membrane and PTFE textile covering along with other cladding materials. Another uses PTFE textile covering, one employs aluminum roofing, and another combines PVC membrane and PTFE textile coverings. Overall, a mixed covering system has been applied in five of the stadiums.

In the Aegean Region, four stadium structures were examined. Of these, two use only PVC membrane covering, one uses a combination of PVC membrane and other (composite cladding) covering systems, and one utilizes an alternative (polycarbonate cladding) system. In the Central Anatolia Region, five stadiums were studied; two of these use a mixed system of PVC membrane and other covering materials, while another two use a combination of PVC membrane and PTFE textile covering. Lastly, one uses an aluminum roof covering. In the Black Sea Region, three stadiums were analyzed, all of which share PVC membrane covering as a common feature. Among these, one employs a combination of PVC membrane and PTFE textile covering, one combines PVC membrane and other covering materials (PVC mesh), and one uses PVC membrane alone. In the Mediterranean Region, of the five stadiums constructed, two use PVC membrane alone, two combine PVC membrane with other covering systems (PVC mesh and standing seam roof), and one uses a combination of PVC membrane, ETFE membrane, and other (standing seam roof) systems. In Southeastern Anatolia, three stadiums were examined: one uses a mixed system of PVC membrane, PTFE textile, and other (GFRC, GRC precast) covering systems, one uses ETFE membrane, and one employs other (composite cladding). In Eastern Anatolia, two stadium coverings were analyzed: one uses PVC membrane, while the other combines polycarbonate and standing seam roofing systems.

Table 1. Material Selections and Stadium Facilities in Türkiye

Region	Photo	Stadium Name	City	Construction Year	Construction Site	Capacity (Spectators)	Classification According to Cover System	Classification According to Stadium Tribune Covering System	Facade and Covering System	Materials
Marmara Region		Atatürk Olympic Stadium (1,2)	İstanbul	2002	240.929 m² (Land Area)	77563	Semi-Covered	Semi-Covered	Steel, Concrete	1. PVC Membrane Covering
		Ali Sami Yen Sports Complex Rams Park (1,3,4,31)	İstanbul	2011	82.000 m²	52600	Semi-Covered	Covered	Steel, Membrane	1. PVC Membrane Covering, 4.Other(Compact Laminate Panel)
		Fenerbahçe Şükrü Saraçoğlu Stadium (1,5,6)	İstanbul	Renewal: 2006	55.000 m²	50530	Semi-Covered	Covered	Steel, Membrane ve Aluminum	1. PVC Membrane Covering, 4.Other(Composite)
		Beşiktaş Park Stadium (1,7,8,9)	İstanbul	2016	50.000 m²	42590	Semi-Covered	Covered	Steel, Concrete, Membrane	2. PTFE Textile Membrane Covering
		Yüzüncüyıl Atatürk Stadium (Bursa Timsah Arena) (1,7,10,11,64)	Bursa	2015	179.611 m²	43361	Semi-Covered	Covered	Steel, Membrane	1.PVC Membrane Covering ,2.PTFE Textile Membrane Covering
		Kocaeli Stadium (7,12)	Kocaeli	2018	90.700 m²	34829	Semi-Covered	Covered	Steel, Aluminum	4.Other (Aluminum Roof Covering)
		Sakarya Stadium (7,14,15,16,69)	Sakarya	2017	128.000 m²	28154	Semi-Covered	Covered	Steel, Membrane	1. PVC Membrane Covering,2.PTFE Textile Membrane Covering ,4.Other (PVC Mesh)
		Başakşehir Fatih Terim Stadium (34,35,36,37)	İstanbul	2014	160.000 m²	17300	Semi-Covered	Covered	Steel, Aluminum	1. PVC Membrane Covering, 4.Other (Glass, Composite)
Aegean Region		İzmir Atatürk Stadium (17)	İzmir	Renewal:2005	216.330 m² (Land Area)	51337	Uncovered	Semi-Covered	Steel, Concrete, Membrane	1. PVC Membrane Covering
		Gürsel Aksel Stadium (38,39,40)	İzmir	2020	94.541 m²	25000	Semi-Covered	Covered	Steel, Aluminum	4.Other (Precast, Polycarbonate)
		İzmir Alsancak Stadium (18,61)	İzmir	2021	22.500 m²	15000	Semi-Covered	Semi-Covered	Steel, Membrane	1. PVC Membrane Covering
		Akhisar Stadium (67)	Manisa	2018	52.137 m² (Land Area)	12139	Semi-Covered	Covered	Steel, Membrane	1. PVC Membrane Covering, 4.Other (Composite)
Central Anatolia Region		Konya Metropolitan Municipality Stadium (1,7,19,65)	Konya	2014	90.000 m²	42000	Semi-Covered	Covered	Steel, Membrane	1. PVC Membrane Covering, 4. Other (Transparent Membrane)
		Yeni Eskişehir Stadium (41,42)	Eskişehir	2016	86.783 m²	34930	Semi-Covered	Covered	Steel, Aluminum	1. PVC Membrane Covering, 4.Other (Aluminum Panel)
		Kayseri Kadir Has City Stadium (32,33)	Kayseri	2009	80.000 m²	32864	Semi-Covered	Covered	Steel, Aluminum	4. Other (Aluminum Roof Covering)
		Sivas 4 Eylül Stadium (43,44,45)	Sivas	2016	58.700 m²	27532	Semi-Covered	Covered	Steel, Membrane	1- PVC Membrane Covering ,2.PTFE Textile Membrane Covering
		Eryaman Stadium (46,47)	Ankara	2016	37.462 m²	20672	Semi-Covered	Covered	Steel, Aluminum	1. PVC Membrane Covering,2. PTFE Textile Membrane Covering
Black Sea Region		Şenol Güneş Sports Complex (Akyazı Stadium) (7,20,21,63)	Trabzon	2016	170.000 m²	41131	Semi-Covered	Covered	Steel, Membrane	1. PVC Membrane Covering,2.PTFE Textile Membrane Covering
		Samsun 19 Mayıs Stadium (22,23,66)	Samsun	2017	140.000 m²	33919	Semi-Covered	Covered	Steel, Membrane	1. PVC Membrane Covering, 4.Other (PVC Mesh)
		Giresun Çotanak Sports Complex (24,62)	Giresun	2022	89.673 m²	21500	Semi-Covered	Covered	Steel, Membrane	1. PVC Membrane Covering
Mediterranean Region		Yeni Adana Stadium (28,29,30)	Adana	2021	78.012 m²	33543	Semi-Covered	Covered	Steel, Membrane	1. PVC Membrane Covering, 4.Other (PVC Mesh)
		Antalya Stadium (48,49,50)	Antalya	2015	87.331 m²	29307	Semi-Covered	Covered	Steel, Aluminum	1. PVC Membrane Covering, 4.Other (Standing Seam Roof)
		Mersin Stadium (1,7,25,68,70)	Mersin	2013	55.000 m²	25534	Semi-Covered	Covered	Steel, Membrane	1. PVC Membrane Covering
		Yeni Hatay Stadium (58,59)	Hatay	2021	55.395 m²	25000	Semi-Covered	Covered	Steel, Aluminum, Standing Seam	1. PVC Membrane Covering
		Alanya Oba Stadium (57)	Alanya	2011	23.000 m²	9789	Semi-Covered	Covered	Steel, Composite	1. PVC Membrane Covering, 3.ETFE Membrane Covering, 4.Other (Standing Seam Roof)
Southeastern Anatolia Region		Gaziantep Stadium (7,13,26)	Gaziantep	2017	61.215 m²	33502	Semi-Covered	Covered	Steel , Aluminum	1. PVC Membrane Covering,2. PTFE Textile Membrane Covering,4.Other (PTFE Mesh, GFRC, GRC Precast)
		Diyarbakır Stadium (27)	Diyarbakır	2018	50.000 m²	33000	Semi-Covered	Covered	Steel,Membrane	4. Other (Composite)
		11 Nisan Stadium (55,56)	Şanlıurfa	2009	36.400 m²	28965	Semi-Covered	Covered	Steel, Aluminum	3.ETFE Membrane Covering
Eastern Anatolia Region		Yeni Malatya Stadium (52,53,54)	Malatya	2017	93.000 m²	25745	Semi-Covered	Covered	Steel, Aluminum	1. PVC Membrane Covering
		Elazığ Atatürk Stadium (51,60)	Elazığ	Renewal: 2023	55.395 m²	17600	Semi-Covered	Covered	Concrete, Steel, Standing Seam	4. Other (Polycarbonate, Standing Seam Roof)

(1): Arslan,2016. , **(2)**: Url-1, **(3)**: Url-2, **(4)**: Url-3, **(5)**: Url-4, **(6)**: Url-5, **(7)**: Bülbül,2017, **(8)**: Uğurlu,2021, **(9)**: Url-6, **(10)**: Kara,2020, **(11)**: Url-7, **(12)**: Url-8, **(13)**: Url-9, **(14)**: Url-10, **(15)**: Url-11, **(16)**: Url-12, **(17)**: Url-13, **(18)**: Url-14, **(19)**: Kurumak,2019, **(20)**: Url-15, **(21)**: Url-16, **(22)**: Url-17, **(23)**: Url-18, **(24)**: Url-19, **(25)**: Url-20, **(26)**: Url-21, **(27)**: Url-22, **(28)**: Url-23, **(29)**: Sürgülü, 2023, **(30)**: Url-24, **(31)**: Gözütok, 2019, **(32)**: Url-25, **(33)**: Url-26, **(34)**: Url-27, **(35)**: Url-28, **(36)**: Url-29, **(37)**: Ceylan,2020, **(38)**: Url-30, **(39)**: Url-31, **(40)**: Url-32, **(41)**: Url-33, **(42)**: Url-34, **(43)**: Url-35, **(44)**: Url-36, **(45)**: Url-37, **(46)**: Url-38, **(47)**: Url-39, **(48)**: Url-40, **(49)**: Url-41, **(50)**: Url-42, **(51)**: Url-43, **(52)**: Url-44, **(53)**: Url-45, **(54)**:Url-46, **(55)**: Url-47, **(56)**: Url-48, **(57)**: Url-49, **(58)**: Url-50, **(59)**: Url-51, **(60)**:Url-52, **(61)**: Url-53, **(62)**: Url-54, **(63)**: Url-55, **(64)**: Url-56, **(65)**: Url-57, **(66)**: Url-58, **(67)**: Url-59, **(68)**: Url-60, **(69)**:Url-61, **(70)**: Url-62

In Table 2, the distribution of materials used in stadiums by region can be seen. In Table 3, the usage rates of materials used in stadiums across Türkiye are shown.
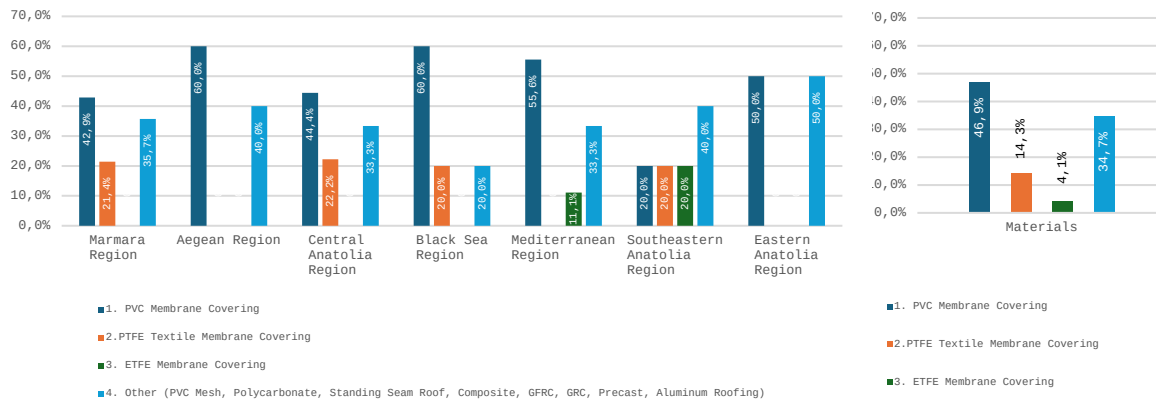
Table 2. Materials Used in Stadiums by Region

Table 3. The Use of Materials in Stadiums in Türkiye

In Türkiye, regarding the roofing material usage in stadiums, a single roof material using is utilized in 43,3% of cases, while 56.7% prefer composite material usage. A stadium roof design plays a critical role in determining the amount of light that penetrates the field, thereby affecting the growth of the turf. If the roof design is not covered with an appropriate light-transmitting material, artificial lighting has to be used to sustain grass growth. This practice contradicts the principle of sustainability and results in significant energy costs. In line with the UN (United Nations)'s SDG 7 and SDG 11 principles, it is recommended that the design of the southern facade and roof sections of stadium structures incorporate a light-transmitting textile material to promote low-energy, sustainable living environments

5. RESULT

Technological advancements playing a role in architectural textile interactions are influencing the shaping of architectural structures. As a sustainable material, the high-performance textile group stands out and diversifies into new composite forms through technological advancements. This diversity not only makes significant contributions to stadium architectural design but also alters the symbolic values of the structure on an urban scale. Among the examined examples, regional differences have been observed in the textile materials used for stadium facades and roofing. Facade and roofing materials selected in harmony with the covering system and structural characteristics play a key role in the formal shaping of stadium structures, enhancing their visibility within the city. Material choices become the focal point of stadium designs, and the way the selected material is used gives the structure an iconic quality. This study has presented that PVC membrane coverings are the most commonly used in stadiums in Türkiye. The study has shown that the use of composite materials is also prevalent as a secondary choice in facade and covering systems.

The findings of the study have shown that in Türkiye, covering materials used in stadiums were not selected in accordance with the climate characteristics of the regions, nor was light permeability taken into consideration. This lack of alignment could lead to issues in the development of grass in stadiums, supporting the hypothesis that this relational mismatch may contribute to such problems. In this context, the study serves as a foundation for further research.

References

1. Alioğlu, T. (2018). Tekstil Esaslı Malzemelerin Mimaride Kabuk Tasarımında Kullanımı ve Sürdürülebilirlik Açısından Değerlendirilmesi. Doktora Tezi, İstanbul Aydın Üniversitesi, Fen Bilimler Enstitüsü, İstanbul, Türkiye.

2. Arslan N. (2016). Stadyum Yapılarının Tasarım Kriterlerinin Uluslararası Yönetmelikler Doğrultusunda İncelenmesi, Yüksek Lisans Tezi, Yıldız Teknik Üniversitesi Fen Bilimleri Enstitüsü, İstanbul, Türkiye.

3. Bülbül E. (2017). Stadyum Yapılarındaki Strüktür Sisteminin Biçim Oluşumuna Etkisi, Yüksek Lisans Tezi, Gazi Üniversitesi, Fen Bilimleri Enstitüsü, Ankara, Türkiye.

4. Ceylan E.E. (2020). Enerji Etkin Stadyum Tasarım Kriterleri Önerisi, Yüksek Lisans Tezi, Konya Teknik Üniversitesi Lisansüstü Eğitim Enstitüsü, Konya, Türkiye.

5. Durgut S. (2019). Stadyum Yapılarında Çekmeye Çalışan Çatı Strüktürleri Kullanımının Kronolojik Değerlendirilmesi, Yüksek Lisans Tezi, Dokuz Eylül Üniversitesi Fen Bilimleri Enstitüsü, İzmir, Türkiye.

6. Göppert, K., & Paech, C. (2015). High-performance materials in façade design Structural membranes used in the building envelope. Steel Construction 8 (4), pp.237-243.

7. Garcia, G., (2006), November- December "Prologue For A History and Theory of Architextiles", Architectural Design- Architextiles, 13-20.

8. Gandhi, U. (2020) Design and Construction of Tension Membrane Structures. [Online] Available from http://homepages.cae.wisc.edu/~ukgandhi/documents/tensile%20structures_paper.pdf, accessed on 25 July 2020.

9. Gezer, H., (2006), "Titanyum'un Konut Mimarisinde ve İç Mekan Düzenlemelerinde Kullanılması", TMMOB Mimarlar Odası Yayını, ISBN 9944-89-196-7, 480-487, İstanbul.

10. Gezer,H., (2008). Üretim Alanında Tekstil ve Mimari Arasındaki Etkileşim. İstanbul Ticaret Üniversitesi Fen Bilimleri Dergisi Yıl:7 Sayı:13 Bahar 2008/1 s.21-49.

11. Gözütok M.M. (2019). Stadyumlarda Uygun Akustik Ortamın Oluşturulması Bağlamında Genel İlkelerin Belirlenmesi, Yüksek Lisans Tezi, Yıldız Teknik Üniversitesi, Fen Bilimleri Enstitüsü, İstanbul, Türkiye.

12. Hernández, M.J.J., (2006). Fabric Membranes As Daylighting Control Systems In Buildings. Doctor of Philosophy, The University of Nottingham.

13. Kamal, A.M.(2020). An investigation into tensile structure system: construction morphology and architectural interventions. Journal of Building Materials and Structures. 7: 236-254

14. Kurumak M. (2019). Stadyum Tasarımında Ulusal/Uluslararası Standartlara Göre Seyirci Mekanlarının Analizi,Konya Büyükşehir Stadyumu Örneği, Yüksek Lisans Tezi, Necmettin Erbakan Üniversitesi, Fen Bilimleri Enstitüsü,Konya, Türkiye.

15. Seçgin M. (2023). Stadyumların Örtü Sistemlerinin Örneklerle İncelenmesi, Yüksek Lisans Tezi, İstanbul Aydın Üniversitesi Lisansüstü Eğitim Enstitüsü, İstanbul, Türkiye.

16. Sürgülü U. (2023). Stadyum Yapılarında Çatı Strüktürlerinin İncelenmesi, Yüksek Lisans Tezi, Yıldız Teknik Üniversitesi, Fen Bilimleri Enstitüsü, İstanbul, Türkiye.

17. Uğurlu İ. (2021). Stadyum Yapılarında Hareketli Cephe ve Örtü Malzemelerinin Mimari Biçim Oluşumu Üzerindeki Etkileri, Yüksek Lisans Tezi, Fatih Sultan Mehmet Vakıf Üniversitesi Lisansüstü Eğitim Enstitüsü, İstanbul, Türkiye.

18. Url 1: https://yuzuncuyilgalerisi.eba.gov.tr/tema/ataturk-olimpiyat-stadyumu 18#:~:text=Atat%C3%BCrk%20Olimpiyat%20Stad%C4%B1%2C%20Uluslararas%C4%B1%20Atletizm,antrenman%20ve%20%C4%B1s%C4%B1nma%20alan%C4%B1%20mevcuttur.

19. Url 2: https://erkel.com.tr/referanslarimiz/turk-telekom-arena/

20. Url 3: http://www.mtfproje.com.tr/portfolios/turk-telekom-arena/

21. Url 4: https://tr.wikipedia.org/wiki/Fenerbah%C3%A7e_%C5%9E%C3%BCkr%C3%BC_Saraco%C4%9Flu_Stadyumu#:~:text=Mimarisi%20dikd%C3%B6rtgen%20%C5%9Feklinde%20olan%20bu,100%20tane%20VIP%20locas%C4%B1%20bulunmaktad%C4%B1r.

22. Url 5: https://www.ozaymuhendislik.com.tr/pg_212_sukru-saracoglu-fenerbahce-stadyumu

23. Url 6: https://www.dbarchitects.com.tr/tr/bjk-vodafone-arena/

24. Url 7: https://tr.wikipedia.org/wiki/Y%C3%BCz%C3%BCnc%C3%BC_Y%C4%B1l_Atat%C3%BCrk_Stadyumu

25. Url 8: https://alperaksoy.com.tr/proje/kocaeli-arena-stadyumu-35000-kapasite-146

26. Url 9: https://www.tensaform.com/tr-TR/catalogue/tamamlanmis-projeler/39?searchText=stadyum

27. Url 10: https://www.asma-germe.com/tr/projeler

28. Url 11: https://alperaksoy.com.tr/proje/sakarya-arena-stadyumu-105#

29. Url 12: https://www.erduman.com.tr/project/sakarya-stadyumu/

30. Url 13: https://en.wikipedia.org/wiki/%C4%B0zmir_Atat%C3%BCrk_Stadium

31. Url 14: https://alperaksoy.com.tr/proje/izmir-alsancak-stadyumu-159

32. Url 15: https://www.erduman.com.tr/project/trabzonspor-senol-gunes-stadyumu/

33. Url 16: https://www.trthaber.com/haber/spor/ktuden-medical-park-stadyumu-aciklamasi-655114.html

34. Url 17: https://tr.wikipedia.org/wiki/Samsun_19_May%C4%B1s_Stadyumu

35. Url 18: https://www.passo.com.tr/tr/mekan/25715/25715

36. Url 19: https://www.tucsa.org/tr/celik_yapilar_yazi.aspx?yazi=1013

37. Url 20: https://tr.wikipedia.org/wiki/Mersin_Stadyumu,

38. Url 21: https://www.tucsa.org/images/celik_yapilar/54/53_celik_yapilar.pdf

39. Url 22: https://tr.wikipedia.org/wiki/Diyarbak%C4%B1r_Stadyumu

40. Url 23: https://www.stendustri.com.tr/adana-stadi-projesinde-serge-ferrari-farki

41. Url 24: https://www.dbarchitects.com.tr/tr/adana-stadyumu/

42. Url 25: https://tr.wikipedia.org/wiki/Kayseri_Kadir_Has_%C5%9Eehir_Stadyumu

43. Url 26: https://bkaarchitecture.com/projects-item/kayseri-kadir-has-stadium/

44. Url 27: https://tr.wikipedia.org/wiki/Ba%C5%9Fak%C5%9Fehir_Fatih_Terim_Stadyumu

45. Url 28: http://www.suldem.com/basaksehir_fatih_terim_stadyumu.html

46. Url 29: https://erketasarim.com/projelerimiz/sosyal-kullanim-amacli-projeler/basaksehir-fatih-terim-stadyumu

47. Url 30: https://www.dbarchitects.com.tr/tr/goztepe-gursel-aksel-stadyumu/

48. Url 31: https://www.polikarbonat.com/goztepe-gursel-aksel-stadyumu-10-mm-solid-polikarbonat-cati-kaplamasi/

49. Url 32: https://www.raf.com.tr/goztepe-gursel-aksel-stadyumu/

50. Url 33: https://www.eskisehirspor.org.tr/stadyum

51. Url 34: https://stadiumdb.com/stadiums/tur/eskisehir_stadyumu

52. Url 35: https://tr.wikipedia.org/wiki/Yeni_4_Eyl%C3%BCl_Stadyumu

53. Url 36: https://bkaarchitecture.com/projects-item/sivas-stadium/

54. Url 37: https://www.passo.com.tr/en/venue/45216/45216

55. Url 38: https://www.dbarchitects.com.tr/tr/ankara-eryaman-stadyumu/

56. Url 39: https://tr.wikipedia.org/wiki/Eryaman_Stadyumu

57. Url 40: https://tr.wikipedia.org/wiki/Antalya_Stadyumu

58. Url 41: https://www.antalyaspor.com.tr/tr/tesislerimiz/antalyaspor-stadyumu.html

59. Url 42: https://eskametal.com/tr/uygulama-birimi/

60. *Url 43: https://alperaksoy.com.tr/proje/elazig-ataturk-stadyumu-ve-spor-salonu-17600-kapasite-200#*

61. *Url 44: https://atakeng.com.tr/portfolio-items/malatya-stadyumu/*

62. *Url 45: https://bkaarchitecture.com/projects-item/malatya-stadium/*

63. *Url46: https://ilci.com.tr/proje/25-000-ki%CC%87s%CC%A7i%CC%87-kapasi%CC%87teli%CC%87-malatya-s%CC%A7ehi%CC%87r/*

64. *Url 47: https://tr.wikipedia.org/wiki/11_Nisan_Stadyumu*

65. *Url 48: https://azaksu.com/tr/spor/urfa-stadyumu*

66. *Url 49: https://tr.wikipedia.org/wiki/Alanya_Oba_Stadyumu*

67. *Url 50: https://alperaksoy.com.tr/proje/hatay-arena-stadyumu-30000-kapasite-136#*

68. *Url 51: https://www.baselyapi.com.tr/projects/proje-adi-03/*

69. *Url 52: https://tucsa.org/tr/celik_yapilar_yazi.aspx?yazi=1443#:~:text=Projede%20çim%20sahanın%20gün%20ışığından,çatıda%20ve%20cephede%20yırtıklar%20açılmıştır.*

EFFECT OF RECYCLED COTTON YARN CONTENT ON FINISHED KNITTED FABRIC PERFORMANCES

Buket Güler[1], Ismet Ege Kalkan[2], Umut Kıvanç Şahin[3], Merve Çelik[4], Ahmet Çöklü[5]

[1]TYH Textile Research and Development Center, Istanbul, Turkey, buketguler@tyh.com.tr
[2] Department of Textile Engineering, Istanbul Technical University, Istanbul, Turkey, kalkani15@itu.edu.tr
[3]Department of Textile Engineering, Istanbul Technical University, Istanbul, Turkey, sahinumut3@itu.edu.tr
[4]TYH Textile Research and Development Center, Istanbul, Turkey, mervecelik@tyh.com.tr
[5]Perge Tekstil İşletmeleri A.Ş., Tekirdağ, Turkey, ahmetcoklu@pergetekstil.com.tr

Abstract:

In order to achieve the objectives of safeguarding human health, maintaining the environment, cutting waste, and leaving a habitable planet for future generations, sustainability is essential. Given the influence of rapid fashion, rising population, and improving living standards, the world's consumption of cotton fiber is steadily rising. Waste yarns are the starting point for studies aiming at giving waste value addition and creating affordable new yarns because in Turkey's yarn sector, they are frequently neither recycled nor sold at low costs. Turkey is a leader in both cotton production and consumption, which indicates the potential for advancements in this area to have a direct impact on the nation's economic growth. Within the scope of the study, fabrics produced from yarns spun from fibers combined in various ratios were compared. Five different yarns were produced: 100% conventional cotton, 80% conventional-20% recycled cotton, 50% conventional-50% recycled cotton, 20% conventional cotton - 80% recycled cotton, and 100% recycled cotton. Single jersey fabrics were developed from the obtained yarns. Pilling and stiffness tests of the fabrics were carried out and analysed. According to the results obtained, the composition containing 50% conventional and 50% recycled cotton was found to be optimum in terms of both stiffness and pilling resistance.

Key words:

Sustainability, Recycle, Knitting, Physical Tests

1. Introduction

The cultivation of cotton is fraught with environmental difficulties, raising questions about its long-term viability. Conventional cotton farming requires a lot of water, a lot of fertilizer and pesticides, and the occupation of arable land that could be used to grow food [1]. Moreover, the increasing need for textiles has amplified the environmental consequences of fiber production, specifically in the textile sector. Studies like those conducted by Choudhury (2014) highlight the threats that the textile industry's reliance on hazardous and toxic chemicals poses to freshwater and atmospheric micro-systems, as well as the fact that these chemicals contribute to environmental degradation and the release of pollutants throughout a textile product's lifecycle [2]. The textile sector faces significant obstacles in recycling cotton due to inadequate waste collection and categorization processes and little awareness, even with the rising market. Positively, producing cotton from recycled materials has significant environmental benefits. It is a major factor in environmental sustainability since it conserves natural resources and uses less water and energy. Furthermore, the production of recycled cotton is essential for reducing waste

throughout the textile manufacturing process, hence addressing issues associated with excessive waste formation. Furthermore, by using less energy and relying less on fossil fuels, the procedure reduces the carbon footprint of textile products. Furthermore, by lowering air pollution produced during the textile manufacturing process, the production of recycled cotton helps to improve the quality of the air [3].

In this project, pilling and stiffness tests of fabrics developed with yarns spun from conventional cotton and recycled cotton were performed and comparative analyses were carried out. In line with the tests, the optimum blend ratio was determined and 3D design and sample production were carried out.

2. Experimental

2.1. Materials

In this project, a total of 5 different 20/1 Ne yarns were used in the following mixing ratios (Table 1). These yarns were produced by the Open-End method.

Table 1. Developed yarn compositions

Sample No	Yarn composition (%)	
	Conventional Cotton	Recycled Cotton
1	100	0
2	80	20
3	50	50
4	20	80
5	0	100

From these yarns, single jersey fabrics knitted on the Mayer circular knitting machine at 26 inches and 22 fine values were supplied by TYH Tekstil A.Ş. All fabrics are dyed in navy blue color.

2.2. Methods

In the scope of the study, different recycled fiber blended yarns were produced and single jersey fabrics were knitted with these yarns. Then, stiffness and pilling tests were performed on these fabrics and comparative analyses were carried out. The stiffness test was carried out with a digital pneumatic hardness tester in accordance with ASTM D4032-08 test method (Figure 1a). Pilling test was carried out with JAMES H. HEAL brand device in accordance with TS EN ISO 12945-1 standard (Figure 1b).
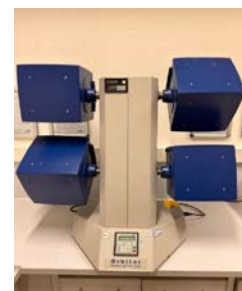
a   b
Figure 1. Test equipment used (a. Stiffness tester; b. ICI pilling tester)

3. Results and discussion

Bending strength and pilling tests were carried out on test specimens of knitted fabrics in different blends. The stiffness results of the test specimens are given in Table 1. When the fabric stiffness test results were evaluated, it was determined that the stiffness decreased up to a certain point in recycled

yarn blended fabrics, and after a certain point, the stiffness increased with the increase in the recycle rate. Pilling test results are presented in Table 2. When these results are considered, it is observed that the pilling values are negatively affected with the increase in the recycling rate. This indicates that recycled yarn may create more roughness and fiber protrusion on the surface of the fabric, thus negatively affecting pilling resistance.

Table 2. Fabric Stiffness Test Results

Sample No	Stiffness (kgF)
1	0,031
2	0,026
3	0,023
4	0,039
5	0,037

Table 3. Pilling Test Results

Sample No	Value
1	4
2	4
3	3/4
4	3/4
5	2/3

Increasing the recycled cotton content slightly increases stiffness while decreasing pilling resistance. 50% conventional and 50% recycled fabric provides a balance of medium stiffness (0.023 kgF) and reasonable pilling resistance (3/4). These results show that as the recycled yarn ratio increases, there is an initial improvement in the softness and flexibility properties of the fabric, but as the recycling ratio increases, fabric stiffness and pilling tendency are negatively affected.

This analysis demonstrates the effect of blending recycled cotton with conventional cotton on the mechanical properties of the fabric, such as stiffness and pilling. This information can be useful in optimizing fabric blends to achieve desired durability and comfort properties. This study provides a basis for understanding the delicate balance between sustainability and performance and can guide the development of textiles containing recycled cotton.

4. CONCLUSIONS

In this study, the effect of recycled cotton yarn content on the stiffness and pilling behavior of finished knitted fabrics was investigated. The results revealed that an increase in recycled cotton content leads to a decrease in fabric durability in general, especially in terms of pilling resistance. Fabrics with higher recycled content exhibited more pronounced pilling which can be attributed to shorter fiber lengths and lower overall strength of the recycled fibers. However, despite these challenges, the sustainable benefits of using recycled cotton yarn, such as reduced environmental footprint and resource consumption, make it a promising option for environmentally friendly textile production. Future work could focus on optimising yarn blends and processes to reduce negative impacts on fabric performance while maximising sustainable benefits.

In the continuation of the study, it is planned to carry out dimensional stability, fastness, bursting strength and air permeability tests and continue studies on optimising yarn blends to reduce the negative effects of recycled cotton yarn content.

ACKNOWLEDGEMENTS

References

1. *Chapagain, A. K., Hoekstra, A. Y., Savenije, H. H., & Gautam, R. (2006). The water footprint of cotton consumption: An assessment of the impact of worldwide consumption of cotton products on the water resources in the cotton producing countries. Ecological economics, 60(1), 186-203.*
2. *Choudhury, A.R. (2014). Environmental Impacts of the Textile Industry and Its Assessment Through Life Cycle Assessment. In Roadmap to Sustainable Textiles and Clothing. Textile Science and Clothing; Muthu, S., Ed.; Springer: Singapore, pp. 1–39.*
3. *Ütebay, B., Çelik, P., & Çay, A. (2019). Effects of cotton textile waste properties on recycled fibre quality. Journal of Cleaner Production, 222, 29-35. https://doi.org/10.1016/j.jclepro.2019.03.033*

NUMERICAL SIMULATIONS OF 3D-DISTANCE FABRICS

Vlastimil Votrubec

Svárovská 619, Liberec XI – Růžodol I, 460 01 Liberec, Czech Republic
VÚTS, a.s., Department of Virtual and Applied Mechanics, vlastimil.votrubec@vuts.cz,
+420485302387

Abstract:

This paper presents the results of numerical simulations conducted on inflated panels made from 3D distance fabrics. 3D distance fabrics constitute a subset of 3D woven fabrics. If coated, the structure of the fabric permits the formation of a panel with parallel layers through the process of air inflation. The pressurised air creates a stiff, lightweight and fail-safe structure that can be utilised in a multitude of applications. The mechanical behaviour of these panels can be described analytically by appropriate mathematical theory; however, this approach remains limited to common loading cases. This paper presents computational method for numerical simulations of inflated panels, including determination of the deflections of skins and the distribution of stress. The simulations are based on the results of material property tests and a nonlinear geometric model. The results are then compared with the mathematical theory and experimental data. The results demonstrate the efficacy of this approach and illustrate its advantages. Furthermore, an illustrative example of a specific loading case is presented to demonstrate the versatility of this approach for predicting the behaviour and conducting structural analysis of loaded 3D fabric panels.

Key words:

Simulations, FEM, distance fabric, 3D fabric

1. Introduction

3D distance fabric is composed of two distinct skins, the upper and lower fabrics, which are simultaneously woven and connected by pile (drop) yarns (Figure 1). The pile yarns serve to lock the two skins together, thereby creating a robust connection. The base fabrics are separated from one another by a distance equal to the length of the pile yarns. This length constitutes a fundamental parameter of the fabric, as it defines its shape and stiffness, and is contingent upon the properties of the weaving machine. This is typically maintained at a constant length, ensuring that the inflated panel exhibits parallel and uniform surfaces. It is likewise feasible to weave distance fabrics with varying lengths of pile yarns; however, the primary advantage of this structure lies in its parallelism of skins. The skins are rendered impermeable through the application of an additional coating material (e.g. PVC, polychloroprene, etc.). The stability and load capacity of inflatable panels depend on their material properties, air pressure, fabric parameters, and shape. During inflation, the air pressure causes biaxial pretensioning of fabric layers and elongation of pile yarns, thereby enabling the panel to achieve the requisite shape and stiffness. 3D distance fabrics, also known as drop-stitched fabrics or space fabrics, offer numerous advantages, including a lightweight structure, portability in a non-inflated state, and a fail-safe mechanism during overload conditions.
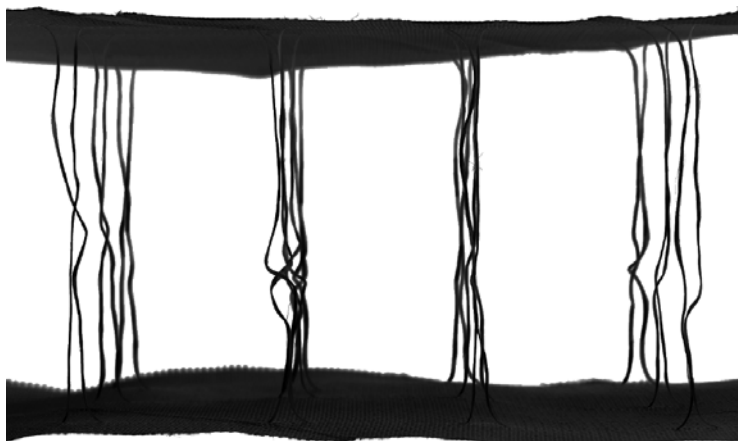
Figure 1. An example of 3D distance fabric.

The research of 3D fabrics is primarily concerned with woven and knitted fabrics in general where yarns in the third axis are present and the thickness of the fabric is negligible. A survey of 3D woven fabrics can be found in references [1, 2, 3]. Earlier research on the mechanics of inflatable fabric structures was limited, with only a few studies conducted on distance fabric panels [4]. Cavallaro [5] described the mechanics of a panel subjected to a four-point bending load, utilising experimental data from material tests to inform his analytical model. Additionally, he conducted an experiment on a bent panel for comparison. Hou [6] employed the finite element method to model knitted spacer fabric. A notable area of development has been the utilisation of these fabrics as reinforced composites [7].

The paper outlines the creation of an appropriate material model and the requisite tests for it (Chapter 2). It then describes the general rules for building FEM model of the panels and presents the building of a specific FEM model of a panel based on real-world testing (Chapter 3). It then presents the results of the simulations and discusses the comparison with the theoretical and experimental results (Chapter 4). Finally, it presents the simulation of an overloaded panel as an illustrative example of the indispensable role of numerical simulations in the design and analysis of distance fabric panels (Chapter 5).

2. Material model

A comprehensive understanding of the material data is essential for the successful development of a model. In order to serve as a point of reference, real coated 3D distance fabric was selected for the purposes of experimental and simulation validation. The fabric is composed of a primary fabric woven on a weaving machine DIFA produced by VÚTS, a.s. All yarns (warp, weft and pile) are made of polyester (PES) with a fineness of 55 tex. The outer surfaces of the fabric skins were coated with polychloroprene on a nylon fabric substrate. The coating does not typically impact the mechanical properties of the material; however, it does ensure airtightness. Figure 2 illustrates the structure of the fabric and its basic textile properties, as produced by the Taiwan Textile Research Institute.

Figure 2. The 3D distance fabric made by Taiwan Textile Research Institute. Total warp pile is 64 650 with different density after warp (150 ends/10 cm) and weft (4.31 ends/ 10 cm). The length of pile yarns is 180 mm.

Textile materials, including yarns and fabrics, typically exhibit nonlinear tensile properties. However, the deviation from linearity is typically minor, with a constant young modulus. Fabrics are composed of two types of yarns: warp and weft. These are woven with varying densities, and warp and weft yarns may also differ in material and fineness. Consequently, fabrics are orthotropic materials, exhibiting nonlinear properties in both the warp and weft directions.

The tensile curves of the fabric were measured on a universal testing machine (Instron) in accordance with the standard ISO 13934-1, which outlines a procedure for determining the maximum force and elongation at maximum force using a strip method. Furthermore, the specimens were modified to a dog-bone shape, thereby ensuring that rupture occurred in the centre of the specimen, rather than in the jaws (Figure 3 on the left). The specimens were marked with white dots on the coated surface in order to facilitate the measurement of strain with an optical extensometer. The pile yarns were measured in accordance with the standard ISO 2062 on the same testing machine with pneumatic textile jaws (Figure 3 on the right). For the purpose of measuring strain, small balls with a through hole were placed and glued on the yarns. A tensile test was conducted on fabric skins and pile yarns using a universal testing machine.

Figure 3: Tensile test of fabric skin and pile yarns using a universal testing machine.

The tensile curves are presented in Figure 4. It is evident that there is a notable distinction between the warp and weft tensile properties, as well as a nonlinear character. However, the divergence from the linear course is not substantial, and for the purposes of simulations, it can be approximated by a line. Notably, in the initial portion of the tensile curve, the variance is minimal. In the textile industry, it is customary to relate the tensile properties, strength of the fabric, and young modulus to the unit width of a fabric. Similarly, this approach is also employed in this case.

It should be noted, however, that FEM software requires the input of a material model in stress/strain quantities. Therefore, both tensile curves of fabric and pile yarns are recalculated in order to obtain the stress-strain dependence, despite the fact that the absolute values lack practical significance.

The combination of a nonlinear tensile curves and an orthotropic material presents a significant challenge for modelling. The nonlinear solver in the Siemens NX software is designed to work with isotropic nonlinear materials or orthotropic linear materials. However, it has been observed that using linear and orthotropic materials results in a smaller error. The calculated Young modulus of fabric is 428 MPa for the warp and 299 MPa for the weft.
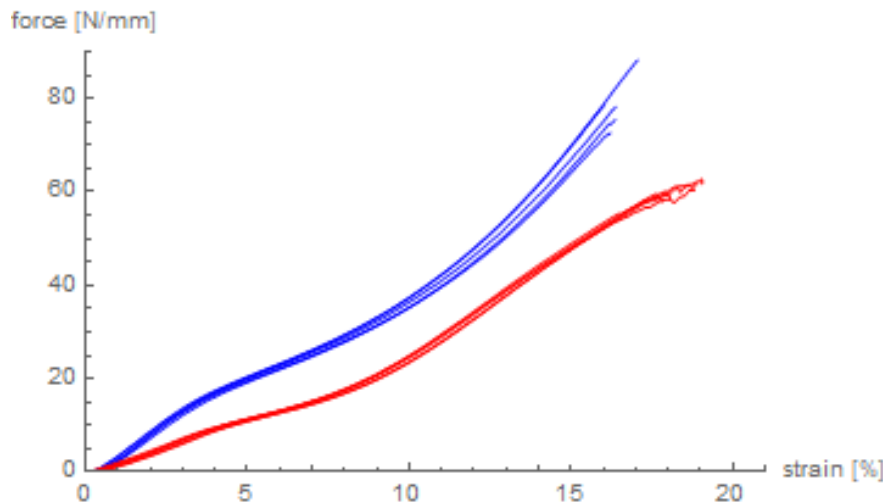
Figure 4. The tensile curves of the fabric skin for both the warp and weft directions. The units are related to the 1 mm width of the fabric.

3. FEM model

The FEM model was built in a manner analogous to that of the tested panel. The dimensions of the panel used for experiments are identical to those of the modelled panel, namely 94 x 94 mm in area, 180 mm in thickness and subjected to a loading pressure of 100 kPa. The tested panel differs in that the edges were affixed by adhering the ends of the fabric and clamping them together with steel bars. The common application of a glued belt necessitates the replication of this panel in the same manner.

It is essential to prepare the geometry of the fabric panel in an inflated state. There is no relevant reason for simulating the panel in its undeveloped state, as this would entail significant difficulties. The model's geometry corresponds to the state, wherein the pile yarns are extended but the axial force is still zero, and the fabric skin between the binding points is not deflected. The side belt of the panel is affixed to the upper and lower skins, and thus is modelled and simulated. However, the model lacks a glue layer, the fabrics (and meshes) are connected directly. This is a reasonable simplification, as the stress distribution is analysed with precision and the computation is considerably more straightforward. Furthermore, potential sources of computational errors in corners are eliminated.
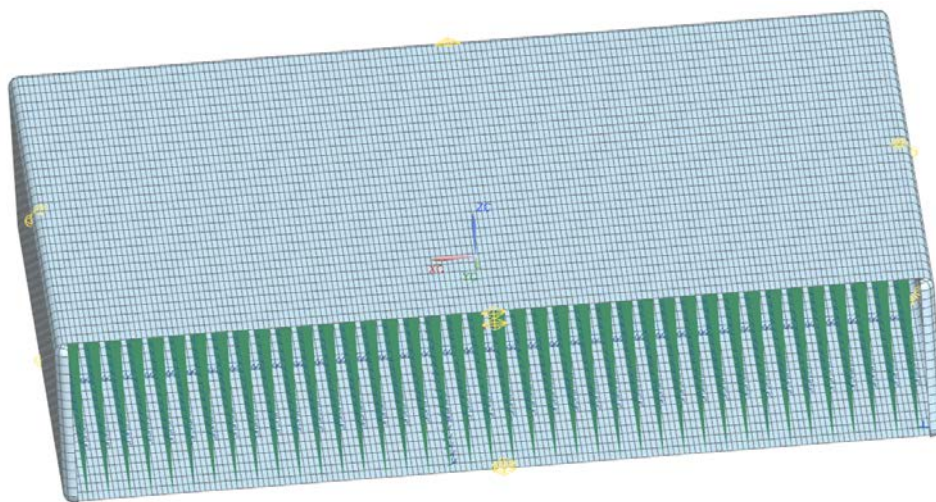
Figure 5. A section of the simulation model of the 3D distance panel. The mesh on the skins is created in such a way that four elements are placed after warp, which ensures an accurate representation of skin deflection. The green lines represent pile yarns, while the blue crosses represent suppressed displacements.

A further significant issue pertains to the question of bending stiffness. The actual bending stiffness of a fabric can be considered to fall between the values of a membrane, which exhibits no bending stiffness, and a solid sheet, which demonstrates full bending stiffness and is dependent on the thickness of the fabric. The modelling of fabric as an aerial body can be achieved through the use of shell elements. These elements permit the setting of arbitrary bending stiffness, although this is limited to a linear solver. Consequently, the bending stiffness cannot be adjusted. The behaviour of coated fabric is further complicated by the fact that the coating is situated on only one side of the fabric. This results in a dependence of the bending stiffness on the direction of bending loading, as the coated side of the fabric exhibits a greater bending stiffness than the uncoated side.

Pile yarns are represented as one-dimensional continuous rod (CROD) elements. The aforementioned elements are responsible for connecting the upper and lower skins, which have been prepared in accordance with the specified nodes, in a regular pattern. Non-linear material is assigned to these elements, thereby allowing for compression without stiffness. The young modulus of the tensile part of the curve is calculated from the measured tensile curve, while the young modulus of the compression part of the curve is set to be almost zero (zero is not a viable option). The inflation of the panel results in significant displacement of the side belt, causing the edgings of the skins to move towards the centre plane of symmetry. Here, the pile yarns undergo a reduction in length with no resistance, while in the middle of the panel, the pile yarns experience an increase in length.

The boundary conditions include the pressure loading on the inner walls and the suppressed displacements at specific nodes. The pressure value was set to 100 kPa, which is typical for common applications. All lower binding points (nodes for pile yarns) were disabled to enable vertical movement, thereby simulating the free inflation of the panel. To suppress displacement of the panel in both horizontal axes, one line of lower nodes in each direction was disabled to move.

4. Simulation results

The simulation results, namely the fabric deflections (Figures 6 and 7), are in accordance with the observed experimental outcomes. The greatest deflection is observed in the panel sides, which lack the fixation provided by pile yarns in the upper and lower skins. However, from the perspective of mechanics and real-world applications, the displacement of the fabric in the vertical direction (z-axis) is of greater significance. It is expected that the elongation of the pile yarns (measured in distance) will correspond to the results obtained from the experimental and analytical studies. A closer examination of the fabric surface reveals a series of undulations, indicative of a pronounced deflection of the fabric between pile yarns following the warp direction. Conversely, the deflection of the fabric between pile yarns after weft is nearly negligible. The discrepancy can be attributed to the notable disparity in the density of the pile yarns following the warp and weft processes. The height of the "wave" (the distance between the binding point and the peak value) is another crucial parameter in panel mechanics. It is also employed for the validation of simulations, with a value of 0.8 mm for a 100 kPa pressure within the panel.
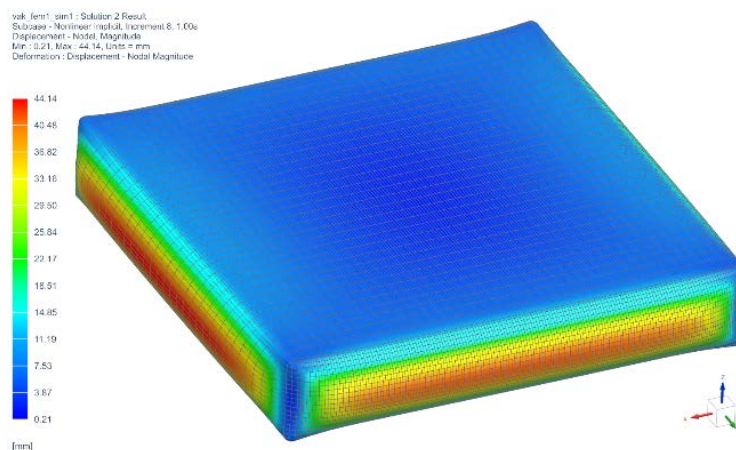
Figure 6. Displacements of pressure loaded fabric panel.
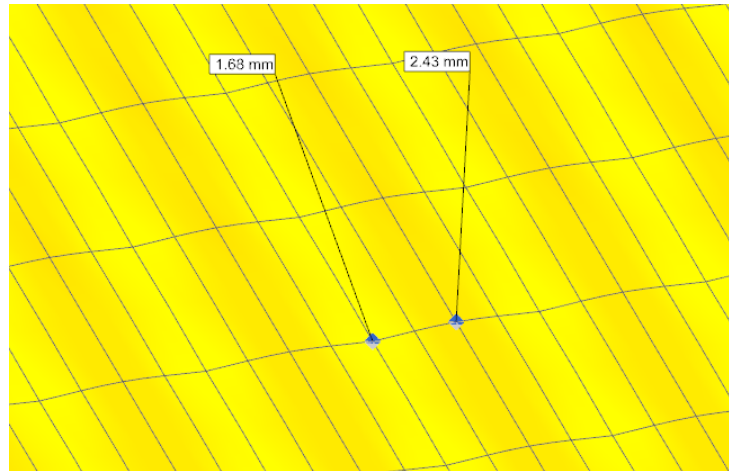
Figure 7. A detail of the displacements of the vertical axis of the bent fabric skin between the pile yarns.

The values of strain and displacement demonstrate that the stresses are minimal, falling below the ultimate strength of the fabric and pile yarns. The concentration of stress is observed to be located around the mesh connections in corners where the simulation consistently produces slight distortions in the results. Another location of concentration of stress is in binding points, where the material exhibits non-standard behaviour. Nevertheless, the stress is consistently below the ultimate strength.

5. A comparison between the experimental and theoretical results

The deflection of skin u between binding points after warp is described by the following relation

$$u(x) = \frac{D}{H}\frac{1}{k}\left(\frac{e^{k(D-x)}+e^{kx}}{e^{kD}-1} - \frac{e^{kD}+1}{e^{kD}-1}\right) - \frac{(D-x)^2}{H} + \frac{D}{H}(D-x),$$

where D represents the distance between the binding points after warp, H denotes the length of the pile yarns, and k incorporates the bending stiffness. This equation integrates the theories of thin plates and membrane theory. If the bending stiffness is disregarded (first bracket), the deflection shape transforms into a parabolic function. The maximum deflection occurs at the midpoint of the arc, where $x = D/2$.

The objective of the experiment was to measure the height of the profile (deflection of the skin) by means of a laser scanner and to compare the experimental data with theoretical predictions and then the simulation results (Figure 8). The vertical distance from the scanner was recorded for an increasing level of pressure. The test was concluded at the level of 120 kPa of air pressure inside the panel. Both the experimental and theoretical aspects were described in detail in paper [8], and thus no further details are provided here.

Figure 8. The 3D distance fabric panel during the safety test. In the center there are visible deflections of the skin between binding points that were measured by a laser scanner.

The data presented in Figure 9 comprises measured data, calculated data derived from aforementioned equation, and data obtained from the simulation. The data demonstrate a high degree of correlation. The displacements calculated from the FEM simulations exhibit discrepancies from the experimental data, particularly in the mid-arc region where the curve intersects with the theoretical curve, which does not account for bending stiffness. Closer to the margins of the arc the simulation curve is getting nearer to the experimental data. However, due to the inherent limitations of the FEM model, as previously discussed, the agreement between the simulation and experimental data is still fine. When considering the absolute values of displacement along the arc, it is evident that the exact value is not a crucial parameter for practical applications. Instead, it serves primarily to validate the mathematical theory and ensure the accuracy of the simulations.
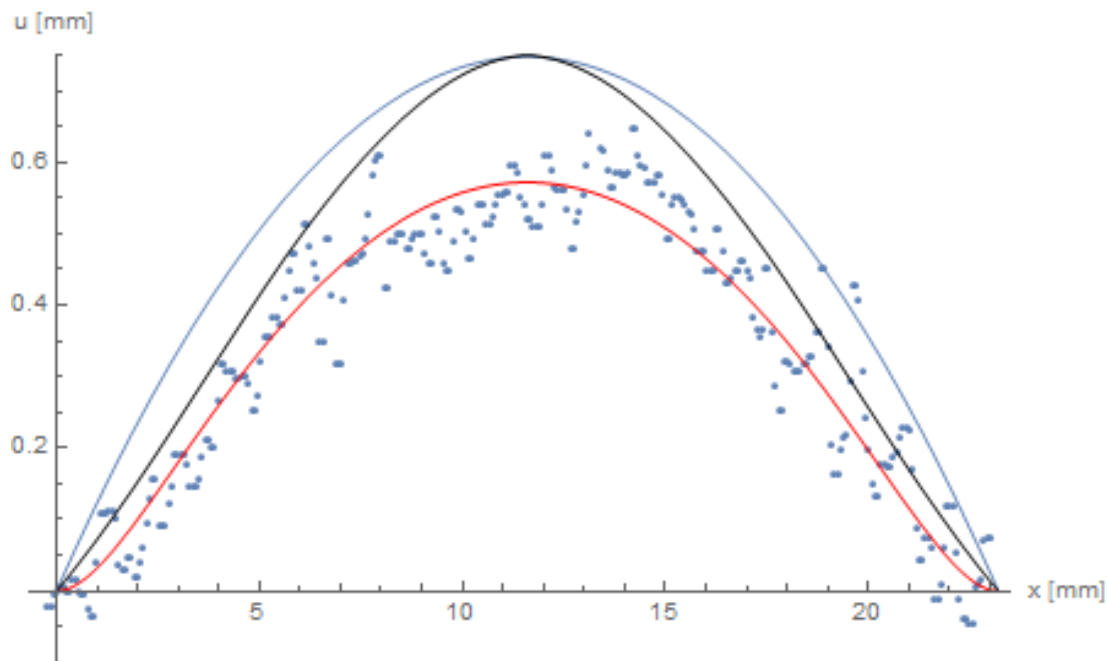
Figure 9. A comparison of the measured deflection of the fabric skin, loaded by 100 kPa (blue dots). The theoretical curve, derived from the equation, is shown in red. The interpolated simulation data is represented in black and a theoretical curve, which neglects the bending stiffness, is illustrated in blue.

6. A case study of an overloaded panel

The advantages of this methodology are readily apparent when considering the example of the overloaded fabric panel. The panel is typically loaded by its working pressure, as illustrated in the preceding example. Additionally, it is subjected to a force 15 kN acting on an area of approximately 120 x 150 mm. This force causes significant deflection of the upper skin, with a maximum value of 78 mm. The depression almost reaches approximately half of the panel thickness, which is clearly unacceptable in practical terms. The maximum values of stress and strain are considerably higher than the typical range, yet they remain within the third of the tensile curve, indicating that the structure remains safe. Nevertheless, a discernible decline in stability is evident, attributable to the considerable displacements. The fabric between the depression and the panel edge exhibits slight warping, which presents numerical challenge. A larger load would result in computational collapse, which is not viable state for the panel. While the expansion of the panel can be well described analytically using the elongation of pile yarns, the external compression of the panel must be computed numerically. As with loading of panel sides, combined loading or complicated boundary conditions require the use of a numerical simulation via the finite element method is irreplaceable.
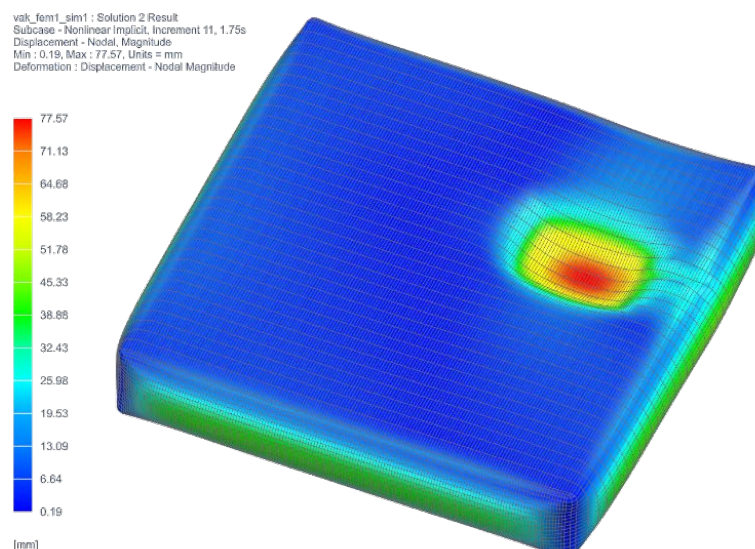
Figure 10. A case study of an overloaded fabric panel. Large displacements occur in the place of loading.

7. CONCLUSIONS

In many cases, numerical simulations are an invaluable tool for the analysis and design of air inflated 3D distance fabric structures. These simulations are based on precise material testing and the nonlinear computation of appropriate FEM software. The correlation between the outcomes of these simulations and the mathematical theory, as well as the results of physical experimentation, is highly satisfactory, thereby substantiating the efficacy of this approach. The benefits of simulation are most evident in the context of structures subjected to challenging boundary conditions, as illustrated by the example of an overloaded panel.

ACKNOWLEDGEMENTS

References

1. *Badawi, S. S. Development of weaving machine and 3D woven spacer fabric structures for light-weight composite materials, Ph.D. Thesis, Technical university in Dresden, Dresden, Germany, 2007.*
2. *Chen, X. Advances in 3D Textiles, Woodhead Publishing, 2015.*
3. *Gokarneshan, N., Alagirusamy, R. Weaving of 3D fabrics: A critical appreciation of developments, Textile Progress 41 (1) (2009) 1-58.*
4. *Falls, J., Waters, J. K. Bending test of inflatable dropstitch panel, Proceedings of the 11ᵗʰ International Conference on Fast Sea Transportation, Hawai, USA, 2011.*
5. *Cavallaro, P. V., Hart, C. J., Sadegh, A. M. Mechanics of air-inflated drop-stitched fabric panels subject to bending loads, Proceedings of ASME International Mechanical Engineering Congress and Exposition, ASME, 2013.*
6. *Hou, X., Hu, H. Silberschmidt, V. V. A study of computational mechanics of 3D spacer fabric: Factors affecting its copmression deformation, Journal of Material Science 47 (2012) 3989-3999.*
7. *Chen, X., Taylor, L. W., Tsai, L. J. An overview on fabrication of three-dimensional woven textile preforms for composites, Textile Research Journal 81 (2011) 932-944.*
8. *Votrubec, V., Žák, J. Mechanics of air-inflated 3D distance fabric. Applied and Computational Mechanics 15 (1), 2021, 85 – 96.*

ANALYSIS OF ELASTIC YARN POSITIONING IN THE KNITTED STRUCTURES

Liudmyla Melnyk[1], Irena Lenfeldová[2], Olena Kyzymchuk[3]

[1]Kyiv National University of Technologies and Design, Kyiv, Ukraine, melnik.lm@knutd.edu.ua
[2]Technical University of Liberec, Liberec, Czech Republic, Irena.Lenfeldova@tul.cz
[3]TUD Dresden University of Technology, Dresden, Germany, olena.kyzymchuk@mailbox.tu-dresden.de

Abstract:

Elastic textile materials, namely knitted structures, are now successfully used for different applications: sports garments, medical products, vanity garments, everyday conventional clothes and so. The biggest application is for medical purposes as elastic materials are the main part of compression garments, prevention and rehabilitation products. This work aims to analyze the methods for introducing an elastomeric thread into the knitted structure. It was found that the use of miss knitting according to a repeat is a promising way to reach both the high level of elastomer fixing in the structure and the requirements for rehabilitation products namely stretchability and elasticity. As a result, 20 novel knitted structures were developed using five miss stitch repeats and four options for elastomeric thread incorporation into the weft knitted structure. Both parameters affect the fabric`s density especially course-wise. The future research steps have been defined.

Key words:

elastic fabric, weft knitting, elastomeric thread, miss stitch, yarn positioning, knitted structure

1. Introduction

Elastic textile materials are successfully used for medical purposes namely for manufacturing rehabilitation products. Knitting is the most common method used, since this technology is characterized by flexibility, the ability to quickly respond to changes in requirements for both the material structure and its properties with minimal costs for the assortment changing. The required physical and mechanical properties of knitted material namely extensibility and elasticity are possible due to the use of elastomeric threads. The peculiarity of such elastic materials is the pressure level exerted on the body when using the product in a stretched state that forms their main functionality. However, the materials' properties largely depend on the positioning and the fixing method of the elastomer threads in the knitted structure. This work aims to analyze the options for introducing elastomeric thread into the knitted structure and to determine the most optimal variant that meets the requirements for rehabilitation products.

Knitted structures are characterized by a wide variety of interlooping due to the use of different elements: loops, tuck and float stitches, and additional inlaid thread. Both weft and warp knitting is used for medical rehabilitation products manufacturing [2]. There are many studies of elastic knitted fabrics produced by using different elastic threads (bare polyurethane or core spun yarn with elastic core) and different methods of their introduction into the structure. When designing a knitted structure with an elastic thread, it is necessary to ensure the following: the reliable fastening elastomer in the structure, uniformity of the loop structure, and certain elastic properties. Additionally, when using bare

elastomer it is important to provide a high cover factor by ground yarn to avoid its contact with the human body.

In warp knitting the elastic materials are produced mostly as a band of a certain width [9]. The elastomeric thread is introduced longitudinally in every wale or according to the repeat [8], which provides the maximum stretchability and elasticity in this direction. In addition, bare spandex or polyurethane is usually used, since the elastomer is located inside the fabric structure and does not contact the environment and the human body [7]. In this case, the elastomeric threads are fixed in the knitted structure due only to the friction between the yarns. Thus the elastomeric thread can escape when a load is applied. The best fixation of elastomer is achieved by loop formation. Warp-knitted power net or sleeknit structures from Lycra are used for compression garment production [12]. The rate of stress relaxation in the lengthwise direction was similar to the weft knitted structure.

The weft knitting enables more possibility in elastic fabric development due to variety of the methods for elastomer incorporation into the knitted structure. The simplest way is to use core-spun yarn with an elastic core and knit it as conventional yarn [1]. Any interlooping both single or double can be used and fabric will be bi-stretch [10]. If bare elastane (lycra, polyurethane, latex) is used, plating with conventional yarn is the preferred method for knitted fabric formation [4]. The elastomer can be fed along conventional yarn in each system [15] or according to certain repeats [16]. It should be noted that such materials are mostly used in sports compression clothing or everyday garments provided low or medium compression levels.

The number of publications regarding elastic fabrics focuses on medical compression stockings. Single jersey [10] or a combination of knit and tuck loops [6] knitted from core-spun yarn along the conventional yarn (cotton or polyester) are the main structures used for their production. To provide high elasticity of the fabric [11] and the necessary compression level [13] of the final product, additionally, elastic yarn is laid horizontally [15] in each course or according to the certain repeat. These structures provide high fixation of inlaid elastomer due to the high density of ground interlooping.

The positioning of an elastomer yarn as weft in single and double weft knitted structures is used as well. In the work [14] it is proposed to introduce an elastomeric thread as weft between the loops from conventional yarn into single jersey and Rib fabric. The assessment of mechanical properties showed a similarity between them. In another research [3] two-layered samples combined jacquard-laid-in patterns with elastomeric weft threads were used for the production of knitted orthopedic supports. As for these structures, the elastomeric thread can escape when a load is applied coursewice similar to warp knitted fabric. The higher fixing level of transverse weft can be achieved by miss-knitting of elastomeric yarn through a certain number of needles [17].

The above review shows that elastomer positioning as an inlaid thread in a double weft knitted structure provides a high cover by ground yarns and high elasticity. At the same time, the elastomer fixing in the structure does not reach the required level. The use of miss knitting according to a repeat for elastomer is a promising way to solve the task but it is not fully investigated. To cover this gap the novel elastic knitted fabrics were developed by incorporating elastomer using miss stitches.

2. Materials and Methods

For this research four options (Figure 1) of elastomeric thread incorporation into the weft knitted structure were chosen using the miss stitches. The loops from elastomer thread were formed in every second course on one or both needle beds, cross or behind each other. One (options A and B) or two (options C and D) elastomeric threads were incorporated into courses. To investigate the effect of miss stitch`s repeat on the fabric`s performance the number (k) of miss stitches in the repeat was from 2 to 10 with 2 needles increments. 20 knitted structures were developed totally. The fabric`s cod

contains a letter reflecting the option of elastomeric thread incorporation A, D, C, or D and a number reflecting the number of miss stitches in the repeat (k=2, 4, 6, 8, or 10).
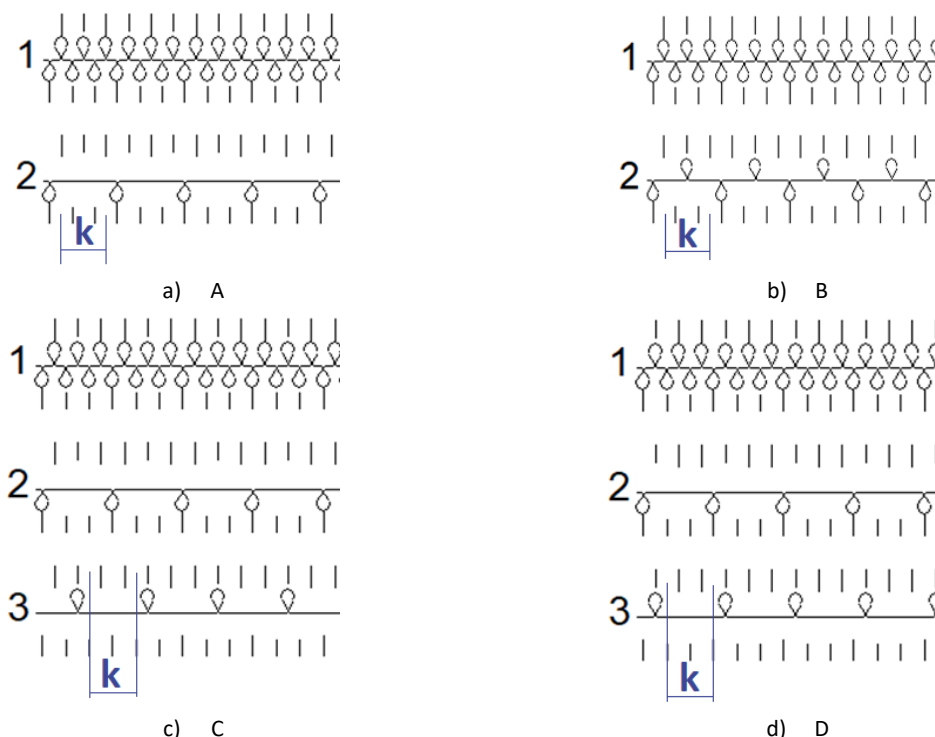
Figure 1 Graphical notation of interloping for different options: 1 – ground yarn; 2 and 3 – elastomer

All samples were produced in the knitting lab of the Technical University of Liberec on a 12-gauge SRY 123LP flat-bed knitting machine with a triple KNITRAN system from Shima Seiki. The two-ply of 32.9±0.02 [tex] cotton yarn was used as a ground for 1x1 rib courses (first knitting system). The core-spun yarn with 90 tex polyurethane yarn covered by two plies of 12.5 [tex] polyester yarn was used as elastomeric. It was fed at every second system (options A and B) or second and third systems (options C and D) for miss-knit repeat (Figure 1).

All fabrics were produced with the same technological setup of the knitting machine: tension level 24 is for cotton yarn (5th yarn`s carriage) and tension level 15 is for elastomeric yarn (6th yarn`s carriage). The interlooping repeat was repeated lengthwise 202 times. After knitting all fabrics were subjected to washing and drying according to ISO 6330:2021 to get the relaxed state specified in ISO 139:2005. The dimensions of the samples (length and width) were measured using a ruler. Each distance was measured 5 times and the mean values were used for result evaluation.
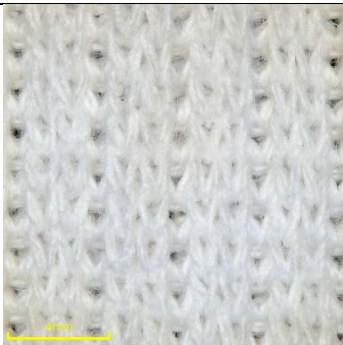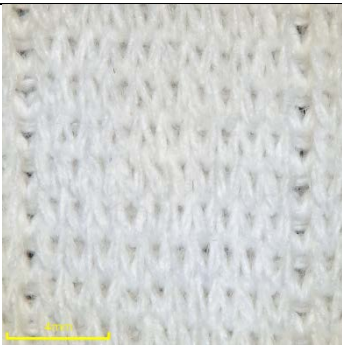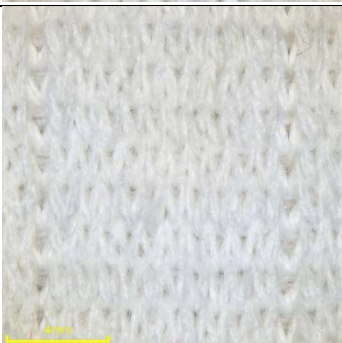
The fabrics' photos were made by using DSX1000 Digital Microscope from Olimpus with x23 magnification. The ImageJ software was used for the wale and courses spacings measurement. Each distance was measured 10 times and the mean values were used for result evaluation.

3. Results

The photos of the fabric`s side formed on the front needle bed are shown in Table 1 and the results of the dimensions measuring are presented in Table 2. The fabric appearance assessment has shown the following. There are two types of wales in the fabric structure, between which there is a significant difference. Some are formed by alternating the loops from cotton yarn and loops from core-spun polyurethane yarn. Others consist only of held loops from cotton yarn, and core spun polyurethane yarn in the form of a float is located behind held loops inside the fabric. Increasing the number (k) of miss stitchers in the repeat leads to an increase in the width of this area where floats form inlay weft

yarn. The effect of an option of elastomeric thread incorporation on the fabric's appearance was not found.

Table 1 Samples photos at the front side (front needle bed)

Options	Miss knit repeat	
	k = 2	*k = 10*
A		
B		
C		
D		

It was found that an increase in the number of miss stitches k in the repeat leads to a decrease in the sample`s width and an increase in the sample`s length (Table 2). It is due to better conditions for elastomer relaxation with increasing the elastomer yarn length between two loops in repeat. The fabrics of option B are wider than others.

Table 2 Dimensions of samples (302 x 2 needles and 202 repeats lengthwise)

Fabrics	Width			Length		
	Mean value [mm]	*Standard Deviation [mm]*	*CV, %*	*Mean value [mm]*	*Standard Deviation [mm]*	*CV, %*
A-2	315.0	1.9	0.6	303.0	1.2	0.4
A-4	294.2	2.4	0.8	310.6	0.9	0.3
A-6	288.4	3.0	1.1	314.2	2.5	0.8
A-8	287.6	3.0	1.0	318.0	1.2	0.4
A-10	279.2	2.4	0.9	318.8	0.8	0.3
B-2	387.0	1.4	0.4	296.0	0.7	0.2
B-4	340.4	2.7	0.8	304.0	1.0	0.3
B-6	321.4	1.7	0.5	311.8	1.9	0.6
B-8	304.4	2.9	0.9	315.4	1.5	0.5
B-10	294.6	2.3	0.8	315.4	2.6	0.8
C-2	312.0	3.1	1.0	298.6	3.4	1.1
C-4	282.2	5.2	1.8	311.0	2.0	0.6
C-6	275.6	4.3	1.6	319.2	3.3	1.0
C-8	269.6	2.9	1.1	324.8	3.7	1.1
C-10	265.6	3.4	1.3	317.2	3.3	1.0
D-2	313.4	2.6	0.8	297.0	5.6	1.9
D-4	284.6	2.7	0.9	307.6	5.0	1.6
D-6	273.0	5.1	1.9	313.4	5.1	1.6
D-8	267.8	1.3	0.5	316.2	5.0	1.6
D-10	265.8	3.1	1.2	315.8	4.1	1.3

The results of the wale and course spacings investigation are presented in Figure 2. An increase in the number of miss stitches k in the repeat leads to a decrease in wale spacing (Fig.2.a). All dependencies are logarithmic. B fabrics have higher values of w thus these structures are less dense coursewise. C and D fabrics with two elastomer yarns in the repeat have smaller values of w thus these structures are denser. The w values for the A structure are a little bit higher compared to the C and the D fabrics. The difference increases with the increase in k number of miss stitches in the repeat.

Figure 2 Dependences of wales (a) and courses (b) spacings on the number of miss stitches (k)

An increase in the number of miss stitches k in the repeat leads to an increase in course spacing (Fig.2.a). All dependencies are polynomials with high similarity for different fabric options. The increase in the number of miss stitches k from 6 to 10 only slightly affects the c values.

4. Conclusion

By the review of the existing structures of elastic weft and warp knitted fabrics and the methods of the elastomer fixing it was found that elastomer positioning as an inlaid thread provides high elasticity but the elastomer fixing in the structure does not reach the required level. The novel elastic double weft knitted structures were developed. The elastomer threads were introduced into the structure according to the miss knit repeats on needles of one or both needle beds.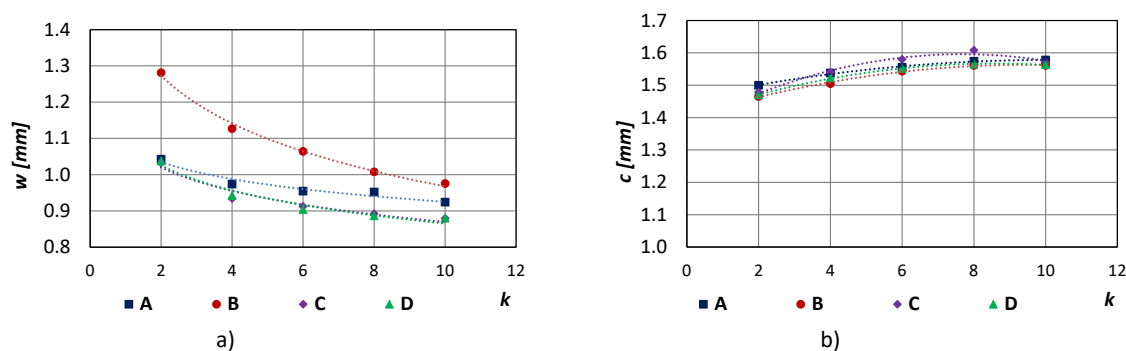 It was found that an increase in the number of miss stitches k in the repeat leads to a decrease in the width and an increase in the length of fabrics due to elastomer relaxation. The option of elastomer`s incorporation (one or two threads in repeat,  connection of loops at the same or different needle bed) affects the fabric`s density course-wise. Future research has to be done on the investigation of tensile properties and elasticity of novel fabrics

ACKNOWLEDGEMENTS

References

1. Adeli B, Ali Akbar Ghareaghaji, Shanbeh M. (2011). *Structural evaluation of elastic core-spun yarns and fabrics under tensile fatigue loading. Textile Research Journal.81(2):137-147. doi:10.1177/0040517510380104*

2. Agarwal, S. and Juneja, S. (2023), *"The effectiveness of compression garment in relieving muscular pain: a review", International Journal of Clothing Science and Technology, Vol. 35 No. 4, pp. 557-564. https://doi.org/10.1108/IJCST-01-2022-0014*

3. Alisauskiene, D.; Mikucioniene, D. (2012) *Investigation on Alteration of Compression of Knitted Orthopaedic Supports during Exploitation. Mater. Sci. (Medžiagotyra), 18, pp. 362–366.*

4. Beceren Y., Candan C., Cimilli S., Ülger K. (2010). *Properties of Plain Knits from Siro-Spun Viscose/Spandex Yarns. FIBRES & TEXTILES in Eastern Europe, Vol. 18, No. 1 (78) pp. 41-46.*

5. Chattopadhyay R., Gupta D. & Bera M. (2012) *Effect of input tension of inlay yarn on the characteristics of knitted circular stretch fabrics and pressure generation, Journal of The Textile Institute, 103:6, pp. 636-642, DOI: 10.1080/00405000.2012.665237*

6. Chen, Q., Ma, P., Mao, H., Miao, X. and Jiang, G. (2017) *The Effect of Knitting Parameter and Finishing on Elastic Property of PET/PBT Warp Knitted Fabric. Autex Research Journal, Vol. 17 (Issue 4), pp. 350-360. https://doi.org/10.1515/aut-2017-0014*

7. R. Chattopadhyay, D. Gupta and M. Bera (2011). *Effect of input tension of inlay yarn on the characteristics of knitted circular stretch fabrics and pressure generation. The Journal of The Textile Institute. DOI: 10.1080/00405000.2011.596664*

8. Kyzymchuk O, Melnyk L, Marmaralı A, et al. (2023). *The effect of weft yarn type and elastomer yarn threading on the properties of elastic warp knitted fabrics. Part 1: Structure and elasticity. Journal of Engineered Fibers and Fabrics, 18. doi:10.1177/15589250231167405*

9. Kyzymchuk O., Melnyk L., Arabuli S. (2020). *Study of Elastic Warp Knitted Bands: Production and Properties. Tekstilec, 63(2). 113-123. DOI: 10.14502/Tekstilec2020.63.113-123*

10. Melnyk L.M., Cherepakhova T.I., Drobyna I.I. (2015). *Investigation of structur parameters stretch fabric for compression hosiery. Visnyk KNUTD, № 1, pp. 164-168.*

11. Messiry M., Mohamed A. (2016). *ANALYSIS OF THE EFFECT OF CYCLIC LOADING ON COTTON-SPANDEX KNITTED FABRIC. International Journal of Automation, Mechatronics & Robotics Volume 3 : Issue 1. pp. 83-88*

12. Sau-fun Ng Yip, F. (1994), *"Medical Clothing: The Stress Relaxation and Shrinkage of Pressure Garments", International Journal of Clothing Science and Technology, Vol. 6 No. 4, pp. 17-27. https://doi.org/10.1108/09556229410063468*

13. *Siddique, H., Mazari, A., Havelka, A., Kus, Z. and Akcagun, E. (2023) Washing Characterization of Compression Socks. AUTEX Research Journal, Vol. 23 (Issue 3), pp. 323-339. https://doi.org/10.2478/aut-2022-0009*

14. *Siddique HF. (2019). Assessment of mechanical properties of compression socks using cut-strip method. J Textile Eng Fashion Technol., 5(5): pp. 228-233. DOI: 10.15406/jteft.2019.05.00206.*

15. *1Tezel, S. ve Kavuşturan, Y. (2008). "Experimental investigation of effects of spandex brand and tightness factor on dimensional and physical properties of cotton/spandex single jersey fabrics". Textile Research Journal, 78(11), 966 - 976.*

16. *Wang Y, Zhang P, Zhang Y.(2014). Experimental investigation the dynamic pressure attenuation of elastic fabric for compression garment. Textile Research Journal., 84(6) pp. 572-582. doi:10.1177/0040517513503726*

EFFECT OF SIZE OF NEGATIVE AIR PRESSURE AND DRAFT ON THE COMPACT SPINNING MACHINE ON THE QUALITY OF YARNS SPUN FROM META-ARAMID FIBRES

Petra Jirásková, Eva Moučková

Technical University of Liberec, Faculty of Textile Engineering, Department of Technologies and Structures, Liberec, The Czech Republic, Studentská 2, 461 17 Liberec 1, The Czech Republic, Telephone: +420 48 535 3328; petra.jiraskova@tul.cz

Abstract:

The paper deals with the analysis of the properties (mass irregularity, tenacity, breaking elongation, hairiness, number of faults) of nomex yarns produced on a compact spinning machine with different settings of the draft and negative air pressure in the additional condensing zone of the drafting device. The effect of negative air pressure and draft on the mass irregularity was expressed by transforming the mass irregularity of the roving through the draft device of the compact spinning machine to the mass irregularity of the produced yarn. The transformation of the mass irregularity was expressed by means of a relative transfer function or experimental modules of the relative transfer function, which were compared with the module of the theoretical transfer function.

Key words:

Nomex staple spun yarn, compact spinning, negative air pressure, mass irregularity, yarn fault, tenacity, breaking elongation, modulus of relative transfer function

1. Introduction

Nomex fiber is a meta-aramid fiber developed by DuPont in 1967. It is a widely used fiber, especially for its thermal resistance properties [7]. Nomex staple spun yarns are also characterized by high strength and flame resistance. Other mechanical properties of Nomex fibre are comparable to conventional textile fibers [9]. The use of Nomex staple spun yarns is prevalent in various industries where flame resistance is crucial, such as in protective clothing for firefighters, military personnel, and industrial workers exposed to high-temperature environments [7]. Today, Nomex staple fibers are spun using the ring spinning machines and their modification - compact spinning machines [20]. Compact ring spinning involves the incorporation of a fiber compression device into a ring spinning frame – positioned immediately after the drafting arrangement. Due to fibrous band compression, the spinning triangle is reduced, different stress of fibers in the spinning triangle is balanced, a higher degree of orientation and arrangement of fibers and their uniform distribution is achieved, all fibers are better integrated with the yarn body and thus the yarn has a lower number of imperfectly spun-in fibers [10], [18], [15], [4]. It leads to producing yarns with increased tenacity, breaking elongation, decreased hairiness, lower mass irregularity, and lower number of yarn faults compared to conventional ring spun yarns (for example [2-4], [6], [10], [11], [15], [18], [19]).

Different methods are employed to compact the fiber strand and thus reduce the spinning triangle before twisting it in the compact spinning machine. These methods include aerodynamical compacting systems such as suction by drum and suction through perforated or lattice aprons, mechanical compacting systems, and magnetic compacting systems [23]. Many studies have addressed compact spinning, comparing properties of compact versus conventional ring spun yarns using short-staple fibers (for example [2-4], [6], [10], [11], [15], [18], [19]), and, to a lesser extent, long-staple fiber (e.g.. [4]). Other works explore comparisons of yarn properties made by compact spinning machines with various

methods of fibers compacting (e.g. [2]), comparison between knitted as well as woven fabrics created from compact and conventional ring spun yarns (e.g.[1], [24], [25]), and the modeling and simulation of fiber behaviour in the condensing zone (e.g. [8], [12], [16], [21], [22], [26], [27], [29], [30]).

Yarn quality can be influenced not only by the kind and properties of fibers, and methods of spinning but also by the setting of machine-technological parameters (spinning variables). In the case of a compact spinning machine, the important spinning variables are among others suction air pressure (negative pressure), which controll the compacting effect of an aerodynamical compacting system. Mouckova and Jiraskova [14] conducted an experimental study focusing on the impact of small changes in the main draft ratio and negative air pressure levels of the Fiomax Suessen Elite compact spinning machine on various properties of blended worsted spun yarn. They found that employing a higher draft ratio (from the observed range) with low negative air pressure resulted in increased thin places, neps, and yarn irregularity, whereas a higher draft ratio with the highest negative air pressure led to the highest yarn breaking elongation. The study conducted by Zhang et al. [28] explores the analysis of the flow field within the condensing zone of compact spinning with an inspiratory groove. The research also experimentally examines the impact of negative pressure on yarn quality. The findings among others suggest that insufficient negative pressure leads to poor fiber compaction, while excessive negative pressure results in increased energy consumption. For optimal fiber compaction and reduced energy consumption, the study recommends maintaining negative pressure below -3 kPa in compact spinning with an inspiratory groove. The study [20] is focused on analyzing the effects of different negative air pressures on fiber condensing in compact spinning with lattice apron using ANSYS. They results are consistent with findings presented in [28] and confirmed that an increase in negative pressure contributes to better convergence, reducing fiber bundle width, and reducing the spinning triangle, ultimately improving yarn quality. Experimental findings in [21] showed that 100 % CO yarns spun under higher negative pressure (they used different levels of pressure) have statistically significant lower hairiness, and better strength, whereas yarn mass irregularity was the same compared to those spun under lower negative pressure conditions. The study by Chakrabortty et al. [5] experimentally explores the impact of suction pressure on the quality of compact yarn by adjusting the inverter frequency to change suction pressure. Although researchers did not mention the type of condensing device of the compact spinning machine, they found out that the negative air pressure -2.3 kPa in the Suessen Elite compacting system is the best level of negative air pressure considering both the quality of experimental 100% CO yarn and energy consumption.

There is a lack of information about Nomex staple fibers spinning and the influence of spinning variables of compact spinning machines on the properties of Nomex staple spun yarns. This work aims to investigate the impact of selected levels of negative air pressure in the compacting zone of a compact spinning machine on key properties of worsted spun yarn, including tenacity, breaking elongation, yarn hairiness, yarn mass irregularity, and number of yarn faults, because negative pressure in the condensing zone of a compact spinning machine is crucial for compacting fiber strands, but it results in increased production costs. Also, the transformation of roving mass irregularity into yarn mass irregularity due to the drafting device with the additional condensing zone was investigated through an analysis utilizing the experimentally determined modulus of a relative transfer function of the drafting device with the additional condensing zone.

2. Experimental
2.1. *Materials*

For the experiment, we utilized the set of meta-aramid (Nomex) staple spun yarns which were successively spun on the Fiomax Suessen Elite compact spinning machine at various levels of air suction pressure (2,4 kPa ; 3,9 kPa) from the same roving bobbins. The machine was equipped with the three-roller double-apron drafting system along with the additional aerodynamical condensing zone with a lattice apron. The technology of yarn production also included low denier tow breaking on the

stretch-breaking tow-to-top converter, and roving formation using the finisher. The experimental yarns and rovings are detailed in Table 1, while the fiber parameters are outlined in Table 2.

Table 1. Basic parameters of staple spun yarns and rovings used for the experiment

Fibre raw material	Spinning technology	Nominal yarn count [tex]	Nominal roving count [tex]	Nominal yarn twist [m⁻¹]	Total draft on compact spinning machine
100% Nomex	compact	25	425	650	17
100% Nomex	compact	25	330	650	13,2
100% Nomex	compact	25	245	650	9,8

Table 2. Basic parameters Nomex fibres

Material	Average fibre staple length [mm]	Average fibre fineness [dtex]
Nomex (DuPont)	71,1 mm	2,2 dtex

2.2. Methods

Roving and yarns were subjected to the measurement of mass irregularity and yarn faults utilizing the Uster Tester IV-SX. The measurement was carried out under the following conditions: rovings: speed of measurement: 10 m/min, time of measurement: 10 min; yarn: speed of measurement: 400 m/min, time of measurement: 2.5 min. Yarn hairiness was tested using the Zweigle hairiness tester G567 at a speed of 50 m/min for 2 minutes. The Instron tensile tester was employed to measure tenacity and breaking elongation, with a clamping length of 500 mm and a crosshead speed of 370 mm/min. The collected data underwent statistical analysis through two-way ANOVA with a significance level of 5%

The transformation of the roving mass irregularity into the yarn mass irregularity due to the drafting arrangement with the condensing zone can be expressed using the modulus of relative transfer function. This modulus is defined as the ratio of output and input signal amplitudes relative to the mean fineness of the fibrous linear product [11]. The input or output signal represents the mass variations of short-length sections of fibrous products based depending on the length of these products. In this work, we expressed the transformation of mass irregularity by the drafting device by the so-called experimentally determined modulus of the relative transfer function. We assume that roving mass irregularities at certain wavelengths λ_{roving} are reflected in the yarn at enlarged wavelengths due to total draft ($\lambda_{roving} \cdot P$), with deepening roving irregularities at short wavelengths due to draft while being constant in the compacting zone. The experimental modules of relative transfer function were determined according to equation (1) and the theoretical modulus of relative transfer function comes from conditions of ideal draft and was expressed by equation (2) [31]:

$$\left| F_{\exp}^{*}(\lambda) \right| = \frac{CV_{yarn}\,(\lambda_{roving} \cdot P)}{CV_{roving}\,(\lambda_{roving})} \tag{1},$$

$$\left| F_{p}^{*}(\lambda) \right| = \left| P \frac{\sin \dfrac{\pi\,l}{\lambda}}{\sin \dfrac{\pi\,l\,P}{\lambda}} \right| \tag{2},$$

where: $\left| F_{\exp}^{*}(\lambda) \right|$ is the experimentally determined modulus of relative transfer function of drafting mechanism; $CV_{yarn}(\lambda_{roving..}P)$ [%] is the variation coefficient of harmonic component of yarn mass irregularity with wavelength corresponding to wavelength of roving λ_{roving} [m] enlarged by draft P; $CV_{roving}(\lambda_{roving})$ [%] is the variation coefficient of harmonic component of roving mass irregularity with

wavelength λ_{roving} ; P is the total draft ratio of drafting mechanism of compact spinning frame, $\left|F_p^*(\lambda)\right|$ is

theoretical modulus of relative transfer function of drafting mechanism as a function of wavelength λ; λ is the wavelength of harmonic component of mass irregularity of result fibrous product [m], l is the average fiber length [m].

Table 3. Results of staple spun yarns properties

Yarn property	Total draft	Negative air pressure [kPa]	Mean value	Confidence interval
Mass irregularity CVm [%]	17	2,4	14,34	(14,18 ; 14,51)
		3,9	14,74	(14,30 ; 15,17)
	13.2	2,4	14,03	(13,83 ; 14,22)
		3,9	14,05	(13,82 ; 14,29)
	9,8	2,4	15,04	(14,62 ; 15,46)
		3,9	14,28	(14,08 ; 14,48)
Hairiness S3 [1/100m]	17	2,4	424,83	(400,73 ; 448,93)
		3,9	353,9	(330,30 ; 377,50)
	13.2	2,4	409,17	(387,87 ; 430,46)
		3,9	301,80	(283,78 ; 319,82)
	9,8	2,4	431,50	(413,72 ; 449,28)
		3,9	277,30	(265,81 ; 288,79)
Tenacity R [cN/tex]	17	2,4	25,05	(24,52 ; 25,58)
		3,9	24,24	(23,68 ; 24,82)
	13.2	2,4	24,96	(24,39 ; 25,54)
		3,9	24,54	(23,96 ; 25,12)
	9,8	2,4	24,23	(23,61 ; 24,82)
		3,9	24,20	(23,71 ; 24,69)
Breaking elongation E [%]	17	2,4	25,84	(25,18 ; 26,50)
		3,9	26,09	(25,26 ; 26,83)
	13.2	2,4	25,85	(25,26 ; 26,83)
		3,9	26,09	(25,38 ; 26,80)
	9,8	2,4	25,02	(24,27 ; 25,78)
		3,9	26,23	(25,45 ; 27,00)
Thin places -50% [1/km]	17	2,4	10,67	(9,50 ; 12,50)
		3,9	9,31	(7,60 ; 10,80)
	13.2	2,4	10,42	(9,10 ; 12,00)
		3,9	7,08	(5,90 ; 8,40)
	9,8	2,4	14,44	(12,75 ; 16,30)
		3,9	3,06	(2,30 ; 3,90)
Thick places +50% [1/km]	17	2,4	6,39	(5,30 ; 7,60)
		3,9	4,31	(3,40 ; 5,30)
	13.2	2,4	5,28	(4,30 ; 6,40)
		3,9	3,19	(2,40 ; 4,10)
	9,8	2,4	5,69	(4,60 ; 6,80)
		3,9	3,06	(2,30 ; 3,90)
Neps +200% [1/km]	17	2,4	9,03	(7,70 ; 10,50)
		3,9	8,06	(6,80 ; 9,40)
	13.2	2,4	9,72	(8,30 ; 11,20)
		3,9	8,09	(6,80 ; 12,70)
	9,8	2,4	8,75	(7,40 ; 10,20)
		3,9	6,67	(5,50 ; 7,90)

To express the structure of mass irregularity of the linear fibrous product, here represented by mass fluctuations at short wavelengths, we used mass spectrograms of rovings and yarns. The spectrogram shows a distribution of amplitudes of harmonic component, or variation coefficients of harmonic

component of mass fluctuation, of roving (input signal) and yarns (output signal) depending on wavelength.

3. Results and discussion

In the experiment, the basic parameters of fibers, rovings and yarns were verified and their results are presented in Tables 1 and 2. The effect of the size of the negative air pressure of the additional compressing zone and the level of the draft on the compact spinning machine on the properties of the produced Nomex spun yarn was evaluated through selected properties – tenacity, breaking elongation, hairiness, mass irregularity and number of faults. The measurement conditions of all properties are presented in chapter 2.2 and their results are presented in Table 3. The results of the measurements of these properties confirmed the assumptions – yarns spun using a higher negative air pressure in the compressing zone and at the same time a lower value of draft showed higher tenacity and breaking elongation, lower hairiness, lower mass irregularity and number of faults. The differences in the results of the individual properties were statistically insignificant in most cases. The effect size of negative air pressure and total draft on the analysed yarn properties was also evaluated by using the statistical analysis through two-way ANOVA, the results are shown in Table 4. These results confirm the theoretical assumptions about the influence of the value of the draft and the negative air pressure on the evaluated properties. The draft and its interaction with negative air pressure has a significant effect on the mass irregularity. The number of yarn faults (thin and thick places) was significantly influenced by the size of the negative air pressure. The yarn tenacity was significantly influenced by both tested factors. Yarn hairiness was also significantly influenced by both factors and their interaction.

**Table 4:** Results of two-way ANOVA – selected yarn properties

Property	Source of variance	F-ratio	Critical quantile	p-value	Results
Yarn mass irregularity	Draft	8,48	3,09	0,000395	significant
	Neg. press.	0,8	3,94	0,374659	insignificant
	Interaction	6,72	3,09	0,001751	significant
Yarn thin places (-50%)	Draft	0,33	3,09	0,71893	insignificant
	Neg. press.	11,52	3,94	0,56	significant
	Interaction	3,48	3,09	0,02	significant
Yarn thick places (+50%)	Draft	0,58	3,09	0,56	insignificant
	Neg. press.	6,06	3,94	0,02	significant
	Interaction	0,04	3,09	0,66	insignificant
Yarn tenacity	Draft	3,23	3,01	0,00399	significant
	Neg. press.	17,6	3,85	0,0000306	significant
	Interaction	0,78	3,01	0,461	insignificant
Hairriness S3	Draft	7,45	3,05	0,000785	significant
	Neg. press.	173,65	3,9	$5,99 \cdot 10^{-28}$	significant
	Interaction	8,21	3,05	0,000391	significant

For the analysis of the influence of the size of the negative air pressure in the additional compressing zone of the drafting device and the value of the applied draft on the mass irregularity, the experimental modules of the relative transfer function $\left| F_{\exp}^{*}(\lambda) \right|$ were determined according to equation (1). The coefficients of variation of the amplitudes of the harmonic components of the mass irregularity were determined from the measured data of the spectrograms of the yarns and rovings with the UT4 - SX apparatus. The average spectrograms and average experimental modules of the relative transfer function were calculated from these data. The average experimental modules of the relative transfer functions of the yarns produced at different levels of applied draft and negative air pressure were

compared with each other. Also, theoretical modules of the relative transfer functions were constructed (equation 2) and their envelope curves with which the experimental module waveforms were compared. Figures 1 and 2 show the experimental modules of the relative transfer functions $\left|F_{\exp}^{*}(\lambda)\right|$ for yarns spun ai higher (3.9 kPa) and lower (2.4 kPa) negative air pressure with different levels of draft on the compact spinning machine. Figures 3, 4 and 5 compare the experimental modules of the relative transfer functions $\left|F_{\exp}^{*}(\lambda)\right|$ for yarns produced at the same level of draft and different negative air pressures in the compressing zone (2,4 kPa; 3,9 kPa).
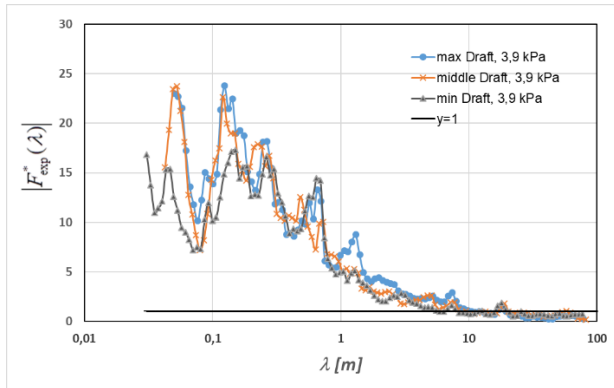
Figure 1. Experimental modules of the relative transfer functions for yarns spun at negative air pressure (3,9 kPa) with different levels of draft
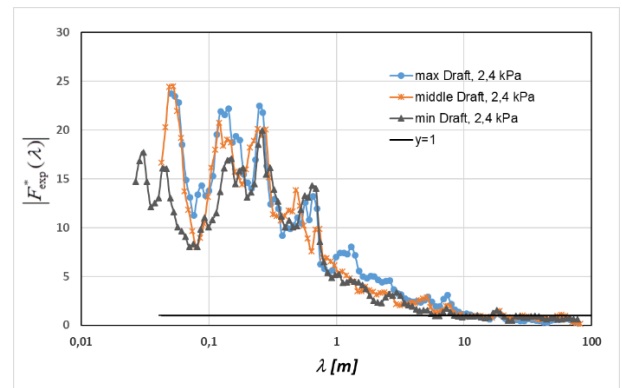
Figure 2. Experimental modules of the relative transfer functions for yarns spun at negative air pressure (2,4 kPa) with different levels of draft
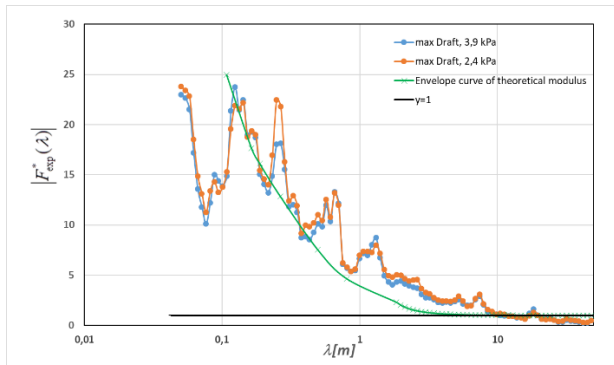
Figure 3. Comparison of the experimental modules of the relative transfer functions for yarns produced at the **max draft** and different levels of negative air pressures
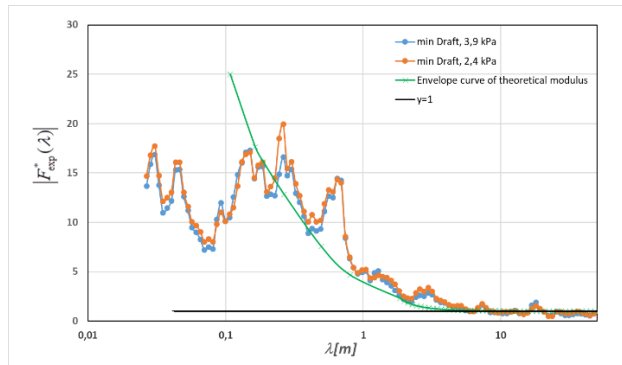
Figure 4. Comparison of the experimental modules of the relative transfer functions for yarns produced at the **min draft** and different levels of negative air pressures
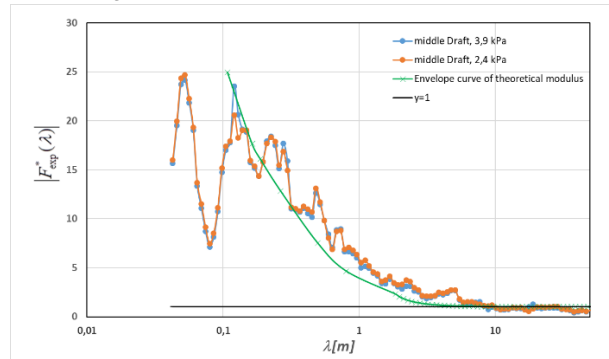
Figure 5. Comparison of the experimental modules of the relative transfer functions for yarns produced at the **middle draft** and different levels of negative air pressures

4. CONCLUSIONS

This work was focused on the analysis of the magnitude of negative air pressure in the compressing zone and draft in the drafting device of a compact spinning machine on selected properties of meta-aramid fibre yarn (Nomex) with a more detailed analysis of mass irregilarity through transfer functions. The results show that the behaviour of the specific fibre material (Nomex) is consistent with the theoretical assumptions and regularities found for other fibre materials (e.g. wool, PES, etc.). The results of this work showed the tendency of Nomex compact apun yarns to have lower mass irregularity, number of faults, hairiness, higher tenacity and break elongation if a higher negative air pressure in the compresing zone is used in the yarn spinning process and at the same time a lower value of draft in the drafting device. It is the additional compressing zone with a small tension draft that proves to be beneficial, due to which the fibre ribbon is narrowed and thus becomes more cohesive with a higher fibre tension and the simultaneous use of finer roving (i.e. lower total draft in the drafting device). The behaviour of the real fibres in spinning processes is difficult to predict, but lower values of draft and a more compact fibre ribbon are prerequisites for a higher quality of the produced yarns, assuming optimum setting of the technological and technical parameters in the preceding technological stages.

References

1. *Abd., N., Hassan E. (2013). An Investigation about Spirality Angle of Cotton Single Jersey Knitted Fabrics Made from Conventional Ring and Compact Spun Yarn, Journal of American Science 2013; 9(11).*

2. *Altas, S., Kadoğlu, H. (2012). Comparison of Conventional Ring, Mechanical Compact and Pneumatic Compact Yarn Spinning Systems, Journal of Engineered Fibers and Fabrics. 7(1), 87-100.*

3. *Basal, G., Oxenham, W. (2006). Comparison of Properties and Structures of Compact and Conventional Spun Yarns, Textile Research Journal, 76 (7), 567 – 575.*

4. *Çelik, P., Kadoğlu, H.: A Research on the Compact Spinning for Long Staple Yarns, Fibres & Textiles in Eastern Europe, October/December 2004, Vol. 12, No. 4 (48) , 27-31.*

5. *Chakrabortty, A., Hossaın, A., & Ghosh, J. (2020). Study on the Effect of Air Suction Pressure on the Quality of Compact Yarn by Changing the Frequency of Inverter. Tekstil Ve Mühendis, 27(119), 154-158.*

6. *El-Banna, M., Nassar, M., Negm, M., El-Banna, A., & Pharoun, A. (2020). Comparison between conventional ring and compact spinning of some egyptian cotton varieties. Journal of the Advances in Agricultural Researches, 25(2), 130-144.*

7. *Glogar, M., Pušić, T., Lovreškov, V., Kaurin, T., & Sutlović, A. (2022). Application issue of anthraquinonoid vat dyes on inherently flame-resistant fabrics. Coloration Technology, 139(2), 190-199.*

8. *Han, Ch., Wei, M., Xue, W., Cheng, L. (2014). Numerical simulation of fiber strands on Condensing Effect of Suction Slot in Compact Spinning with Lattice Apron, Fibers and Polymers 2014, Vol.15, No.5, 1084-1091.*

9. *Hearle, J. W.S. (2005). Fibres and fabrics for protective textiles in Textile for protection, Woodhead Publishing Series in Textiles. Edited by Scott, R.A.. ISBN 1845690974.*

10. *Jackowski, T., Cyniak, D., Czekalski, J. (2004). Compact cotton yarn, Fibres & Textiles in Eastern Europe, October/December 2004, Vol. 12, No. 4 (48).*

11. *Jirásková, P., Moučková, E. (2022). Analysis of mass irregularity of worsted ring and compact staple spun yarns, 23rd International Conference STRUTEX Structure and Structural Mechanics of Textiles, Conference Book, Liberec, Technical University of Liberec, 2022, pp. 205 - 212, ISBN 978-80-7494-621-9.*

12. Khurshid, M.F., Nadeem, K., Asad, M., Chaudhry, M.A., Amanullah, M. (2013). Comparative Analysis of Cotton Yarn Properties Spun on Pneumatic Compact Spinning Systems, Fibres & Textiles in Eastern Europe, 21, 5(101), 30-34.

13. Liu, X. and Liu, X. (2015). Numerical simulation of the three-dimensional flow field in four pneumatic compact spinning using the finite element method. Textile Research Journal, 85(16), 1712-1719.

14. Moučková, E., Jirásková, P. (2016). Influence of Selected Process Variables on Worsted Compact Yarn Properties, 21st International Conference STRUTEX Structure and Structural Mechanics of Textiles Conference Book, Liberec, Technical University of Liberec, 2016, pp. 145-152, ISBN 978-80-7494-269-3.

15. Nikolič, M., Stjepanovič Z., Lesjak, F., Štritof, A. (2003). Compact Spinning for Improved Quality of Ring-Spun Yarn, Fibres & Textiles in Eastern Europe, October / December 2003, Vol. 11, No. 4 (43) 30-35.

16. Omerlogu, S., Ulku, S. (2007). An investigation about tensile strength, pilling and abrasion properties of woven fabric made from conventional and compact ring-spun yarn, Fibres & Textiles in Eastern Europe, January/March 2007, Vol. 15, No. 1 (60), 39-42.

17. Özgüney, A., Kretzschmar, S., Özçelik, G., & Özerdem, A. (2008). The comparison of cotton knitted fabric properties made of compact and conventional ring yarns before and after the printing process. Textile Research Journal, 78(2), 138-147.

18. Rajaney, J.P.: Comparative Analysis of Compact Spun Yarns and Ring Spun Yarns, Indian Jounal of fibre & textile research, Vol.40, March 2015, pp 43-50.

19. Rashid, M. R., Ahmed, E., Azad, A.K., Ullah, A.N.M.A., (2011). Comparative Study On Cotton Yarn Quality Made From Compact And Conventional Ring Frame, Journal of Innovation & Development Strategy, 5 (3), December 2011, 61-66.

20. Rengasamy' R.S., Kothari, V. K., Gotipamul, R.L. (2000). Flame retardancy of Nomex/cotton ring-spun blended yarn fabrics, Indian Journal of Fibre & Textile Research, Vol. 25, December 2000, 241-245.

21. Saty, M. Y. H., Akankwasa, N. T., & Wang, J. (2021). Numerical simulation and analysis of airflow in the condensing zone of compact spinning with lattice apron. Autex Research Journal, 22(3), 258-263.

22. Saty, M. Y., Akankwasa, N. T., & Wang, J. (2021). Numerical and experimental approach towards an energy-efficient compact spinning system. Textile Research Journal, 92(5-6), 730-738.

23. Sayed, M., Uddin, M., & Begum, H. (2022). Comparative study of cotton yarn properties using central-fan and multi-fan for vacuum generation in aerodynamic compact spinning systems. Textile & Leather Review, 5, 240-252.

24. Shahid,A., Fossain, D., Hasan, N.U., Islam, A. (2013). Comparative Study of Ring and Compact Yarn-Based Knitted Fabric, 10-th International Conference of Mechanical Engineering, ICME 2013.

25. Wan, A., Yu, W., & Jiang, G. (2013). Pilling properties of wool single jersey made of compact and conventional ring yarns after anti-felting treatment. Textile Research Journal, 84(7), 673-683.

26. Zhang, X., Zoe, Z., Cheng, L. (2010). Numerical study of three dimensional Flow Field in Compact Spinning with Inspiratory Groove, Textile Research Journal, 2010, Vol. 80(1):84-92

27. Zhang, X., Zou, Z., & Cheng, L. (2009). Numerical study of the three-dimensional flow field in compact spinning with inspiratory groove. Textile Research Journal, 80(1), 84-92.

28. Zhang, X.C., Zhang, H.X., Cheng, L.D. (2013), Effect of Negative Pressure on Yarn Quality in Compact Spinning with Inspiratory Groove, Advance Material Research, 627, 288-292.

29. Zou, Z. Y., Zhu, Y.D., Hua, Z.H., Wang, Y., Cheng, L.D. (2010). Studies of Flexible Fiber Trajectory and Its Pneumatic Condensing Mechanics in Compact spinning with Lattice Apron, Textile Research Journal, Vol.80(8): 712-719.

30. Zou, Z.Y., Di Cheng, L., Hua, Z. H. (2010). A Numerical Approach to Simulate Fiber Motion Trajectory in an Airflow Field in Compact Spinning with a Perforated Drum, Textile Research Journal, 80(5), 395-402.

31. Sevosťanov, A.G., Chavkin, V. P., Divinskij, L. A. (1967). Kinematičeskaja teorija vytjagivanija voloknistogo produkta. Izvestija vyšších učebnych zavedenij, Technologia Textilnoj promyšlennosti, 1967 (5). 68-75.

STUDY OF WARP-KNITTED DESIGNS SUITABLE FOR BIOMASS COLONIZATION FOR WATER PURIFICATION

Irena Lenfeldova and Martina Ryvolova

Technical University of Liberec, Faculty of Textile Engineering, Department of Technologies and Structures, Liberec, Czech Republic, martina.ryvolova@tul.cz, irena.lenfeldova@tul.cz

Abstract:

As a highly efficient and economical method with environmental advantages, biological wastewater treatment based on removing various nitrogen forms using activated sludge has been an important research topic. The early concept behind designing a warp-knitted fabric structure (spacer fabric, WKSF) with holes is based on the similar appearance of a solid carrier and three-dimensional fabric. Potential possibility of the industrial application and production is a necessary request for developing of spacer biomass carriers. This study concentrates on determining warp-knitted structure differences and their structural parameters. The weight, thickness, loop length, density, and filament consumption are determined. This concept is expected to serve as a database of suitable warp-knitted designs for producing a spacer biomass carrier for quick start-up of colonization in bioreactor for wastewater treatment with maximum achievable efficiency.

Keywords:

Warp-knitted structure, structural parameters, misslapping, biomass carrier, water treatment

1. Introduction

The computer modelling of textiles has indeed developed considerably in the last decades, but the complexity of fibrous structures in the case of loose and porous textiles does not allow such a prediction of properties as for conventional, e.g. metallic components. The modelling of knitted textile, is very complicated, especially the knitted fabrics, both weft and warp. Each level of the textile structure hierarchy can contribute to the overall dimensional changes in the fabric, so that the overall shrinkage is the result of structural changes in the multifilament and changes in the loop geometry, especially overlap and underlap inclination. [1,2] In any case, the most important influence on the change of the total weight with the same machine setting will be the dimensional changes caused by the rearrangement of the knitted fabric structure, which consist of the change of the loop shape and size. Calculating the consumption using SW can be useful for predicting the behavior of other fabric variants, e.g. made from multifilament of different material composition or fineness.

"The engineering design of warp knitted fabrics today requires the estimation of their main properties, where at the first place this is the specific weight of the fabrics. For the calculation of the weight, the yarn length in a unit cell has to be known. The yarn length is required as well for the preparation of beams, the production process and for the adjustment of the machine." [3]

This work presents some problems with predicting and evaluating structural properties, related to the warp-knitted structures especially if the structure is too loose. This structure morphology is necessary to know and described with regard to the use of the produced fabric (suitability for the bacteria attachment for wastewater treatment). [4–6] The aim was to design a loose, simple, lightweight and porous structure consisting of two GBs, which should also have a greater thickness for 3D bacteria growth. This could be achieved by misslapping of one GB or changing the partial threading of one GB.

2. Experimental

Five variants of the two-guide bars single-face fabric with full or partial threading were designed.

2.1. Materials

Different designs variants of knitted fabrics were produced from textured polyester multifilament (*16.7/2 tex, f 36*). The differences between the designs were determined using structural parameters (densities, length, width, weight, thickness, and consumption) and image analysis.

2.2. Methods

The fineness and diameter of polyester multifilament were measured and compared with the producer's data. The multifilament fineness *T [tex]* represents the relationship between the multifilament weight m_m [g] and the length l_m [km]. It is determined according to the calculation (1).

$$T = \frac{m_m}{l_m}$$ (1)

T – Fineness [tex], m_m – multifilament weight [g], l_m – multifilament length [km]

The multifilament diameter was determined by calculation (substance diameter) and experimentally by measurement. According to equation (2), the substance diameter ds [mm] is the diameter with maximum fiber filling (filling equals 1). The actual diameter is always larger.

$$d_s = \sqrt{\frac{4T}{\pi \rho \mu}}$$ (2)

ds – substance diameter [mm], T – multifilament fineness [tex], ρ – fibers density [kg/m^3], μ – filling [-]

Measurement of multifilament diameter was realized using a Constant Tension Transport (CCT) device. The CTT is a LAWSON-HEMPHILL measuring device that allows various tests, including determining the multifilament diameter. The tester first measures the diameter of the filament at a speed of 100 m/min over a length of 100 m and defines a reference diameter. They followed by the actual measurement of the multifilament diameter (signed dCTT) over the next 100 m of length under the same conditions.

A Raschel single-bar machine, Karl-Mayer (12E", 6GB), was used for sample production. Samples from polyester multifilament were analyzed after a relaxation process (5 days at RT and 50 % RH) without stress, friction, and heat fixation. The following measurements were carried out on the samples:

- Course density and wale density according to Standard EN 14 971 (80 0886) -Textiles - Knitted fabrics - Determination of the number of stitches per unit length and unit area.
- Weight and thickness of the knitted fabric (balance KERN PHB to 1200 g; Thickness Gauge D-2000, DIN EN ISO 5084).
- Size of the structural unit.
- Multifilament consumption.

2.3. Structural parameters modelling

The Tex-Mind Warp Knitting Pattern Editor by Prof. Y. Kyosev was used to calculate the model area weight. The computing module is part of the software. To calculate the structural parameters (loop length, consumption per Rack, and area weight), it is necessary to enter the following parameters: fineness, yarn diameter, material density, elasticity modulus, elongation, breaking force, friction coefficient, course density, machine type, gauge, needle head diameter and number of bars. [7]

3. Results and discussion

3.1. Material properties

The material properties of the polyester multifilament determined by the experiment are summarized in Table 1. The fineness value is higher than the value declared by the producer (*33.4 tex*). The multifilament diameter is almost twice the substance diameter ($\mu = 1$). The measured diameter value corresponds because the yarn contains a lot of air ($\mu \approx 0.5$).

Table 1. Properties of polyester multifilament.

Fineness *[tex]*	Density *[kg/m³]*	Diameter d_s *[μm]*	Diameter d_{CTT} *[μm]*
37,2 ± 0.1	1380	185	344 ± 1

3.2. Warp-knitted fabrics design

All designs are produced using two guide bars (GB). The basis of all designs is the tricot lapping (GB1). The lapping of GB2 is a fully threading tricot for all samples. The design depends on GB1 threading (full or patterned) and the guide bar movement (equal or counter-lapping). The option of misslapping GB1 in specific rows has also been used. All possibilities have been used to achieve maximum design, structural variability and morphology. The knitted fabrics' graphic designs (Figure 1) were created using TexMind software by Prof. Y. Kyosev. Designs A – E are graphically shown using with the lapping (guide bar movement), supplemented by the threading of GB1 and GB2.
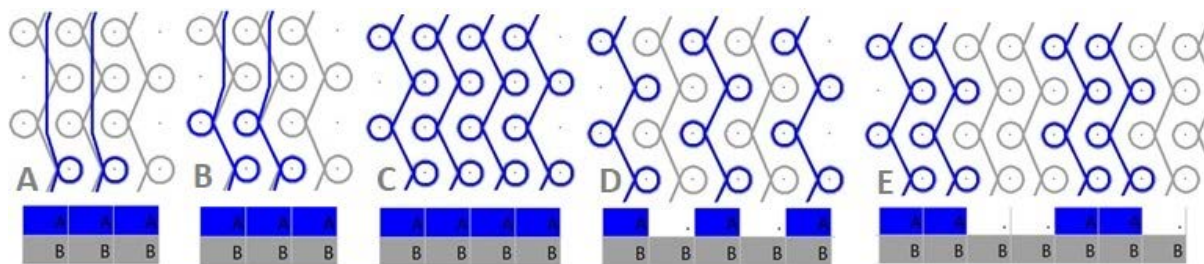
Figure 1. Warp-knitted designs and threading.

3.3. Warp-knitted fabric's structural parameters

The area weight of the samples was determined experimentally by weighing them on a Metler Toledo analytical balance, and the thickness was measured on a Thickness Gauge D-2000 device. The results of both measurements are presented in the graph in Figure 2. Higher thicknesses have samples with misslapping (A and B); the thicknesses of the remaining other samples are between 0.9 – 1.1mm. The increase in the thickness of structure A compared to C is due to the lapping of GB 1, which causes a ridge to form.

Figure 2. Warp-knitted fabric parameters   **Figure 3.** Warp-knitted structure parameters

Sample C (with full threading GB1 and GB2) has the highest area weight. The weight of the other specimens is similar, although they differ in the threading and lapping methods. Course, wale, and loop density values are shown in the graph in Figure 3. Values were determined according to the ISO Standard EN 14 971. The value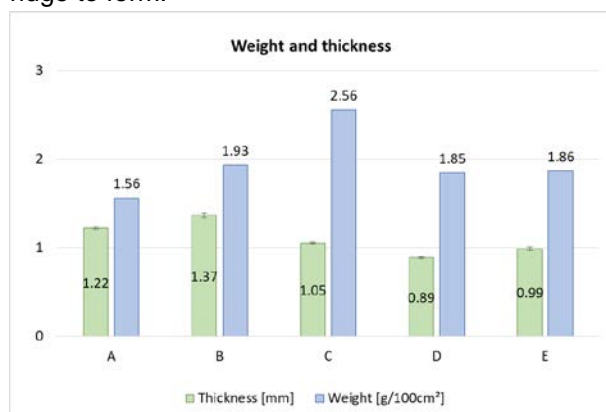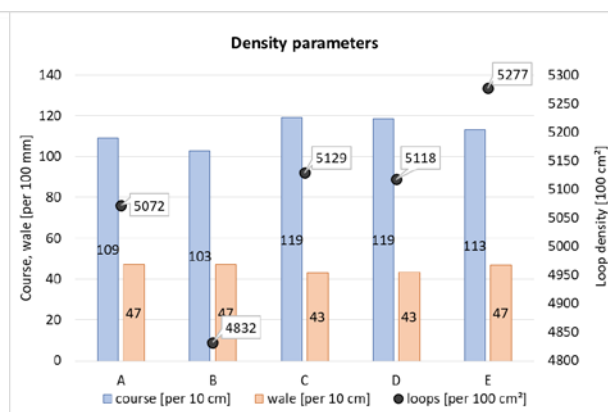s per 100 mm/ 10 000 mm^2 are shown in the graph in Figure 3. Loop density is an essential indicator of design differences. The densities per 1 m were used for model calculations of area weight and multifilament consumption in the guide bars.

Simulation Module LOOP3D of Tex-Mind software was used to create models of the designed warp knits, see Figure 4. The knitting models are composed of a GB2 knitting pattern in black (in the pattern notation in Figure1 the lapping is in grey) and a GB1 pattern in red (in Figure 1 the lapping is in blue). The lapping for designs A and B (Figure 4) combines closed loops lapping/ misslapping and full threading. Design C is knitted with two GBs, full threading, and closed loops lapping (Figure 4). Designs D and E are based on the 1:1 (1 in, 1 out) and 2:2 (2 in, 2 out) threading with closed loops lapping (Figure 4).

All knitting models created in the software are ideally stretched (simulation parameters depend on the warp-knitting machine and needle parameters) and do not consider the shrinkage parameter. Actually, knits relax and shrink, and this change significantly affects the thickness and area weight of the knit, resulting in the deformation of the whole structure.

A   B   C   D   E
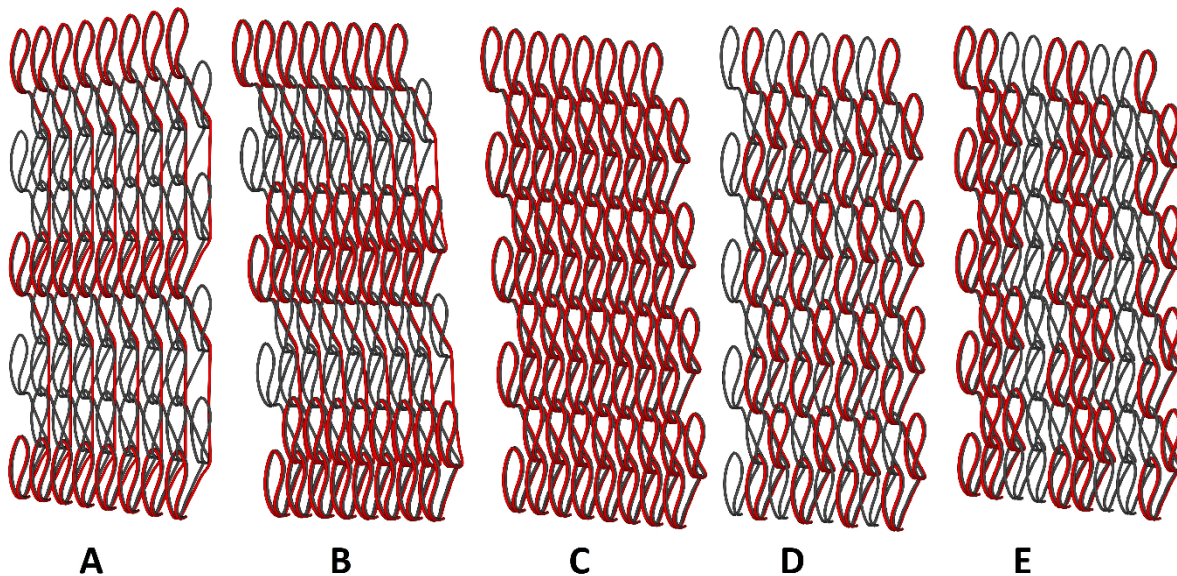
Figure 4. Warp-knitted models from Tex-Mind software.

The compact, relatively rigid and stable C-structure with smaller gaps between the overlap and underlap relaxed after fabrication with the specified wale and course spacing values, see graph in Figure 5. Design D, differing with a GB1 (1 in, 1 out) threading, does not exhibit the expected shrinkage in the horizontal direction due to the wale of single loops. The tensile force of tension rails causes the small value of course spacing of design A in relation to B during production since GB1 creates only one loop and three misslapping. I.e., structure A is designed of one row of double stitches and other three row of simple stitches. Therefore, there is a horizontal waviness of the structure and spatial deformation of some rows of the fabric. Due to the area weight, the 3D deformation of this sample was probably the most visible. If the lapping of GB1 of design B is two loops and two misslapping the course spacing increases and contrary the wale spacing decreases in relation A, Figure 7. Vertical wrinkling of the warp-knitted structure (resembling a rib) is achieved by design E. The wale spacing of design E relative to design C (Figure 7) decreases due to the looseness of the single loops and the possible slippage of the multifilament (shrinkage) of the single columns. The bending properties and stiffness of the multifilament become more apparent.

The average values of loop length, fineness, wale, and course densities were used to calculate area weight (CALC—values in graph in Figure 6). Values named in 2.3 were used to predict the model's area weight (MOD—values in graph in Figure 6). EXP is an experimentally measured area weight values of all designs.

In regards to MOD and EXP access, the measured value fits the model for designs B - E excellent. The fact that the model includes not only the basic parameters of the knitted fabric but also respects the material and machine parameters makes the model prediction very accurate. The exception is design A, which contains 75% misslapping - unstable vertical-oriented yarns with only one loop per structural unit of GB1 (see Figure 1). Calculated values (CALC) are mainly depend on experimental average loop lengths. This value corresponds very closely with the experimental value in the misslapping design A; for other designs, it is less accurate than the model.
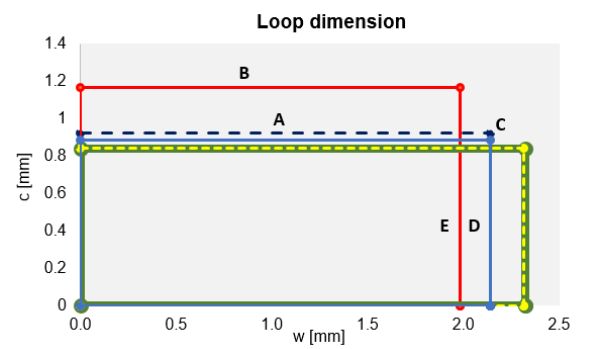
Figure 5. Loops size comparison
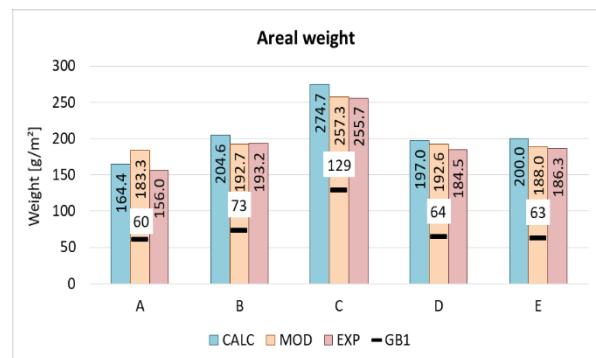
Figure 6. Area weight comparison: CALC-calculated value, MOD-modelled value from Tex-Mind software, EXP- measured value, GB1-weight of GB1 multifilament
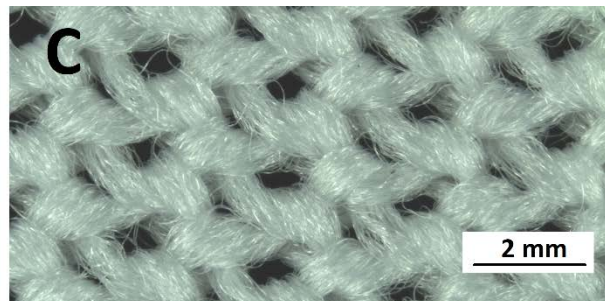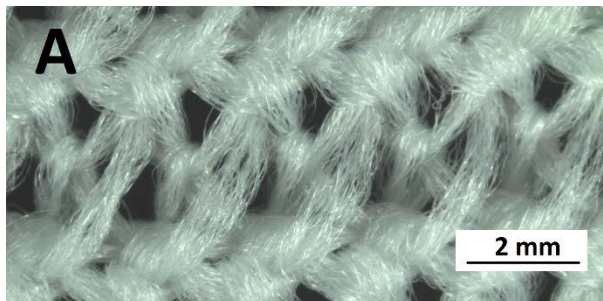
Figure 7. Design of warp-knitted samples A and C

During the fabrication of the designed samples, the multifilament consumption (Figure 8) in each guide bars per rack was investigated. „In warp-knitting one rack is used for the yarn length measurement, which covers 480 stitches." [3] The modelled consumption lengths are based on the theoretical assumptions of a rather compact loop and loop head as a circular arc with radius according the needle shaft diameter and the yarn diameter. Therefore, the actual multifilament consumption for all designs of both GBs was assumed to be higher (Figure 8). However, what might have caused the relatively good agreement between experimental and modelled consumption values for design A remains to be investigated. The mechanical feeding device, the formation of large tensile forces and also the pattern could be the cause. Since only every fourth row double loops are created, there is a large tightening of these overlaps and the aforementioned increase in thickness of design A.
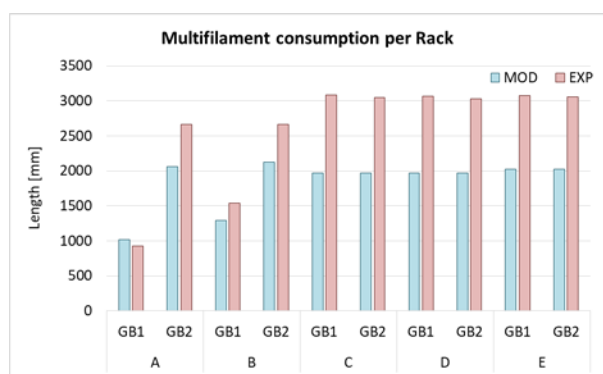
Figure 8. Comparison of multifilament consumption; MOD- modelled value from Tex-Mind software, EXP-measured value.

4. Conclusion

In general, it can be stated that the thickness of warp-knitted fabrics increases with increasing area weight. Our aim was to achieve a higher thickness in two guide bar designs and at the same time a looser, slightly more unstable knitted fabric, which could be favourable for bacterial colonisation during wastewater treatment due to its open and porous structure. With application GB misslapping (designs A and B), spatial deformation was achieved to a greater extent than with the patterned GB threading (designs D and E). O the patterning methods available on the machines in the KTT laboratory for the production of warp knits, misslapping has proven to be the most efficient and beneficial for the purposes and requirements of the biomass carriers. Moreover, subjectively, warp-knitted fabrics A and B appear more porous, which will be the subject of further research.

References

1. *W. Renkens, Y. Kyosev, Geometry modelling of warp knitted fabrics with 3D form, Textile Research Journal 81 (2011) 437–443. https://doi.org/10.1177/0040517510385171.*
2. *W. Renkens, Y. Kyosev, About the automated pattern creation of 3D jacquard double needle bed warp knitted structures, IOP Conf. Ser.: Mater. Sci. Eng. 141 (2016) 012010. https://doi.org/10.1088/1757-899X/141/1/012010.*
3. *Y. Kyosev, Warp Knitted Fabrics Construction, 1st ed., CRC Press, 2019. https://doi.org/10.1201/9780429094699.*
4. *L. Svobodová, K. Havlíček, M. Nechanická, R. Špánek, B.K. Sirková, I. Lenfeldová, O. Louda, E. Moučková, T. Lederer, Microfiber structure for enhanced immobilization of nitrifying bacteria in a post-nitrification reactor, Environmental Technology & Innovation 21 (2021) 101373. https://doi.org/10.1016/j.eti.2021.101373.*
5. *B. Kolcavová Sirková, I. Lenfeldová, K. Havlíček, M. Ryvolová, M. Vysanská, T. Lederer, P. Jirásková, Warp knitted spacer microfiber biomass carrier for wastewater treatment, Journal of Industrial Textiles 53 (2023) 152808372311545. https://doi.org/10.1177/15280837231154533.*
6. *D. Kortusová, Studium vlivu tvaru nanovlákenného nosiče na účinnost biodegradačního procesu v hybridním bioreaktoru, Technická Univerzita v Liberci, 2012. https://dspace.tul.cz/items/bf9a8875-224e-4ab6-a660-cd1cf77f00f7 (accessed September 7, 2023).*
7. *Y. Kyosev, TexMind Warp Knitting Pattern Editor 3D, (2021).*

PULLULAN / COLLAGEN SCAFFOLDS PROMOTE CHRONIC WOUND HEALING VIA MESENCHYMAL STEM CELLS

Elçin Tören [1*], Adnan Ahmed Mazari [1]

[1] Technical University of Liberec, Faculty of Textile Engineering, 1402/2, 461 17, Liberec, Czech Republic,
*elcin.toren@tul.cz; adnan.ahmed.mazari@tul.cz

Abstract:

This study investigates the use of pullulan-collagen nanofiber scaffolds integrated with mesenchymal stem cells (MSCs) for chronic wound healing. SEM analysis revealed that pullulan fibres had a larger average diameter (274 ± 20 nm) compared to collagen fibres (167.03 ± 40.04 nm), with composite fibres averaging 280 ± 102 nm. FTIR analysis showed molecular interactions between pullulan and collagen. Cell viability experiments showed that the pullulan-collagen scaffold achieved a cell viability rate of 99%, while pullulan alone was 91%. The fact that the solvent is distilled water is critical to increase cell viability in pullulan-collagen solutions, allowing cells to grow and proliferate in a healthy way without damage. Apoptosis experiments showed that pullulan-collagen scaffolds resulted in 1.29% necrosis, lower than 2.35% of pullulan. Reduced platelet activation and macrophage activity (0.75-fold for both) further confirmed the biocompatibility of the composite scaffold, demonstrating its potential in tissue engineering and chronic wound treatment.

Keywords:

Pullulan, Collagen, Mesenchymal Stem Cells (MSCs), Electrospinning, Chronic Wound Healing, Nanofiber Wound Dressing, Tissue Engineering.

1. Introduction

Nanofibers, with their high surface area-to-volume ratio, small pore size, and high porosity, protect against microbial infections and facilitate gas and fluid exchange in wound dressings, mimicking the extracellular matrix (ECM) to support cell adhesion, proliferation, and tissue regeneration [1,2]. Electrospinning allows the incorporation of bioactive agents, enhancing healing, while the structural flexibility of nanofibers enables controlled, sustained release of therapeutic agents.

Incorporating collagen, the most abundant protein in the human body, into needleless electrospun wound dressings is promising for chronic wound healing [3,4]. The combination of collagen's regenerative properties with electrospun nanofibers fosters an optimal environment for cell growth. During healing, fibroblasts produce collagen III initially, followed by collagen I in mature skin, with enzymes facilitating the maturation and alignment of collagen fibers [5,6]. Integrating these dressings with mesenchymal stem cells (MSCs), known for their self-renewal, differentiation abilities, and immunomodulatory properties, can enhance healing and promote tissue repair [7,8,9].

This study investigates the integration of Type I Collagen scaffolds with MSCs as a novel therapy for chronic wounds. Collagen mimics the ECM, promoting MSC adhesion, growth, and differentiation, which is particularly beneficial for diabetic wounds that often experience delayed healing and increased infection risk. The combination of MSCs' regenerative capabilities with collagen's biocompatibility is hypothesized to accelerate healing, reduce inflammation, and improve recovery, demonstrating significant potential as a novel treatment for chronic wound care.

2. Materials and Methods

2.1. Materials

P2-P4 of adipose tissue-derived stem cells (hASCs) from ScienCell Research Laboratories (Carlsbad, CA) were used for cell cultures. Cells were plated in T75 culture-treated flasks at approximately 1 million cells per cell and the culture medium was changed every 3-4 days during culture. The collagen peptide powder used for the experiment was sourced from Peptan, sourced from bovine, porcine and fish origins by (Darling Ingredients, China) Pullulan, with a purity of 99 %, was purchased from Sigma Aldrich, Czech Republic.

2.2. Methods

A 1:1 volume ratio of Pullulan and Collagen solutions is prepared and homogenized, then gently heated on a stirring hot plate for 20–30 minutes to ensure uniform solubilization. The solution is heated to 40°C to facilitate complete dissolution, then cooled to 37°C to maintain cell viability. A cell pellet containing 1×10^6 mesenchymal stem cells or human monocytes is introduced to the Pullulan/Collagen solution, resulting in a cell-containing polymeric mixture suitable for further processing. This mixture is transferred to the reservoir of a needleless electrospinning apparatus. The collector plate, a petri dish, is positioned approximately 7.5 cm from the spinning rotating wire electrode, with an applied voltage of 10 kV. Electrospinning is conducted for a maximum duration of 15 minutes. Control cells utilizing the same Pullulan/Collagen solution are deposited onto a petri dish at an equivalent rate without voltage application. Figure 1 illustrates the three principal phases in the preparation and processing of Pullulan/Collagen scaffolds with cells for wound healing applications.
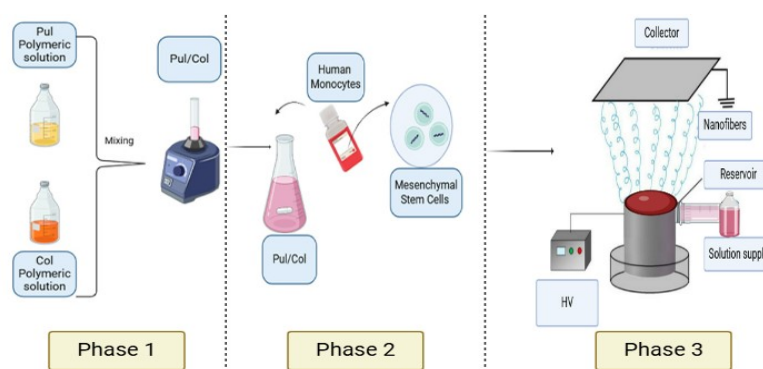
Figure 1. Schematic representation of Pullulan/Collagen scaffold preparation and integration with Mesenchymal Stem Cells for needless electrospinning

2.3 Material Characterization

2.3.1. Spinnability of Pullulan/Collagen (Fiber Morphology)
Pullulan/Collagen spinnability was examined without P2-P4 of adipose tissue-derived stem cells (hASCs) using a scanning electron microscope (SEM). Samples were attached to the SEM Phenom (Prague, Czech Republic) stage with conductive tape and analyzed at an accelerating voltage of 10 kV after gold sputter-coating. Fiber diameters were measured at 100 random points per SEM image, with statistical analysis to ensure accuracy. Measurements were conducted using ImageJ 1.8.0 software (National Institute of Mental Health, Bethesda, MD, USA).

2.3.2. Fourier-Transform Infrared Spectroscopy (FTIR)
The composition of the scaffolds was analyzed using an attenuated total reflectance (ATR) attachment and a Thermo Scientific Nicolet iS 50 FTIR (Thermo Fisher, Waltham, MA, USA). After obtaining the data, it was processed and plotted using Python (Python Software Foundation, Wilmington, DE, USA).

2.4. Cellular Viability and Cytotoxicity Assays

2.4.1. Cellular Viability
Cell viability was assessed using a live/dead assay kit and analyzed via fluorescence microscopy (Nikon Eclipse Ti2, Prague, Czech Republic). Approximately six hours post-electrospinning, the culture medium was removed from each well. Cells were then treated with a solution of calcein (2 µM) and ethidium (4 µM) in phosphate-buffered saline (PBS) for 10 minutes at 37°C. After incubation, the samples were rinsed with PBS to remove excess staining agents, enabling cell viability visualization under fluorescence microscopy.

2.4.2. Cytotoxicity
Two days after electrospinning, the media was aspirated, and the cells were washed with PBS. A *Lactate Dehydrogenase (LDH) cytotoxicity assay* (Cytotox96 kit, Promega, Madison, WI, USA) was carried out on the attached cells according to the manufacturer's protocol. This assay evaluates cell viability by measuring LDH activity in the cell lysate, indicating cellular membrane integrity and potential cytotoxic effects.

$$Viability \% = \frac{Average\ OD\ of\ sample}{Average\ OD\ of\ control} \times 100 \tag{1}$$

2.5. Gene Expression by Reverse Transcription-Polymerase Chain Reaction (RT-PCR)

2.5.1. Gene Expression by RT-PCR (SOX2 and OCT4 Markers)
Seven days post-electrospinning, RNA was extracted using the RNeasy Plus Mini Kit (Qiagen, Germantown, MD, USA) as per the manufacturer's instructions. Reverse transcription-polymerase chain reaction (RT-PCR) was then performed according to the protocol provided in the One-Step RT-PCR kit (Qiagen, Germantown, MD, USA). The expression of the pluripotency markers SOX2 and OCT4 was analyzed to assess gene activity.

2.5.2. Immunocytochemistry
Cell morphology was examined on Day 2 using fluorescence microscopy. Cells were fixed with 4% paraformaldehyde (PFA) in PBS (pH 7.4) for 15 minutes at room temperature (RT). After being rinsed three times with PBS, the samples were permeabilized with 0.1% (v/v) Triton X-100 for 10 minutes, followed by another three rinses with PBS. The cells were then stained with Phalloidin 488 to visualize f-actin and DAPI to stain the nuclei. The staining reagents were from Life Technologies (Carlsbad, CA, USA). Cellular visualization was carried out using a Nikon Eclipse Ti2fluorescence microscope (Prague, Czech Republic).

2.6. CytoViva Microscopy for Cell Incorporation

Cells were pre-labeled with green CMFDA dye (Invitrogen, Germantown, MD, USA) prior to incorporating them into the scaffold via electrospinning. Post-electrospinning, cells were stained with DAPI for nuclear visualization. Imaging was conducted using CytoViva's enhanced darkfield transmitted light condenser (NA 1.2–1.4) and the Dual Mode Fluorescence (DMF) module. These components were mounted on an Olympus BX51 upright microscope with a 100X oil UPL Fluorite objective (NA 0.60–1.30) optimized for darkfield imaging. Illumination was provided by a Prior Lumen 200 metal halide lamp with adjustable light attenuation. High-resolution optical images were captured using a DAGE-MTI XLMCT cooled CCD camera with a 7.4 µm pixel size.

2.7. Apoptosis and Necrosis Evaluation by Annexin V/PI Staining

The MSC and HSF nuclei (2×10^5 cells/well) were dyed with PI after 24 hours of incubation and then investigated by flow cytometers. Apoptotic cells were studied in an Annexin V and PI double dye (Sigma-Aldrich, Burlington, MA, United States) protocol and quantified in a flow cytometer. In fact, early apoptosis cells tend to expose phosphatidylserine (PS) on the extracellular surface of plasma membranes that can be specifically targeted by anannex V. Moreover, PI can permeabilize

chromosomes in late apoptosis cells. Dead cells (V^+/PI^- and V^-/PI^+) and apoptosis/necrosis (V^+/PI and V/PI^+) cells were detected by BD Biosciences' BD FACScalibur flowcytometer and analyzed by FlowJo 7.6 software (Bennett Dickinson, Canton, United States). All experiments were performed in three parts.

2.8. Monocyte and Platelet Activities

Human monocytes were obtained from healthy volunteers' whole blood using the Percoll protocol (Sigma-Aldrich, Burlington, MA, USA) with IRB approval (CE12164) [10]. Monocytes (1×10^5/well) were seeded in a 24-well plate coated with each nanocomposite and incubated in RPMI medium (10% FBS and 1% (v/v) antibiotics (10,000 U/mL penicillin G and 10 mg/mL streptomycin)) for 96 h at 37°C. Cells were then collected using a 0.05% trypsin solution. Monocyte and macrophage morphology was assessed via microscopy. Monocyte conversion yield was calculated using the formula: monocyte conversion yield (%) = ((Macrophages)/(Monocytes + Macrophages)) × 100%. The inflammatory response was further examined by CD68 (macrophage marker) immunofluorescence staining with a primary anti-CD68 antibody (GeneTex Inc, Irvine, CA, USA). To study platelet adherence and activation by the nanomaterials, 2×10^6 platelets per well were incubated for 24 h, then fixed with 2.5% glutaraldehyde for 8 h. Platelets were washed with PBS, dehydrated using 30% to 100% alcohol, and dried. After sputter-coating with gold, platelet morphology was observed using SEM (JEOL JEM-5200, JEOL Ltd., Akishima, Tokyo, Japan).

3. Results
3.1. Material Characterization

The scanning electron microscopy (SEM) image presented in Figure 2 provides a detailed view of the nanofibrous architecture, revealing a highly organized and interconnected network.
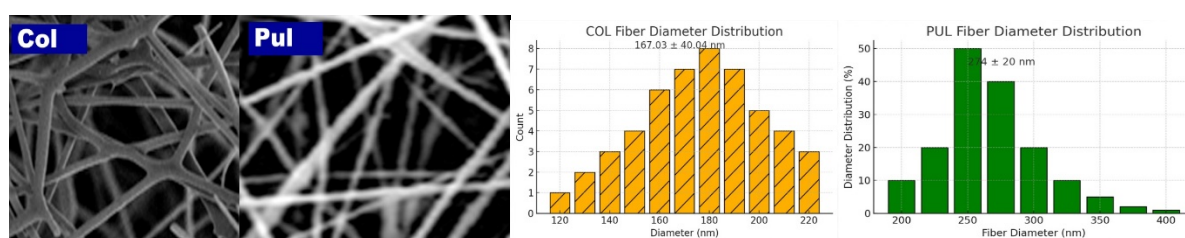
Figure 2. Comparative SEM Micrographs and Fiber Diameter Distributions of COL and PUL Fibers Showing Average Diameters of 167.03 ± 40.04 nm and 274 ± 20 nm.

Figure 2 compares COL and PUL fibers, highlighting their structural and dimensional features through SEM micrographs and fiber diameter distributions. SEM images show that COL fibers form a uniform, tightly interconnected network, whereas PUL fibers are looser, less compact, and have visibly thicker fibers, indicating differences in fabrication or material composition. Diameter analysis reveals COL fibers average 167.03 ± 40.04 nm with a narrow distribution, indicating uniformity, while PUL fibers average 274 ± 20 nm with a broader distribution, indicating variability. These structural and diameter differences likely affect their mechanical and functional properties.
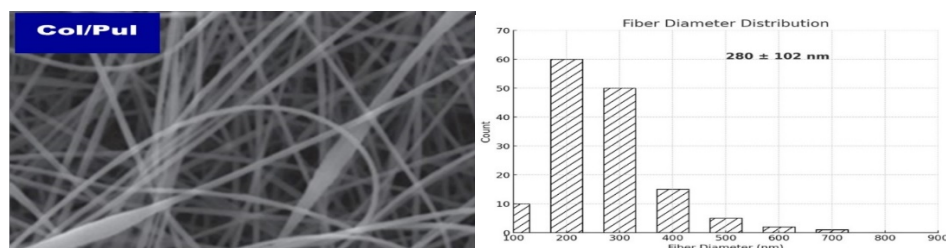
Figure 3. SEM analysis and fiber diameter distribution of col/pul nanofibers) with an average diameter of 280 ± 102 nm

Figure 3 illustrates that Col/Pul composite fibers have a smooth, uniform morphology without bead formation, unlike pure pullulan fibers. Blending collagen and pullulan has resulted in continuous, well-formed fibers, suggesting that this polymer combination enhances fiber structure by stabilizing the electrospinning process. The absence of bead defects indicates optimal viscosity and solution properties for this composition. The fiber diameter distribution shows an average of 280 ± 102 nm, with most fibers ranging from 200 to 300 nm and a few reaching up to 500 nm or slightly higher. Despite some variability in size, the majority of fibers are consistently thin, typical of electrospun nanofibers. This combination of pullulan and collagen at the specified ratio yields nanofibers with a smooth, uniform morphology and an average diameter suitable for applications like tissue engineering or biomaterials, where controlled fiber diameter and morphology are essential.

3.2. Fourier-Transform Infrared Spectroscopy (FTIR)

The FTIR spectrum for pure Pul (red line) shows characteristic absorption bands at several key regions. Figure 4 shows the FTIR spectra of Pul, Col, and their combination (Pul + Col), highlighting the characteristic absorption peaks of each material. The shifts in the absorption bands after the combination of Pul and Col indicate molecular interactions between the two components, as evidenced by changes in the C–O–C, C–O, and CH_2/CH_3 stretching regions. These shifts suggest the formation of a composite material with modified functional group interactions compared to their individual spectra. A peak at 929 cm^{-1} represents the C–O–C bond, characteristic of ether groups, while the band at 1029 cm^{-1} corresponds to the C–O stretching vibrations. Additionally, a peak at 2931 cm^{-1} is attributed to the CH_2 and CH_3 groups, typical of alkyl chains in the Pul structure. These peaks reflect the functional groups present in Pul, highlighting its typical structural components.
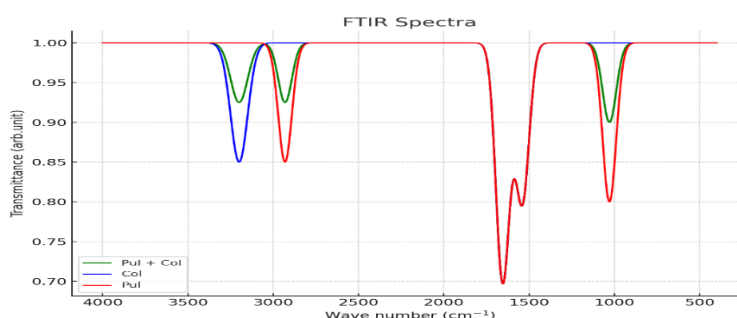
Figure 4. FTIR Spectra of Pul, Col, and Pul + Col Samples Showing Peaks at 2931 cm^{-1} (C-H), 1655 cm^{-1} (Amide I), and 1540 cm^{-1} (Amide II)

The spectrum of pure collagen (Col) reveals notable absorption bands: a peak at 1540 cm^{-1} for amide II vibration and another at 1655 cm^{-1} for amide I vibration. A broad peak around 3200 cm^{-1} is attributed to O–H stretching vibrations, linked to hydroxyl or hydrogen-bonded N–H groups in proteins like collagen. These bands indicate peptide bonds and hydroxyl groups in the pure collagen. When Pul is combined with Col, shifts in key absorption bands occur. The C–O–C vibration from Pul shifts from 929 cm^{-1} to 910 cm^{-1}, suggesting interactions like hydrogen bonding or other intermolecular forces. The C–O stretching vibration shifts from 1029 cm^{-1} to 1033 cm^{-1}, and the CH_2/CH_3 group shifts from 2931 cm^{-1} to 2935 cm^{-1}, indicating slight structural changes. Additionally, the amide II band of Col shifts from 1540 cm^{-1} to 1550 cm^{-1} in the combined sample, further indicating molecular-level interaction. These shifts confirm the interaction between Pul and Col, likely due to physical or chemical bonding, suggesting the formation of a composite structure with modified functional groups.

3.3. Cellular Viability

Control cells were administered at a uniform rate onto the petri dish, devoid of any voltage application. In this study, the Collagen/Pullulan polymeric solution was dissolved in distilled water, which resulted in a significant improvement in cell viability. The group achieved 99% viability compared to the control, while the pullulan/cell scaffold alone had a 91% viability rate. The use of distilled water as a solvent for

the Collagen/Pullulan solution appears to be a critical factor in promoting cell viability while maintaining the stemness of the mesenchymal stem cells, making it a promising approach for tissue engineering applications. Importantly, the differences between groups were not statistically significant ($p > 0.05$), suggesting that the observed variations in cell viability are within the margin of experimental error.

3.4. Cytotoxicity

Cell cytotoxicity was evaluated using lactate dehydrogenase (LDH) release. LDH is an enzyme that is released when the cell membrane is compromised, thus serving as a reliable marker for cell death and cytotoxicity. The LDH assay was conducted on the cell lysates of both control and electrospun groups. Figure 5a presents a quantitative analysis of LDH levels released from cell lysates on various biomaterial surfaces (Collagen, Collagen/Pullulan, and Pullulan).

To further elucidate the protective role of Collagen/Pullulan in the scaffold, cells were electrospun using only culture media (Figure 5b). In this instance, cell viability significantly decreased to 40%, compared to cells sprayed with the same media directly onto the petri dish. This observation underscores the beneficial effect of dissolving the Collagen/Pullulan solution in distilled water, which appears to enhance cell viability.
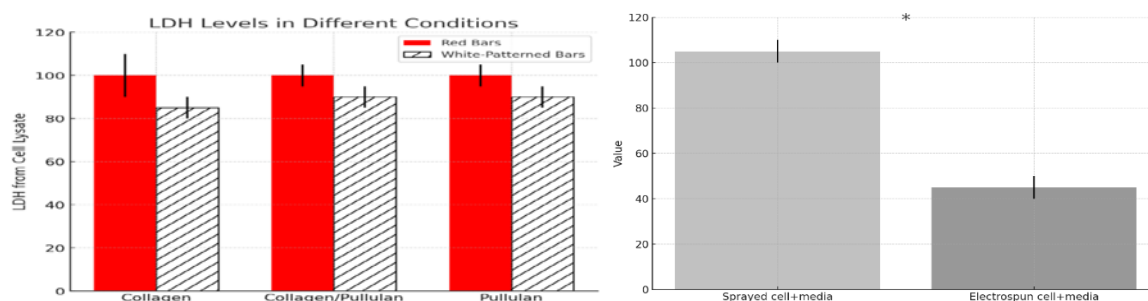
Figure 5. (a) Comparison of LDH release from cell lysate of nanofibers **(b)** Analysis of lactate dehydrogenase (LDH) levels in cell lysates from electrospun and control groups *shows p-value < 0.05.

3.5. Gene Expression by RT-PCR (SOX2 and OCT4 Markers)

The expression of SOX2 and OCT4 genes is analyzed using Reverse Transcription-Polymerase Chain Reaction (RT-PCR) to confirm the pluripotency of stem cells. This method quantifies the levels of mRNA from these genes, which are critical markers of self-renewal and the capacity of stem cells to differentiate into various cell types. The maintenance of SOX2 and OCT4 expression is essential to ensure that cells retain their pluripotent properties, even after processes such as electrospinning.

7 days post-electrospinning, staining with Oil Red O, toluidine blue, and Alizarin Red S was conducted to assess adipogenic, chondrogenic, and osteogenic differentiation. All cells exhibited negative results for these stains, indicating the absence of differentiation into adipocytes, chondrocytes, or osteoblasts. Furthermore, PCR analysis revealed no significant alterations in the expression of stem cell markers SOX2 and OCT4, confirming that the stemness of the cells was maintained both prior to and following electrospinning (see Figure 6).
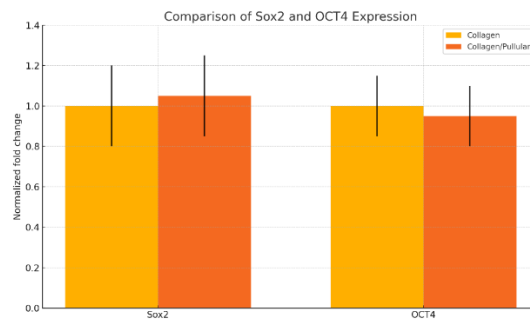
Figure 6. Gene expression in Collagen and Collagen / Pullulan electrospun groups normalized to control. Control groups are cells cultured with 5 mg/mL Collagen.

SOX2 expression exhibits a fold change approximating 1.0 for cells cultured on both collagen and collagen/pullulan scaffolds, indicating stable expression across these conditions when normalized to the control group. A marginal increase in SOX2 expression is observed in the collagen/pullulan group compared to the collagen-only group, with a fold change slightly exceeding 1.0, suggesting potential upregulation with pullulan incorporation. However, the substantial overlap in error bars indicates that the difference is likely not statistically significant. OCT4 expression demonstrates a similar pattern, with both scaffold types exhibiting a fold change of approximately 1.0 compared to the control. The collagen/pullulan scaffold group again displays slightly higher OCT4 expression than the collagen-only scaffold. However, the minimal differences and overlapping error bars suggest that these changes are likely not statistically significant. Both scaffold types effectively maintain stem cell pluripotency, with the collagen/pullulan scaffold showing a slight, though statistically insignificant, enhancement in SOX2 and OCT4 expression. Further investigation is warranted to determine any definitive advantage of the collagen/pullulan scaffold over the collagen-only scaffold.

3.6. Immunocytochemistry

Immunocytochemistry analysis is employed to evaluate cellular morphology and structural integrity. In this investigation, the analysis compares actin filament organization between the control group (Figure 7a) and cells cultured on a Pullulan/Collagen scaffold (Figure 7b). The presence of the scaffold induces alterations in cytoskeletal alignment, reflecting cellular adaptation to the three-dimensional environment, in contrast to the more uniform arrangement observed in the control (two-dimensional surface). Notwithstanding the changes in alignment, cell viability and structural integrity (cytoskeleton and nuclei) remain preserved, suggesting that the scaffold facilitates appropriate cell attachment and proliferation.
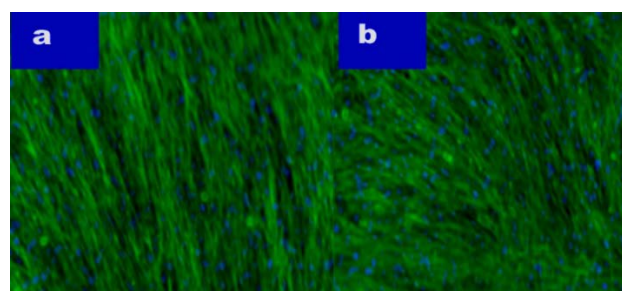
Figure 7. a) Actin staining of adipose-derived stem cells in control and in (b) Pullulan/Collagen cells at 10×. Phalloidin 488 (green) labels actin, while DAPI (blue) labels the nucleus.

In this experiment, Phalloidin 488 labeled actin filaments green, and DAPI stained the nuclei blue. Comparing control cells with those on a pullulan/collagen scaffold reveals notable differences in cell morphology and cytoskeletal organization. In the control group (Figure 8a), actin filaments are densely and uniformly aligned, indicating healthy cells with strong attachment. The DAPI-stained nuclei are evenly distributed, suggesting normal proliferation and a typical two-dimensional monolayer. Without a

scaffold, cells spread uniformly, resulting in a well-organized cytoskeletal structure. Conversely, cells on the pullulan/collagen scaffold (Figure 8b) show a more varied cytoskeletal arrangement. Although the actin cytoskeleton remains intact, filament alignment and distribution are less uniform. The three-dimensional scaffold influences cell morphology, leading to complex structural adaptations as cells interact with the substrate. Despite this, nuclei remain well-preserved and normally distributed, indicating the scaffold does not compromise cell viability.

This study elucidates the pullulan/collagen scaffold's influence on ADSC structural organization. While altering the flat monolayer arrangement seen in the control, the scaffold supports cell attachment and growth. Cells adapt to the three-dimensional scaffold without losing cytoskeletal integrity, making it a promising material for tissue engineering, where a three-dimensional environment closely mimics natural tissue conditions and is essential for effective cell growth and differentiation.

3.7. CytoViva Microscopy for Cell Incorporation

The study aimed to assess the incorporation and spatial distribution of adipose-derived stem cells (ADSCs) within a highly porous pullulan/collagen scaffold produced through electrospinning. CytoViva imaging was employed to visualize cell embedding efficacy and evaluate if the scaffold's porous architecture supports cell attachment and proliferation. The scaffold's ability to maintain cell viability and function is critical for tissue engineering applications, where preserving a three-dimensional cellular organization is essential for mimicking natural tissue environments.
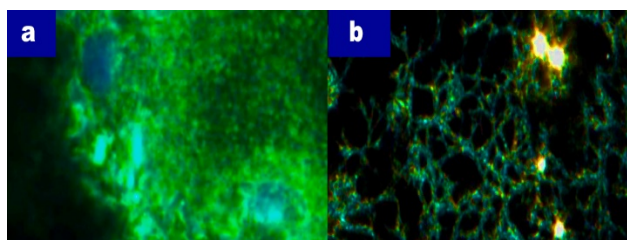

Figure 8. CytoViva Imaging of Adipose-Derived Stem Cells Embedded in Pullulan/Collagen Scaffold;(a) Cells pre-stained with CellTracker Green CMFDA and stained with DAPI post-electrospinning, showing cell integration into the scaffold,(b) CytoViva image of the scaffold structure without pre-stained cells, revealing the porous architecture that facilitates cell embedding.

Figure 8 illustrates CytoViva imaging of the scaffold's porous structure, crucial for cell embedding. In Figure 8a, cells pre-stained with CellTracker Green CMFDA before electrospinning are evenly distributed, indicating their incorporation. Green fluorescence marks viable cells, and blue DAPI staining shows nuclei, confirming cell integration. The pores, around 10 μm in diameter, allow cell penetration while maintaining scaffold stability. Figure 8b, without pre-staining, shows the scaffold's three-dimensional structure through reflection and scattering, highlighting its interconnected, porous architecture. This structure provides ample surface area and space for cell attachment, enabling cells to spread and embed within the pores, essential for tissue regeneration requiring robust cell-scaffold interaction. These results suggest that the pullulan/collagen scaffold supports cell integration, indicating its potential for tissue engineering by facilitating cell attachment and penetration in a three-dimensional environment necessary for functional tissue development.

3.8. Apoptosis and Necrosis Evaluation by Annexin V/PI Staining

In this study, the effects of various nanocomposites, especially Pullulan, Collagen and Pullulan/Collagen electrospun scaffolds, on mesenchymal stem cells (MSCs) were investigated. Cell apoptosis and necrosis were assessed using Annexin V/PI double staining assay and then analysed by flow cytometry. Apoptosis study was performed to investigate the biocompatibility of Pullulan/Collagen scaffolds and early apoptosis (Annexin V-positive), late apoptosis/necrosis (PI-positive) and cell survival rates were determined. The results were used to evaluate the effects of electrospun scaffolds on cell viability and the biocompatibility of the scaffold (see Figure 9).
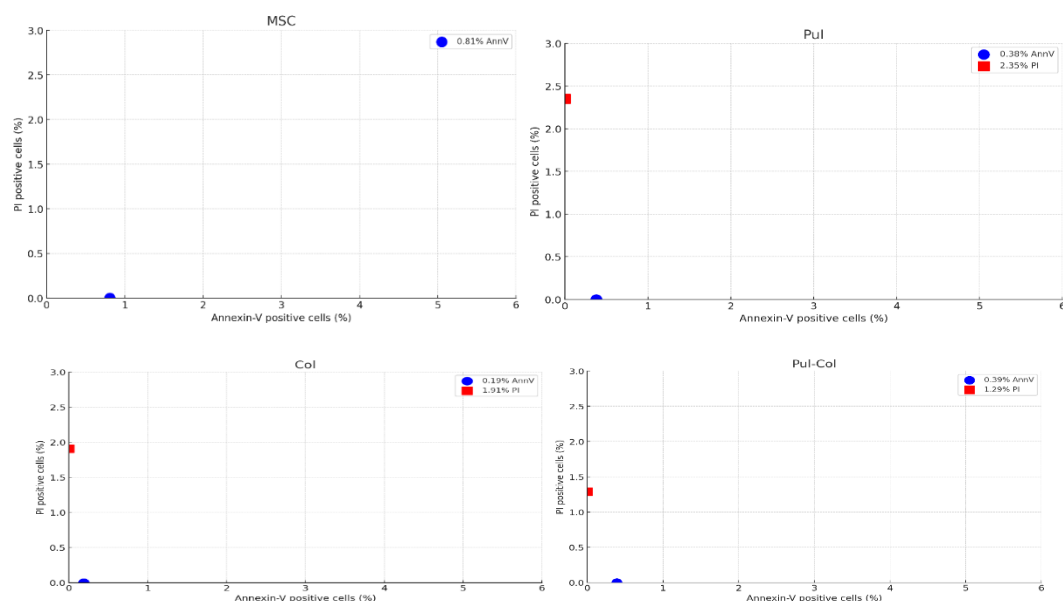
Figure 9. Comparison of apoptosis and necrosis levels in different cell groups with Annexin-V and PI positivity

Figure 9 shows that MSCs, used as a control group without a scaffold, have 0.81% Annexin V-positive cells and no PI-positive cells, indicating high cell viability with minimal apoptosis or necrosis. MSCs on Pullulan scaffolds (Pul) show 0.38% early apoptosis and 2.35% necrosis or late apoptosis, suggesting increased cell stress. MSCs on Pullulan/Collagen composite scaffolds (Pul-Col) demonstrate 0.39% early apoptosis and 1.29% necrosis, indicating superior biocompatibility relative to pure collagen. MSCs on collagen scaffolds (Col) exhibit 0.19% early apoptosis and 1.91% necrosis, indicating moderate stress but acceptable viability. The Annexin V/PI assay results indicate that the Pullulan/Collagen scaffold has the highest biocompatibility, with lower late apoptosis and necrosis compared to individual components. Collagen alone causes moderate necrosis, while Pullulan shows the highest necrotic effect. The Pullulan/Collagen composite scaffold mitigates the adverse effects of each material, enhancing cell survival and biocompatibility.

3.9. Monocyte and Platelet Activities

The assessment of platelet activation and monocyte activity is crucial for determining the biocompatibility of nanocomposites, particularly in medical applications. Excessive platelet activation may result in thrombosis, while elevated monocyte activity can potentially induce inflammation, both of which present risks for implants or wound healing materials. These evaluations ensure that the material does not induce undesired blood coagulation or elicit detrimental immune responses, rendering them essential for assessing the safety and efficacy of nanocomposites in clinical contexts.
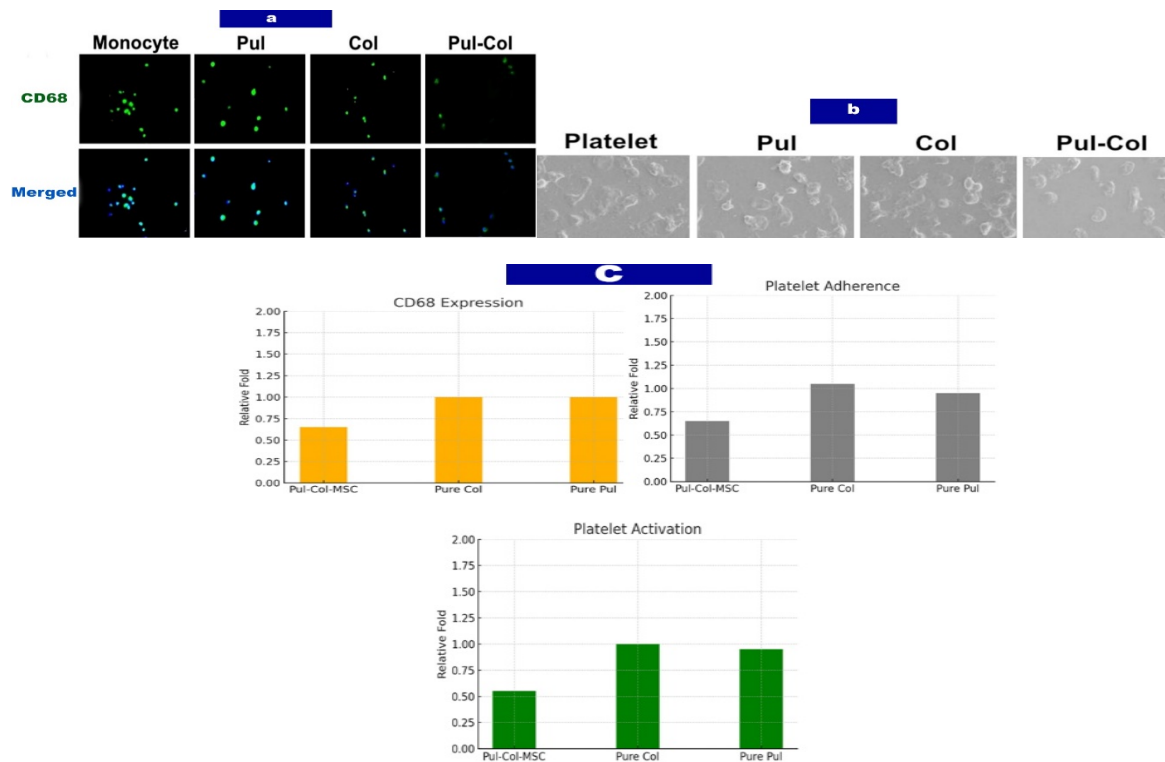
Figure 10. Effects of various materials in macrophage and platelet activation. (a) The macrophage marker CD68 (green color) was investigated by immunofluorescence staining at 96 h. DAPI was used to locate cell nuclei (blue color). Scale bar = 20 μm. (b) The morphology of platelets was observed by SEM analysis. Scale bar = 10 μm. (c) The CD68 positive cells were semi-quantified for macrophage activation. Quantitative data are presented as mean ± SD from three independent experiments, with statistical analysis conducted using ANOVA to determine The significance of differences (*p < 0.05).

This study investigated the biocompatibility of pullulan (Pul), collagen (Col), and Pul-Col nanocomposites by evaluating macrophage activation (CD68 expression) and platelet activation. Immunofluorescent staining (Figure 10a) revealed that CD68 expression was 1.25-fold higher in pure Pullulan and Collagen groups, while the Pul-Col-MSC group showed a 0.75-fold reduction, indicating decreased macrophage activation. Scanning electron microscopy (SEM) (Figure 10b) demonstrated extensive platelet spreading in pure Pullulan and Collagen groups, suggesting higher activation, whereas the Pul-Col group exhibited reduced spreading, indicating lower thrombogenic risk. Quantitative data (Figure 10c) confirmed increased CD68 expression (1.25-fold) and platelet adhesion (1.00 and 1.25 times) in pure Collagen and Pullulan groups, while the Pul-Col-MSC group showed lower values (0.75-fold and 0.75 times, respectively). Platelet activation rates were 1.25-fold in pure Collagen and Pullulan groups but only 0.50-fold in the Pul-Col-MSC group. These findings indicate that Pul-Col nanocomposites reduce inflammatory response and platelet activation, improving biocompatibility and demonstrating their potential for clinical applications, particularly in wound healing.

4. Conclusions

This study investigates pullulan-collagen nanofiber scaffolds with MSCs for chronic wound healing. Collagen was dissolved in distilled water, maintaining higher cell viability and biocompatibility compared to acetic acid. SEM revealed smooth morphology and stable formation of the electrospun pullulan-collagen fibers, while FTIR confirmed molecular interactions enhancing scaffold integrity. The pullulan-collagen scaffold demonstrated 99% cell viability, lower necrosis (1.29%), and reduced cell membrane damage compared to pullulan alone. The scaffold also exhibited a favorable immunogenic response, with decreased macrophage activation (0.75-fold) and significantly lower platelet activation and adhesion, crucial for wound healing. The water-based pullulan-collagen scaffold minimizes cytotoxicity, maintains cell viability, and reduces immune activation, showing promise for regenerative medicine applications.

References

1. Olson JL, Atala A, Yoo JJ. Tissue Engineering: Current Strategies and Future Directions. Chonnam Med J 2011;47:1–13. https://doi.org/10.4068/cmj.2011.47.1.1.

2. Roacho-Pérez JA, Garza-Treviño EN, Moncada-Saucedo NK, Carriquiry-Chequer PA, Valencia-Gómez LE, Matthews ER, et al. Artificial Scaffolds in Cardiac Tissue Engineering. Life (Basel) 2022;12:1117. https://doi.org/10.3390/life12081117.

3. Xiao H, Chen X, Liu X, Wen G, Yu Y. Recent advances in decellularized biomaterials for wound healing. Mater Today Bio 2023;19:100589. https://doi.org/10.1016/j.mtbio.2023.100589.

4. Ataide JA, Zanchetta B, Santos ÉM, Fava ALM, Alves TFR, Cefali LC, et al. Nanotechnology-Based Dressings for Wound Management. Pharmaceuticals (Basel) 2022;15:1286. https://doi.org/10.3390/ph15101286.

5. Costela-Ruiz VJ, Melguizo-Rodríguez L, Bellotti C, Illescas-Montes R, Stanco D, Arciola CR, et al. Different Sources of Mesenchymal Stem Cells for Tissue Regeneration: A Guide to Identifying the Most Favorable One in Orthopedics and Dentistry Applications. Int J Mol Sci 2022;23:6356. https://doi.org/10.3390/ijms23116356.

6. Kolimi P, Narala S, Nyavanandi D, Youssef AAA, Dudhipala N. Innovative Treatment Strategies to Accelerate Wound Healing: Trajectory and Recent Advancements. Cells 2022;11:2439. https://doi.org/10.3390/cells11152439.

7. Barhoum A, Bechelany M, Hamdy Makhlouf AS. Handbook of Nanofibers. 2019. https://doi.org/10.1007/978-3-319-53655-2.

8. Sasithorn N, Martinová L, Horakova J, Mongkholrattanasit R. Fabrication of Silk Fibroin Nanofibres by Needleless Electrospinning, 2016, p. 95–113. https://doi.org/10.5772/65835.

9. Xiong J, Liu Y, Li A, Wei L, Wang L, Qin X, et al. Mass production of high-quality nanofibers via constructing pre-Taylor cones with high curvature on needleless electrospinning. Materials & Design 2021;197:109247. https://doi.org/10.1016/j.matdes.2020.109247.

10. Stammers M, Ivanova IM, Niewczas IS, Segonds-Pichon A, Streeter M, Spiegel DA, et al. Age-related changes in the physical properties, cross-linking, and glycation of collagen from mouse tail tendon. J Biol Chem 2020;295:10562–71. https://doi.org/10.1074/jbc.RA119.011031.

EFFECTS OF PRINTING ON LUXURIOUS SCARF WITH SILK BLENDS

İsmet Ege Kalkan*1 , Ayşegül İlketapar2, Figen Temiz-Dişlioğlu3, Jülide Doğan4, Hamit Kaya5, Tuğçe Savaşkan6 , Umut Kıvanç Şahin7

1 Department of Textile Engineering, Istanbul Technical University, Istanbul, Turkiye, e-mail: kalkani15@itu.edu.tr
2Vakko, Esenyurt Design Center, Istanbul, Turkiye, e-mail: aysegule@vakko.com.tr
3Vakko, Esenyurt Design Center, Istanbul, Turkiye, e-mail: figen.temizdislioglu@vakko.com.tr
4Vakko, Esenyurt Design Center, Istanbul, Turkiye, e-mail: julide.dogan@vakko.com.tr
5Vakko, Esenyurt Design Center, Istanbul, Turkiye, e-mail: hamit.kaya@vakko.com.tr
6Vakko, Esenyurt Design Center, Istanbul, Turkiye, e-mail: tugce.savaskan@vakko.com.tr
7 Department of Textile Engineering, Istanbul Technical University, Istanbul, Turkiye, e-mail: sahinumut3@itu.edu.tr

Abstract:

Unlike many other items incorporating fiber, silk fiber is a type of fiber that requires a very sensitive and particular production and procedure in the fashion industry. Because of its desirable qualities, including softness, drape, and water absorbency, it is a sought-after fabric for shawls and related textile items. In terms of cost and characteristics, silk fiber has also been utilized by mixing it with other threads. As a result, the targeted optimal values can be obtained for a lower cost. Thanks to the color designs created on the 100% silk fabric used to make the shawl, it responds to the growth of the fashion industry. Various motifs and colors are included in the patterns found on the shawl. It also sought to determine the optimal value by analyzing various silk blends and the modifications that various blend structures bring about during the finishing process. The project looked into the aspects influencing the fabrics under examination's touch as well as the impact of fiber mixtures. As a result, the structure that yields the best test results has been chosen, and it has helped the industry produce high-quality goods.

Key words:

Silk, Comfort, Luxury Textiles, Yarn Blend, Printing

1. Introduction

When the right circumstances are met, a caterpillar insect known technically as Bombyx mori—which feeds on mulberry leaves—weaves a cocoon to complete one of its life phases and yields silk, a textile fiber. East Asia and the Mediterranean region are the silkworm's native habitat. The Marmara region of the nation produces the majority of it [1].
Cream or pale yellow is the color of raw silk. It has very low electrical conductivity. Of all the animal fibers, it is the most resilient. Stretching it by 10% to 25% won't break it. When wet, it loses 15% of its strength. A cocoon's fibers can reach lengths of 1000–3000 meters [2].
A delicate and high-quality final product is achieved by the combination of cashmere and silk fibers, which stand out for their luster and beauty and have lovely drape, hold, and gloss, respectively [3]. According to the blending kinds, the silk/cashmere blending yarn produced using the spiral grooved ceramic production method and opening pin roller offers the best breaking strength, irregularity, and defect (thin, thick, and neps) values.

Silk is a thin, natural material that needs special processing; as such, printing and dying silk fabric call for caution and delicacy. The composition and sensitivity of the fabric mean that changes in temperature and chemical usage can affect its structure and appearance. For this reason, in order to preserve the natural sheen of the silk fabric, the methods must be properly followed and with the appropriate techniques.
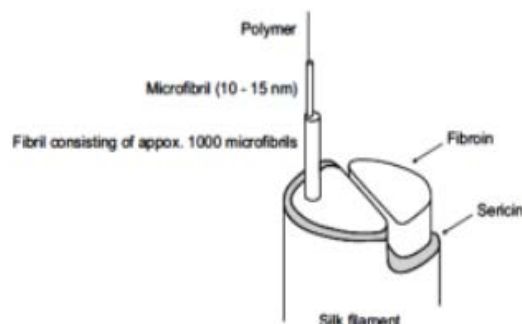
Figure 1. Structure a silk thread from fibroin and sericin [2]

The characteristics of silk cloth allow for the application of screen, digital, and hand printing techniques. For better fastness, reactive, metal complex, and acid dyes are recommended above other dye types[4]. Silk textiles are prized for their exquisite and opulent structures, and their qualities are enhanced and preserved by a variety of finishing techniques. These procedures improve the fabric's functional and aesthetic qualities while extending its lifespan. Water-repellent treatments help silk materials resist water better, making them more comfortable to use over time. Water-repellent finishing techniques involve coating the fabric's surface with chemicals based on silicone or fluorocarbon. These substances preserve the fabric's air permeability and stop water droplets from penetrating it [5].

By analyzing the yarn blends, as well as the dye and finishing techniques applied to the fabric with laboratory research, the goal is to ascertain the touch values. Finding the parameters that affect the touch will guarantee that the end product has the desired outcome and is error-free. This project will therefore limit the margin of error brought about by the touch in the sector and enable the creation of a touch value that complies with the standards. The primary goal is to conduct the required experiments in order to investigate how touch affects the silk fabric.

2. Experimental
2.1. _Materials_

The fabrics used in this study were weave silk fabric, silk cashmere blend fabric raw and with direct printed, supplied from VAKKO.

2.2. _Method_

A comparison was made using raw silk and blended silk fabric types. Fabrics were examined based on the final product obtained by different finishing processes of 100% silk and blended silk. A comparison was made for the applied dyeing, printing and finishing processes. The table 1 indicates the fabric blends of the woven fabric samples and the finishing processes applied.

Table 1. Experimental Design

Sample	Construction	Method
1	Silk	Raw
2	Silk/Cashmere	Raw
3	Silk	Printing+Finishing
4	Silk/Cashmere	Printing+Finishing

All samples have been tested with the following their own respective standards: abrasion resistance ISO 12947-2, pilling resistance 12945-1, air permeability ISO 9237 (100Pa), fabric hardness ASTM D4032 and water vapour permeability ISO 15496.

3. Results and discussion

Table 2. Abrasion Resistance Results

Fabric name	Weight of before test	Weight of after 2000 cycle	Weight of after 4000 cycle	Weight of after 8000 cycle	Cycle in which break occurs
1	0,0785	0,0771	0,0743	0,0593	8000
2	0,0554	0,0503	0,0413	-	4000
3	0,0811	0,0801	0,0747	-	4000
4	0,0585	0,0419	-	-	2000

From the results we can see that silk outperforms cashmere blend, but after 4000 cycles silk has also showing degradation but not breakage in the first test. In the second test silk have yarn breakage at 4000, but overall at each measurement after the cycles we can see that weight loss percentage is lower in %100 silk.

Table 3. Pilling Resistance Results

Sample	1.	2.
1	3	4/5
2	1	1
3	4/5	4/5
4	2/3	2/3

According to pilling resistance we can say that cashmere can not withstand constant pilling and not good for skin comfort. %100 silk has better resistance to pilling and therefore better for skin comfort.

Table 4. Air Permeability Results

Sample	1. (l/m2/s)
1	274.38
2	1080.17
3	114.50
4	1985.44

For air permeability, cashmere blend have higher breathability, this part has to be enhanced on %100 silk.

Table 5. Fabric Hardness Results

Sample	1. (kgf)	2. (kgf)	3. (kgf)
1	0,014296	0,022645	0,016383
2	0,032313	0,030226	0,023964
3	0,027559	0,024098	0,025313
4	0,059461	0,05754	0,05178

Hardness test shows us that %100 silk is much softer and much less impacted with the printing as cashmere blend had nearly got twice as its weight.

Table 6. Water Vapour Permeability Results

Sample	Result
1	1,3471
2	1,5682
3	1,3579
4	1,4243

Water vapour permeability shows us that nearly the same results as air permeability, cashmere blends have more breathability.

4. CONCLUSIONS

That's why the touch is affected in the textile sector, especially during the dyeing and printing operations. The many types of fibers in a fabric alter its structure and characteristics, which in turn modifies the techniques that need to be used. Consequently, it is important to observe the touch value while taking these factors into account. By determining the appropriate test values and taking into account the touch-influencing factors, the desired touch value can be achieved. It is possible to place the touch value on a value when specific tests achieve the causes impacting the touch of a value controlled by human initiative.

In conclusion, the study demonstrates that 100% silk fabric, especially with finishing and printing processes outperforms cashmere in various performance parameters. Silk fabric showed superior results in abrasion resistance and pilling also softer than the blends. However, the addition of cashmere fibers improved air permeability, making cashmere silk fabrics more breathable than pure silk. The results suggest that silk's performance characteristics can be optimized through specific finishing techniques, though certain drawbacks, such as color release in blended fabrics, require attention.

Tests and comparisons can also result in the touch value being placed on a standard, even though the textile industry is still working to digitize each value within certain standards. As a result, it is possible to avoid loss and unwanted texture after production. The touch value offers the chance to choose ahead of time the procedures that must be followed in order to accomplish this goal while achieving the intended result with the type of weaving, type of fiber, dyeing procedures, and finishing procedures in conscious and controlled manufacturing.

ACKNOWLEDGEMENTS

References

1. *Shahriar, A., (2019), The Optimization of Silk Fabric Production Process. International Journal of Current Engineering and Technology*
2. *Nibikora I., Wanga J,(2010), Optimum Selection of the Opening Roller and Navel for Rotor Spun Silk/Cashmere Blended Yarn.Fibres and Textiles in Eastern Europe. Vol. 18, No. 5 (82) pp. 35-38.*
3. *Sheikh I. Ishrat, Nigel P. Grigg, Nihal Jayamaha and Venkateswarlu Pulakanam, Cashmere Industry: Value Chains and Sustainability. Springer Series in Fashion Business, https://doi.org/10.1007/978-981-10-8878-0_7*
4. *Hanan A. Othman a , Nanees Gamal a , Aya Sedik a , Fedaa Saad a , Bouthaina M. Hegazy a , Hala M. Elmorsy a , Sherif A. Aly b , and Ahmed G. Hassabo, (2024). Printing Techniques of Silk Fabric. Journal of Textiles, Coloration and Polymer Science*
5. *Schindler, W. D., & Hauser, P. J. (2004). Chemical Finishing of Textiles (Woodhead Publishing Series in Textiles). Woodhead Publishing..*

SHOES WITH RUBBER/WOOD-SHAVINGS MIXED SOLE AND VEGETABLE TANNED LEATHER

**Ismet Ege Kalkan* [1] , Gunseli Aksoy Oral [2] , Aysegul Ilkentapar [3] , Figen Temiz-Dishlioglu [4,]
Nurcan Tiryaki [5] , Sena Sahin [6] , Umut Kıvanç Sahin [7]**

[1] Department of Textile Engineering, Istanbul Technical University, Istanbul, Turkey, e-mail: Kalkani15@itu.edu.tr
[2] Vakko, Nakkaştepe Design Center, Istanbul/Turkey e-mail:gunseli.oral@wcollection.com.tr
[3] Vakko, Esenyurt Design Center, Istanbul, Turkey, e-mail: aysegule@vakko.com.tr
[4] Vakko, Esenyurt Design Center, Istanbul, Turkey, e-mail: figen.temizdislioglu@vakko.com.tr
[5] Vakko, Nakkaştepe Design Center, Istanbul/Turkey e-mail:nurcant@wcollection.com.tr
[6] Vakko, Nakkaştepe Design Center, Istanbul/Turkey e-mail:sena.sahinl@wcollection.com.tr
[7] Department of Textile Engineering, Istanbul Technical University, Istanbul, Turkey, e-mail: sahinumut3@itu.edu.tr

Abstract:

Today, technology is constantly developing and instead of conventional textile products, new techniques are being developed under the principles of sustainability and environmentalism, which are at the forefront today. These production methods provide sustainable, environmentally friendly alternatives that do not affect the environment or living things. One of the methods we have focused on in this study is vegan leather, which is one of the non-woven materials that can be used instead of leather obtained from animals and produced from various raw materials. Vegan leather, which has become very prominent and popular recently, was used in shoe design in this study. Artificial leather was produced from apple peel and was also supported with a rubber-sawdust mixture sole and corn tassel lace detail. In the continuation of this study, different media shoes will be designed and both a sustainable and animal-friendly approach will continue to be kept in the foreground.

Key words:

Synthetic leather, Design, Sustainability, Vegan Textile, Shoes

1. Introduction

It is important to note that the fashion industry has recently been focusing on environmental awareness. Since materials made from leather and fur are produced, this industry has unethical practices when it comes to animal rights, such as harming foxes, minks, raccoons or crocodiles to harm animals for dye testing purposes (Ahuja, 2010). The fashion industry is constantly evolving to provide affordable products to consumers, but most consumers are not aware that the industry contributes greatly to global pollution due to the enormous amount of garbage it produces (Rathinamoorthy) . The entire ecosystem is polluted by the discharge of toxic chemicals during the fashion production process, thousands of chemicals such as phthalates, nonylphenol ethoxylate, alkylophenol, formaldehyde, amines, heavy metals, etc. are used in textile stages and processes, which are converted into normal components in clothing products. Toxicity in the textile and apparel industry has undesirable consequences for human health; The continuous disposal of synthetic microfibers that are difficult to decompose pollutes the environment and contaminates human food resources (fish, wildlife, etc.) (Minh, 2021).

For vegan fashion, thanks to the development of production technology, artificial fur has become an alternative material to natural fur; the texture and shine of artificial fur have improved (Kim, 2018). Artificial fur can be dyed, bleached, stored, easily washed and, above all, has low production costs. It

attracts the attention of nature lovers who want to protect the environment but also care about elegance. In the last two decades, the footwear industry has played a significant role in increasing material efficiency at the time of production. It also focuses on eliminating or reducing the use of hazardous materials in footwear production. The footwear industry "consumes" a significant percentage (60%) of the leather produced annually. The leather industry has even contributed significantly to the improvement of the overall economy of the country. The increasing demand for footwear products has significantly increased the production rate and has even outpaced the environmental gains achieved (Jadhav,2020).

2. Experimental
2.1. Materials

The materials were provided by VAKKO. Quebracho tree extract, sodium bisulfite, formic acid, calcium diformate, alkyl polyethylene glycolester, naphthalene sulfone-based synthetic tannin and acacia extract were used in the shoe content.

Apple pulp, a byproduct of apple juice production, is collected. This includes the peels, seeds, and other fibrous parts of the apple. The collected apple waste is dried to remove moisture. Once dried, it is ground into a fine powder. The apple powder is mixed with polyurethane or other environmentally friendly binders. This mixture helps create a malleable and durable material. Natural pigments can also be added at this stage to achieve the desired color. The mixture is spread onto a backing material, usually a textile fabric. It is then cured with a heating process that helps the mixture solidify and bond to the fabric. The material can be embossed or textured to mimic the look and feel of traditional leather. Additional finishes can be applied to increase durability, water resistance, and aesthetic appeal. Once the apple vegan leather sheets are ready, they are cut and shaped according to the needs of the product being produced.

2.2. Methods

Spray dried Quebracho tree extract for the base has been treated with a small amount of sodium bisulfite and formic acid to remove color.

Alkyl polyethylene glycolester, naphthalene sulfone-based synthetic tannin and acacia extract were also used for the upper part of the shoe as vegan leather.

Figure 1. Shoe Example

The rubber/chip part of the shoe was tested using density (ISO 2781), hardness (ISO 868), abrasion ISO 4649, elongation ISO 37 and tensile strength ISO 37 standards.

3. Results and discussion

Table 1 shows the test results.

Table 1. Test Results

	Density (g/ cm2)	Hardness (Kg/cm)	Wear (mm 3)	Elongation (%)	Rupture (Mpa)
Sample	1.06	70	249	566	7.46

According to the results, the soles of our shoes turned out to be durable. In addition, its elasticity feature stand out.

4. CONCLUSIONS

Since sustainability and environmentalism are quite popular today, new alternatives to traditional textile products are being created with the rapid advancement of technology. These production techniques offer environmentally friendly, sustainable substitutes that do not have a negative impact on the environment or living things. In this study, vegan leather, which has recently become more popular and important, was used in shoe design. Artificial leather was produced using apple peels and this leather was further strengthened with a sole made of rubber and sawdust and a corn silk lace pattern. Within the scope of this project, different medium-sized shoes will be designed with sustainability and animal welfare at the forefront.

In future studies, chemical experiments will be carried out on the upper part of the shoe, and then tests will be carried out for the entire shoe.

References

1. *V. Ahuja, T. Platzek, H. Fink, A. Sonnenburg and R. Stahlmann, Study of the sensitizing potential of various textile dyes using a biphasic murine local lymph node assay, Arch. Toxicol, 84, pp. 709-718 (2010)*
2. *R. Rathinamoorthy, Consumer's awareness on sustainable fashion, Sustainable fashion: consumer awareness and education, ed SS Muthu (Singapore: Springer, 2019), pp. 1- 36..*
3. *Minh, N.T., & Ngan, H.N. (2021, September). Vegan leather: An eco-friendly material for sustainable fashion towards environmental awareness. In AIP Conference Proceedings (Vol. 2406, No. 1). AIP Publishing.*
4. *NH Kim and SH Park, The current situation of vegan fashion brands as alternative strategy, J. Fash. Desi, 18, pp. 17-33 (2018).*
5. *Jadhav, N.C., & Jadhav, A.C. (2020). Waste and 3R's in Footwear and Leather Sectors. Leather and footwear sustainability: Manufacturing, supply chain, and product level issues , 261-293.*

TECHNOLOGICAL POSSIBILITIES OF COATING WEFT KNITTED FABRICS WITH A NANOFIBRE LAYER

Jana Ornstová, Lukáš Čapek

Technical University of Liberec, Faculty of Textile Engineering, Department of Technologies and Structures, Liberec, Czech Republic, jana.orsntova@tul.cz

Abstract:

This paper presents the possibilities of creating a hybrid structure, which was created by combining a weft-knitted fabric and a nanofibrous layer. The technological tests of coating the weft-knits with a nanofiber layer, subsequent investigation of their structural parameters, and testing the cohesion of the two layers are described. For the formation of the backing layers, weft knitting technology was chosen, as it allows the creation of flat- and spatially-shaped products with non-unravelling edges, and the input can be only one lengthwise textile (multifilament, yarn, etc.). For the experiment, DC electrospinning on the Nanospider was chosen to allow the formation of a compact layer of nanofibers. Six samples of weft knitted fabrics - made in two structures from three types of material - were coated by PVB fibres. The structural parameters and the areal weight of the knitted fabric samples were determined. The average diameter of the nanofibers was examined for each sample. All fabricated structures were subjected to layer cohesion testing (peel test), and the effect of structures and fibril fineness of the input material on the cohesion of the knitted fabric and nanofibrils was sought.

Keywords:

Weft knitted fabrics, electrospinning, peel test

1. Introduction

Nanofiber production technology, called electrospinning or electrostatic wetting, is the best-known nanofiber production technology. Nanofiber layers from this technology are cohesive, easy to handle and have many applications. The principle of this technology is as follows: a needle, syringe, pump, high DC voltage and a grounded collector are required for needle wetting. The polymer solution is pushed by the syringe into the needle where the high voltage is applied. By charging the solution with the same charge, repulsion occurs, and a so-called Taylor cone begins to form, from which the filament emerges when the critical voltage is exceeded. The solvent is evaporated during the flight of the filament, which falls due to the different polarity on the grounded collector or on the oppositely charged counter electrode [1], [2]. After crossing a critical voltage, the liquid body, in this case a polymer solution, breaks up, a Taylor cone is formed, and a very narrow liquid column or nanofiber is ejected due to the viscosity and entangled chains of the polymer [3]. Electrostatic wetting can also be realized by using a differently shaped electrode, such as a string. The Nanospider™ device from Elmarco, Czech Republic, works on this principle. The polymer solution is deposited on a string, on which Taylor cones are formed from which nanofibers are wetted and a grounded/oppositely charged collector, in front of which there is a substrate textile that can be simultaneously drawn off. With this technology, it is possible to produce nanofibrous layers on an industrial scale as opposed to needle electrospinning [4].

The nanofibrous layers produced in this way are deposited in the device onto a running backing fabric, usually also a nonwoven fabric. They can be peeled off the fabric or used together with the substrate. Under certain technological conditions, nanofibers can also be deposited on the support conventional thread core (e.g. monofilament or multifilament) to form composite yarns [3]. This "yarn" can be processed into textiles using classical mechanical technologies such as weaving and knitting or braiding, but the nanofiber envelope is very delicate and can be damaged during processing.

Another option is to use a different flat textile as a base fabric that will bring specific mechanical properties. Examples are the scaffold for tendon repair [5] or composite meshes composed of

nonabsorbable and absorbable material [6]. These are examples of implantable applications. When we talk about non-implantable medical devices, we talk about wound covers. Nanofibrous coverings are investigated and applied, e.g., in veterinary practice [7] and human medicine [8]. It is also a suitable substrate for binding drugs subsequently absorbed in the wound [9]. However, these are mainly planar formations that are not spatially shaped and ideal for anatomically structured places such as supraorbital arches, parts of the skull, nose, coccyx, etc. In such areas, the unshaped covering must be bent and folded in various ways, thus creating a thicker layer in some parts; on the contrary, in some parts, tension may arise because the material is not reaching or the covering does not adhere to the wound. A suitable option could be flat- and spatially-shaped weft-knitted fabrics with a nanofiber layer. The technological tests of coating the weft-knitted fabrics with a nanofiber layer, subsequent investigation of their structural parameters, and testing the cohesion of the two layers are described. For the formation of the base layers, the technology of weft knitting was chosen, as it allows the creation of both areal and spatially shaped products, and the input can be only one lengthwise textile (multifilament, yarn, etc.). Products made using the weft knitting technology can have all unravel-resistant edges, which is an undeniable advantage.

2. Experimental part

2.1. *Materials*

On a flat knitting machine, Shima Seiki NewSES 122FF, with the gauge 18E, the knits were prepared in two structures. These were a double-face Milano Rib with reduced transverse tension and a single-jersey all-over tuck stitch (see pattern in Fig. 1 and Fig. 2). The Milano Rib structure is characterized by a higher areal weight and reduced transverse tensile [10]. On the other hand, its surface roughness is less because both the face and reverse side of the knit exhibit smooth face loops. The requirement for low stress in course direction corresponds to the fact that the nanofiber coating will combine a highly flexible material (weft-knitted fabric) with a material with minimal directional ductility. On the other hand, the all-over tuck stitch is characterized by a lower areal weight, and the tuck stitches' effect leads to an increase in surface roughness [10].
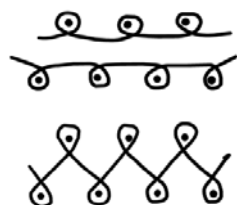
Fig. 1: Knit pattern notation of Milano Rib

Fig. 2: Knit pattern notation of All-over tuck stitch

The following threads were chosen as input material:
- Polyester multifilament - count 100 dtex, 96 fibrils, textured – fibril count 1,04 dtex
- Polyester multifilament – count 120 dtex, 36 fibrils, textured - fibril count 3,33 dtex
- Viscose ring yarn combed – count 20 tex

The input material was chosen because polyester and viscose are standard materials in manufacturing medical supplies for external use [11]. Polyester multifilament was used in two qualities concerning the count of the individual fibrils and, thus, their diameter. The approximate fibre (fibril) diameter of polyester multifil with 96 fibrils is 9.86 µm, and with 36 fibrils, it is 17.66 µm.

The knits for the coating were made in the following material and weave combinations and labelled with the names of samples 1-6, see Table 1.

DC electrospinning was selected as the preferred method for nanofiber coating. AC electrospinning was tested, but the layers produced were too fluffy and uncomplianced. DC electrospinning was realized on the Nanospider NS 1W500U from Elmarco, where a string is used as the electrode. A solution of 10% PVB and ethanol was used as feedstock for the production of nanofibers. As standard, the nanofibers are trapped on a nonwoven fabric made with spun bond technology, which passes through the guide rollers of the device. Samples of the weft knits were attached to this fabric as yardage.

Tab. 1: Marking of experimental material

Label	Type of weft knitted fabric	Structure	Material	Count [tex], doubling, number of fibrils	Technology
Sample 1	double faced	Milano rib	viscose	20 x 2	comb. ringS
Sample 2	double faced	milano rib	polyester	10 x 2 (96f)	multif, text.
Sample 3	single jersey	tuck knit	viscose	20 x 2	comb. ringS
Sample 4	single jersey	tuck knit	viscose	20 x 1	comb. ringS
Sample 5	single jersey	tuck knit	polyester	12 x 1 (36f)	multif, text.
Sample 6	single jersey	tuck knit	polyester	10 x 1 (96f)	multif, text.

Images of knitted fabrics taken under a macroscope are shown in Fig. 3.
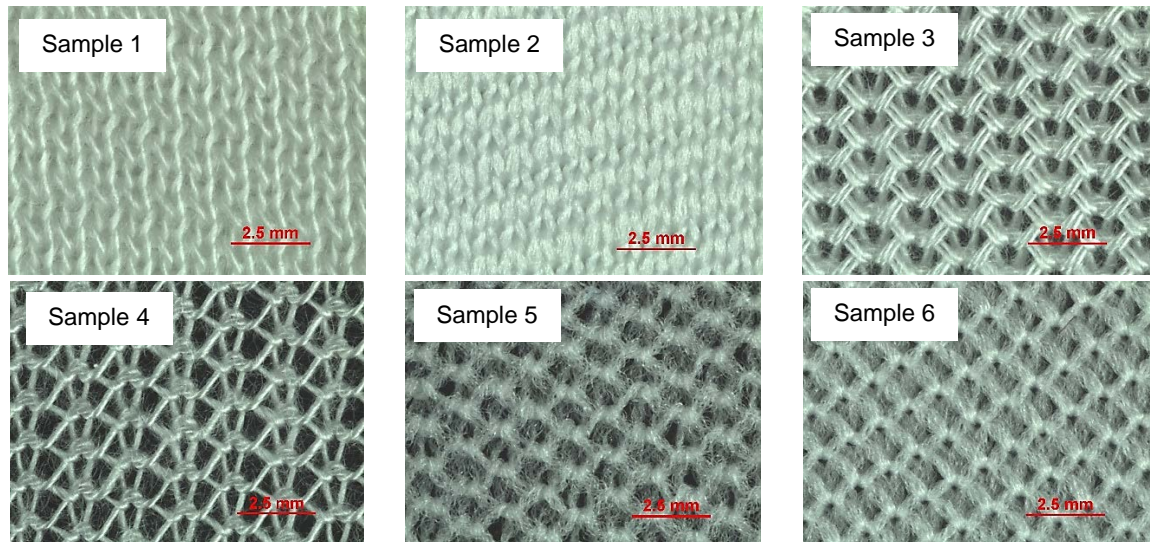

Fig. 3: Appearance of knitted fabric samples - taken from the reverse side of the knitted fabrics

2.2. Methods

2.2.1. Structural parameters of the underlying knitted fabrics

Areal weight was determined on dimensionally stable knits and wales, and course densities were measured. The samples were air-conditioned at 20°C and 65% relative humidity. Areal weight was determined experimentally according to *EN 12127 (800849) Textiles—Flat fabrics—Determination of areal weight using small samples.* The specific gravity values are given in Table 2. The knitted fabrics cover a range in basis weight from approximately 60 g.m^{-2} to 370 g.m^{-2}.

Tab. 2: Weight per unit area determined experimentally

Label	Areal weight [g.m^{-2}]
Sample 1	361,7 ± 3,8
Sample 2	220,5 ± 4,2
Sample 3	183,3 ± 3,8
Sample 4	77,7 ± 1,0
Sample 5	72,3 ± 2,1
Sample 6	61,0 ± 2,5

The basic structural parameters were determined according to *EN 14971 Textiles - Knitted fabrics - Determination of the number of stitches per unit length and per unit area,* and the specific values are given in Table 3. These were wales density D_w [wales/m], courses density D_c [courses/m] and total density D_t [loop/m^2]. For double knits, the wales density was determined only on the face side of the knit (in these patterns, the face and reverse sides are identical). The total density was calculated as the product of wales density and courses density; therefore, the 95% confidence interval is not shown in Tab. 3. For double-faced knits, the reverse side was also considered in the calculation of D_t (i.e., the wales density was considered twice as high).

Discussion

From the point of view of weight per unit area, we can see that there are basically two groups of knitted fabrics. There are knitted fabrics with lower areal weight in the single jersey (samples 4, 5, 6). Higher areal weights were obtained with the Milano rib weave (samples 1 and 2). Sample 3 was also produced

in a single jersey, but the choice of input material, 2x doubling 20 tex viscose, also resulted in a higher areal weight. It can, therefore, be placed in the second group - heavier knits.

Tab. 3: Structural parameters of the knitted fabrics

	D$_w$ [wales/m]	D$_c$ [courses/m]	D$_t$ [loop/m^2]
Sample 1	930 ± 15	1315 ± 20	2 445 900
Sample 2	1030 ± 15	1215 ± 22	2 502 900
Sample 3	728 ± 29	1613 ± 12	1 174 261
Sample 4	656 ± 19	1503 ± 38	985 067
Sample 5	822 ± 19	1728 ± 56	1 421 124
Sample 6	914 ± 24	1421 ± 45	1 298 948

2.2.2. *Areal weight of coated structures*

The areal weight of the final product was determined experimentally according to EN 12127 (800849) Textiles - Flat fabrics - Determination of basis weight using small samples. The specific values of the specific areal weight are given in Tab. 4. There are three columns of data in the table. The first column of data is the areal weight of the knitted fabric, the second column shows the areal weight of the coated structures, and the third column shows the calculated area weight of the layer of nanofibres. From the values, it is clear that although an identical Nanospider setup was maintained, it failed to produce identical nanofiber layers (in terms of their areal weight). The measurement results are always burdened by the sum of errors. Some of them arise directly during the measurement due to the influence of the measuring instruments, the laboratory technician, etc. Furtherm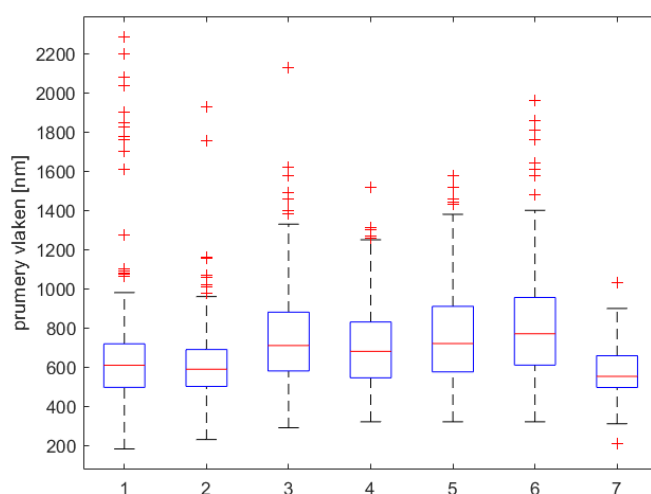ore, we must not forget a rather strong factor, which is especially evident in textile structures, namely their non-uniformity. However, even so, the differences in the surface masses of the nanofibres are significant. The largest difference in the weights is between samples 1 and 6.

Tab. 4: Weight per unit area determined experimentally – areal weight [g.m^{-2}]

	Only knitted fabrics	Knitted fabrics coated by nanofibers	Only layers of nanofibers
Sample 1	361,7 ± 3,8	387,5 ± 4,7	25,8
Sample 2	220,5 ± 4,2	232,5 ± 4,0	12,1
Sample 3	183,3 ± 3,8	199,7 ± 5,3	7,8
Sample 4	77,7 ± 1,0	85,5 ± 1,3	16,4
Sample 5	72,3 ± 2,1	74,2 ± 2,5	8,7
Sample 6	61,0 ± 2,5	69,7 ± 1,1	1,9

2.2.3. *Nanofiber layer analysis - determination of nanofiber diameter*

Images of the nanofibers were analyzed and captured on a Vega3 Tescan scanning electron microscope (SEM). Nanofiber diameters were measured in NisElements image analysis. The diameter of 360 fibres was measured for each sample of the coated structure. Furthermore, the nanofiber layer deposited on the underlying nonwoven fabric (produced by spunbond technology) was also analyzed. The data were statistically processed. The normality and homogeneity of the data were tested. In Fig. 4, box plots showing the distribution of fibre diameters are shown. Samples 1-6 are labelled 1-6. Nanofibers from the spunbond backing layer are labelled 7 in the graph. The box plot consists of a central "box" part, which is bounded by the 3rd quartile from above, the 1st quartile from below, and a red line between them showing the median. The red crosses indicate the

Fig. 4: Boxplot of diameter of nanofibers

so-called outlying data. By definition, nanofibers are considered to be fibres that have a diameter of less than 1000 nm [2]. The graph shows that all tested samples consist mainly of nanofibers, as most of the data lie below 1000 nm. However, the samples also contain a certain (but relatively small) percentage of fibres larger than 1000 nm. Sample 1 has the highest number of such microfibres, namely 15. The other samples contain less than 15 such microfibres. The normality and homogeneity of the data was rejected due to the outlying fibres in all data samples.

2.2.4. *Adhesion analysis of nanofiber and knitted fabric layers*

The adhesion of the nanofiber layer to the knitted fabric layer was tested on samples of coated structures (the test can also be found under the term peel test). The adhesion test of the two layers determines the force required to separate them at a constant crossbar feed rate. By varying the angle that is created when the layers separate, it is possible to simulate the condition that the fabric gets into during use. From Fig. 31 it can be seen that adhesion can be tested at angles of 180° or 90°. In our case, the 180° adhesion test was chosen also because of the possibilities provided by the measuring instrument. Although, from the point of view of application, a 90°peel test would be preferable as the overlap will be sensed from the wound at a similar angle.

The test was carried out on the MTest Quattro uniaxial stress tester from Admet. The instrument has two opposing mechanical jaws into which the ends of the test specimen were fixed. One as a single knit without a nanofiber layer and the other as a knit+nanofibre sandwich, see Fig. 5.
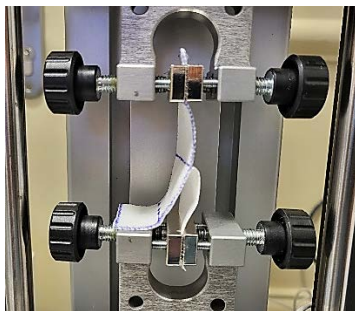
Fig. 5: Clamping the knitted fabric sample in the jaws of the MTest Quattro
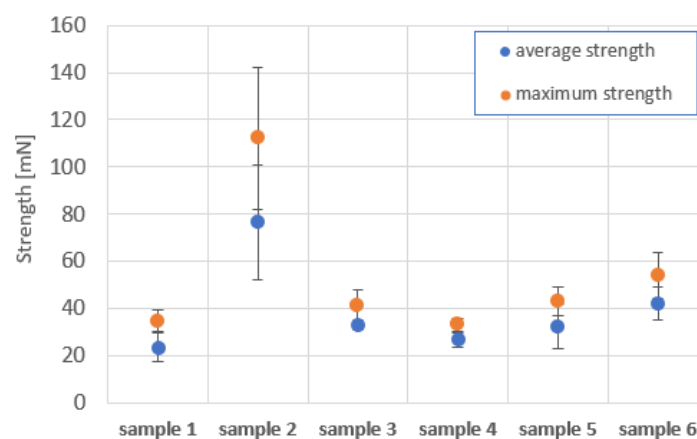
Fig. 6: The force required to separate weft knitted fabric and layer of nanofibers

The average and maximum force in the interval of 2-20 mm (displacement of the crossbar during measurement) was determined on the instrument. The data are graphically displayed in Fig. 6.

3. Results and discussion

The resulting values of the average and maximum forces required to separate the nanofiber layer from the knitted fabric are in Fig. 6. The highest value of average force needed to separate the layers was achieved by the hybrid fabric labelled sample 2. However, with a significant variation of measurements, wide confidence intervals are seen. The other materials did not show such a massive variation in average forces see Fig. 6 (samples 3, 4 and 6).

Sample 2 is a double-faced fabric Milano rib made of polyester multifilament thread with a single fibril diameter of 9.86 μm. Similarly, in the group of single-jersey fabrics, sample 6, which, like sample 2, is made of multifilament with finer fibrils, shows the highest average strength. From this, we could conclude that if the knitted fibres' diameter approaches the nanofibers' diameter, slightly stronger cohesive forces will be generated. We are comparing samples 2 and 6 with each other. The Milano rib shows greater cohesion of the nanofibers and knitted fabric, which has a lower surface roughness than the single jersey

with tuck knits. The less structured surface of the knit offers a larger contact area for the nanofibers binding.

4. CONCLUSIONS

In this paper, a technological experiment of coating knitted fabrics with a layer of nanofibers made of polyvinyl-butyral is presented. Six types of knitted fabrics were coated. These knits were made in two bindings and three material combinations. The DC electrospinning method on the nanospider was selected as the most suitable method for coating knitted fabrics. The nanofiber layer produced by the device was sufficiently compact. All samples were subjected to experimental investigation of the structure - in terms of basic structural parameters such as wale and course densities, areal weight, nanofiber diameter, etc. In addition, an adhesion test (peel test) was performed to determine the average force required to tear the nanofiber layer from the knitted fabric. The highest average strength of the double-faced knitted fabrics was exhibited by the Milano rib made of 100 dtex polyester multifilament with 96 fibrils (sample 2). Of the single-jersey, the knit marked sample 6, made from the same material as sample 2, showed the highest average strength. The fibril diameter of the multifilament was 9.86 μm (the smallest of the fibrils used). The knitted fabric and nanofiber exhibited the highest fabric and nanofiber cohesiveness when knitted in the Milano rib (sample 2), which has a smoother surface than the all-over tuck knit. It can be argued that the fineness of the input material for knitting and the chosen bindings influences the cohesiveness of the layers.

ACKNOWLEDGEMENTS

References

1. *Z. Li a C. Wang, One-dimensional nanostructures electrospinning technique and unique nanofibers. 2013.*
2. *"An Introduction to Electrospinning and Nanofibers". Viděno: 30. září 2024. [Online]. Dostupné z: https://www.worldscientific.com/worldscibooks/10.1142/5894?srsltid=AfmBOooXozzEfKdQId5h9u kyprLCBtaCj4reW117SgygA7MzZuY7LXRj*
3. *J. Valtera et al., "Fabrication of dual-functional composite yarns with a nanofibrous envelope using high throughput AC needleless and collectorless electrospinning", Sci Rep, roč. 9, č. 1, s. 1801, úno. 2019, doi: 10.1038/s41598-019-38557-z.*
4. *K. Havlíček, L. Svobodová, T. Bakalova, a T. Lederer, "Influence of electrospinning methods on characteristics of polyvinyl butyral and polyurethane nanofibres essential for biological applications", Materials & Design, roč. 194, s. 108898, zář. 2020, doi: 10.1016/j.matdes.2020.108898.*
5. *O. Hakimi, P. A. Mouthuy, N. Zargar, E. Lostis, M. Morrey, a A. Carr, "A layered electrospun and woven surgical scaffold to enhance endogenous tendon repair", Acta Biomaterialia, roč. 26, s. 124–135, říj. 2015, doi: 10.1016/j.actbio.2015.08.007.*
6. *Y. Lu, Y.-C. Chen, a P.-H. Zhang, "A membrane coated composite mesh for repairing pelvic floor defects using electrospinning method", industria textila, roč. 66, s. 9, 2015.*
7. *A. Novotná, „Nanovlákenné kožní kryty pro použití ve veterinární medicíně", Technická Univerzita Liberec, Liberec, 2020.*
8. *S. Karbasi, F. Fekrat, D. Semnani, S. Razavi, a E. Zargar, "Evaluation of structural and mechanical properties of electrospun nano-micro hybrid of poly hydroxybutyrate-chitosan/silk scaffold for cartilage tissue engineering", Adv Biomed Res, roč. 5, č. 1, s. 180, 2016, doi: 10.4103/2277-9175.194802.*
9. *Y.-F. Goh, I. Shakir, a R. Hussain, "Electrospun fibers for tissue engineering, drug delivery, and wound dressing", J Mater Sci, roč. 48, č. 8, s. 3027–3054, dub. 2013, doi: 10.1007/s10853-013-7145-8.*
10. *V. Kočí, Vazby pletenin, První. Praha: SNTL - Nakladatelství technické literatury, 1980.*
11. *A. Pospíšilová, „Léčba chronických ran moderními krycími prostředky", s. 6.*

CELLULOSE AEROGEL IN TEXTILE COMPOSITE STRUCTURE

Sebnem Sozcu, Jaroslava Frajova, Jakub Wiener, Mohanapriya Venkataraman, Blanka Tomkova, Jiri Militky

Department of Material Engineering, Faculty of Textile Engineering, Technical University of Liberec, 46117 Liberec, Czech Republic. Correspondence: sebnem.sozcu@tul.cz; mohanapriya.venkataraman@tul.cz

Abstract:

This work is focuses on the effect of the freeze-drying method on the pure BCAs (bacterial cellulose aerogels). The enhancement of physical properties with the coating of different types of structures such as the laboratory beads and various thickness of nonwoven (NW) fabric structures is described. NW fabrics are used as a supportive material for BC to evaluate its potential positive impact on the surface structure of BC aerogels.

The study explores the different freezing conditions of the BC, such as freezing speed (slow and fast freezing), use of cryogenics material or conventional freezing methods, and their impact on the mechanical, physical, and thermal performance of BC aerogels. Additionally, physical modifications, including coating with the different thickness of textile nonwoven fabrics and laboratory glass beads, are investigated to determine their effectiveness in improving the structural integrity of BC aerogels.

The main research question is: "How can the physical and mechanical properties of bacterial cellulose aerogels be significantly improved through the use of freeze-drying methods and physical modifications?

Key words:

Bacterial cellulose hydrogel; lyophilization; structure of bacterial cellulose; physical properties

1. Introduction

The rise in consumption has raised concerns about sustainability and waste management [1]. Population growth, climate change, urbanization, and industrial expansion have caused water and energy shortages, impacting various sectors [2]. The textile industry faces environmental challenges from pesticide use, high energy and water consumption, chemical usage, and improper waste disposal. Achieving sustainability requires industrial improvements and changes in consumer behavior [3]. Bio-based materials like cellulose offer mechanical strength, biocompatibility, and thermal comfort [4], but producing high-purity cellulose is energy-intensive and costly [5], emphasizing the need for affordable sources [6].

Aerogels, with about 90% porosity, are produced using supercritical drying. Their low thermal conductivity and density make them efficient insulators [7]. Aerogels can be made from various materials, including cellulose, which is renewable, biodegradable, and lightweight, making them ideal for adsorption, thermal insulation, biomedical uses, and more [8].

Bacterial cellulose (BC) was first identified by Brown in 1886 during vinegar fermentation, described as a gelatinous substance similar to vegetable cellulose (VC) [10]. In 1931, Hibbert and Barsha confirmed BC's molecular formula matched VC but noted distinct characteristics [11]. BC is purer and has superior mechanical properties, including higher compressibility, elongation, porosity, crystallinity, and biodegradability compared to VC, which contains hemicellulose and lignin. BC is used across biotechnology, pharmacy, cosmetics, packaging, paper, food, wastewater treatment, and insulation

sectors [12]. Classified as GRAS (Generally Recognized as Safe), it is eco-friendly, renewable, and has attracted interest in the fashion industry [13].

This study aims to synthesize an environmentally friendly, sustainable, biocompatible, and highly porous textile structure for potential insulation applications, diverging from traditional textile structures. The research explores a new research direction involving bacterial cellulose strains processed by freeze-drying methods. This includes investigating modifications, challenges, and potential applications, with a focus on thermal and sound insulation properties.

2. Experimental

2.1. *Materials*

In this work, to synthesize the bacterial cellulose aerogels, first, the below materials are used for growing the bacterial cellulose, and then the samples have been dried using the lyophilization method. Table 1 depicts the condition of the main source of cultivation for the preparation of BC samples. Densitometer McFarland was used for determining concentration of bacterial cells.

Table 1. BC growing conditions

Bacteria strain	Fermentation Source	Cultivation condition
Acetobacter Xylinum	Black tea, Sugar, water	26 °C ideal temperature 3-5pH

Gregor -L10-55 Pro, and Lyotrade-Amaru were used as freeze drying devices; Tescan VEGA3 LMU and Zeiss, Ultra Plus Model Scanning Electron Microscope (SEM) have been used for morphology of the samples. Polyester (PES) NW fabric (Milife & Meftex) (15 & 30 gsm) has been purchased by JX Nippon ANCI Corporation and Bochemia, respectively for modification of BC aerogels.

2.2. *Methods*

Preparation of Bacterial Cellulose Aerogels

The preparation of bacterial cellulose involves using a sweet black tea solution. The process starts by measuring the bacteria amount with a Densitometer McFarland type DEN. One-tenth volume of Acetobacter Xylinum bacteria is added to the tea solution to initiate fermentation. Optimal fermentation occurs at 24-32°C with a pH range of 3-5. After four days, a 3 mm thick fungus layer forms, which hardens to 5 mm in seven days. However, for comparable results, we have completed the BC production with different thicknesses. The bacterial cellulose is then purified by washing in water to remove residual particles.

Modification of BC Samples:

Modification no-1 (M1): The samples were physically modified to obtain the homogeneous-smooth surface structure of BC aerogels. First, as Figure 1 depicts, the specifically arranged frame structure with Milife NW fabric has been prepared and frozen.
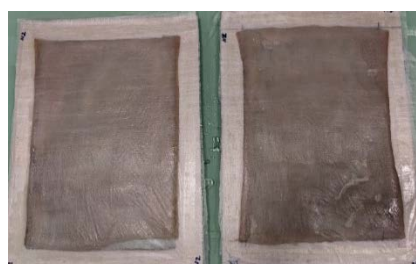
Figure 1. BC sample with the arranged frame structure and Milife NW fabric.
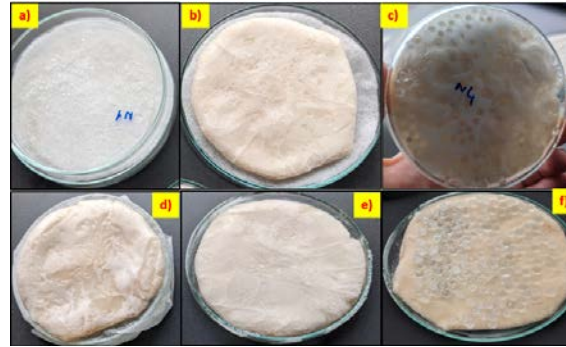
Figure 2. The prepared BC samples with 15 gsm Milife, 30 gsm Meftex NW fabrics and laboratory beads [a) Meftex NW at the bottom and on top of the BC; b) Meftex NW at the bottom of BC; c) the laboratory beads at the bottom of BC; d) the Milife NW covered over the petri dish and on the top of NW fabric placed BC sample; e) at the bottom of BC placed the Milife NW; f) on the top of BC placed laboratory beads].

Modification no-2 (M2): Secondly, as depicted in Figure 2, the BC samples were prepared with PES Milife, Meftex NW fabrics, and laboratory beads with different forms.

Freeze-Drying-1: All purified BC samples with and without modification were frozen at -3/-4°C in the standard refrigerator freezer and subsequently freeze-dried for 48 hours at -52°C to obtain bacterial cellulose aerogels with Gregor -L10-55 Pro lyophilization device.

Modification no-3 (M3): Herein after, we have changed the freezing condition of BC samples by using liquid nitrogen (LN_2) instead of the conventional method of refrigerator freezer and freeze-drying device, which has heating layer and pre-freezing condition before the drying process (Lyotrade-Amaru). Both sides of BC samples were prepared with 15 gsm Milife NW fabric (Figure 3).

Figure 3. The prepared BC samples with Milife NW fabric.

Freeze-Drying-2: All purified BC samples with M3 were frozen with LN_2 at -196°C and subsequently freeze-dried for 48 hours with 3 hours pre-freezing at -30 °C and heating the shelf, then freeze-drying process at -40°C with 506.6 mBar to obtain bacterial cellulose aerogels with Lyotrade-Amaru lyophilization device.

Calculations of porosity and areal mass density of BCAs

To determine the porosity, the size and weight of each BC sample were measured. The apparent total volume of sample V_a [m³] was calculated using the average thickness of the sample h [m]) and the surface area of BCA sample A [m²].

$$V_a[m^3] = h\,A \qquad\qquad \text{Equation (1)}$$

The actual volume of cellulose in sample V_c [m³] was determined based on the weight of the samples m [kg] and the cellulose density ρ [1560 kg/m³].

$$V_c[m^3] = {m}/{\rho} \qquad\qquad \text{Equation (2)}$$

The porosity of BCA P [%] is then calculated according to equation [14]:

$$P = 100 \left(1 - {V_c}/{V_a}\right)$$
Equation (3)

At the end of the sample preparation, scanning electron microscopy (SEM) was performed on a Zeiss (Germany) Ultra Plus. The basic parameters of BCAs, which are thickness/diameter of single fibrous fragments from SEM pictures, size of the porous/gap between fibers, porosity, and density, were calculated according to sample results.

3. Results and discussion
3.1. Production of Bacterial Cellulose

When *Acetobacter xylinum* is cultured under stationary conditions, it synthesizes bacterial cellulose as a film on the nutrient medium surface. The yield is affected by factors such as temperature, duration, and the surface area-to-volume ratio, which is crucial for oxygen availability. Both insufficient and excessive oxygen levels can negatively impact cellulose synthesis [7]. Using this method, we successfully produced bacterial cellulose films of varying thicknesses and dimensions, as shown in Figure 4.

Figure 4. BC samples were obtained after the cultivation process without any modification.

3.2. Physical properties

The appearance of freeze-dried BCAs without any modification is shown in Figure 5. In image (a), which is visible, the BCAs do not have homogeneous surface structures. In the literature, the comparable appearance of BC samples that are dried in the oven and with lyophilization has been studied. Their studies show that while the oven-dried samples were transparent, the freeze-dried samples were like a "Styrofoam," and it preserved their shapes [7,15]. Thus, our studies prove that image freeze-drying preserved our samples' shape (thicknesses) and appearance, which were also like a foam form (Figure 5 (b)).

Figure 5. Freeze-dried BCAs without any modification [a] showing the non-homogeneous surface structure of BCAs, b) showing the thicknesses of BCAs].

On the other hand, even though we have different types of surface modifications on BCAs, we were still not able to obtain homogeneous surface structures. Figures 6 and 7 show the applied modifications (M1, M2), respectively.
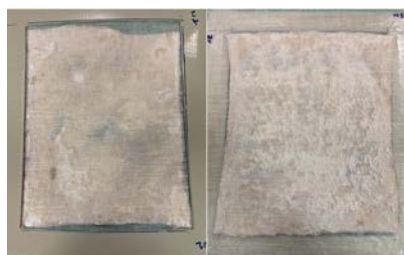
Figure 6. Freeze-dried BCAs with arranged frame structure and Milife NW fabric-M1.

Figure 7. Freeze-dried BCAs with Milife, Meftex NW fabrics, and laboratory beads- M2.

The two modifications aimed at achieving a smooth surface for the BCAs were unsuccessful, and another issue emerged: the incompatibility between polyester and bacterial cellulose. During the second modification (no. 2), we observed that the freeze-dryer's default settings were ineffective, as we couldn't adjust parameters. No changes were seen in the BCAs during drying, which led us to examine the pre-freezing conditions. Extended storage in the freezer caused excessive ice crystal formation and sample damage. Literature indicates that freezing speed before drying is as crucial as the drying process itself. Therefore, we used liquid nitrogen (LN2) instead of the conventional freezer [8]. Figure 8 displays the LN2 freeze-dried BCAs.
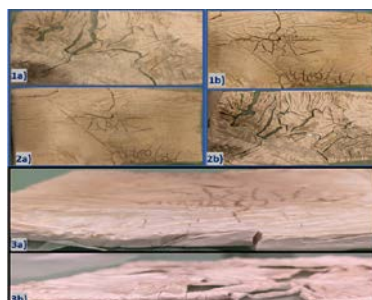
Figure 8. The freeze-dried BCAs with LN$_2$ [1a-2a: images of BCAs with Milife NW fabric; 1b-2b: images of BCAs without Milife NW fabric; 3a-3b: images of thicknesses of BCAs].

According to Zhang et al., aerogels frozen with liquid nitrogen displayed a uniform, smooth surface, whereas those frozen at slower speeds had rougher surfaces with streaks due to ice crystal formation. Rapid freezing with liquid nitrogen preserved the highly porous network structure, resulting in aerogels with a homogeneous three-dimensional network composed of fine fibrils (10-100 nm wide). In contrast, aerogels cooled more slowly in ultra-low temperatures (-80°C), and regular (-20°C) freezers exhibited less porous structures [15]. Our studies indicated that using LN2 prior to the freeze-drying process was more effective for BCAs, resulting in a smoother surface despite the occurrence of crack formation.

3.3. <u>Structural properties</u>

SEM imaging

The structural analysis of the investigated bacterial cellulose samples reveals a three-dimensional porous network structure composed of randomly arranged ribbon-shaped ultrafine fibers. Rapidly freezing the BC aerogels with liquid nitrogen effectively preserved the highly porous network, resulting in aerogels with a uniform three-dimensional structure in Figure 9 (a-b).
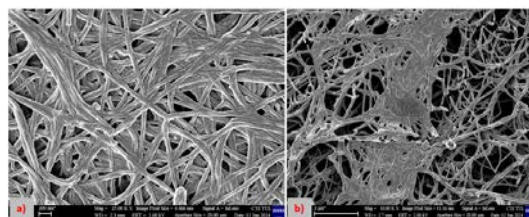
Figure 9. SEM images of BCAs with LN$_2$ freezing (Fast freezing) [a)cross-sectional image; b) longitudinal image].

However, BC aerogels cooled more slowly in a conventional freezer (-3/4 °C) showed less porous structures (Figure 10 (1a-2a-3a)). Aerogels frozen at a slower speed consisted of aggregated bacterial cellulose aerogel bundles and fewer individualized BCAs.
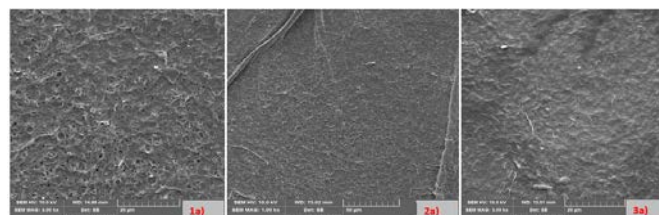
Figure 10. SEM images of BCAs with slow freezing (Freezer in the refrigerator).

Based on these findings, liquid nitrogen was chosen as the preferred method for freezing in the preparation of bacterial cellulose aerogels with varying thicknesses.

Porosity Properties

The porosity of the bacterial cellulose network depends significantly on the drying method used [16]. Thermal drying under atmospheric or reduced pressure leads to non-porous sheets and fibre agglomeration due to water vapor diffusion and hydrogen bonding. In contrast, freeze-drying and supercritical CO$_2$ drying are preferred for preserving the pristine 3D network in bacterial cellulose aerogels. In line with the observed density of cellulose (1560 kg/m³), it was noted that BCAs exhibit porosity exceeding 99% using both pre-freezing methods, whether slower or rapid, before the drying process (Table 2 and Table 3). Our studies proved that BCAs dried with freeze drying have the highest porosity structure [8,16]. Since porosity is directly linked to thermal insulation properties, the high porosity observed in our samples enhances their effectiveness as insulating materials for various applications.

Table 2. Basic parameters of BC aerogels frozen with conventional freezer.

Basic Statistical Assessment	Wet Thickness (cm)	Dry Thickness (cm)	Wet Mass (g)	Dry Mass (g)	Radius (cm)	Volume Density (g/cm3)	Porosity (%)
Mean	0.5541	0.2770	41.4744	0.7667	5.0378	0.0100	99.3611
Stand. Deviation	0.3069	0.2664	23.3855	0.4360	0.6570	0.0068	0.4370
CI lower bound (5%)	0.2609	0.0996	19.6981	0.2528	4.5966	0.0048	99.3074
CI upper bound (95%)	0.6571	0.2784	71.3119	1.2572	5.3534	0.0108	99.6926

When comparing the volume density and porosity of BCAs frozen with liquid nitrogen to those frozen conventionally, our studies found that conventionally frozen samples were slightly denser and had higher porosity, contrary to literature reports [8,16]. Statistical analysis showed that the confidence intervals (CI) for all samples were close, reflecting high precision in estimating the population mean. However, the wet mass of samples had a larger standard deviation and CI range, likely due to some samples having higher water content.

Table 3. Basic parameters of BC aerogels frozen with LN_2.

Basic Statistical Assessment	Wet Thickness (cm)	Wet Mass (g)	Dry Thickness (cm)	Dry Mass (g)	Volume Density (g/cm3)	Porosity (%)
Mean	0.4973	174.0967	0.4707	3.3600	0.0111	99.2900
Stand. Deviation	0.2103	59.8915	0.2995	0.4321	0.0003	0.0173
CI lower bound (5%)	0.0859	59.8247	-0.4238	2.5212	0.0103	99.2570
CI upper bound (95%)	1.1311	357.5053	1.0648	4.6688	0.0116	99.3430

Our observations with BC aerogels frozen using LN2 confirmed similar outcomes as those with different freezing techniques. The data showed that the confidence intervals (CI) for the LN2-frozen samples are slightly more compact than those for samples frozen in a conventional freezer, indicating a higher level of precision in estimating the mean of the population. However, it is worth noting that the wet mass of the samples before LN2 freezing had a larger standard deviation and CI range, which we attribute to varying levels of water content in the samples.

4. CONCLUSIONS

This study partially assessed the impact of freeze-drying conditions on bacterial cellulose aerogels (BCAs) with surface modifications for potential use in the insulation industry as an eco-friendly solution. It evaluated the physical properties of BCAs with varying thicknesses, modification methods for a homogeneous surface, and the effect of freeze-drying. The optimization of freezing speed and chemical treatments was also explored. The analysis showed moderate variability in the data, with confidence intervals (CI) indicating an acceptable level of precision in estimating the population mean.

ACKNOWLEDGEMENTS

References

1. D.G.K. Dissanayake, D.U. Weerasinghe, L.M. Thebuwanage, U.A.A.N. Bandara, *An environmentally friendly sound insulation material from post-industrial textile waste and natural rubber*, Journal of Building Engineering 33 (2021) 101606. https://doi.org/10.1016/j.jobe.2020.101606.

2. M. Ul-Islam, M.W. Ullah, S. Khan, J.K. Park, *Production of bacterial cellulose from alternative cheap and waste resources: A step for cost reduction with positive environmental aspects*, Korean J. Chem. Eng. 37 (2020) 925–937. https://doi.org/10.1007/s11814-020-0524-3.

3. A.M. Mazotto, J. de Ramos Silva, L.A.A. de Brito, N.U. Rocha, A. de Souza Soares, *How can microbiology help to improve sustainability in the fashion industry?*, Environmental Technology & Innovation 23 (2021) 101760. https://doi.org/10.1016/j.eti.2021.101760.

4. D. Klemm, B. Heublein, H.-P. Fink, A. Bohn, *Cellulose: Fascinating Biopolymer and Sustainable Raw Material*, Angewandte Chemie International Edition 44 (2005) 3358–3393. https://doi.org/10.1002/anie.200460587.

5. I.V. Moise, M.M. Manea, S. Vasilca, C. Pintilie, M. Virgolici, M. Cutrubinis, I.R. Stanculescu, V. Meltzer, *The crosslinking behaviour of cellulose in gamma irradiated paper*, Polymer Degradation and Stability 160 (2019) 53–59. https://doi.org/10.1016/j.polymdegradstab.2018.12.005.

6. D. Andriani, A.Y. Apriyana, M. Karina, The optimization of bacterial cellulose production and its applications: a review, Cellulose 27 (2020) 6747–6766. https://doi.org/10.1007/s10570-020-03273-9.

7. M. Yan, Y. Fu, Y. Pan, X. Cheng, L. Gong, Y. Zhou, H. Ahmed, H. Zhang, Highly elastic and fatigue resistant wood/silica composite aerogel operated at extremely low temperature, Composites Part B: Engineering 230 (2022) 109496. https://doi.org/10.1016/j.compositesb.2021.109496.

8. Y. Jiang, S. Chowdhury, R. Balasubramanian, New insights into the role of nitrogen-bonding configurations in enhancing the photocatalytic activity of nitrogen-doped graphene aerogels, Journal of Colloid and Interface Science 534 (2019) 574–585. https://doi.org/10.1016/j.jcis.2018.09.064.

9. W.-J. Yang, A.C.Y. Yuen, A. Li, B. Lin, T.B.Y. Chen, W. Yang, H.-D. Lu, G.H. Yeoh, Recent progress in bio-based aerogel absorbents for oil/water separation, Cellulose 26 (2019) 6449–6476. https://doi.org/10.1007/s10570-019-02559-x.

10. C. Sharma, N.K. Bhardwaj, Bacterial nanocellulose: Present status, biomedical applications and future perspectives, Materials Science and Engineering: C 104 (2019) 109963. https://doi.org/10.1016/j.msec.2019.109963.

11. P. Cazón, G. Velázquez, M. Vázquez, Bacterial cellulose films: Evaluation of the water interaction, Food Packaging and Shelf Life 25 (2020) 100526. https://doi.org/10.1016/j.fpsl.2020.100526.

12. X. He, H. Meng, H. Song, S. Deng, T. He, S. Wang, D. Wei, Z. Zhang, Novel bacterial cellulose membrane biosynthesized by a new and highly efficient producer Komagataeibacter rhaeticus TJPU03, Carbohydrate Research 493 (2020) 108030. https://doi.org/10.1016/j.carres.2020.108030.

13. F. Sederavičiūtė, P. Bekampienė, J. Domskienė, Effect of pretreatment procedure on properties of Kombucha fermented bacterial cellulose membrane, Polymer Testing 78 (2019) 105941. https://doi.org/10.1016/j.polymertesting.2019.105941.

14. N. Mao, 6 - Methods for characterisation of nonwoven structure, property, and performance, in: G. Kellie (Ed.), Advances in Technical Nonwovens, Woodhead Publishing, 2016: pp. 155–211. https://doi.org/10.1016/B978-0-08-100575-0.00006-1.

15. A. Hoseini, C. McCague, M. Andisheh-Tadbir, M. Bahrami, Aerogel blankets: From mathematical modeling to material characterization and experimental analysis, International Journal of Heat and Mass Transfer 93 (2016) 1124–1131. https://doi.org/10.1016/j.ijheatmasstransfer.2015.11.030.

16. M. Sambucci, F. Savoni, M. Valente, Aerogel Technology for Thermal Insulation of Cryogenic Tanks—Numerical Analysis for Comparison with Traditional Insulating Materials, Gels 9 (2023) 307. https://doi.org/10.3390/gels9040307.

PYTEXLIB – OPEN SOURCE PYTHON LIBRARY FOR SCRIPTING TEXTILE STRUCTURES

Yordan Kyosev, Anselm Naake, Ann-Malin Schmidt

TU Dresden, ITM, Chair of Development and Assembly of Textile Products, Dresden, Germany, Hohe Strasse 6, 01069 Dresden, Yordan.kyosev@tu-dresden.de

Abstract

This work presents a small, minimalistic, pure Python based open source library, which was designed to simplify the parametric creation of textile structures. The library comes as result of long years of teaching modelling of textiles at master and PhD level, where the difficulties with all existing packages and the learning outcomes from such one course were considered. The idea of the library is that the students learn at the same time first steps of programming Python using small library, it is running on any operation system and from other point of view, the user is able to concentrate on the textile architecture, not getting lost in the coding style, data structures etc. PyTexLib is used since 4 years successful in the education at TU Dresden and in WE-TEAM program and is available as open source at GitHub.

Key words

Modelling, textile structures, library, open source, 3D modelling, Python

1. Introduction

There are many professional CAD packages for automatic creation of textile structures, which cover single type or groups of textiles. For weaving – there are more than 20 CAD packages [1] , which creates photorealistic simulation of the fabrics and can export machine data, but only few of these can provide real 3D data for FEM simulation or other analysis of the structures (as pore size, CFD, etc.). Only WiseTex provides mechanical computations of the minimal potential energy of the yarns in order to provide mechanically correct geometry [2]. For knitted structures the CAD packages are very limited. Both leading machine producers Stoll and Shima Seiki have excellent photorealistic representations of the weft knitted structures, but 3D view can be generated only by the software of Shima Seiki, but until now is no reported any export option for more simulations. Several types of weft knitted structures and warp knitted structures and as well braided can be generated in 3D and exported to various format by the software of company TexMind (https://texmind.com/). These are convenient for work and export, but are as well limited to the programmed structures inside. Only the software TexGen [3] is open source, which allow scripting and creation of custom structures. Actually, there are few shortcomings working with TexGen which have prevented the authors of using it in the research and caused the creation of a new library. Once problem is, that TexGen works fine with unit cells, but is (or at least during the last year was) not capable to operate fast with large structures with more yarns and filaments (like knitted). The second problem is, that it is GPL Licensed and any advances of the software have to remain GPL License, which is potential problem in case of performing applied research together with industrial partners. Another, third problem is, that although TexGen can be compiled on MACOS and Linux, it does not provide direct installation files for such systems, which was causing troubles during the education of students in a classroom.

Based on this analysis and experience the authors decided in the past to develop small (minimalistic), open access, pure Python based library for scripting textile structures, which can be effiziently used in

the education and for creation of complex or custom structures, which are not covered in the packages of TexMind or else. This was already successful applied in one PhD thesis [4,5] . In the education of the WE-TEAM master students (https://we-team.education/) during the course of Computation Sciences and Engineering Principles for Textiles and during the lectures at TU Dresden.

2. Library structure

Python was chosen as language, because it is currently wide used, free, open source and available on all systems. The library is hosted on GitHub https://github.com/virtualtextiles/pytexlib and a MIT License was chosen, so that any person is free to use it and apply in any projects – public and commercial, without any limitations.

The goal is to have simple library for creating textile structures, where the develop concentrates on the textile and not on the programming structures in Python. For this several classes were developed:

The *fibre* class (file fiberlib.py) is the basic class in the library in the same way as the fibers are the basic elements of all fiber based structures. Each fiber is at the current state with circular cross section and has defined fibre diameter d, colour with the red, green and blue values and has list of coordinates of the fibre axis. The generation of fibre with two points of the axis is as simple as follows:

```
fi=fiber()
fi.diameter=0.2
fi.setcolour(123,23,230)
fi.append_point(1.0,2,3)
fi.append_point(12.0,2,3)
```

The first line constructs new fiber "fi". The second and third lines specify its diameter and color. After that the developer has to add points with their x,y,z, coordinates and can use not only numbers, but as well parameters with all possible options of the Python syntax.

Before one fibre is assigned to a yarn (or other structure), this has to be created by the constructor

```
ya=yarn()
```
In this case as yarn can be created as well non-woven structure, the meaning of one yarn is that it represents *a group of fibers*.
Adding the fiber is then one simple line:
```
ya.add_fiber(fi)
```
Analogously, the yarn has to be assigned into textile structure
```
t=textile()
```
and added there
```
t.add_yarn(ya)
```

With these steps, the textile structure with one yarn and one fiber is ready and can be saved into CSV file
```
t.write_file("mysample.csv")
```
so that this can be visualized by the TexMind Textile Viewer (free software), used as wellin the book Warp Knitting Fabrics Construction [6] and can apply all types of exports (for instance LS-Dyna, Abaqus, Ansys, gltf, STL, x3d etc, Wisetex, Texgen script) in the standard TexMind packages.
The structure can be visualized by the simple command:
```
t.plot()
```

3. Discussion points with open issues

The current library does not contain class for "groups of yarns" which is the case for all ply yarns. Actually two- and three-ply yarns are used very often and even more than the single ply yarns. Additionally, contrary to the structures in the software and the data formats of TexMind for instance, there is no implemented class for groups of (ply) yarns. Such grouping helps significantly for selection and visualization of warp or weft yarns only at woven structures, or different systems of multilayer woven structures (upper layer, bottom layer, connecting warp etc.). Such grouping is efficient in the warp knitting, too, where each guide bar represents separated group of yarns. Both the ply yarns and group of yarns represents two levels of lists of existing objects. During the creation of the library the developers decided initially to skip these levels, in order to simplify the coding. Because in the case of structure with single yarn, it has to be added into ply yarn with one yarn, and this ply yarn has to b added to a group of yarns, which could contain only one yarn, too, if all levels have to be represented. One alternative option for sorting, which is less efficient but more convenient for beginners is the adding of attributes like "Ply Yarn ID" or "Yarn Group ID", which can be used internally for searching and sorting and visualization of the objects from one group without the need of implementation of two more levels of grouping.

Fibre

Yarn

Ply Yarn (group of yarns)

Groups of (ply) yarns
(warp/weft,guide bars)
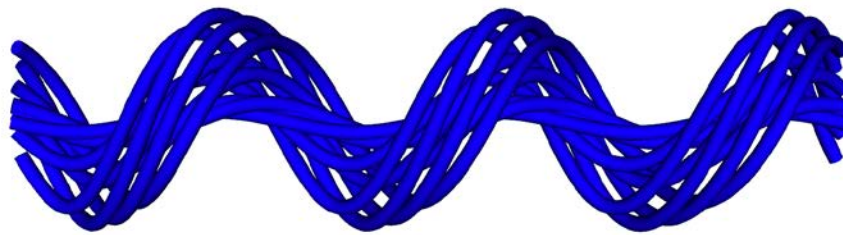
Piece of textile structure

Product

Figure 1. Objects in PyTexLib. The red objects are not implemented for simplicity at the current time

Another aspect is the 3D visualization of the structures. At the current time one option is the export of the geometry as text file with specific format (CSV) and visualization with the free TexMind Viewer. This visualization is better than the using only the 3D axis. The integration of the 3D visualization of the library is possible but had some disadvantages during the teaching. One very powerful 3D library is vtk, actually used in TexMind Viewer. Vtk can be used in Python, too, but requires C++ compiler during the installation. This requires often administrative rights and was trouble for the installation in classroom environments. A very nice and simpler to use, compared to vtk library are pyVista, open3D, or Vedo. They actually all present python warping of vtk, and this brings the same troubles as vtk itself. The authors are looking at the current time for suitable, pure python based 3D library for visualization, which has as less dependencies as possible and works on multiple platform without needs of administrative rights at this point.

4. Results

Figure 2 presents one example of a multifilament yarn created with PyTexLib. This is a yarn with spiral effects, where some core filaments are placed almost straight in the middle of the structure and the remaining filaments are around these. The generation is done within 14 lines of code for this structure, (not considering the PyTexLib and the visualization libraries itself).

Figure 2. Created yarn with spiral effects within PyTexLib.

5. CONCLUSIONS

The new open source python library PyTexLib allows quick start in creating 3D geometries of textile structures. It requires only basic understanding of programming and elementary syntax in order to implement parametric geometric models into 3D visualizations. It can be a good tool for quick start in the 3D modelling of textile structures, especially for such structures, which are not covered in the available CAD packages.

References

1. *Kyosev, Y., Simulation of wound packages, woven, braided and knitted structures, in Veit, D., (Editor), Simulation in Textile Technology, Woodhead Publishing, (2012)*

2. *Lomov, S., Modeling the geometry of textile composite reinforcements: WiseTex, in: Boisse, Ph. (Editor): Composite Reinforcements for Optimum Performance (Second Edition, Woodhead Publishing, (2021)*

3. *Brown, L.P., TexGen, in Advanced Weaving Technology, Y. Kyosev and F. Boussu, Editors. 2022, Springer International Publishing: Cham. p. 253-291. (2022)*

4. *Storck JL, Gerber D, Steenbock L, Kyosev Y. Topology based modelling of crochet structures. Journal of Industrial Textiles,52, (2022)*

5. *Storck, J. L., Feldmann, B. A., & Kyosev, Y.. Design tool for automated crocheting of fabrics. Communications in Development and Assembling of Textile Products, 4(2), 254–272,(2023)*

6. *Kyosev, Y., Warp knitting fabrics construction, CRC Press, (2019)*

FABRICATION OF NANOFIBROUS PVA AND PA4,6 MATERIALS WITH IMPROVED ELECTRICAL CONDUCTIVITY BY INCORPORATING ULTRASONICATED EXPANDED GRAPHITE PARTICLES

Divan Coetzee[1], Juan Pablo Perez Aguilera[2], Thabang Thekiso[3],Jakub Wiener[1]

[1] Department of Material Engineering, Faculty of Textile Engineering, Technical University of Liberec, Liberec, Czech Republic
[2] Faculty of Mechatronics, Informatics and Interdisciplinary Studies, Technical University of Liberec, Liberec, Czech Republic
[3]Department of Nonwovens and Nanofibrous Materials, Faculty of Textile Engineering, Technical University of Liberec, Liberec, Czech Republic

Abstract:

Expanded graphite is an allotrope of carbon which is produced by thermal expansion of graphite, which has been intercalated by acids. This expansion results in an up to 150x increase in the c-axis of graphite particles, allowing for greater access to the graphene sheets in its structure. It is these graphene sheets with their delocalized electrons which are responsible for the electrical conductivity of graphitic structures. To promote access to the graphene sheets, the expanded graphite was ultrasonicated to exfoliate the particles. This ultrasonicated graphite was blended with PVA and PA solutions before electrospinning to produce a nanofibrous material with improved electrical conductive properties. The ultrasonicated expanded graphite had a better effect on the improvement of the electrical conductivity of PVA compared to PA due to the ease of spinning; however, adapting the spinning technique could solve this and improve the overall electrical conductivity for both polymers.

Keywords:

Expanded Graphite; Ultrasonicated Expanded Graphite; Electrospinning; Polyvinyl Alcohol; Polyamide; Nonwoven Composite

1. Introduction

Graphite/graphene-based nanofibrous composites have a wide range of potential applications in energy storage, sensors, fuel cells, radiation shielding, flexible electronics, and specific filtration membranes. An area of interest is also the potential biomedical applications for the material due to their biocompatibility and antibacterial properties, making them suitable for tissue engineering, medical implants and drug delivery systems [1], [2], [3]. Expanded graphite can be considered as an intermediary between graphite and graphene due to its degree of exfoliation. Expanded graphite is commonly produced via the thermal expansion method. Natural graphite is used as the starting material, followed by intercalation using hydrogen peroxide and acids, typically sulfuric or nitric acid, to form expandable graphite. The material is then washed to remove excess intercalant, followed by drying and rapidly heating it to temperatures around 900 °C. This causes the intercalant to rapidly convert to gas, expanding the spacing between the graphite layers to 300 times the original interlayer distance. This expansion between the graphene sheet planes forms a worm-like particle structure with large porosity. The thermal expansion process is illustrated in Figure 1, and a scanning electron microscope image is

presented in Figure 2. The expanded graphite can also be processed into other non-particle forms, such as flexible graphite foils and tapes [4], [5].
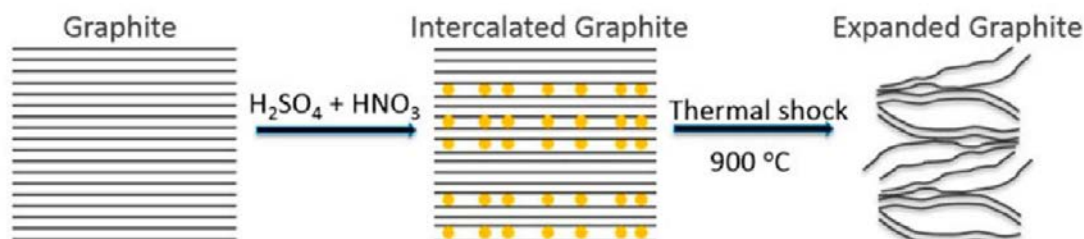
Figure 1: Thermal expansion process of expanded graphite [6]
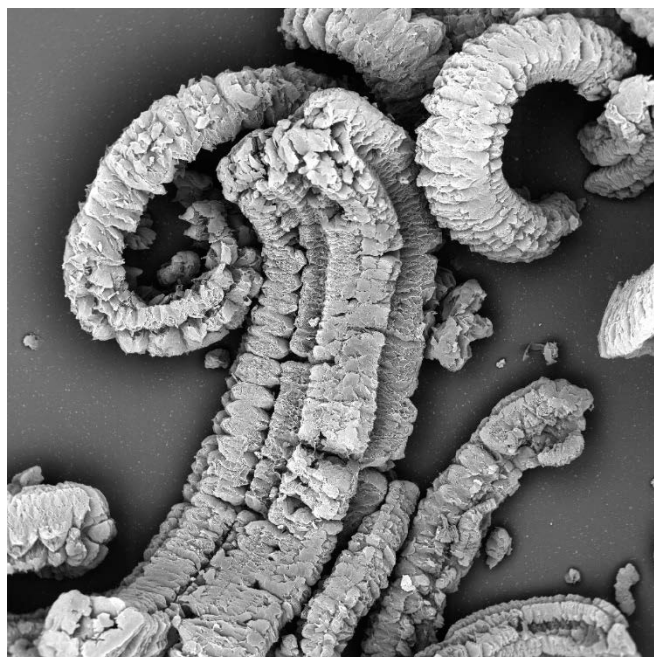
Figure 2: SEM of expanded graphite [7]

Electrospinning is a versatile technique for producing nanofibers with unique properties. Polymers such as polyvinyl alcohol (PVA) and polyamide (PA) are electrically insulative in their pure form and, therefore, could benefit from the improvement in electrical properties offered by graphite to widen their array of applications. This could also have a positive effect on the material's mechanical properties since graphite is a known reinforcer of matrices [8], [9].

2. Experimental
2.1. _Materials_

Expanded Graphite (Sorbetin s.r.o., Czech Republic) was used as filler. Polyamide 4,6 (Stanyl® (PA 4,6), Envalior), glacial acetic acid, and formic acid (PENTA Chemicals) were used as received. Polyvinyl Alcohol (130.000 Mw and 88-89% hydrolyzed, Sigma-Aldrich) was used as obtained with deionized water.

2.2. _Methods_
2.2.1. Sample preparation and measurement

Expanded graphite was ultrasonicated at 45W for 1 h in distilled water to produce ultrasonicated expanded graphite (uEG). This was done until no porous material floated on the water's surface. The material was then dried at 80 °C for 30 minutes and stored partially covered in a dry cupboard. To

prepare the PA 4,6 stock solution, 14 wt% PA 4,6 was dissolved in a 1:1 mixture of glacial acetic acid and formic acid and stirred magnetically for 24 hours at room temperature. The PVA stock solution was prepared by magnetically stirring 10% PVA in deionized water at 90°C for 24 hours. The uEG was added in the required proportion for each solution and ultrasonicated for 10 minutes. The inclusion of uEG had a major impact on the solution viscosity; therefore, for PA 4,6, 10%, 15%, and 20% uEG in the dry material were prepared for electrospinning. For PVA, 10%, 20%, and 30% uEG in the dry material were chosen for electrospinning. Solutions could not be prepared with higher uEG concentrations due to viscosities high enough to impede electrospinning. Samples were visually characterized using a Scanning Electron Microscope (Vega3 Tescan). Electrical surface resistivity measurements were made according to the EN61340-5-1:2001 standard for protection of electronic devices from electrostatic phenomena. Measurements were made on a Hewlett Packard 4339B resistance meter.

2.2.2. DC Electrospinning parameters

A simple needle to grounded steel plate collector DC electrospinning device was employed to produce the nanofibrous materials from the selected solutions and a negative control for each polymer. The electrospinning parameters are presented in table 1.

Table 1. Electrospinning parameters.

| Solution	Voltage [kV]	Distance from collector [cm]	Syringe pump rate [mL/min]	Needle gauge
Pure PVA	16	12	0,03	22
Pure PA 4,6	15,4	13,5	0,01	21
PVA:uEG	18	13	0,007	18
PA 4,6:uEG	18,5	13	0,01	18

3. Results and discussion

3.1. *Electrical conductivity*

Electrical surface resistivity measurements are presented in Table 2 and graphically in Figure 3. Measurements were made at 50 % RH and 24.5 °C.

**Table 2:** Electrical surface resistivity of PVA and PA composite samples

Sample	Surface resistivity (Ohm)	Standard deviation (Ohm)
PVA	2.09E+13	2.67E+13
PVA10%uEG	8.43E+11	4.93E+11
PVA20%uEG	5.51E+10	8.05E+10
PVA30%uEG	1.29E+10	3.27E+09
PA	1.35E+12	3.65E+10
PA10%uEG	8.61E+11	6.75E+11
PA15%uEG	2.78E+12	2.00E+12
PA20%uEG	7.21E+11	7.13E+11
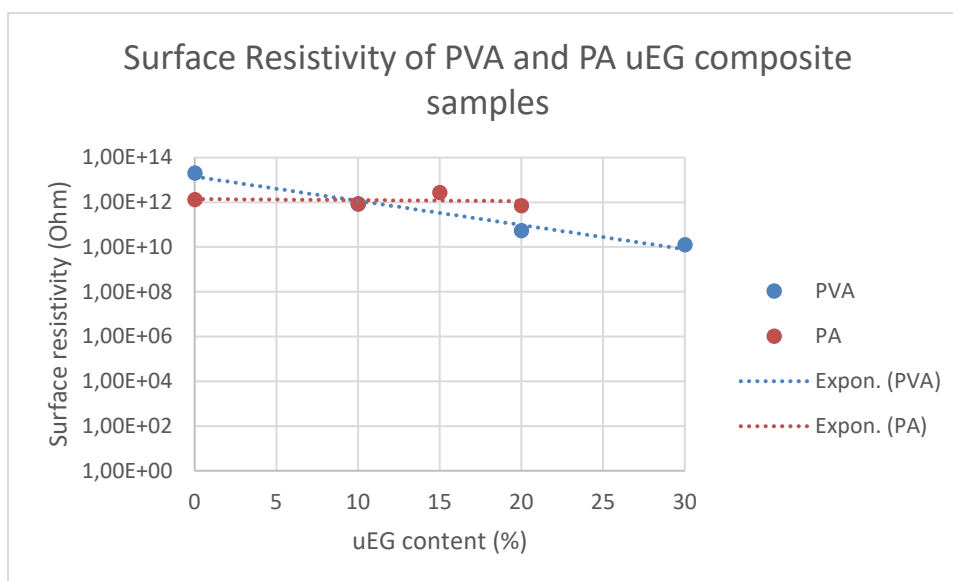
Figure 3: Surface resistivity of PVA/PAuEG samples

Both PVA and PA composite samples fared very differently in terms of electrical conductivity. This was measured as a function of the material's electrical resistivity, where the PVA sample Showed a consecutive improvement upon particle loading. This resulted in an electrical resistivity decrease of 10^2 Ω at 10 % uEG loading and a further 10^1 Ω magnitude when loading at 20 %. The electrical resistivity decreased slightly when loading up to 30 % uEG. The PA samples exhibited mixed results where electrical resistance decreased by a factor of 10^1 Ω when loading up to 10 % uEG and then increased again when loading up to 15% uEG, before decreasing back to the same level as the 10 % uEG sample upon 20 % loading. This can be attributed to the spinnability of the material, where graphite's effect on the solution viscosity played a role. This effect was visually confirmed on the final material using SEM. Both samples exhibited lower electrical conductivity than expected. However, this was attributed to the low sample volume obtained from the spinning technique and the influence of air on the nonwoven structure acting as an insulator.

3.2. *SEM and fiber morphology*
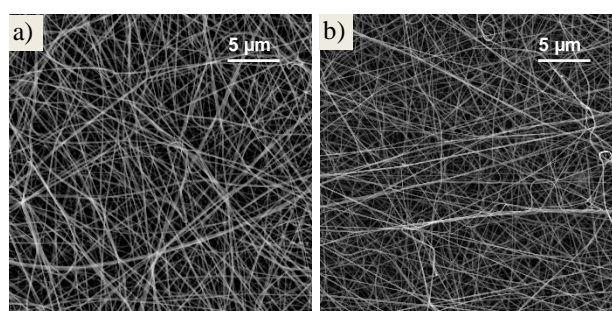
Figure 4. SEM images for a) pure PVA and b) pure PA 4,6.

Figures 4, a, and b show the morphology of the electrospun nanofibers from the pure polymers as control samples. The nanofibers appear uniform and well-defined in both cases, with smooth surfaces and consistent diameters. No visible particulates or structural irregularities were observed, confirming the baseline characteristics of each polymer without particle addition. The PVA nanofibers were determined to have a fiber diameter of 381.47 ± 123.25 nm, and the polyamide fibers have a diameter of 221.50 ± 58.19 nm.
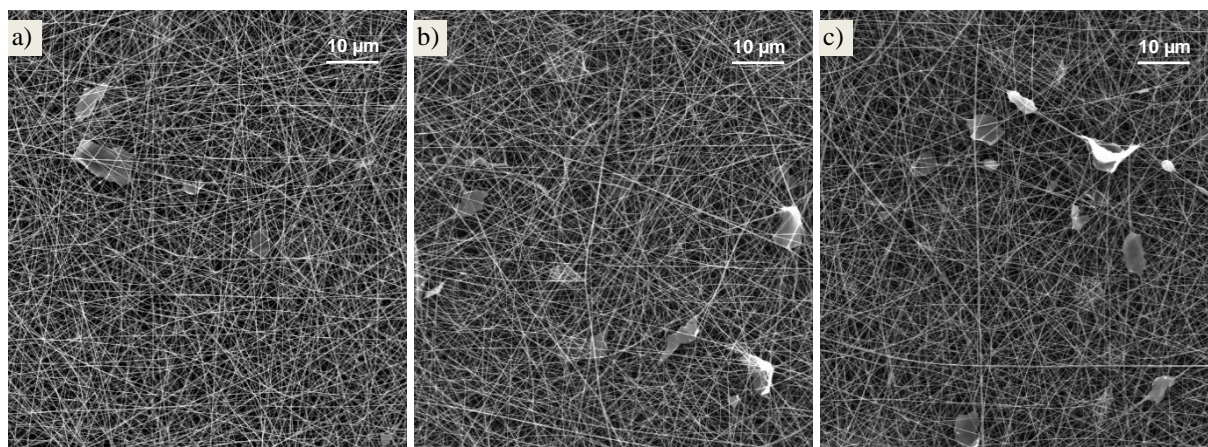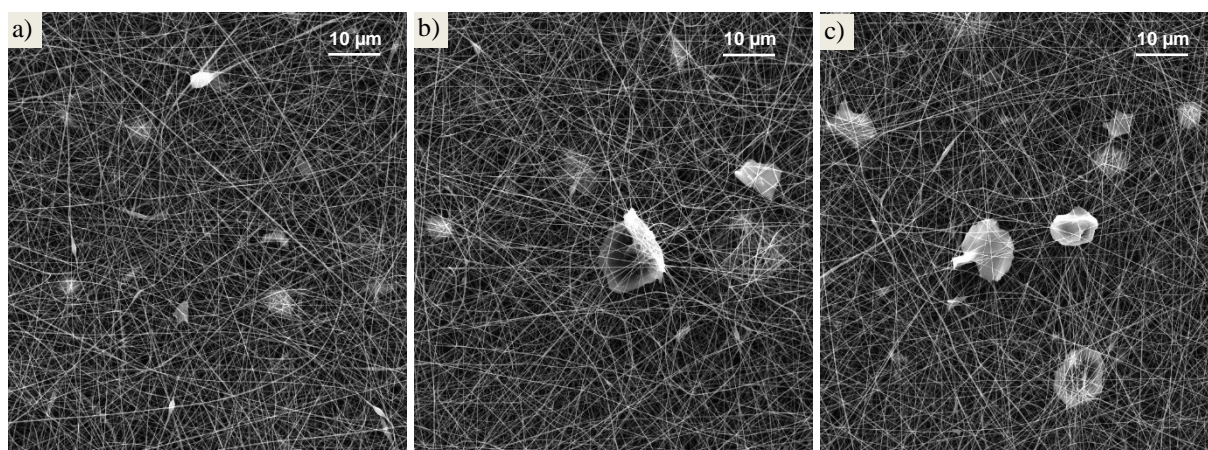
Figure 5. SEM images for PVA electrospun samples with a) 10% uEG, b) 20% uEG, and c) 30% uEG.

Figure 5 displays the results of electrospinning PVA with uEG. Fig. 5 a) shows how graphite particles of varying sizes (up to 15 µm) appear in the material. These dispersed graphite layers appear enclosed inside a polymer matrix that connects with the surrounding fibers. This is due to how the polymer chains interact during the jet formation event in the electrospinning process. The electric field drives the entangled chains out of the polymer jet. In this process, chains wrap around the graphite layers as they are expelled and dry over them in the trajectory toward the collector. This way, the nanofibers seem to have sections that encapsulate the graphite layers. The fiber diameter for this sample is 260.38 ± 78.98 nm, which is a significant decrease both in size and variability. This could be explained by the increase in conductivity caused by the uEG.

In Fig. 5 b), the higher concentration of uEG in the solution results in more enveloped graphite layers appearing in the material. The sizes remain the same as in the previous sample, but they seem to be better distributed. This sample presented a fiber diameter of 253.29 ± 44.88 nm, which is not a significant change, but the size-decreasing trend seems to be maintained. The last sample shown in Fig. 5 c) showed the highest occurrence of the encapsulated graphite layers in the nanofibers. This confirmed that increasing the uEG concentration in solution results in a higher loading of graphite layers in the dry material. The fiber diameter slightly decreases to 243.66 ± 75.10 nm, following the trend observed previously.

Figure 6. SEM images for PA 4,6 electrospun samples with: a) 10% uEG, b) 15% uEG, and c) 20% uEG.

Figure 6 shows the PA 4,6 samples with uEG. In Fig. 5 a), small graphite particles are present; they appear to be encapsulated in polymer just as with the PVA samples mentioned above. The fiber

diameter in this sample is 208.96 ± 62.68 nm, a slight decrease from the pure polymer. In the next figure (Fig. 6.b)), more graphite is present in the material. In this case, the graphite appears to be distributed in bigger and thicker clusters, which are still enveloped in polymer. This poor distribution of graphite in the material could hinder the intended improvement in conductivity. The fiber diameter is 208.54 ± 54.36 nm, no change from the previous sample. Finally, Fig. 6.c) displayed a higher number of voluminous graphite particles encased in polymer throughout the material. This confirmed that a higher amount is present in the dry material due to the higher loading in the solution, even with poor distribution. The fiber diameter slightly increased to 225.32 ± 112.68 nm, which seems to be a result of the dramatic increase that the uEG has on the viscosity of the PA 4,6 solutions.

When comparing the results for PVA and PA 4,6, it is evident that uEG is more effectively exfoliated in the PVA solution. As shown in Fig. 5, the PVA samples exhibit thinner and more uniformly distributed graphite layers throughout the material. In contrast, the PA 4,6 samples depicted in Fig. 6 contain larger graphite particles with poor planar distribution. This distribution of graphite within the polymer matrix plays a critical role in determining the system's conductivity. Consequently, it is anticipated that PVA samples will demonstrate more significant conductivity enhancements compared to PA 4,6 samples. The exfoliation of uEG in the solution also impacts the solution's conductivity, as evidenced by a notable reduction in fiber diameter and variability in the PVA samples. A similar trend was observed in the PA 4,6 samples.

While the electrospinning process successfully produced nanofibers for both polymers, its efficiency was significantly limited by the use of a needle electrode. The presence of large particles frequently caused needle clogging, making the production of thicker samples both labor-intensive and time-consuming. To address this limitation, an open-surface spinning electrode could be employed (using either DC or AC electrospinning). This approach would facilitate the production of thicker layers, increasing the likelihood of graphite particles forming conductive pathways and thereby enhancing the material's overall conductivity.

4. CONCLUSIONS

Expanded graphite in its pure form cannot be electrospun due to its large particle size. Due to this limitation, it was decided to process it using ultrasonication. Therefore, expanded graphite, in the form of ultrasonicated expanded graphite, was successfully incorporated into a nonwoven electrospun PVA and PA matrix. Due to increased conductivity by incorporating the carbon filler, the PVA fibers were finer at higher particle loading. The uEG also appeared to be very well distributed in the polymer matrix, and the electrospinning process appeared to easily incorporate thin layered graphite into the structure. The uEG had a different effect on the Polyamide material, where it would appear that it would be less evenly distributed throughout the material, and the increase in viscosity resulted in larger graphite particles entering the matrix during electrospinning. Both these effects are known to result in lower electrical conductivity and therefore could explain why the PA samples performed so poorly compared to the PVA samples. Both samples exhibited lower electrical conductivity than expected. However, this was attributed to the low sample weight obtained by electrospinning and the presence of air in the sample due to the porosity of nonwoven materials, in which air acts as an insulator. This can be improved by improving the electrospinning technique to increase the production volume to increase the sample areal weight by producing a thicker layer of nonwoven material.

ACKNOWLEDGEMENTS

References

1. H. Abdali and A. Ajji, "Functionalized Graphene/Polymer Nanofiber Composites and Their Functional Applications," in Graphene Functionalization Strategies, A. Khan, M. Jawaid, B. Neppolian, and A. M. Asiri, Eds., in Carbon Nanostructures. , Singapore: Springer Singapore, 2019, pp. 127–156. doi: 10.1007/978-981-32-9057-0_5.

2. B. Kouini and H. Belhamdi, "Graphene Nanofiber-Based Composites for Fuel Cell Application," in Electrospinning of Graphene, S. K. Tiwari, S. Sahoo, and N. Wang, Eds., in Carbon Nanostructures. , Cham: Springer International Publishing, 2021, pp. 149–177. doi: 10.1007/978-3-030-75456-3_6.

3. A. Kausar, I. Ahmad, T. Zhao, O. Aldaghri, K. H. Ibnaouf, and M. H. Eisa, "Nanocomposite Nanofibers of Graphene—Fundamentals and Systematic Developments," J. Compos. Sci., vol. 7, no. 8, p. 323, Aug. 2023, doi: 10.3390/jcs7080323.

4. P. Murugan, R. D. Nagarajan, B. H. Shetty, M. Govindasamy, and A. K. Sundramoorthy, "Recent trends in the applications of thermally expanded graphite for energy storage and sensors – a review," Nanoscale Adv., vol. 3, no. 22, pp. 6294–6309, 2021, doi: 10.1039/D1NA00109D.

5. D. Coetzee, J. Militký, J. Wiener, and M. Venkataraman, "Comparison of the Synthesis, Properties, and Applications of Graphite, Graphene, and Expanded Graphite," in Advanced Multifunctional Materials from Fibrous Structures, vol. 201, J. Militký and M. Venkataraman, Eds., in Advanced Structured Materials, vol. 201. , Singapore: Springer Nature Singapore, 2023, pp. 71–87. doi: 10.1007/978-981-99-6002-6_4.

6. B. Mazela, A. Batista, and W. Grześkowiak, "Expandable Graphite as a Fire Retardant for Cellulosic Materials—A Review," Forests, vol. 11, no. 7, p. 755, Jul. 2020, doi: 10.3390/f11070755.

7. D. Coetzee et al., "Effects of expanded graphite's structural and elemental characteristics on its oil and heavy metal sorption properties," Sci Rep, vol. 14, no. 1, p. 13716, Jun. 2024, doi: 10.1038/s41598-024-64695-0.

8. M. Ahmadi Bonakdar and D. Rodrigue, "Electrospinning: Processes, Structures, and Materials," Macromol, vol. 4, no. 1, pp. 58–103, Feb. 2024, doi: 10.3390/macromol4010004.

9. L. Jianxin, Y. Hengzhe, C. Xuedi, Z. Xiaolei, and F. Junlin, "Review of electrospinning technology of photocatalysis, electrocatalysis and magnetic response," J Mater Sci, vol. 59, no. 24, pp. 10623–10649, Jun. 2024, doi: 10.1007/s10853-024-09788-x.

Tato publikace neprošla redakční ani jazykovou úpravou